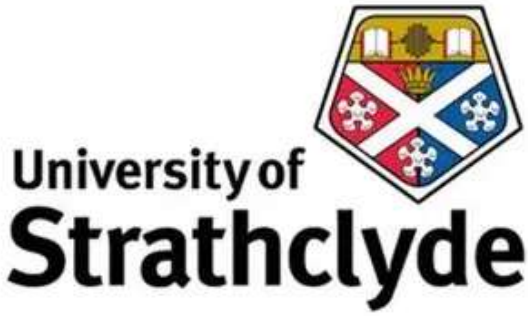

University of Strathclyde

Electrical and Electronic Engineering Department

Glasgow, UK

Modelling and Stability Analysis of Power Systems Considering Multiple Converter Interactions

by

Tesfu Gebremedhin

A thesis presented in fulfilment of the requirements for the degree of Doctor of Philosophy

March 2026

Declaration

This thesis is the result of the author's original research. It has been composed by the author and has not been previously submitted for examination which has led to the award of a degree.

Acknowledgements

I would like to express my deepest and most sincere gratitude to everyone who supported, guided, and encouraged me throughout my PhD journey at the University of Strathclyde, Glasgow. This journey has been one of the most challenging, transformative, and rewarding experiences of my life.

First and foremost, I thank God for granting me strength, patience, clarity of mind, and perseverance during the most difficult times. Without His guidance and blessings, this important milestone would not have been possible.

I am profoundly grateful to my principal supervisor, Professor Lie Xu, for his outstanding guidance, continuous encouragement, and unwavering support throughout my research. His deep knowledge, valuable advice, and dedication to excellence have played a crucial role in shaping both my research and my development as a researcher. I also sincerely thank Dr. Yen Chen for her kind guidance, support, and constructive advice, which greatly contributed to the success of this work.

I would like to express my sincere thanks to my industrial supervisors, Dr. Dong Chen and Benjamin Marshall, and to my second academic supervisor, Professor Agustí Egea-Álvarez, for their valuable feedback, technical insight, and practical advice, all of which played a vital role in improving the quality of this research. I am also grateful to Dr. Sam Harrison for his expertise, helpful suggestions, and friendly support. My appreciation is further extended to the PEDEC research group, whose teamwork, encouragement, and positive research environment made this journey both productive and enjoyable.

This thesis is dedicated to the loving memory of my beloved father, Berhane Gebermedhin, and my youngest brother, Merhawi. Their love, strength, and inspiration live on in my heart and continue to guide me in all that I do.

Finally, my deepest appreciation goes to my beloved family my mother, Genet and my brothers, Awet and Hailat for their endless love, patience, sacrifice, and unwavering belief in me. This achievement would not have been possible without your support.

Abstract

The rapid integration of converter-based renewable generation is fundamentally changing the dynamic behaviour of modern power systems. The progressive displacement of synchronous machines reduces natural inertia and short-circuit capacity, thereby increasing the system's sensitivity to oscillatory, frequency, and voltage instabilities. These challenges are particularly severe in weak networks characterised by long transmission distances, high impedance levels, and a high penetration of power electronic converters. Under such conditions, dynamic interactions between converter control systems and the surrounding network may introduce resonances, restrict controllability, and reduce stability margins. This thesis addresses these challenges through a systematic impedance-based stability analysis of multi-converter power systems. The work first develops detailed small-signal models of converters and networks. Converter control dynamics, including phase-locked loop and current control effects, are represented together with the frequency-dependent behaviour of cables and transmission components. Both single-input single-output and multi-input multi-output impedance representations are formulated. The multi-input multi-output framework enables the analysis of cross-coupling effects that cannot be captured by conventional scalar impedance methods. Stability assessment is conducted using the Generalized Nyquist Criterion, ensuring consistency with established impedance-based theory. A principal contribution of this thesis is the formulation and application of two impedance-based stability measures: the Impedance Ratio (IR) and the Eigenvalue-Impedance Ratio (EIR). Although impedance ratios and eigenvalue analysis are established concepts, their structured combination within a multi-converter, frequency-dependent framework has not previously been formalised in this manner. The novelty lies in integrating impedance interactions with eigenvalue sensitivity information to provide a quantitative link between impedance characteristics and system pole movement. This integration enables the identification of dominant interaction paths and the quantification of stability margins under realistic operating conditions. Unlike conventional grid-strength indices such as Short Circuit Ratio (SCR), General Short Circuit Ratio (GSCR), Grid Strength Impedance Matrix (GSIM), and Multi-Infeed Interaction Factor (MIIF), the proposed application of IR and EIR explicitly incorporates converter control dynamics and frequency-dependent network behaviour. The contribution therefore lies in their methodological integration, analytical interpretation, and validation within multi-converter systems. The methods are validated through frequency-domain analysis and time-domain simulations for two-converter and multi-converter case

studies. The results demonstrate how converter spacing, control mode selection, and impedance composition influence resonance formation and stability margins. The relationship between IR, EIR, and pole trajectories is explicitly demonstrated, providing physical insight into interaction mechanisms. The impact of grid-following and grid-forming converter placement is systematically examined, showing how their proportion and location affect system strength and interaction patterns. To improve computational efficiency, a structured model-reduction approach is also developed. An error index is defined to quantify deviations between full-order and reduced-order models. The results show that weak grids require higher-order representations to preserve critical dynamics, whereas stronger grids permit simplification without significant loss of accuracy. The limitations of this work are acknowledged. The analysis is based on linearised small-signal models around specific operating points and does not address large-disturbance transient stability or electromagnetic transients. In addition, the validation is conducted through simulation studies rather than experimental implementation. Despite these limitations, the thesis provides a coherent and methodologically justified extension of impedance-based stability analysis and offers practical guidance for the design and operation of converter-dominated power systems.

Nomenclature

Abbreviation	Definition
AC	Alternating Current
DC	Direct Current
DQ	Direct Quadrature Domain
EIR	Eigenvalue Impedance Ratio
FFT	Fast Fourier Transformation
GFL	Grid-Following Converter
GFM	Grid-Forming Converter
GNC	Generalised Nyquist Criterion
GSIM	Grid Strength Impedance Metric
ICC	Inner Current Controller
IF	Interaction Factors
IR	Impedance Ratio
LPF	Low Pass Filter
MIMO	Multiple-Input and Multiple-Output
MIIF	Multi- Infeed Interaction Factor
MVSC	Multi-Voltage Source Converter
EMT	Electromagnetic Transient
PCC	Point of Common Coupling
PI	Proportional-Integral
PLL	Phase-Locked Loop
p.u.	Per-Unit
PWM	Pulse Width Modulation
RHP	Right-Half Plane
SCR	Short Circuit Ratio
SISO	Single-Input and Single-Output
VSC	Voltage Source Converter

List of Figures

Figure 1.1: Classification of Power system stability [17] 3
Figure 1.2: Small-Signal Stability Analysis of AC system with Power Electronic Converters[12] 5
Figure 1.3: Progression towards and electric energy system with dominant Converter technology [26] 7
Figure 1.4: Converter-Dominated Renewable Power System 9
Figure 1.5: Small -signal representation and minor loop-gain of a system portioned into two subsystems: (a) Voltage-Source Configuration (b) Current-Source Configuration. 13
Figure 1.6: Illustration defining the stationary αβ reference frame, the rotating dq reference frame, and the three-phase abc reference frame. 14
Figure 1.7: Illustration of transformations between various reference frames [40] 14
Figure 1.8: Schematic of Two -Level Voltage source converter 17
Figure 1.9: Schematic and Simplified Representation of the Converter Model 25
Figure 2.1: Voltage Source Converter connected to network. 31
Figure 2.2: Control System Architecture of a Grid-Connected GFL Converter 33
Figure 2.3: Block diagram of the PLL loop Control Structure 35
Figure 2.4: (a) Schematic Representation of Voltage-Oriented d-q Reference Frames (b) steady -state voltage vector diagrams the d-q frame. 37
Figure 2.5: relationship between Δθ and ΔVq 38
Figure 2.6: Schematic Diagram Illustrating the Calculation of VSC Admittance 43
Figure 2.7: Control System Architecture of a Grid-Connected GFM Converter 49
Figure 2.8: Frequency-droop controller for GFM 50
Figure 2.9: Different control structure of the PSL-based GFM Control 52
Figure 2.10: Simulation model with perturbation voltages injection analysis 57
Figure 2.11: GFL Admittance Validation Considering Only Inner Current Controller 62
Figure 2.12: Validation of GFL(PV/PQ) Admittance Model Including Outer Control Loop 63
Figure 2.13: Validation of GFM Converter Admittance Model (a) pp and (b) pn 64
Figure 2.14: Validation of GFM vs. GFL Admittance Model 66
Figure 2.15: Small-signal representation of a converter-connected system 67

Figure 2.16: Definition of gain margin and phase margin..... 68
Figure 2.17: Stability Assessment Across Different PLL Frequencies..... 70
Figure 2.18: Converter Admittance at Various PLL Bandwidths and Its Intersection with Grid Admittance 71
Figure 2.19: Eigenvalue of Nyquist stability analysis at Frequency of PLL 40 Hz 72
Figure 2.20: Nyquist plot for PLL frequency 40 Hz 72
Figure 2.21: Simulation Waveforms of (I_d , I_q) and active power (P) in p. u. 73
Figure 3.1: Schematic Representation of a Two-Terminal VSC System Connected to AC Grid with Remote and Local Converters 80
Figure 3.2: Schematic Diagram for Outer-Loop Control Strategies (a) PV Control and (b) PQ Control 81
Figure 3.3: VSC Converters Under Different Control Modes Connected to AC Network . 81
Figure 3.4: Small-Signal Stability Analysis via Disturbance Injection at Local Converter 85
Figure 3.5: Equivalent Impedance Model of Converter-Grid Interaction 86
Figure 3.6: Impedance Validation of Converter under (PV) Control and $Z_{network+network}$ Under PQ and PV Control System Under Coupling One Parameter..... 90
Figure 3.7: IR change Under PQ and PV Control System Under Coupling One Parameters 91
Figure 3.8: Eigenvalue of IR changes Under PQ and PV Control Under Coupling One Parameters..... 92
Figure 3.9: Impedance $Z_{network+netw}$ Under PQ and PV Control System Under Coupling Two Parameters..... 93
Figure 3.10: IR change Under PQ and PV Control System Under Coupling Two Parameters 94
Figure 3.11: Eigenvalue of IR changes Under PQ and PV Control Under Coupling Two Parameters 94
Figure 3.12: Nyquist Plots for Remote Converter (PV and PQ) and GFM Control Mode, with Local Converter in PV Mode under a Specific Coupling one Parameter 96
Figure 3.13: (a) Nyquist Plots Without and with Remote Converter in PV and PQ modes, and with Local Converter operating in PV mode under two coupling parameter conditions; (b) Impedance comparison between $Z_{network+conv}$ and $Z_{network}$ 97

Figure 3.14: Stability Analysis via Eigen of Nyquist Criterion for PV Control Under Resonance (a)λ1 (b) λ2 98
Figure 3.15: Nyquist Analysis with and without Remote Converter Under PQ Control 100
Figure 3.16: Time domain simulations under varying power levels, (a): with remote converter under PQ control; and (b): without remote converter 101
Figure 3.17: IR change at different PLL and PI value 102
Figure 3.18: Time domain simulation of local converter d-axis voltage and current and active power (P) Under Coupling Two PV with modified PLL parameters in PV mode 103
Figure 3.19: Effect of varying the (P) value in the outer-loop controller on (a) IR, (b-c) EIR, and (d) the Nyquist stability analysis 105
Figure 3.20: Impedance-based analysis with remote converter in PQ mode and local converter in PV mode: (a) IR, (b-c) EIR, (d) Nyquist stability analysis 106
Figure 3.21: Time-domain response with remote PQ mode (inverter/rectifier) and local PV mode 107
Figure 3.22: To Reshaping GFL Impedance Under PV Control System 108
Figure 3.23: Reshaping of the converter impedance for GFL operation under PV control, showing (a) IR, (b-c) EIR, and (d) Nyquist stability analysis 110
Figure 3.24: SCR Correlation with IR and EIR in IF for Coupling Two PV 111
Figure 4.1: Network Topology of Multiple Connected Converters 114
Figure 4.2: Topological Representation of Multi-VSCs (Three-N) Integrated into an AC Network 116
Figure 4.3: Equivalent-Impedance Model of Middle and Remote Converters in AC Network 118
Figure 4.4: (a)IR and (b, c) Eigenvalue of IR variations Under PQ and PV Control of Coupling One Parameter 120
Figure 4.5: Zconv + network variations in GFL Control Under Coupling Two Parameters 122
Figure 4. 6: (a, b) IR and (c, d) EIR variations in GFL Control Under Coupling Two Parameter 122
Figure 4.7: IR in GFM and GFL Control Under Coupling Two Parameters 124
Figure 4.8: (a) and (b) EIR changes in GFM and GFL Control Under Coupling Two Parameters 124

Figure 4.9: Nyquist Stability Analysis of GFL Control Mode in a Three-Converter System 125
Figure 4.10: Nyquist Stability Analysis of GFL Control Mode in a Three-Converter System 126
Figure 4.11: Nyquist Stability Analysis of GFM Control Mode in a Three-Converter System 128
Figure 4.12: IR (a) and EIR (b, c) changes Under GFL Control in Rectifier and Inverter Modes Under Coupling Two..... 129
Figure 4.13: Nyquist Plots for Rectifier and Inverter Modes of a Three-Converter System Under Coupling Two Parameters..... 130
Figure 4.14: IR (a) Phase and (b) Magnitude and Stability Across Various Converter Configurations Illustrated Using Bar Graph Representation..... 135
Figure 4.15: Outer Control-Induced Impedance Reshaping in GFL (PQ/PV) Operated MVSCs 137
Figure 4.16: IR (a) and EIR (b, c) Changes and Nyquist Plots(d), Due to Reshaping of GFL 138
Figure 4.17: Time Domain Simulation -Impedance Reshaping of GFL in (PV, PV, PV) Control System 139
Figure 4.18: Impedance Reshaping through Virtual Resistance in GFM Control..... 140
Figure 4.19: IR (a) and EIR (b, c) Changes and Nyquist Plots(d) Due to Reshaping of GFM 141
Figure 4.20: Time-Domain Simulation of (GFM, PV, PV) Configuration with Impedance Reshaping Applied to GFM-Controlled Converter 142
Figure 4.21: Multiple Converters in a Network with Cable Connections 143
Figure 4.22: The Impact of shaping the Network system with Cable design..... 145
Figure 4.23: Nyquist stability with the Impacts of Cable design 146
Figure 5.1: Impedance Characteristics of Simplified GFL Converter Model 153
Figure 5.2: Current injection to Analysis Time domain simulation 157
Figure 5.3: Impedance of remote converter with (a) PV and (b) PQ Control mode 158
Figure 5.4: (a) Impedance of $Z_{network}$ v.s. $Z_{network+conv}$ and (b) IR change..... 159
Figure 5.5: EIR Analysis for Detailed and Simplified Models Under PV/PQ Control..... 160
Figure 5.6: (a) Impedance comparison between $Z_{network+conv}$ and $Z_{network}$; (b) IR..... 162
Figure 5.7: Eigenvalue Movement with Variation in Inertia Ratio (a) λ_1 (b) λ_2 163

Figure 5.8: Nyquist Stability Comparison between Detailed and Simplified Local PV Converter Models in Coupled System with Remote PV and PQ Converters (Coupling -One parameters) 164
Figure 5.9: Nyquist Stability Comparison between Detailed and Simplified Local PV Converter Models in Coupled System with Remote PV and PQ Converters (Coupling -Two parameters) 165
Figure 5.10: Time-Domain Response of Local Converter d-axis Voltage, Current, and Power for Detailed Model Under Coupling Condition Two 166
Figure 5.11: Time-Domain Dynamics of Local Converter d-axis Voltage, Current, and Power Using Simplified Model ($T_{d1} = 0.1\text{ms}$) Under Coupling Two 166
Figure 5.12: Remote converter Impedance error magnitude in (%) and phase (°) for (a) PV and (b) PQ Control modes 168
Figure 5.13: IR Mangitude (%) and Phase(°) error for (a) PV (b)PQ Control Modes ... 168
Figure 5.14: Eigenvalue of IR change error Magnitude in (%) and phase (°) PV 169
Figure 5.15: Eigenvalue of IR change error Magnitude in (%) and phase (°) PQ 169
Figure 5.16: Impedance of remote converter percentage error Magnitude in (%) and phase (°) (a) PV and (b) PQ Control mode 171
Figure 5.17: IR percentage error Magnitude in (%) and phase (°) (a) PV (b)PQ 171
Figure 5.18: EIR change error PV Magnitude in (%) and phase (°) 172
Figure 5.19: EIR change error Magnitude in (%) and phase (°) PQ 172
Figure 5.20: Error Reduction analysis of the Remote Converter 174
Figure 5.21: Impedance of remote converter comparison between detailed and simplified with lead-lag (a) PV and (b) PQ Control mode 176
Figure 5.22: Nyquist Plots with Lead-Lag Compensation Under Coupling-One PV Control 176
Figure 5.23: Nyquist Plots with Eror Reduction Under Coupling-Two PV Control 177
Figure 5.24: 3D chart of Error Metrices Index for Different Coupling Configuration 184
Figure A1:1 Assessment of Different PLLs for the (PV, PV) System 207
Figure A1:2 Influence of Control Parameter Interactions on Network Dynamics 209
Figure A1: 3 Stability Sensitivity Heat Map for Varying Active Power (P) 210
Figure B1:1 Impedance-Based Stability Indices Highlighting Best (Green) and Worst (Red) Delay Performance 211

List of Tables

Table 1:Stability Analysis of Converter Dominated Network System..... 22
Table 2.1: Control Parameters for VSCs Controller 34
Table 2.2: The system parameter for weak and strong Coupling 34
Table 3.1: The system parameter for weak and strong Coupling..... 80
Table 3.2: The system parameter for weak Coupling..... 80
Table 4.1: The system parameter for weak and strong Coupling 119
Table 4.2: Summary of Converter Control Interaction and Stability Impact 132
Table 4.3: Simulation Results under Coupling-One Parameters in Frequency range 80-130 Hz with $Z_{l23} = 0.15$ and $Z_{l21} = 0.15$, PLL frequency: 30 Hz 133
Table 4.4 :Simulation Results under Coupling-One Parameters in Frequency range $Z_{l23} = 0.1$ and $Z_{l21} = 0.2$, PLL frequency: 30 Hz..... 134
Table 4. 5: Simulation Results under Coupling-Two Parameters in Frequency range $Z_{l23} = 0.15$ and $Z_{l21} = 0.15$, PLL frequency: 30 Hz..... 134
Table 4.6: Simulation Results under Coupling-Two Parameters in Frequency range $Z_{l23} = 0.1$ and $Z_{l21} = 0.2$, PLL frequency: 30 Hz..... 134
Table 5.1: Coupling one Index results under PV control model..... 179
Table 5.2: Coupling one Index results under PQ control model 179
Table 5.3: Coupling Two Index results under PV control model 180
Table 5.4: Coupling Two Index results under PQ control model 181
Table 5.5: Coupling one Index results under PV control model..... 182
Table 5.6: Coupling one Index results under PQ control model 182
Table 5.7: Coupling Two Index results under PV control model 182
Table 5.8: Coupling Two Index results under PQ control model 183

Table of Content

Declaration ..... **ii**
Acknowledgements ..... **iii**
Abstract ..... **iv**
Nomenclature ..... **vi**
List of Figures ..... **vii**
List of Tables ..... **xii**
Table of Content ..... **xiii**
Chapter 1: Introduction **1**
1.1 General Introduction 1
1.2 Challenges of Multi-Converter Dynamics in Modern Power Networks 5
1.2.1 Shift from Synchronous to Converter-Dominated Systems 6
1.2.2 Stability Challenges in Multi-Converter Systems 7
1.2.3 Modelling Complexities in Multi-Converter Networks 8
1.2.4 Global Trends in Converter-Dominated Network 9
1.3 Power System Stability 2
1.4 Impedance Modelling and Stability Analysis 10
1.4.1 Impedance-Based Stability Analysis 10
1.4.2 Voltage-Source and Current-Source Systems 12
1.4.3 Definition of reference frame and frame transformation 13
1.5 Impedance Modelling of Grid-Connected Converters 15
1.5.1 Two -Level Voltage-Source Converter 17
1.5.2 Modular Multilevel Converter (MMCs) 18
1.5.3 AC/DC System Interactions 18
1.6 Stability Analysis of Multiple Converter Interaction Systems 19
1.7 Model Simplification in Converter-Dominated Networks 23
1.8 Motivation and Aims of the Work 26
1.8.1 Research Motivation and Objectives 26
1.8.2 Main Contributions: 27

1.9 Structure of the thesis: 28
Chapter 2: Small-Signal Impedance Modelling and Stability Analysis of Grid-Connected Converters 30
2.1 Introduction 30
2.2 Converter Modelling 30
2.3 Impedance Modelling of GFL Converters 31
2.3.1 GFL Control Topology 32
2.3.2 Synchronization Mechanism 34
2.3.3 Inner Loop Control 35
2.3.4 Outer Loop Control 35
2.4 Linearisation and Small-Signal Modelling for GFL Impedance 36
2.4.1 Admittance in **dq** frame 36
2.4.2 Admittance Representation in the **pn** Frame 43
2.5 Impedance Modelling of GFM Converters 46
2.5.1 GFM Control Topology 48
2.5.2 Power Synchronization 49
2.5.3 Linearization and Small-Signal Modelling for GFM Impedance Derivation 52
2.5.4 Inner current controller 55
2.5.5 Outer Loop Control 56
2.6 Impedance Measurement in the Time domain Model 56
2.6.1 Time-Domain Simulation Approach for Measuring VSC Small -Signal Admittance 56
2.6.2 Validation 60

2.6.2.1 GFL with Inner Current Controller (ICC) 60
2.6.2.2 GFL with outer controller Loop 62
2.6.2.3 GFM Validation 64
2.6.2.4 Comparison: GFM vs GFL Admittance Characteristics 65
2.7 GNC for Impedance-based Stability Analysis 66
2.7.1 SISO Stability Framework 67
2.7.2 Transition to MIMO Stability Analysis 69
2.8 Frequency-Domain Stability Analysis 70
2.9 Time -Domain Analysis 72
2.10 Summary 73
Chapter 3: Analysis of Converter-Network Interaction Dynamics 75
3.1 Introduction 75
3.2 Interaction Mechanisms in Two-VSC Networks 76
3.2.1 System Configuration 78
3.2.2 Impedance Formulation 81
3.3 AC Network and Impedance Interaction Characteristics 83
3.4 Time domain model development 84
3.5 Impedance Calculation for a Two-Converters AC Network 86
3.5.1 Interaction Indicator: IR and EIR 87
3.5.2 Converter- Network Interaction: Impedance Results 87
3.5.2.1 Strong-Grid (Coupling-One) Case 88
3.5.2.2 Weak-Grid (Coupling-Two) Simulation Results 92
3.6 Stability Assessment of Two-Converter Networks 95
3.6.1 Stability Under Coupling-One Condition 95
3.6.2 Coupling -Two Conditions 96
3.7 System Stability and Varied Converter Characteristics 99
3.7.1 Stability under Changing PLL Bandwidths and Control Modes 99
3.7.2 Stability Impact of Active Power Setpoint in PV Control 103

3.7.3 Operating Modes: VSC 1 Rectifier/Inverter and VSC 2 Inverter 105
3.8 Designing Proposed Impedance Reshaping Method 107
3.8.1 GFL under PV Control with LPF-Based Outer Loop 107
3.8.2 Simulation Results for Reshaped GFL 109
3.9 SCR, IR, and EIR Relationship in Multi-Converter Networks 110
3.10 Summary 111
Chapter 4: Multiple Converter-Network Interactions and the Impact of Control Systems 113
4.1 Introduction and System Configuration 113
4.2 Interaction of Multiple Converters and Network Analysis 116
4.3 Impedance Analysis of AC Networks with Multi-VSCs 117
4.3.1 Multiple Converters -Network Interaction: Impedance Results 118
4.3.1.1 Coupling-One Simulation Results 119
4.3.1.2 Weak-Grid (Coupling Two) Simulation Results 120
4.3.1.3 GFM System Performance Under Coupling-Two 123
4.4 Stability Analysis for Multi-VSCs 124
4.4.1 Stability Assessment Under Coupling-One 125
4.4.2 Stability Assessment Under Weak-Grid Coupling 125
4.4.3 Stability Implications of GFM Integration in M-VSCs 127
4.4.4 Impact of Power flow Direction on System Stability 128
4.4.5 Stability Outcomes of Muti-VSCs Control Configurations 130
4.5 IR/EIR Analysis with Varying Electrical Separation 132
4.6 Converter Impedance Reshaping 136
4.6.1 Impedance Reshaping in GFL Converters 136
4.6.2 Impedance Reshaping of GFM Converters 139
4.7 Effect of Cable Connection on MVSC System Stability 142
4.8 Summary 146
Chapter 5: Impedance-Based Model Simplification for Converter Network Interaction Analysis 149

5.1 Introduction 149
5.2 Model Simplification Approaches for Multi-VSC Systems 150
5.3 Time-Scale Separation Model Reduction 152
5.3.1 Dynamic Modelling LCL Filters for Robust Current Regulation 152
5.3.2 Simplified Current and Voltage Control Models 155
5.4 Small-Signal Modelling of the Simplified Systems 156
5.5 Impedance Changes in Simplified vs. Detailed Model Simulations 157
5.5.1 Impedance Simulation Results Under Coupling-One 158
5.5.2 Impedance Simulation Results Under Weak-Grid Conditions 161
5.5.3 Nyquist Stability Analysis Under Coupling One and Two 163
5.6 Percentage Error: Detailed vs. Simplified Models 167
5.6.1 Simulation Results for Impedance Error under Coupling-One Configuration 167
5.6.2 Simulation Results for Impedance Error under Coupling-Two Configuration 170
5.7 Lead-Lag Compensation for improved Modelling Accuracy 173
5.7.1 Proposed Lead-lag Compensator 174
5.7.2 Improving Model Accuracy with Lead-Lag Compensation 175
5.8 Stability Assessment of PV/PQ-Controlled Converters Using Impedance-Based Indices 177
5.8.1 Index-Based Analysis Under Coupling-One 178
5.8.2 Index-Based Analysis Under Coupling-Two 180
5.8.3 Quantitative Model Validation Using Euclidean Distance 181
5.8.4 Error Metrics Index for Different Coupling Configurations 183
5.9 Chapter Summary 184
Chapter 6: Conclusions and Future Work 186
6.1 General Conclusions 186
6.2 Prospects for Further Research 188
Bibliography 189
Appendix A: Chapter 3 Figures 207

Appendix B: Chapter 5 Figures 211
Appendix C: Derivation and Calculation Concept..... 211
Appendix D: Chapter 5 Derivation of Equations 212
Author's Publications..... 215

Chapter 1: Introduction

1.1 General Introduction

The global urgency to mitigate climate change has driven an unprecedented transition towards renewable energy sources (RES) such as wind and solar power [1] . This shift is supported by ambitious governmental policies and rapid technological advancements that make large-scale RES integration increasingly feasible. Forecasts suggest that renewables could account for nearly two-thirds of the global electricity supply by 2050 [2] , with several nations such as Denmark, Germany, China, and India already exceeding 30% penetration, and the European Union averaging 24% [3]. Achieving such targets requires power systems that are not only robust but also adaptable to the operational characteristics of high renewable penetration.

A central technology enabling this transition is the power electronic converter, which precisely regulates voltage, current, and frequency to connect RES to the grid. While these converters offer superior controllability and flexibility compared to conventional synchronous generators, they fundamentally change the dynamic behaviour of power systems. Synchronous generators inherently provide rotational inertia and natural damping, stabilising the grid during disturbances. In contrast, converter-based systems have no inherent inertia, making them more sensitive to grid faults and dynamic disturbances. For example, the United Kingdom's achievement of 51.6% renewable electricity generation in 2024 illustrates both the progress made and the operational complexities that arise in geographically dispersed wind and solar installations [4][5][6].

Converter-rich grids display dynamic behaviours that differ significantly from conventional systems. Their fast control loops improve power regulation accuracy but may also introduce resonances and instabilities, particularly in weak or spatially distributed networks [7][8]. Reduced fault current contributions complicate protection coordination, while increased sensitivity to frequency and voltage deviations poses additional operational risks. The challenge becomes more critical in multi-converter environments where devices with distinct control objectives interact. Under such conditions, harmonic interference, oscillatory

behaviour, and instability may arise due to weak grid strength, wide control bandwidths, or unfavourable converter-to-converter coupling [6][9][10].

Traditional stability metrics, such as the SCR, are no longer sufficient for assessing converter-dominated systems. They cannot capture the frequency-dependent interactions and resonant phenomena introduced by advanced control strategies [10][11][12]. This limitation motivates the need for analytical methods capable of characterising system dynamics over a wide frequency range.

To address this gap, this thesis develops impedance-based stability analysis methods specifically tailored for evaluating converter interactions in converter-dominated power networks. The United Kingdom provides a representative example of these developments. Offshore wind generation is projected to reach approximately 42 GW by 2030 and could exceed 80 GW by 2050. In parallel, HVDC interconnectors are expected to provide more than 45 GW of transfer capacity [13][14][15].

The geographical distribution of future wind farms and interconnection projects-including embedded links, offshore connections, and international interconnectors-will transform the UK grid into a predominantly converter-based system. This transition introduces stability challenges that differ fundamentally from those encountered in conventional synchronous machine-dominated networks.

1.2 Power System Stability

Power system stability describes the ability of an electrical network to remain in a secure operating state after a disturbance and to return to normal steady-state conditions without losing synchronisation, acceptable voltage, or frequency limits [16][17]. As shown in Figure 1.1, stability can be grouped into rotor-angle, voltage, frequency, resonance, and converter-driven categories. Each group reflects the dominant physical or control-based mechanism that governs system behaviour following a disturbance.

In traditional power grids, synchronous machines provide natural inertia and damping, which slow frequency and voltage changes and help the system settle after a disturbance. Modern networks include a large share of converter-interfaced generation such as wind, solar, and HVDC links. These sources replace rotating mass with fast electronic control. The lack of

physical inertia makes power systems react quickly, and in weak grids this can lead to oscillations or loss of stability if the control systems are not designed correctly. Converter-dominated grids therefore introduce additional stability challenges, particularly in networks with low short-circuit strength or many interacting converters.

To understand these challenges, it is essential to consider stability mechanisms across different time scales. Rotor-angle stability concerns the synchronisation of generating units following small or large disturbances. Voltage stability focuses on maintaining acceptable voltage levels over both short and long durations. Frequency stability deals with the balance between active power supply and demand, which determines system frequency. Resonance stability considers the risk of electrical or torsional resonances triggered by interactions between power electronic converters and grid elements. More recently, converter-driven stability has emerged as an increasingly important category, capturing fast and slow interactions within converter control systems and between converters and the network [17].

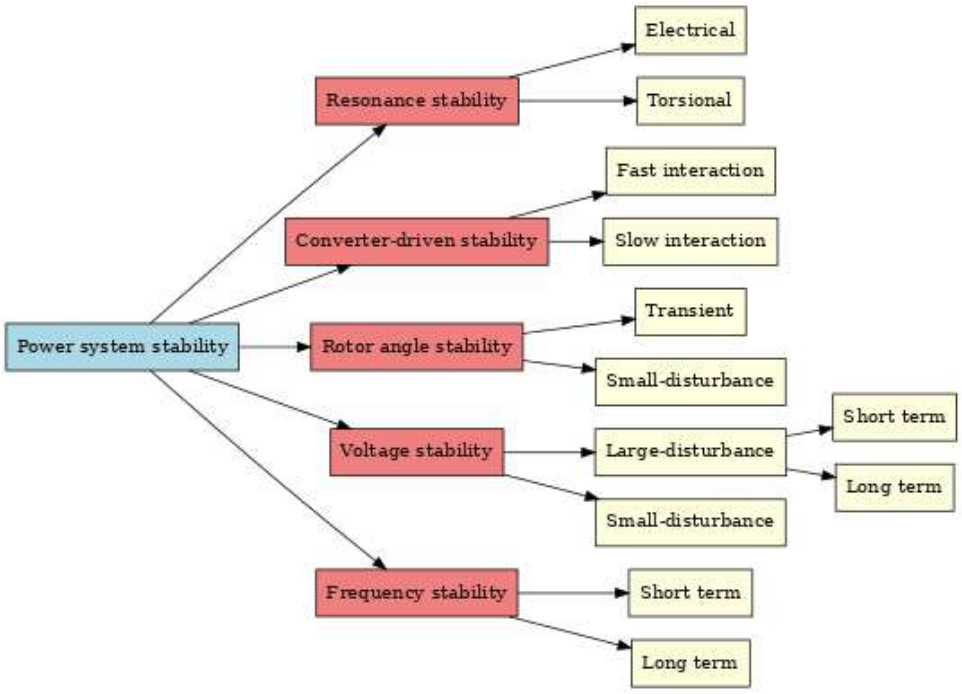

Figure 1.1: Classification of Power system stability [17]

Among these, small-signal stability has become particularly critical in converter-rich power systems. Small-signal analysis examines the system response to minor disturbances such as small load variations or fluctuations in renewable output. While synchronous machines rely on mechanical inertia to moderate such disturbances, converter-based units depend entirely

on control algorithms, making them more sensitive to control interactions and frequency-dependent changes in network impedance [18]. In systems with many converters operating simultaneously, stability is strongly influenced by the behaviour of current and voltage control loops, PLLs, and the impedance characteristics of both converters and the surrounding network. These interactions can give rise to new forms of instability, including harmonic resonances, sub-synchronous oscillations, and high-frequency oscillations driven by converter control dynamics [19].

Several analytical tools are used to assess stability in this context. Eigenvalue analysis identifies oscillatory modes and their damping, providing insight into the conditions that may lead to instability. Impedance-based analysis, which considers the interaction between converter and grid impedances at the point of common coupling, enables stability assessment across a broad frequency range. When combined with the Nyquist stability criterion, impedance-based methods can effectively highlight weak stability margins and detect potential resonances[12][20].These frequency-domain approaches are particularly advantageous in large converter-dominated systems, as they offer wide-ranging insight without requiring extensive time-domain simulations.

Despite significant progress, accurately modelling converter dynamics under different operating conditions remains a challenge. Ongoing research is exploring the integration of impedance-based techniques with data-driven and machine-learning approaches to enable real-time stability assessment and adaptive control. Such advancements are expected to enhance system robustness and support secure operation as the penetration of converter-based resources continues to grow [21]. Figure 1.2 illustrates a comparison of the main small-signal stability techniques, including impedance-based analysis, dq -domain modelling, and sequence-domain analysis, and highlights their role in evaluating the stability of AC converter-based systems across a broad frequency range[12][22].

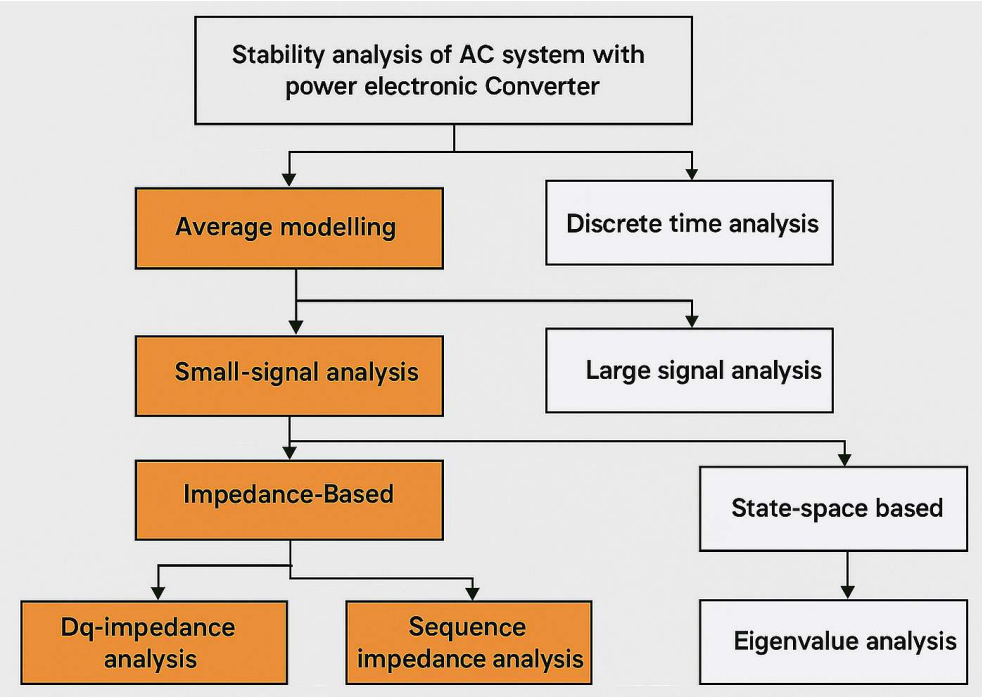

Figure 1.2: Small-Signal Stability Analysis of AC system with Power Electronic Converters[12]

1.3 Challenges of Multi-Converter Dynamics in Modern Power Networks

The increasing penetration of power electronic converters has redefined the operational behaviour of electrical grids, making traditional synchronous generator-based stability mechanisms less relevant. In legacy systems, synchronous machines supplied inertia, damping, and natural voltage regulation, ensuring robustness during disturbances. The absence of such intrinsic characteristics in converter-based systems results in higher rates of change of frequency (ROCOF) [23], voltage instability, and reduced fault current capability [1][24][25].

One major challenge in converter-rich systems is their vulnerability to rapid frequency deviations following disturbances. GFL converters are prone to losing synchronism in weak networks. Sub-synchronous oscillations (SSO), control-induced resonances, and strong converter-converter coupling can lead to unstable oscillatory modes. Additionally, these systems are more sensitive to harmonics, especially when connected through high-impedance lines or long transmission corridors. Without mechanical inertia, operators must rely on synthetic inertia or fast frequency response controls, which add complexity and place new demands on system protection and coordination [11][26].

Conventional modelling approaches, such as RMS-based phasor simulations, cannot adequately represent the fast electromagnetic transients inherent to converter operation. These limitations necessitate the use of high-accuracy EMT simulations and frequency-domain impedance analysis to accurately capture system dynamics and predict stability boundaries in converter-dominated grids [26].

1.3.1 Shift from Synchronous to Converter-Dominated Systems

Historically, electrical power systems were built upon synchronous generators driven by thermal, hydroelectric, or nuclear power plants. These machines inherently supplied inertia and damping through their rotating masses, allowing grid frequency to recover smoothly after disturbances. In contrast, the global move toward renewable generation especially large-scale solar photovoltaic (PV) plants and wind farms has significantly reduced the share of synchronous machines. Modern renewable plants are almost exclusively connected through VSCs, which do not store kinetic energy and therefore provide negligible natural inertia.

The absence of rotational mass causes converter-dominated systems to exhibit faster frequency deviations and reduced tolerance to sudden faults or load changes [24][25]. Figure 1.3 illustrates the operational contrast between high-inertia conventional grids and present-day low-inertia systems dominated by converters. The transition has increased the complexity of maintaining frequency stability, making advanced control frameworks and accurate stability evaluation tools essential for future grid reliability or grid system robustness.

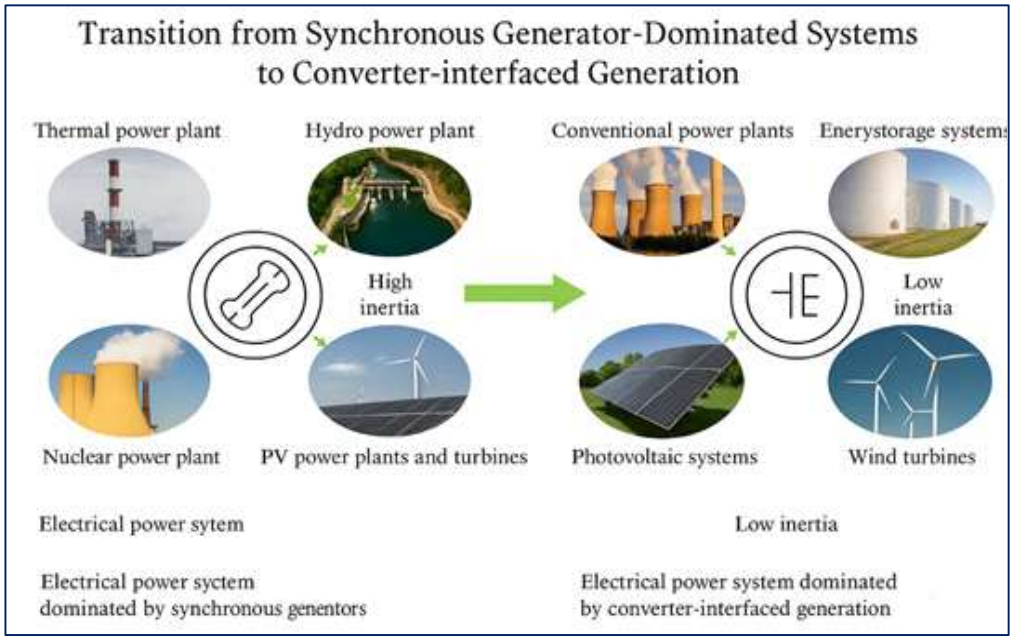

Figure 1.3: Progression towards and electric energy system with dominant Converter technology [26]

1.3.2 Stability Challenges in Multi-Converter Systems

The growing share of converters has introduced distinctive stability concerns in modern power networks. These include frequency instability, voltage oscillations, harmonic resonance, and reduced fault current capability. Such issues are often triggered by the interaction between converter control loops, grid impedance, and the varying operating conditions of interconnected systems.

A principal challenge is frequency instability. In converter-based grids, the lack of mechanical inertia allows frequency to change rapidly after a disturbance, potentially destabilising the network. GFM converters have been developed to emulate synchronous generator behaviour by introducing synthetic inertia, thereby improving frequency recovery [27]. Another common issue is voltage oscillation, which may occur when converter control dynamics interact unfavourably with network impedance, producing resonance and degrading power quality [28].

Additionally, converters typically deliver fault currents much lower than those of synchronous generators, complicating relay coordination and increasing the probability of protection mis-operation during faults [29][30]. Harmonic resonance, especially in networks with high converter density, further amplifies instability risks and distorts voltage

waveforms[10]. Overcoming these challenges demands advanced impedance-based stability assessment techniques and carefully tuned control designs tailored to multi-converter interaction scenarios.

1.3.3 Modelling Complexities in Multi-Converter Networks

Accurate models of multi-converter power networks are required to explain observed behaviour. Yet capturing interactions among converters, cables, and the grid remains difficult. Frameworks created for synchronous machine grids fail to represent fast transients, switching nonlinearities, and tightly coupled control loops typical of power electronic interface [10][11]. Impedance-based and frequency-domain formulations address part of this gap by describing small-signal dynamics around operating points while keeping computational cost manageable [30][31]. However, applying these models to large converter networks is difficult because of scalability limits, uncertain parameters, and strong interactions between components. The level of detail used in the model whether at the device, converter, or system level directly affects both its accuracy and its practicality. Figure 1.4 depicts a converter-dominated network: renewable sources connect through converters to an electrical bus. PLLs coordinate with grid measurements, but inject states that interact with current control, power control, and protection, provoking resonances and weak-grid instabilities. These features motivate hybrid methods that combine physics-based modelling with data-driven learning. Recent work explores Artificial Intelligence (AI) and Machine Learning (ML) to refine parameter estimation, identify couplings, and enable adaptive control tuning under operating conditions [32]. Integrated with established models, these methods improve prediction and support reliable, secure operation in converter-rich networks.

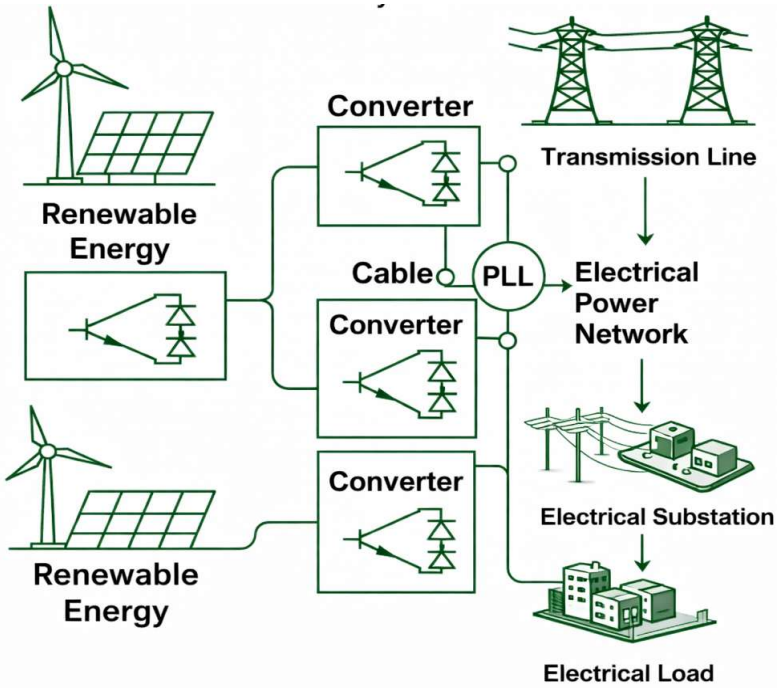

Figure 1.4: Converter-Dominated Renewable Power System

1.3.4 Global Trends in Converter-Dominated Network

The shift toward converter-interfaced generation is a defining feature of modern power systems. Countries such as Germany, Denmark, the United Kingdom, China, and India are at the forefront, deploying extensive solar PV, wind energy, and battery storage facilities to meet ambitious decarbonisation targets [3].

Germany's Energiewende programme and China's rapid expansion of renewable capacity exemplify large-scale adoption of converter-based infrastructure. Such developments underscore the urgent requirement for research into multi-converter stability, optimal deployment of GFM inverters, and advanced impedance-based modelling to predict and mitigate adverse interactions [6][7].

While converter technologies enable deeper renewable integration and enhance grid flexibility, they also introduce operational vulnerabilities emerging from reduced inertia, complex control coupling, and frequency-dependent resonances. Addressing these challenges will require continued optimisation of modelling tools, further development of stability indices, and innovative control strategies that maintain security of supply in converter-dominated power systems.

1.4 Impedance Modelling and Stability Analysis

The derivation of converter output impedance is central to impedance-based stability analysis. This process begins by defining the mathematical relationship between the voltage at the point of PCC and the current delivered to the network. Under steady-state conditions, linearization yields a transfer function representation, which forms the basis for stability evaluation [33][34].

AC systems exhibit nonlinear behaviour due to converter switching operations and the complexity of control loops. Consequently, linear impedance models represent an approximation rather than the exact system response. Small-signal analysis addresses this limitation by linearizing the system around a chosen operating point, enabling the use of frequency-domain techniques.

Challenges arise when the system lacks a fixed operating point, as in time-varying or weakly damped networks. In such cases, direct linearization in the natural abc-domain becomes impractical. To overcome this, variables are transformed into the dq-domain or the sequence-domain, as described in Section 1.4.3 and illustrated in Figure 1.8. These domains allow the decoupling of system variables and provide an accurate representation of impedance under both steady-state and slowly varying conditions [21].

1.4.1 Impedance-Based Stability Analysis

Impedance-based stability analysis is a foundational method for assessing system dynamics in the frequency domain, especially within networks involving power electronic converters. This technique converts time-domain signals $f(t)$ into the frequency domain $F(s)$ using the Laplace transform [34]. The system's frequency-dependent response is described by the transfer function $G(s) = \frac{Y(s)}{U(s)}$, where $Y(s)$ and $U(s)$ represent the system output and input in the Laplace domain, respectively.

Stability is evaluated using graphical tools such as Bode plots, Nyquist criteria, and impedance transfer characteristics [33][35]. These tools allow engineers to examine the phase and magnitude relationships over a range of frequencies, making it possible to predict instability due to resonance or poor damping. A key advantage of this approach is that it supports both experimental and analytical modelling, even when the full internal structure

of a network is unknown. As a result, impedance-based analysis is widely used in both research and industrial settings for its efficiency and adaptability [36][37][38].

Originally, this method was developed for DC-DC converter systems [39]. Its application has since expanded to analyses partitioned subsystems within more complex networks, including AC and DC systems with multiple voltage-source or current-source devices [40][41][42][43]. For voltage-source systems, stability assessment relies on the Nyquist criterion applied to the impedance ratio $\frac{Z_{con}}{Z_{grid}}$ where Z_{con} is the converter output impedance and Z_{grid} is the grid input impedance [41]. In some cases, an admittance-based approach is also used [42]. For current-source systems, including many grid-tied converters, stability is analysed using the inverse ratio $\frac{Z_{grid}}{Z_{con}}$ [44]. However, in cascaded voltage-source networks, further modifications to the stability criteria are necessary due to specific limitations identified in [43].

While analytical models can provide theoretical estimates of converter output impedance, practical systems often lack detailed parameter information. In such cases, experimental methods are used. Perturbation signals are injected into the system, and the resulting terminal voltages and currents are measured to determine the impedance. This “black box” approach enables impedance estimation without requiring full internal knowledge of the converter [37]. However, this method can only observe certain system states, so stability should be evaluated at multiple interaction points. Additionally, impedance-based analysis may lose validity if the source or load impedances contain right-half-plane zeros, as these introduce instability effects not captured by conventional criteria.

For three-phase power systems, impedance-based analysis was first implemented by representing the system in a synchronous rotating dq reference frame. In this frame, impedance is described as a 2×2 transfer matrix. At least two perturbation tests are required to measure the dq impedance, and the reference frame must be aligned with the grid voltage angle. This angle is typically obtained through FFT analysis or a PLL. The FFT approach assumes a fixed fundamental frequency, which may introduce errors when frequency deviations occur [45][46]. Conversely, the PLL method can introduce inaccuracies due to the interaction between injected perturbations and the PLL response. These errors can be reduced by using a low-bandwidth PLL or compensation techniques.

An alternative approach employs positive and negative-sequence impedance representations for stability analysis in three-phase systems. Under balanced operating conditions, the sequence impedances of inverters and wind turbines are decoupled, allowing the use of SISO Nyquist or Bode-based analyses. This simplifies the process compared to the more complex generalized Nyquist criterion required for MIMO systems [38][46].

1.4.2 Voltage-Source and Current-Source Systems

Figure 1.5 illustrates small-signal models for partitioned electrical subsystems. In VSCs configurations, as shown in Figure 1.5(a), the converter injects a current $I_{con(s)}$ into the network, which is governed by:

$$I_{con}(s) = \frac{V_{con}(s)+Z_{grid}(s).I_{grid}(s)}{Z_s(s)+Z_{grid}(s)} \tag{1.1}$$

This equation can be rearranged to

$$I_{con}(s) = \left(\frac{V_{con}(s)}{Z_{grid}(s)} + I_{grid}(s)\right).\frac{1}{1+\left(\frac{Z_{con}(s)}{Z_{grid}(s)}\right)} \tag{1.2}$$

The system's closed-loop transfer function is then:

$$\mathrm{CL(s)} = \left(1 + \frac{\mathrm{Z_{con}(s)}}{\mathrm{Z_{grid}(s)}}\right)^{-1} \tag{1.3}$$

For the system to be stable, the Nyquist plot of $\mathrm{CL(s)}$ must not encircle the point (–1,0), as stated by the Nyquist criterion [41][42][43]. In addition, the subsystems themselves must be independently stable, meaning that neither $\mathrm{I_{grid}(s)}$ nor $\frac{1}{\mathrm{Z_{grid}(s)}}$ should have RHP poles [47] .For current-source systems, a similar principle applies, as shown in Figure 1.5(b). The Nyquist criterion is used to analyses the impedance ratio $\frac{\mathrm{Z_{con}(s)}}{\mathrm{Z_{grid}(s)}}$, ensuring the independent stability of each subsystem [48]. This methodology is especially relevant for renewable energy inverters connected to weak grids, where grid impedance plays a crucial role in determining overall system stability [44].

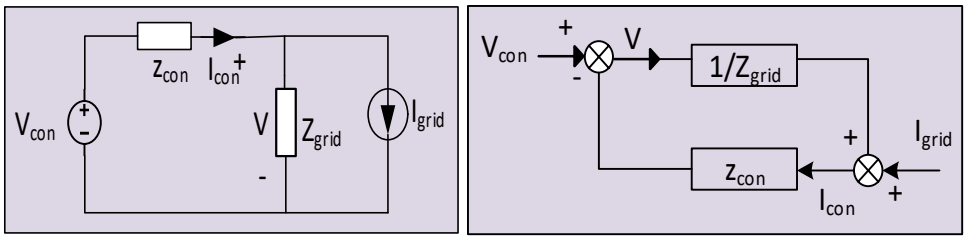

Thevenin equivalent circuit representation Block diagram representation

(a) Equivalent Voltage Source System

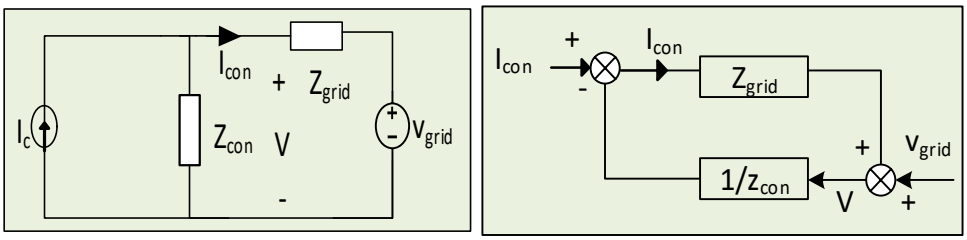

Norton equivalent circuit representation Block diagram representation

(b) Equivalent current source system

Figure 1.5: Small -signal representation and minor loop-gain of a system portioned into two subsystems: (a) Voltage-Source Configuration (b) Current-Source Configuration.

1.4.3 Definition of reference frame and frame transformation

The choice of reference frame is fundamental in the modelling, analysis, and control of power electronic converters. Different frames are used to simplify system variables and enable efficient impedance-based analysis.

In electrical networks, the three-phase abc frame naturally describes physical quantities such as voltages and currents. For analysis and control, however, transformations into the stationary αβ frame and the rotating dq frame are widely applied. As shown in Figure 1.6, the αβ frame represents the stationary orthogonal components, while the dq frame rotates synchronously with the system voltage at angular frequency ω_n. This rotation transforms sinusoidal variables into constant quantities, which are easier to handle in control design [49][50].

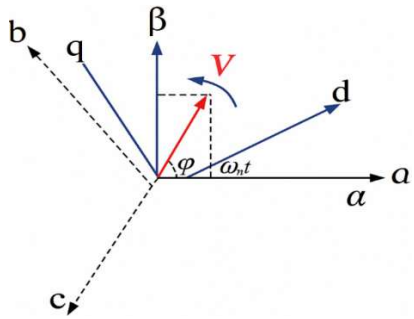

Figure 1.6: Illustration defining the stationary αβ reference frame, the rotating dq reference frame, and the three-phase abc reference frame.

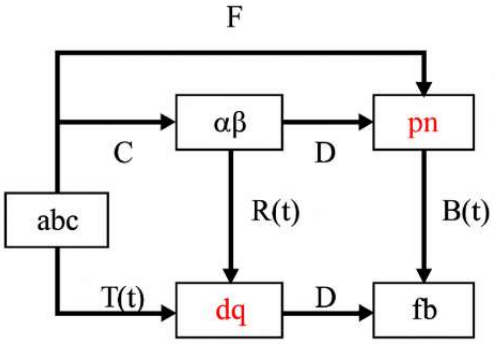

Figure 1.7: Illustration of transformations between various reference frames [40]

The transformation from abc to dq is performed in two steps: first, the Clarke transformation (C) projects the three-phase signals into the αβ frame; then, the rotation matrix (R(t)) maps αβ into dq coordinates. Together, they define the Park transformation matrix T(t):

$$T(t) = R(t)C \tag{1.4}$$

with the following definitions:

$$T(t) = \left(\frac{2}{3}\right)\begin{bmatrix} \cos(\omega_n t), \cos\left(\omega_n t - \frac{2\pi}{3}\right), \cos\left(\omega_n t + \frac{2\pi}{3}\right) \\ \cos(\omega_n t), \cos\left(\omega_n t - \frac{2\pi}{3}\right), \cos\left(\omega_n t + \frac{2\pi}{3}\right) \end{bmatrix} \tag{1.5}$$

$$C = \left(\frac{2}{3}\right)\begin{bmatrix} 1 & -\frac{1}{2}, & -\frac{1}{2} \\ 0 & \sqrt{\frac{3}{2}} & -\sqrt{\frac{3}{2}} \end{bmatrix} \text{ (1.6)}, \quad R(t) = \begin{bmatrix} \cos(\omega_n t) & \sin(\omega_n t) \\ -\sin(\omega_n t) & \cos(\omega_n t) \end{bmatrix} \tag{1.7}$$

For balanced and harmonic-free systems, these transformations yield constant dq values, which significantly simplify converter modelling and control.

When unbalanced or faulted conditions occur, positive/negative-sequence (pn) frames are employed. As shown in Figure 1.7, the dq signals can be converted into pn quantities through the sequence transformation matrix D and the frequency shift operator B(t):

$$\begin{bmatrix} \Delta v_{p(t)} \\ \Delta v_{n(t)} \end{bmatrix} = B(t)D \begin{bmatrix} \Delta v_{d(t)} \\ \Delta v_{q(t)} \end{bmatrix} \tag{1.8}$$

Where, $D = \frac{1}{2}\begin{bmatrix} 1 & j \\ 1 & -j \end{bmatrix}$, $B(t) = \frac{1}{2}\begin{bmatrix} e^{jw_n t} & 0 \\ 0 & e^{-jw_n t} \end{bmatrix}$, while $\Delta v_d(t)$ and $\Delta v_q(t)$ are the dq variables, while $\Delta v_p(t), \Delta v_n(t)$ represent positive- and negative-sequence components.

In summary, the transformations among abc, αβ, dq, and pn frames (Figures 1.7-1.8) establish a consistent mathematical framework for analysing converter behaviour in both balanced and unbalanced operating conditions. This framework is essential for accurate impedance modelling, stability assessment, and control design in converter-dominated networks. The dq frame remains the most effective for balanced systems and conventional control, while pn and frequency-based frames are required to capture asymmetries and dynamic interactions [51][52][53]. By selecting the proper frame, the analysis can be adapted to the system condition, providing clarity and precision in stability studies and control development [43] .

For GFM and GFL converters, synchronization with the network is a critical function. A GFL converter requires alignment with the grid voltage phase. This is achieved through a PLL, which locks onto the grid phase and frequency. The PLL relies on the dq0 (direct-quadrature-zero) transformation as its key control strategy. By converting sinusoidal three-phase voltages and currents into constant dc quantities, the dq0 transformation reduces control complexity. It allows a time-varying ac system to be represented in a time-invariant form, which is particularly useful for controller design [54][34]. In practice, the oscillatory three-phase signals of the utility grid (abc) are transformed into non-oscillatory d, q, and 0 components, enabling efficient synchronization and stable operation of the converter.

1.5 Impedance Modelling of Grid-Connected Converters

The increasing deployment of VSCs is fundamentally reshaping the dynamic behaviour of modern power networks. Unlike synchronous machines, whose electromechanical properties are well established, VSCs rely on fast digitally controlled switching, leading to new modes

of system interaction. To study their stability, impedance modelling has become a rigorous and practical framework. By representing converters and surrounding networks as interconnected source and load impedances, small-signal stability and interaction mechanisms can be systematically examined.

The development of insulated-gate bipolar transistors (IGBTs) was pivotal in enabling fully self-commutated VSCs [10][55][56]. In contrast to line-commutated converters, which depend on a strong AC source for commutation, IGBTs allow both turn-on and turn-off control. This capability made it possible to establish a fixed-polarity DC link voltage, maintained by a large capacitor, which in turn allows VSCs to behave like controlled inverters with independent regulation of active and reactive power [56].

VSCs offer several advantages over current-source converter technologies. Power reversal is achieved by changing the current direction without altering the DC voltage polarity, and they can provide reactive power support and voltage regulation in weak grids [57] These features explain why VSCs have become the preferred choice for large-scale integration of renewables and interconnection of converter-dominated grids.

Early implementations employed two-level topologies, illustrated in Figure 1.8, where each converter arm consists of IGBTs connected in parallel with freewheeling diodes [58]. Although relatively simple, this structure laid the foundation for advanced topologies, notably the Modular Multilevel Converter (MMC), which addresses efficiency and scalability in large power applications.

Impedance modelling techniques are based on linearizing the nonlinear dynamic equations of a converter around a selected operating point. To be effective, the modelling approach must accurately represent the influence of the converter topology, the internal control loops, and the coupling between AC and DC dynamics. These aspects can be explained under the following categories:

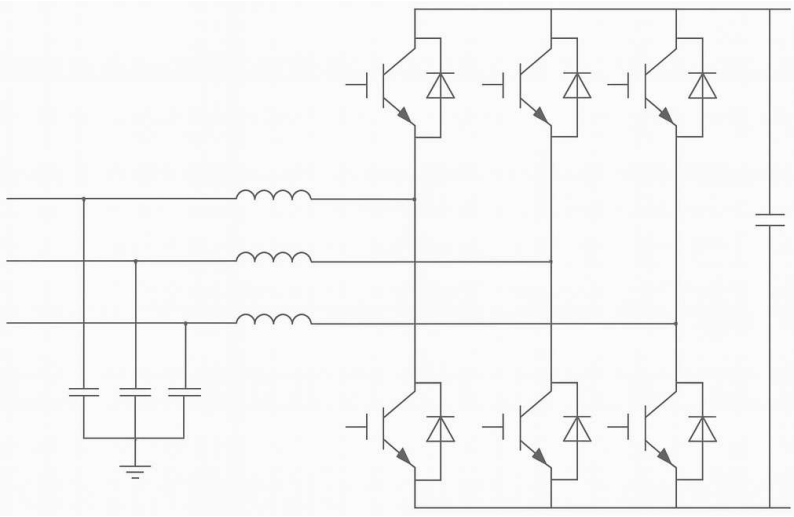

Figure 1.8: Schematic of Two -Level Voltage source converter

1.5.1 Two -Level Voltage-Source Converter

The two-level VSC is the most widely studied topology, and its impedance modelling often serves as a reference. The modelling process follows a hierarchical procedure. First, an averaged model is obtained by averaging the switching function over one switching period. This continuous, time-invariant model neglects high-frequency harmonics and retains only the fundamental dynamics relevant for small-signal analysis [38]. The nonlinear averaged equations are then linearized around a steady-state operating point, such as a defined active and reactive power injection. This results in a small-signal AC model [59].

Next, the converter's control loops are integrated. These include the PLL, the inner current controllers-typically implemented in the synchronous dq reference frame-and the DC-link voltage controller. Among these, the PLL plays a particularly critical role, as it can introduce negative resistance characteristics into the dq-frame impedance, especially under weak grid conditions [11][60].

Finally, impedance extraction is performed by applying a small-signal perturbation to either voltage or current and observing the corresponding response. The resulting frequency-dependent input impedance, converter impedance ($Z_{vscon(s)}$) , can be represented as a SISO transfer function in the stationary αβ frame, or as a MIMO transfer matrix in the synchronous dq frame [59].

1.5.2 Modular Multilevel Converter (MMCs)

In comparison, the impedance modelling of a Modular Multilevel Converter (MMC) is substantially more complex due to its internal dynamics and distributed energy storage. Each submodule capacitor introduces dynamic states that strongly influence the converter's response. A rigorous MMC impedance model must account for three key phenomena.

First, the arm energy dynamics reflect the oscillation of energy between the upper and lower arms, which manifests as circulating currents. Second, the submodule capacitor voltage ripples occurring at both fundamental and double-line frequency must be represented, as they introduce low-frequency variations that couple with external system dynamics [61]. Third, the control interactions inherent to the MMC add further complexity. In addition to the controllers found in two-level VSCs, the MMC employs circulating current suppression and capacitor voltage balancing control loops, which interact with the current controller and PLL.

Unlike two-level converters, MMC impedance cannot be described as a single equivalent value. Instead, the AC and DC impedances are strongly coupled, and neglecting this interdependence can lead to inaccurate stability assessments, particularly for higher-frequency phenomena [62].

1.5.3 AC/DC System Interactions

The stability of converter-based systems cannot be examined in isolation; it requires analysing the coupling between the AC and DC networks. Impedance modelling offers a unified approach to describe these interactions. From the PCC, the AC system can be represented by its equivalent impedance, $Z_{grid}(s)$, On the converter side, the AC input impedance, $Z_{con,ac}(s)$, and the DC output impedance, $Z_{con,dc}(s)$, are obtained using the procedures introduced earlier.

For two-level converters, the DC impedance is mainly influenced by the DC-link capacitance and the interaction with AC-side controls. In Modular Multilevel Converters (MMCs), the DC impedance is shaped by arm dynamics and capacitor behaviour [63] . Instabilities may arise in either domain or can propagate through the converter. For example, a disturbance in the AC network may pass through the control loops and affect the DC side, while DC fluctuations can destabilise the connected AC system.

To capture these bidirectional effects, a multi-port impedance model is required. Such a model enables the design of controllers that maintain the stability of integrated AC/DC systems [62] .

Impedance modelling therefore provides a structured framework for representing converter behaviour and understanding how networks interact with converters. Two-level VSCs offer a relatively simple but instructive case, while MMCs exhibit more complex dynamics due to distributed storage and advanced control features. Both topologies highlight the critical role of AC/DC coupling in defining stability boundaries.

The concepts developed in this section establish the foundation for analysing more complex converter interactions in later chapters. In general, power electronic converters (PECs) are widely applied and can be grouped into four categories: AC-DC converters (rectifiers), DC-AC converters (inverters), DC-DC converters, and AC-AC converters [54]. In this thesis, the focus is on AC-DC and DC-AC conversion, as these dominate the operation of converter-based power systems.

1.6 Stability Analysis of Multiple Converter Interaction Systems

The rapid growth of renewable energy generation, predominantly through power electronic converters, has fundamentally reshaped the dynamic behaviour of electrical networks. As conventional synchronous generator-based systems are progressively replaced by converter-dominated grids, new mechanisms of interaction have emerged that cannot be fully addressed by conventional stability assessment methods. Well-documented incidents, such as the UK blackout caused by the disconnection of offshore wind farms [64] and the occurrence of persistent low-frequency oscillations in converter-rich grids [12][19], have demonstrated the urgency for analytical techniques specifically designed to address these emerging phenomena.

In multi-converter environments, stability evaluation is generally performed using eigenvalue analysis, impedance-based frequency-domain methods, and time-domain simulations. Eigenvalue analysis, derived from a linearised state-space representation, allows the identification of oscillatory or unstable modes and is particularly effective for examining the influence of control parameter settings on system dynamics [65]. Impedance-based methods use the Nyquist stability criterion applied to the ratio of source and load impedances, providing direct insight into stability margins over a broad range of operating

conditions and making them suitable for both operational and planning stages [66]. Time-domain simulations complement these methods by capturing nonlinear responses, protection operations, and transient behaviours that cannot be fully represented in the frequency domain.

Recent investigations into offshore wind farms connected through HVDC links have shown that combining impedance-based and time-domain approaches significantly improves the detection of instabilities, particularly in weak-grid conditions where converter and network impedances are of similar magnitude [12][22][66][67]. Such conditions facilitate resonances and complex interactions that a single analysis technique may overlook. Offshore collector networks, characterised by the close proximity of multiple wind turbine converters, create strong electrical coupling and distinctive dynamic behaviours not typically present in large transmission systems. Current industry guidelines, such as those in the CIGRÉ Technical Brochure [68], remain focused on bulk power transmission and provide limited direction for these compact offshore arrangements.

The complexity of stability assessment increases further when converters from different manufacturers operate in the same network. Variations in proprietary control structures can produce unexpected interactions, as observed in the Johan Sverdrup offshore project [22]. While hardware-in-the-loop testing using detailed vendor-specific models can replicate such phenomena, its use is often restricted by computational demands and limited access to confidential control parameters. This highlights the importance of reduced-order models that preserve essential dynamic characteristics while remaining computationally efficient, and of model-independent assessment techniques for cases where proprietary information is unavailable. Standardised test procedures are also necessary to ensure consistent and comparable stability evaluations across different systems.

Traditional impedance-based stability assessment assumes GFL converters operating against strong voltage sources, where the converter regulates current without controlling terminal voltage [30][31]. The growing deployment of GFM converters, which actively regulate terminal voltage, fundamentally changes converter-grid interaction mechanisms and alters the underlying stability dynamics [22]. Single converter-to-grid impedance models, which perform adequately in isolated scenarios, often fail in multi-converter systems where strong device-to-device and network couplings dominate the overall behaviour.

In these cases, dq-domain impedance models extend analysis capabilities by representing coupled dynamics across multiple converters, but they require all variables to be transformed into a common global reference frame. This transformation introduces sensitivity to PLL synchronisation errors, which can distort stability assessment. Sequence-domain impedance models, formulated in the stationary reference frame, avoid these alignment issues and inherently operate within a unified reference framework. This enables accurate development of MIMO feedback models capable of representing harmonic interactions and frequency coupling [12][20]. Sequence-domain approaches have demonstrated high accuracy in weak grids and densely interconnected converter systems; however, applying them to meshed networks containing both GFM and GFL converters remains challenging. Differences in control algorithms, synchronisation methods, and dynamic behaviour, especially in the presence of asynchronous or mismatched PLLs, require high-fidelity modelling to ensure correct stability prediction.

Maintaining stable operation in converter-dominated power systems therefore demands analytical frameworks that combine precision, scalability, and validation through real-world data. Sequence-domain, frequency-based methods, when applied alongside time-domain simulations, show strong potential for providing reliable and accurate stability assessment. As the penetration of renewable energy and power electronics continues to grow, these advanced approaches will play a critical role in safeguarding the reliability, security, and dynamic performance of future power systems.

Table 1 offers a concise, evidence-based comparison of impedance-based stability analysis methods, detailing their accuracy, limitations, and applicability to specific converter-dominated network configurations. This structured evaluation supports precise method selection, ensuring reliable stability assessment across varying control architectures, grid strengths, and interaction complexities in modern power electronic systems.

Table 1:Stability Analysis of Converter Dominated Network System

Method	Advantages	Limitations	Practical Applications	References
IF	Useful for early identification of instability scenarios in multi-infeed systems.	Limited to fundamental frequency; neglects dynamic control interactions.	Applied in offshore wind power clusters for initial stability assessments.	[31][69]
SCR	Well-known and widely used for assessing system strength.	Does not consider converter controls or unbalanced grid conditions.	Commonly used in conventional power systems and HVDC links.	[10][31][20][70]
GSIM and Impedance Margin Ratio (IMR)	Captures converter action and impedance characteristics over frequency range.	Still under development, it requires more validation for broad adoption.	Proposed for use in renewable-dominated grids to evaluate strength.	[31][69]
Impedance-Based	Effective across different converter control types; allows for MIMO modeling.	Dependent on chosen frame of reference and parameter accuracy.	Ideal for systems with multiple converters and varying grid strengths.	[10][22], [38][43][49][20][46]
Transfer Function	Well-suited for frequency-domain analysis and controller design.	Less applicable for large-scale networks and high-order systems.	Primarily used for converter internal loop tuning.	[71][72]
Passivity-Based	Simple and intuitive framework for frequency domain analysis.	Limited accuracy in low-frequency range and large systems.	Useful for modular multi-level converters and filter design.	[22][73]
Eigenvalue/Modal-Based	Highlights resonant and unstable modes under varying conditions.	Requires detailed modeling and computational resources.	Valuable in high-fidelity analysis of control-tuned converters.	[11][72], [74]
Frequency sweeping /Scanning	Supports impedance model validation across frequencies. Useful for multiple controller configurations and online system data acquisition.	Model must be derived separately per case. Computationally expensive for large parameter spaces.	Used to extract converter impedance and derive small-signal models from field test data.	[12][74], [75]

Stability analysis of multiple converter interaction systems requires a reassessment of traditional indices such as the SCR, the Effective SCR (ESCR), and the MIIF. While these indices have historically provided valuable insights in grids dominated by synchronous machines, they are fundamentally based on static short-circuit strength. Such a representation is insufficient for converter-dominated systems, where dynamic control interactions and frequency-dependent impedance characteristics play a central role. The

reliance on these traditional measure's risks overlooking critical phenomena that arise from the coupling of fast control loops, weak grid conditions, and the high penetration of power electronic devices. When applied to offshore wind integration or large-scale HVDC interconnections, their limitations become evident, as they cannot reliably predict oscillatory modes or resonance mechanisms that may compromise stability. Consequently, stability assessments in modern grids require more advanced methodologies that explicitly incorporate dynamic converter behaviour and network impedance characteristics across a wide frequency range [10][11].

1.7 Model Simplification in Converter-Dominated Networks

Modern grids rely on power-electronic converters that operate through several control layers acting on different time scales. Full electromagnetic-transient models include switching and filter details, which give accurate fast-dynamic behaviour but require small time steps and high computational effort. For network studies, such detail is rarely practical. Simplified models are therefore needed to capture essential dynamics while allowing efficient simulation.

Time-scale separation remains a key tool for reduction. When variables evolve at different speeds, fast states may be removed while slow behaviour is kept without major loss of accuracy. Singular perturbation theory gives a formal basis for this process and explains how to remove fast modes while preserving stability features [70]. This idea is helpful in large-signal analysis, where electromechanical and control-interaction modes shape system behaviour.

State-variable transformation also assists simplification by removing terms with negligible effect on dominant modes [76]. In addition, detailed transfer-function descriptions for current and voltage controllers can be replaced with lower-order forms that keep phase and gain behaviour within a relevant frequency range [77]. First-order current-loop models have been validated in converter-based microgrids and can track inner-loop behaviour when bandwidth separation is clear [78]. These simplified forms support impedance-based studies because they preserve features that define terminal impedance. Network elements can also be simplified. Distributed-parameter cable and line models may be replaced with reduced equivalents that still capture resonant effects important for converter interaction. This reduces order while preserving the impedance seen at the terminals.

Figure 1.10(a) shows a converter with droop control, measurement filters, voltage and current loops, and an LCL filter linking the unit to the grid. Figure 1.10(b) gives a simplified view by replacing the current regulator with a first-order lag of time constant T_d and grouping passive parts to highlight the dominant path to the grid [79]. Average-value models (AVMs) offer another route to simplification by replacing switching functions with continuous sources that represent fundamental and low-frequency behaviour [80]. AVMs allow larger time steps, yet they still contain many states when many converters are connected, which increases computational cost in large plants [81][82].

- **Aggregation and System -Level Considerations**

Large renewable plants contain many converter-interfaced units. When each device is modelled individually, the number of states becomes high, and long simulations can be required to study slow dynamics. Aggregation addresses this challenge. Many units are grouped into one equivalent that reproduces the dynamic behaviour at the point of common coupling [83][84]. This approach supports studies of frequency support, grid interaction, protection, and disturbance behaviour. Aggregation of distant network regions also helps focus accuracy on areas where, local effects matter most.

Although aggregation improves efficiency, it must be applied with care. Equivalent models may miss interactions among controllers from different manufacturers or operating in different modes. Important resonance modes or coupling effects can be lost, especially in photovoltaic plants where non-linear I-V curves and shading effects are relevant [80][83][85]. When such features matter, reduced models may give inaccurate predictions. Validation against detailed models or measurements is therefore essential.

Neglecting coupling among fast and slow loops may lead to incorrect stability margins [83][86]. In some networks, bandwidth separation is weak, and fast and slow modes interact strongly. In those cases, classical model reduction may not be reliable. Reductions should therefore retain loops and elements that define impedance in the study frequency range and remove only those that have limited impact.

Overall, singular perturbation, transfer-function reduction, average-value modelling, and aggregation provide a foundation for efficient modelling in converter-dominated systems [77][78][80][82][83][85][86]. The models used in this thesis follow these ideas and are

parameter tuned to impedance-based analysis. Fast states that do not affect stability in the relevant band are removed, while key control and network terms remain. Figure 1.10(a)-(b) guides this selection by highlighting filters and control loops kept in the reduced model. This approach develops clear and efficient models that reflect physical interaction and support the analysis in later chapters. Detailed developments follow in Chapter 5.

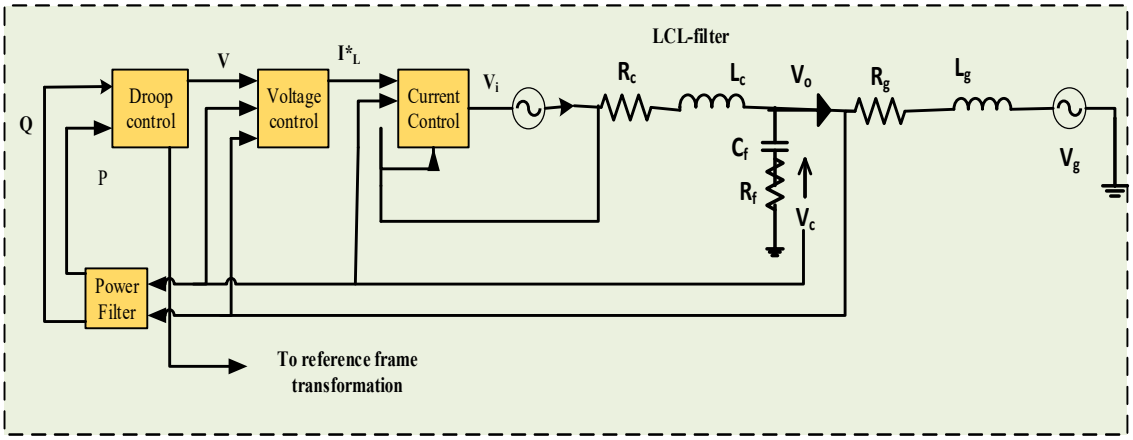

(a) Complete Converter and Filter Model

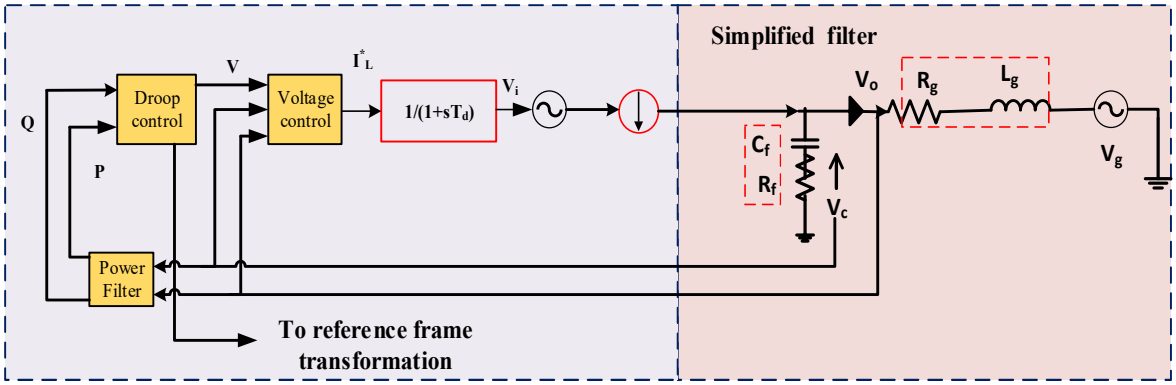

(b) Simplified Representation of the Current Control Loop

Figure 1.9: Schematic and Simplified Representation of the Converter Model

1.8 Motivation and Aims of the Work

1.8.1 Research Motivation and Objectives

The transition towards low-carbon energy systems is progressively replacing synchronous machines with converter-based renewable generation. Power electronic converters provide flexible control and fast dynamic response. However, their behaviour differs fundamentally from that of synchronous generators. As the share of converters increases, traditional grid strength measures, such as the short-circuit ratio (SCR), composite short-circuit ratio (CSCR), and effective short-circuit ratio (ESCR), become less reliable in converter-dominated systems. These indices are mainly derived from steady-state assumptions and do not fully represent the frequency-dependent characteristics introduced by converter control systems [87].

In weak grids, interactions between converters and the network can lead to oscillatory behaviour or instability. Several studies in the literature have addressed this issue using impedance-based and small-signal stability analysis methods. However, there remains a need for systematic approaches that clearly quantify interaction strength in multi-converter systems and indicate when simplified modelling assumptions remain valid. The motivation of this thesis is therefore not to claim that the problem has not been studied, but to contribute additional tools that improve clarity in assessing interaction mechanisms and model adequacy.

Impedance-based analysis provides a suitable framework for this purpose. It represents both converters and networks as frequency-dependent impedances and enables the use of established stability assessment tools such as the Generalised Nyquist Criterion. This approach has been widely adopted in the literature for studying converter-grid interactions. In this thesis, it is further developed to examine interaction effects in multi-converter systems and to define quantitative metrics that describe the strength and nature of these interactions.

The analysis in this work is conducted in the pn reference frame. The pn frame is selected because it separates positive- and negative-sequence components, which is particularly useful when studying weak grids and converter control systems that may introduce coupling between sequences. This representation simplifies the interpretation of impedance matrices and facilitates the application of impedance-based stability criteria. The choice of the pn

frame is therefore based on analytical clarity and consistency with frequency-domain stability analysis methods.

The objectives of this work are aligned with this motivation and are presented in the same logical order:

- To study converter impedance under different control structures and validate impedance-based models in the pn frame across a range of network strengths.
- To develop a frequency-domain framework for assessing stability and interaction in converter-dominated systems.
- To investigate how network strength and control parameters influence converter–converter and converter-network interactions, using the proposed IR and EIR metrics.
- To establish criteria that indicate when simplified models can be used without reducing the accuracy of stability assessment.

All claims and developments presented in this thesis are supported by analytical derivations, simulation studies, and where applicable, comparison with established methods reported in the literature.

1.8.2 Main Contributions:

This thesis makes the following contributions to impedance-based stability analysis in multi-converter power systems.

1. Development of IR and EIR**:** This work introduces the IR and the EIR as quantitative metrics for analysing converter-network interactions. These metrics represent the relative influence of neighbouring converters on the impedance seen at a given terminal. They provide measurable quantities that can be evaluated under different control modes, controller parameters, and grid strengths. The formulation shows how GFL and GFM converters modify the effective system impedance and alter interaction patterns. All definitions are derived from impedance models and validated through frequency-domain analysis.
2. Application of IR and EIR to multi-converter stability analysis: The proposed metrics are applied to identify oscillatory behaviour and interaction mechanisms in systems

with more than two converters. The analysis links variations in impedance characteristics to changes in stability margins. The results demonstrate how converter location, control structure, and operating conditions influence overall system behaviour. Case studies show that the metrics can indicate frequency ranges where interaction effects become significant, thereby supporting systematic stability assessment in converter-dominated networks.

3. Stability-oriented assessment of model simplification: This thesis investigates the impact of impedance model reduction on stability conclusions. The results show that the validity of simplified models depends on grid strength and control configuration. In strong grids with limited interaction, simplified representations can provide consistent stability predictions. In weak grids with strong coupling, accurate impedance representation becomes necessary. An error index is introduced to quantify deviations caused by simplification, with emphasis on high-interaction conditions.

Overall, this work contributes new interaction metrics, extends their application to multi-converter systems, and establishes structured guidelines for model simplification based on stability considerations.

1.9 Structure of the thesis:

This thesis is organised into five additional chapters, whose contents are outlined as follow:

Chapter 2 Provides an overview of impedance and admittance modelling approaches for converters and their control systems, including all relevant system components. The chapter outlines the linearisation techniques required to obtain small-signal models and compares GFL and GFM control strategies. Through comprehensive linearised system modelling, it demonstrates the superior stability performance of GFM control in weak grid.

Chapter 3 Focuses on two-converter networks and the interaction between converters and the surrounding grid under varying system strengths. It introduces two new methods-the IR and the EIR-to capture the behaviour of a converter after interacting with the network, as well as the resulting impact on a second converter. The analysis relies on small-signal impedance methods and is validated through detailed simulation studies. Furthermore, the

chapter evaluates how different control architectures influence impedance characteristics across critical frequency ranges, enabling the determination of interaction severity.

Chapter 4 Extends the investigation to multi-converter systems involving three or more units. The chapter analyses the complex interaction dynamics between converters and network components using the IR and EIR approaches. Particular attention is given to the role of additional elements such as cables and transformers, and how they influence local and inter-converter interactions under different grid strengths. The implications of these factors for overall system stability are systematically examined.

Chapter 5 Introduces a novel approach to assess the influence of remote converters on a designated reference converter. A model simplification method is proposed, where the stability impact is evaluated by quantifying the error between a detailed reference model and its simplified counterpart. Based on this comparison, an index is developed to evaluate the accuracy of the simplified model, ensuring its validity for use alongside detailed models. The methodology is examined within the framework of IR and EIR analysis.

Chapter 6 Concludes the thesis by summarising the main findings and providing recommendations for future research directions.

Chapter 2: Small-Signal Impedance Modelling and Stability Analysis of Grid-Connected Converters

2.1 Introduction

The principal contribution of this chapter is the development of a unified small-signal impedance modelling approach for both GFM and GFL converters, enabling direct comparison of their stability characteristics within a common analytical framework. Unlike conventional studies that treat these converter types separately, this chapter establishes a consistent modelling procedure that captures their distinct control structures while enabling comparative stability assessment within a common analytical platform. The formulation integrates converter control dynamics and network impedance, allowing frequency-domain representation of converter-grid interactions using established impedance-based stability criteria, as widely reported in the literature on impedance modelling and stability analysis.

This chapter adds to the overall thesis by providing the analytical basis required for later investigation of multi-converter systems and weak-grid conditions. The derived impedance models allow identification of oscillatory modes, assessment of grid strength effects, and determination of stable controller parameter regions.

Validation through MATLAB/Simulink® time-domain simulations confirms agreement between theoretical analysis and dynamic performance, supporting the thesis objective of impedance-based stability assessment in converter-dominated power systems.

2.2 Converter Modelling

This Section 2.2 introduces the standard representation of a grid-connected converter and clarifies its relevance to the thesis. The system considered is a conventional two-level VSC interfaced with the network through an LCL filter, as illustrated in Figure 2.1. The converter is modelled as a controlled voltage source that regulates active and reactive power via high-frequency switching.

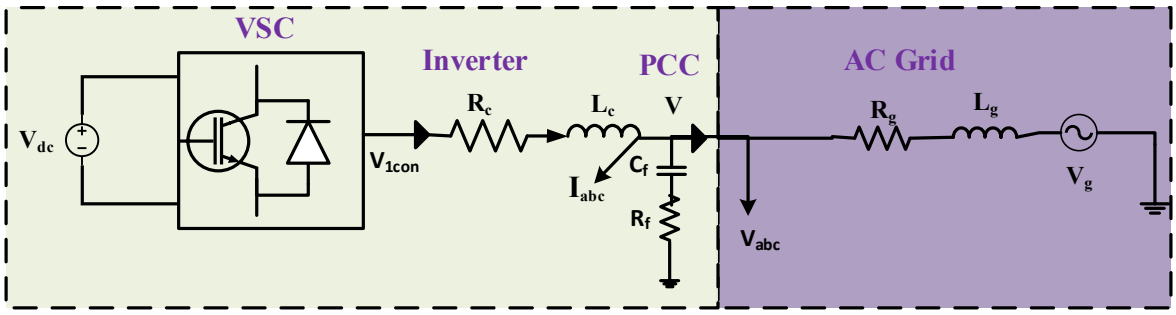

Figure 2.1: Voltage Source Converter connected to network.

For analytical purposes, an averaged formulation is adopted. Measurement signals are processed in the natural abc frame to reflect sensor bandwidth limits and then transformed into the synchronous dq frame for control design [88]. Although pulse-width modulation introduces nonlinear behaviour, the averaged description, together with first-order approximations of controller and modulation delays, preserves the dominant phase and gain characteristics.

This modelling approach reproduces the converter's frequency-dependent impedance response, forming the foundation for stability assessment. It also aligns with well-established methods used for analysing converter dynamics under small perturbations.

2.3 Impedance Modelling of GFL Converters

GFL converters remain the most widely adopted technology in renewable-dominated power systems, achieving grid synchronisation through a PLL. Their control architecture typically consists of an inner current loop and an outer power control loop. The inner loop regulates current in the dq frame with voltage feedforward and cross-coupling compensation, while the outer loop governs active and reactive power flow.

Recent developments have extended GFL capability to provide frequency response and fast inertial support [54][83][86][85]. Methods such as [89] allow the converter to adjust power output proportionally to frequency deviations, with energy supplied from the DC-link capacitor if voltage stability is preserved [90].

However, the current-source nature of GFL converters limits voltage regulation capability, particularly in weak grids [91]. The PLL becomes a critical factor under low SCR conditions, where improper tuning may cause oscillations or loss of synchronisation [92]. Although improved control methods enhance performance to approach GFM behaviour [93],

achieving stable operation in very weak networks remains challenging. Overly aggressive tuning to suit for weak grid conditions can potentially introduce resonances in strong grids, particularly when large shunt capacitances are present.

Consequently, GFL converters cannot fully substitute GFM units in all applications [94]. Nevertheless, their tunability, flexible control, and applicability in both grid-connected and islanded modes make them indispensable in modern systems. Stable operation requires careful coordination of impedance shaping, damping contributions, and controller bandwidths [54]. Emerging techniques, including adaptive tuning and impedance reshaping, present promising strategies for improving stability margins in high-penetration converter-based grids [95].

2.3.1 GFL Control Topology

The GFL topology considered in this work is shown in Figure 2.2. It consists of a generic two-level VSC, an LCL filter with parameters (R_c, L_c, C_f) and a Thevenin-equivalent grid model defined by grid impedance (R_g, L_g).

The cascaded control structure employs an inner current loop and an outer power or voltage loop. The inner loop regulates current in the dq frame, while the outer loop generates current references depending on the operating mode. A PLL maintains synchronisation by aligning the converter's reference frame with the grid voltage phase. Feedback signals are taken from the converter-side capacitor voltage (V_{abc}) and converter current (i_{abc}). The DC-link is modelled as an ideal voltage source.

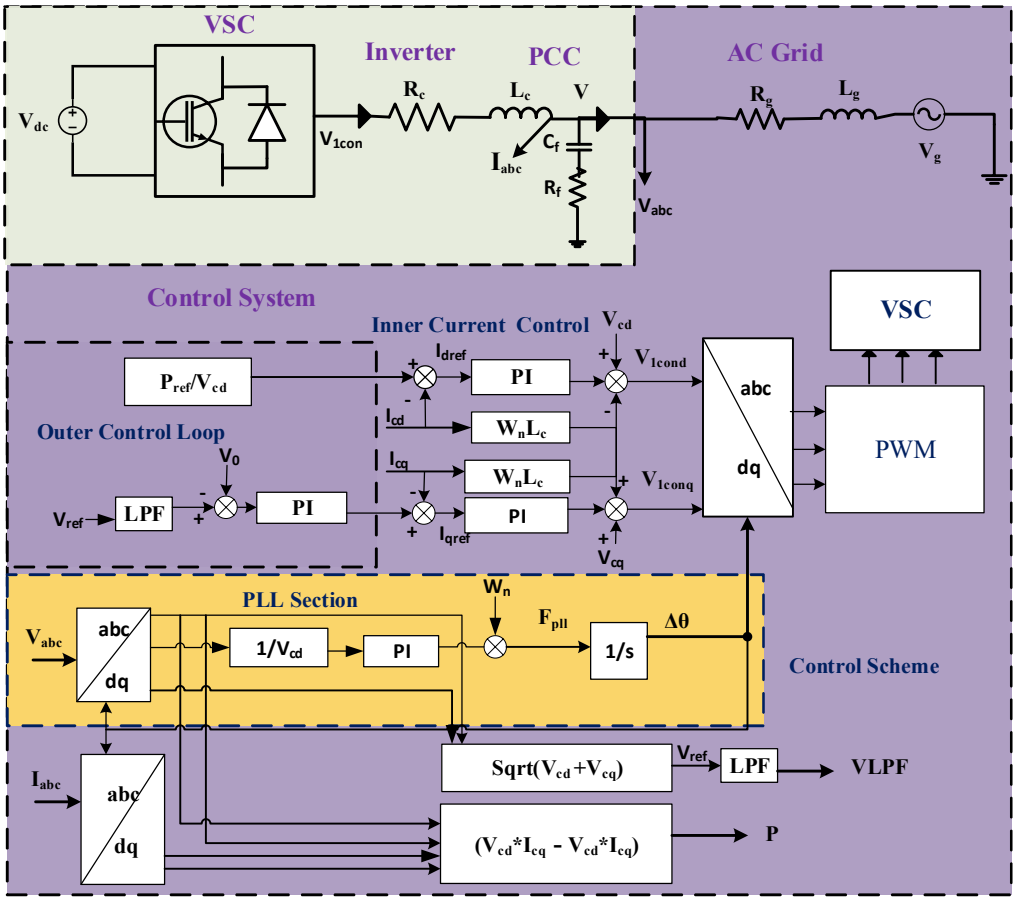

Figure 2.2: Control System Architecture of a Grid-Connected GFL Converter

Grid strength is characterised using parameters listed in Tables 2.1 and 2.2. For example, $L_g = 0.56$p.u corresponds to SCR = 1.8 (weak grid), while $L_g = 0.33$p.u. corresponds to SCR = 3.0 (strong grid). An SCR of 1.8 is close to the stability boundary and therefore enables investigation under demanding operating conditions. In contrast, an SCR of 3.25 provides a sufficiently stiff grid for benchmarking purposes. These configurations allow assessment of converter performance across a range of grid conditions. The system dynamics in the dq frame is given by:

$$R_c i_d + L_c \frac{di_d}{d_t} = V_{1cond} - V_d + w_n L_c i_q \tag{2.1}$$

$$R_c i_q + L_c \frac{di_q}{d_t} = V_{1conq} - V_q + w_n L_c i_d$$

Based on (2.1), relevant control systems are designed to ensure adequate dynamic response and control, as will be detailed in the following subsections.

Table 2.1: Control Parameters for VSCs Controller

Parameters	Values
ω_n	$2\times \pi \times 50$
Current loop PI gains: K_{pic}, K_{ic}	$Lc\times\omega_n\times 2$, $Lc\times\omega_n^2$
PLL PI gains: K_{ppll}, K_{ippll}	$2 \times \pi \times 60$, $(2 \times \pi*60)^2$
AC voltage controller PI gains: $K_{p;}$ K_u	1.2, 6 and 1.5, 7.5pu
L_c and R_c	0.1 and 0.01pu

Table 2.2: The system parameter for weak and strong Coupling

Parameter	Coupling One (Strong-Grid)	Coupling Two(Weak-Grid)
L_1	0.1pu	0.3pu
R_g	0.0167pu	0.0167pu
R_{g1}	0.0167pu	0.0167pu
L_g	0.2pu	0.36pu
L_{g1}	0.2pu	0.38pu
L_{cg1}	0.16pu	0.25pu
L_{cg2}	0.18pu	0.26pu
R_{cg1}	0.0167pu	0.0167pu
R_{cg2}	0.0167pu	0.0167pu
SCR	3.25	1.92pu

2.3.2 Synchronization Mechanism

Accurate phase alignment is fundamental to the reliable operation of GFL converters. Synchronisation is achieved through the PLL, which tracks the grid voltage angle by processing PCC measurements. The q-axis voltage component is forced to zero using a PI regulator, thereby aligning the converter's reference frame with the grid voltage phasor.

In steady state, the d-axis voltage component is aligned to the grid voltage, while the q-axis voltage becomes zero. This ensures that the converter's internal frame follows the actual grid angle (θ) without deviation. As illustrated in Figure 2.3, the PI controller continuously adjusts the estimated angle until $V_{cq} = 0$. This alignment enables the converter to deliver accurate active and reactive current under different grid conditions, preserving stability during variations in SCR and system impedance.

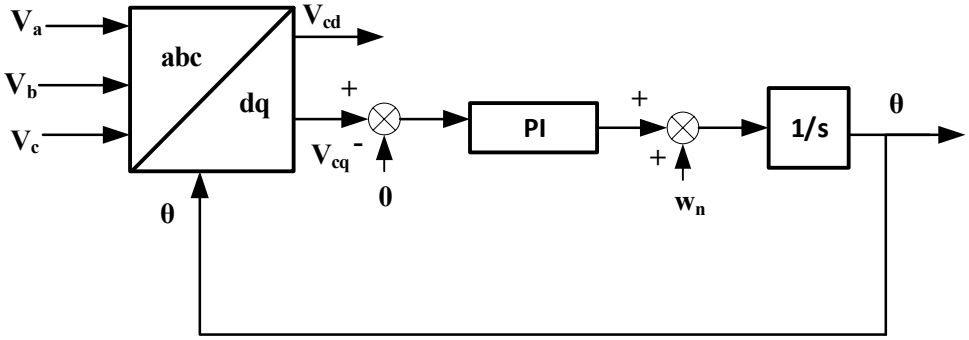

Figure 2.3: Block diagram of the PLL loop Control Structure

2.3.3 Inner Loop Control

The inner loop regulates the converter output current in the synchronous reference frame. Separate PI controllers govern the d-axis and q-axis currents, ensuring fast dynamic response and minimal steady-state error:

$$K_{pll} = K_{p,cc} + \frac{K_{i,cc}}{s} \tag{2.2}$$

Different parameter turning methods can be adopted, e.g., the controller gains are derived using the modulus optimum criterion with a tuning factor α, given as:

$$K_p, cc = \frac{L_f}{\alpha} \tag{2.3}$$

$$K_i, cc = \frac{R_f}{\alpha} \tag{2.4}$$

With L_f and R_f representing the filter inductance and resistance.

Since the inner loop operates at a higher bandwidth than the outer loop, it provides strong current regulation, which is essential for stability and power quality in both weak and strong grid conditions [96].

2.3.4 Outer Loop Control

The outer loop defines the active and reactive power exchange between the converter and the grid by generating current references for the inner loop. Its function depends on the selected operating mode. In PQ mode, the loop maintains the desired values of active power (P) and reactive power (Q). The reactive power reference may be fixed at zero for unity

power factor or adjusted to provide voltage support. In this mode, power setpoints are converted into d-axis and q-axis current references (i_{dref}, i_{qref}) using established mathematical relationships.

In PV mode, often used with weak grids, the outer loop regulates active power and the PCC voltage magnitude by adjusting reactive power. This approach improves stability when the short-circuit ratio is low and helps avoid voltage collapse.

In this study, a simple method is used where the active and reactive power references determine the current components in the rotating dq-frame. The d-axis and q-axis current reference is obtained as:

$$i_{d\,ref} = \frac{P_{ref}}{V_{cd}}, i_{q\,ref} = \frac{Q_{ref}}{V_{cd}} \tag{2.5}$$

where P_{ref} and Q_{ref} denote the active and reactive power references, respectively, and V_{cd} is the d-axis capacitor voltage. The instantaneous voltage magnitude at PCC is obtained as:

$$v = \sqrt{v_{cd}^2 + v_{cq}^2} \tag{2.6}$$

Where, V_{cq} is the q-axis capacitor voltage. The q-axis current reference, i_{qref}, is provided by the AC voltage regulator in the inner current loop. To ensure accurate tracking under steady-state operation, a PI regulator is employed, as illustrated in Figure 2.3.

2.4 Linearisation and Small-Signal Modelling for GFL Impedance

GFL converters exhibit nonlinear behaviour due to switching actions and internal control loops. To obtain their small-signal impedance for frequency-domain stability analysis, linearisation is required. This section presents a structured modelling approach for small-signal impedance derivation. The full mathematical development from first principles is provided in Appendix C.

2.4.1 Admittance in dq frame

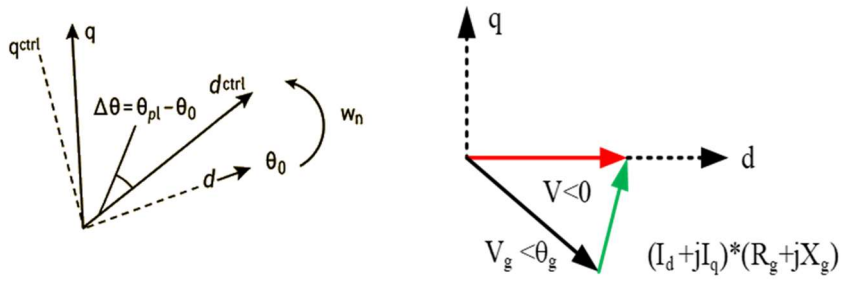

(a) (b)

Figure 2.4: (a) Schematic Representation of Voltage-Oriented d-q Reference Frames (b) steady -state voltage vector diagrams the d-q frame.

Step 1: Reference Frame Selection

The modelling process is most effectively carried out in the synchronous rotating dq-frame. Two frames are considered, as shown in Figure 2.4. The first is the actual grid reference frame, which is aligned with the instantaneous voltage phasor at the PCC, denoted by the angle θ_0. The second is the control reference frame, aligned with the phase estimated by the PLL, θ_{pll}. The angular displacement between these two frames, $\Delta\theta = \theta_{pll} - \theta_0$, quantifies the synchronization error. Under nominal steady-state conditions this deviation is negligible, but disturbances, faults, or rapid parameter variations can cause significant misalignment, directly influencing converter dynamics and system stability.

Step 2: Steady-State Power Flow and Converter Equations

The steady-state representation is obtained by aligning the PCC voltage along the d-axis such that $V_q = 0$. In this configuration, the grid voltage vector shown lags PCC voltage by an angle θ_g. Based on this orientation, the fundamental equations governing the interaction between converter and grid are derived from Figure 2.4(b), as:

$$v_d - v_{gd} = R_g i_d - \omega_n L_g i_q \,, \quad v_q - v_{gq} = R_g i_q + \omega_n L_g i_d \qquad (2.7)$$

Where, v_d and v_q denote the steady state values of the capacitor voltage v_{gd} and v_{gq} represent the grid voltage components, i_d and i_q are the converter currents, while R_g and L_g denote the grid resistance and inductance, respectively.

The instantaneous active and reactive power exchanged at the PCC are expressed as:

$$P = V_d i_d + V_q i_q \,,\; Q = V_q i_d - V_d i_q \tag{2.8}$$

With the conditions $v_q = 0$, and $v_d = v_g$, the active and reactive power at the PCC is

$$P = V_d i_d \;\;,\;\; Q = -V_d i_q \tag{2.9}$$

These expressions define the operating point and provide the base for linearisation and reference-current generation.

Step 3: Small-Signal Linearization and PLL Modelling in GFL converters, synchronization with the external network is maintained through a PLL. This mechanism introduces two reference frames in the dq-domain, as previously described in step1.

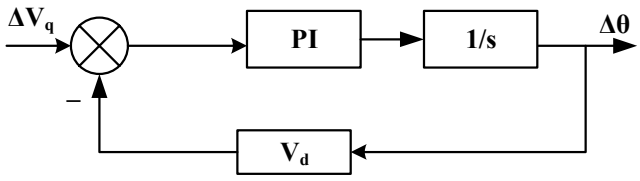

Figure 2.5: relationship between $\Delta\theta$ and ΔV_q

Figure 2.5 demonstrates that a small perturbation in the q-axis voltage(ΔV_q) produces an angular deviation $\Delta\theta$, which the PLL attempts to minimize through its PI controller. The PLL acts to minimise $\Delta\theta$ through its proportional-integral controller, as:

$$\Delta\theta = F_{pll}(s)\Delta V_q \tag{2.10}$$

With the transfer function:

$$F_{pll}(s) = \frac{K_{ppll}(s)+K_{ipll}}{s^2 + V_d K_{ppll}(s) + V_d K_{ipll}(s)} \tag{2.11}$$

where K_{ppll} and K_{ipll} the proportional and integral gains of the PLL, and V_d is the steady-state d-axis voltage.

Step 4*:* dq - Frame Perturbation Transformation

The transformation between the control PLL and grid reference frames is governed by a rotational matrix. For small angular deviations, this relationship is linearized as:

$$\begin{bmatrix} V_{cd} \\ V_{cq} \end{bmatrix} = \begin{bmatrix} \cos(\theta) & \sin(\theta) \\ -\sin(\theta) & \cos(\theta) \end{bmatrix} \begin{bmatrix} V_d \\ V_q \end{bmatrix} \tag{2.12}$$

Here, K_{ppll} and K_{ipll} are the proportional and integral gains, respectively. Voltage perturbations ΔV_d and ΔV_q passing through the PLL results in:

$$\begin{bmatrix} V_{cd} + \Delta V_{cd} \\ V_{cq} + \Delta V_{cq} \end{bmatrix} = \begin{bmatrix} \cos(0 + \Delta\theta) & \sin(0 + \Delta\theta) \\ -\sin(0 + \Delta\theta) & \cos(0 + \Delta\theta) \end{bmatrix} \begin{bmatrix} V_d + \Delta V_d \\ V_q + \Delta V_q \end{bmatrix} \tag{2.13}$$

The voltage perturbation of the PLL frame is obtained by subtracting (2.12) from (2.13):

$$\begin{bmatrix} \Delta V_{cd} \\ \Delta V_{c_q} \end{bmatrix} = \begin{bmatrix} \Delta V_d + \Delta\theta V_q + & \Delta\theta\Delta V_q \\ \Delta V_q - \Delta\theta V_d - & \Delta\theta\Delta V_d \end{bmatrix} \tag{2.14}$$

Neglecting the high-order terms, the voltage perturbation in the PLL frame is approximated as:

$$\begin{bmatrix} \Delta V_{cd} \\ \Delta V_{cq} \end{bmatrix} = \begin{bmatrix} \Delta V_{cd} + & \Delta\theta V_q \\ \Delta V_{cq} - & \Delta\theta V_d \end{bmatrix} \tag{2.15}$$

Substituting (2.10) into (2.15) yields a direct mapping from small voltage disturbances to frame transformation errors:

$$\begin{bmatrix} \Delta V_{cd} \\ \Delta V_{cq} \end{bmatrix} = \begin{bmatrix} \Delta V_d + & \Delta\theta V_q \\ \Delta V_q - & \Delta\theta V_d \end{bmatrix} = \begin{bmatrix} 1 & V_q F_{pll}(s) \\ 0 & 1 - V_{cd} F_{pll}(s) \end{bmatrix} \begin{bmatrix} \Delta V_{cd} \\ \Delta V_{cq} \end{bmatrix} \tag{2.16}$$

$$\begin{bmatrix} \Delta V_{cd} \\ \Delta V_{cq} \end{bmatrix} = \begin{bmatrix} \Delta V_d + & \Delta\theta V_{cq} \\ \Delta V_q - & \Delta\theta V_{cd} \end{bmatrix} = \begin{bmatrix} 1 & \Delta\theta \\ -\Delta\theta & 1 \end{bmatrix} \begin{bmatrix} V_d + \Delta V_d \\ V_q + \Delta V_q \end{bmatrix}$$

$$\Delta V_{cd} \approx \Delta V_d + \Delta\theta V_q \ , \Delta V_{cq} \approx -\Delta\theta V_d + \Delta V_q$$

A similar linearization applies to the current perturbations, linking the system's electrical and control variables and allowing for consistent small-signal analysis throughout the model, as:

$$\begin{bmatrix} \Delta i_{cd} \\ \Delta i_{cq} \end{bmatrix} = \begin{bmatrix} \Delta i_d + & \Delta\theta i_q \\ \Delta i_q - & \Delta\theta i_d \end{bmatrix} = \begin{bmatrix} 0 & i_q F_{pll}(s) \\ 0 & -i_d F_{pll}(s) \end{bmatrix} \begin{bmatrix} \Delta V_d \\ \Delta V_q \end{bmatrix} + \begin{bmatrix} \Delta i_d \\ \Delta i_q \end{bmatrix} \tag{2.17}$$

The small-signal output voltage references by the current controller in the system dq frame is given by:

$$\begin{bmatrix}\Delta V_{1cond}\\ \Delta V_{1conq}\end{bmatrix} = \begin{bmatrix}\Delta V_{1cd} - \Delta\theta V_{1cq}\\ \Delta V_{1cq} + \Delta\theta V_{1cd}\end{bmatrix} = \begin{bmatrix}0 & -\Delta V_{1cq}F_{pll}(s)\\ 0 & V_{1cd}F_{pll}(s)\end{bmatrix}\begin{bmatrix}\Delta V_d\\ \Delta V_q\end{bmatrix} + \begin{bmatrix}\Delta V_{1cd}\\ \Delta V_{1cq}\end{bmatrix} \quad (2.18)$$

In Equation (2.18), V_{1cond}, V_{1conq} , ΔV_{1cd} and ΔV_{1cq} represents steady-state and perturbation voltages at the output of the current loop within the control reference frame, respectively.

Step 5: Converter Filter and Admittance:

These relationships capture the propagation of small perturbations in voltage and current through the PLL dynamics and into the converter's control loops. The converter-side filter and its interaction with the grid are captured through the following admittance equation in the dq frame:

$$\begin{bmatrix}\Delta V_{1cond}\\ \Delta V_{1conq}\end{bmatrix} - \begin{bmatrix}\Delta V_d\\ \Delta V_q\end{bmatrix} = \begin{bmatrix}L_c s + R_c & -w_n L_c\\ w_n L_c & L_c s + R_c\end{bmatrix}\begin{bmatrix}\Delta i_d\\ \Delta i_q\end{bmatrix} \quad (2.19)$$

In these expressions, ΔV_{1cond} and ΔV_{1conq} are the small-signal perturbations in converter terminal voltages, ΔV_d and ΔV_q are the small perturbations at the PCC, Δi_d and Δi_q are current perturbations, L_c and R_c are the converter-side filter inductance and resistance, and ω_n again is the grid angular frequency. The linearisation in Equation (2.19) is obtained by applying first-order Taylor expansion around the steady-state operating point and neglecting higher-order perturbation terms.

Step 6: Matrix Formulation and Control Structure:

To simplify the analysis, the following matrices are defined as:

$$\Delta V_c = \begin{bmatrix}\Delta V_{cd}\\ \Delta V_{cq}\end{bmatrix},\ \Delta i_c = \begin{bmatrix}\Delta i_{cd}\\ \Delta i_{cq}\end{bmatrix}, \Delta V = \begin{bmatrix}\Delta V_d\\ \Delta V_q\end{bmatrix},\ \Delta i = \begin{bmatrix}\Delta i_d\\ \Delta i_q\end{bmatrix},\ \Delta V_{1c} = \begin{bmatrix}\Delta V_{1cd}\\ \Delta V_{1cq}\end{bmatrix},$$

$$\Delta V_{1con} = \begin{bmatrix}\Delta V_{1cond}\\ \Delta V_{1conq}\end{bmatrix}$$

Additionally, the matrices A, B, E, and Z_{con} are defined as:

$$A = \begin{bmatrix} 1 & V_q F_{pll}(s) \\ 0 & 1 - V_d F_{pll}(s) \end{bmatrix}, B = \begin{bmatrix} 0 & i_q F_{pll}(s) \\ 0 & -i_d F_{pll}(s) \end{bmatrix}, E = \begin{bmatrix} 0 & -V_{1conq} F_{pll}(s) \\ 0 & V_{1cond} F_{pll}(s) \end{bmatrix}, \text{ and}$$

$$Z_{con} = \begin{bmatrix} L_c s + R_c & -w_n L_C \\ w_n L_c & L_c s + R_c \end{bmatrix}$$

A: Encapsulates PLL voltage perturbation effects.

B: Captures PLL-induced current perturbation impacts.

E: Accounts for reference frame transformation errors in the current controller.

Z_{con}: Describes the filter dynamics.

Using these definitions, the small-signal equations (2.16), (2.17), (2.18), and (2.19) can be compactly expressed as:

$$\Delta V_{1con} - \Delta V_c = Z_{con}\, \Delta i_c \tag{2.20}$$

$$\Delta V_c = A \Delta V \tag{2.21}$$

$$\Delta i_d = B \Delta V \ + \Delta i \tag{2.22}$$

$$\Delta V_{1c} = E \Delta V - \Delta V_{1con} \tag{2.23}$$

When the VSC is under direct current loop control, the current control is represented by the matrix C.

Furthermore, the decoupling term within the current control can be designated. For a VSC under direct current control, the current control matrix C and decoupling term D are defined as:

$$C = \begin{bmatrix} G_{ic} & 0 \\ 0 & G_{ic} \end{bmatrix} \qquad (2.24) \qquad D = \begin{bmatrix} 0 & -w_n L_c \\ w_n L_c & 0 \end{bmatrix} \qquad (2.25)$$

Here, $G_{ic} = K_{pic}$ and $\frac{K_{ic}}{s}$, where K_{pic} and K_{ic} are the proportional and integral gains of the current-loop PI controller, respectively. The decoupling effect within the current controller is modelled in equation (2.25).

The impact of digital control and PWM induced delays is incorporated as:

$$T_{del} = \begin{bmatrix} G_d & 0 \\ 0 & G_d \end{bmatrix} \tag{2.26}$$

Where $G_d = \frac{1}{0.5T_{del}s+1}$

The small-signal output voltage at the current controller is then given by:

$$\Delta V_{1c} = T_{del}(-C\Delta i_c + D\Delta i_c + \Delta V_c) \tag{2.27}$$

Step 7: Inner -Loop Admittance

Including PLL, current control, decoupling, and delay, the VSC small-signal admittance is

$$Y_{vscon} = -\frac{\Delta i}{\Delta V} = \frac{E - T_{del}\,CB + T_{del}\,DB + T_{del}\,A - I}{T_{del}\,D - Z_{con} - T_{del}C} \tag{2.28}$$

This yields a 2x2 frequency-dependent matrix admittance:

$$Y_{vscon}(s) = \begin{bmatrix} Y_{vscondd}(s) & Y_{vscondq}(s) \\ Y_{vsconqd}(s) & Y_{vsconqq}(s) \end{bmatrix} \tag{2.29}$$

Step 8: Outer Control Loops and Reference Current Generation

The outer controllers regulate active power and AC voltage, and their linearized dynamics further influence the converter's small-signal admittance. The corresponding matrix equation is:

$$\begin{bmatrix} \Delta i_{dref} \\ \Delta i_{qref} \end{bmatrix} = \begin{bmatrix} 1 & 0 \\ 0 & K_{pu} + \frac{K_{iu}}{s} \end{bmatrix} \begin{bmatrix} -\frac{P_{ref}}{V_d^2} & 0 \\ V_d & V_q \end{bmatrix} \begin{bmatrix} \Delta V_{cd} \\ \Delta V_{cq} \end{bmatrix} \tag{2.30}$$

where K_{pu} and K_{iu} are the PI gains for the voltage controller and P_{ref} is the power setpoint.

Defining $U = \begin{bmatrix} 1 & 0 \\ 0 & K_{pu} + \frac{K_{iu}}{s} \end{bmatrix}$ and $P_0 = \begin{bmatrix} -\frac{P_{ref}}{V_d^2} & 0 \\ V_d & V_q \end{bmatrix}$, the total small-signal admittance, now encompassing PLL and outer control loop influences, is:

$$Y_{vscon} = -\frac{\Delta i}{\Delta v} = \frac{E - T_{del}CB + T_{del}DB + {}_{del}A + T_{del}CUAP_0 - I}{T_{del}D - Z_{con} - T_{del}C} \tag{2.31}$$

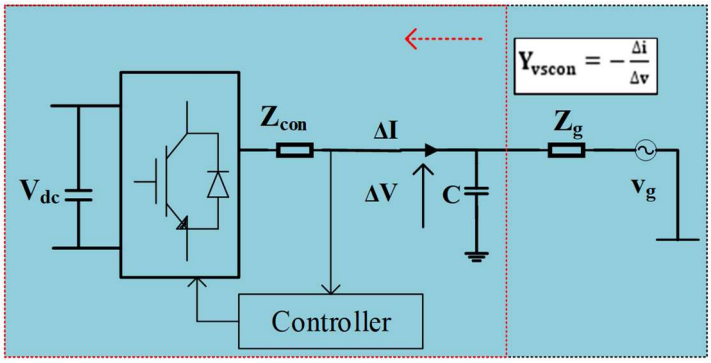

Figure 2.6: Schematic Diagram Illustrating the Calculation of VSC Admittance

Step 9: Schematic and stability use

Figure 2.6 shows the admittance calculation. The converter, filter, and control system are connected to the grid through Z_{con}. Voltage and current disturbances at the PCC provide the converter frequency response. This response is used for stability assessment and controller tuning [70][97][70][53]. The schematic therefore links the analytical derivation of admittance to the physical behaviour of the converter under small disturbances, forming a foundation for controller evaluation and stability studies in converter connected to networks.

Furthermore, this section presented a clear and systematic linearisation and admittance-modelling framework for a GFL converter. The model includes the PLL, current controller, filter, digital delay, and outer control loops. It provides a complete small-signal representation used for impedance-based stability analysis.

2.4.2 Admittance Representation in the pn Frame

Transforming the small-signal admittance matrix from the dq frame to the pn sequence frame constitutes a crucial step in advanced stability analysis of GFL Voltage Source Converters (GFL-VSCs), as outlined in Chapter 1 [10][51][98]. Unlike the dq frame, where

each converter requires an individual representation, the pn frame allows all converters to be described in a unified reference. This common formulation eliminates the need for multiple rotating frames when analysing interconnected converters, thereby simplifying the modelling of large-scale systems.

The motivation for employing the pn frame lies in its ability to provide a unified representation for all converters in the network. By expressing the system variables in positive - and negative-sequence components, all subsystems can be described within a common stationary framework. This approach removes the need for separate rotating references and enables a consistent description of converter interactions. As a result, the modelling process becomes more structured and better suited for large-scale converter-dominated systems.

Furthermore, the pn representation improves the clarity of stability analysis. In the dq frame, the system is naturally formulated as a coupled MIMO structure, which often requires complex matrix-based stability criteria. In contrast, the pn domain allows stability to be interpreted more directly through impedance or admittance characteristics. The sequence-based formulation separates dominant interaction paths and facilitates the identification of critical frequency regions associated with instability.

Therefore, the use of the pn frame is not only a mathematical transformation but a deliberate methodological choice. It provides a common analytical platform, reduces structural complexity, and enhances the physical interpretation of converter interactions in modern power systems.

(a) Transformation of the Admittance Matrix:

The procedure begins with the small-signal admittance originally derived in the dq frame (Equation 2.29). By applying the appropriate frequency shifts and linear transformations, the admittance is expressed in terms of positive- and negative-sequence variables. The resulting elements are:

$$Y_{vsconpp}(s) = \frac{1}{2}\left[Y_{vscondd}\,(s - jw_n) - jY_{vscondq}(s - jw_n) + \; jY_{vsconqd}(s - jw_n) + Y_{vsconqq}(s - jw_n)\right]$$

$$Y_{vsconpn}(s) = \frac{1}{2}\left[Y_{vscondd}\,(s + jw_n) + jY_{vscondq}(s + jw_n) + \; jY_{vsconqd}\,(s + jw_n) - Y_{vsconqq}(s + jw_n)\right]$$

$$Y_{vsconnp}(s) = \frac{1}{2}\left[Y_{vscondd}\,(s - jw_n) - jY_{vscondq}(s - jw_n) - jY_{vsconqd}(s - jw_n) - Y_{vsconqq}(s - jw_n)\right]$$
$$Y_{vsconnn}(s) = \frac{1}{2}\left[Y_{vscondd}\,(s + jw_n) + jY_{vscondq}(s + jw_n) - jY_{vsconqd}(s + jw_n) + Y_{vsconqq}(s + jw_n)\right]$$

(2.32)

where $Y_{vsconpp(s)}$, $Y_{vsconpn(s)}$, $Y_{vsconnp(s)}$, and $Y_{vsconnn(s)}$ denote the positive-positive, positive-negative, negative-positive, and negative-negative sequence admittances, respectively. These terms describe the relationship between voltage perturbations in one sequence and the resulting current responses in either the same or the opposite sequence. The mapping inherently captures frequency coupling introduced by converter control loops and the reference frame transformation The resulting admittance can then be arranged in a compact matrix form:

$$Y_{vscon}pn\,(s) = \frac{\begin{bmatrix} i_p(s+jw_n) & i_p(s+jw_n) \\ i_n(s-jw_n) & i_n(s-jw_n) \end{bmatrix}}{\begin{bmatrix} V_p(s+jw_n) & V_p(s+jw_n) \\ V_n(s-jw_n) & V_n(s-jw_n) \end{bmatrix}} \tag{2.33}$$

Further simplifying,

$$Y_{vscon}pn(s) = \begin{bmatrix} Y_{vsconpp}(s) & Y_{vsconpn}(s) \\ Y_{vsconnp}(s - 2jw_n) & Y_{vsconnn}(s - 2jw_n) \end{bmatrix} \tag{2.34}$$

This matrix links the positive- and negative-sequence voltage and current phasors through the Laplace variable s. It explicitly shows that a disturbance in one sequence may propagate to both sequences, depending on the strength of the cross-coupling terms. The formulation also highlights that frequency-shifted components arise naturally due to the converter's dynamics.

By adopting the pn frame, stability evaluation becomes more transparent compared to the dq representation. The impedance can be assessed directly from this unified matrix, without the need for MIMO formulations, which are often required in the dq frame. This reduction in analytical complexity is particularly advantageous for large-scale converter-dominated grids, where strong coupling between multiple devices and across frequencies must be evaluated consistently.

(b) Physical Interpretation

As shown in (2.34), a positive-sequence voltage disturbance ΔV_p at f_p not only generate the positive-sequence current Δi_p at f_p through $Y_{vsconpp}(s)$ but also the negative -sequence current Δi_n at $(f_p - 2f_0)$ through $Y_{vsconnp}(s - 2j\omega n)$. Similarly, effects arise for negative-sequence disturbance voltage ΔV_n at f_p will cause both the negative-sequence current Δi_n at f_p through $Y_{vsconn}(s - 2j\omega n)$ and the positive current Δi_p at $(f_p + 2f_0)$ through $Y_{vsconpn}(s)$.

Under ideal conditions where the dq - frame admittance matrix satisfies both symmetry ($Y_{vscondd} = Y_{vsconqq}$) and anti-symmetry ($Y_{vscondq} = -Y_{vsconqd}$), the cross-coupling terms $Y_{vsconpn}$ and $Y_{vsconnp}$ in (2.32) becomes zero. This results in complete decoupling between positive- and negative-sequence components, meaning ΔV_p only generates the positive-sequence current Δi_p at f_p and the negative- sequence voltage ΔV_n only generates negative-sequence current Δi_n at f_p. However, practical grid-connected converters rarely exhibit such perfect symmetry due to phase-locked loop dynamics and outer-loop control interactions [99]. Consequently, these cross-coupling terms $Y_{vsconpn}$ and $Y_{vsconnp}$ may have significant impact on stability analysis, as their neglect may yield inaccurate assessments [51]. Section 2.6 will examine their impact in detail.

2.5 Impedance Modelling of GFM Converters

GFM converters represent a fundamental advancement in converter technology, as they can independently control both terminal voltage magnitude and phase angle. This inherent autonomy enables stable operation without the need for an external synchronising reference. Unlike GFL converters, which rely on a PLL, GFM units establish a local voltage and frequency reference, thereby supporting both interconnected and islanded conditions [100][101].

The principal strength of GFM converters lies in their ability to emulate synchronous machine behaviour. Through this emulation, they can regulate frequency directly, deliver synthetic inertia, and provide robust voltage control, which is essential in networks with declining levels of rotating inertia [102][103][54]. Although definitions of GFM operation

vary, the agreed attributes include autonomous voltage and frequency regulation, resilience during low-inertia events, and the capability for black-start operation [104][105] [106][107][108][109]. These features make GFM technology central to the reliable functioning of future grids dominated by inverter-based generation.

Historically, network integration has been dominated by GFL units because of their simplicity and alignment with traditional synchronous-machine-based systems. However, the increasing penetration of renewable resources and the progressive displacement of synchronous machines have exposed stability vulnerabilities, particularly in frequency regulation and voltage support [110]. This challenge has accelerated the adoption of GFM architectures, as their ability to provide direct frequency and voltage control addresses these deficiencies [111].

Accurate impedance modelling of GFM converters is essential for predicting their influence on stability and for quantifying their dynamic interaction with surrounding networks. The impedance profile defines the converter's contribution to power exchange, disturbance rejection, and oscillation damping [112]. Early research concentrated on islanded operation, showing that GFM converters suppress disturbances more effectively than GFL units [113]. Later studies extended the modelling approach to grid-connected scenarios, confirming that the control-induced shaping of converter impedance improves overall stability margins and enhances robustness against grid disturbances [114][54].

Recent control advancements have expanded the range of GFM strategies. Virtual Synchronous Machine (VSM) control replicates the electromechanical dynamics of synchronous machines, enhancing inertia and voltage support [115][116]. Droop-based methods provide decentralised frequency and voltage control, enabling scalable operation across multiple units [86][117]. Other approaches focus on impedance matching to strengthen dynamic interaction with weak networks, thereby improving transient stability, and reducing oscillatory risk [118]. Field implementations in Europe and Australia have demonstrated that GFM deployment enhances grid stability, particularly in regions with high renewable penetration and low synchronous inertia [119][120]. Large-scale demonstration projects further confirm that GFM units can sustain operation through severe system disturbances and enable grid restoration following blackouts [121].

2.5.1 GFM Control Topology

The control topology of GFM converters distinguishes them from their GFL counterparts by allowing independent setting of both terminal voltage magnitude and phase angle [112][122][54]. This capability ensures stable operation across diverse scenarios, including strong grids, weak grids, and islanded networks.

Among the control approaches, droop-based regulation, Virtual Synchronous Machine (VSM), and VSM with current control (VSMCC) are the most established. The present work focuses on the droop-based GFM design, which integrates an inner current control loop to guarantee fast and precise current tracking. This loop is indispensable for maintaining converter stability under disturbances, while higher-level layers regulate power and voltage.

The control hierarchy comprises three layers, as illustrated in Figure 2.7: Control System Architecture of a Grid-Connected GFM Converter.

- Inner Layer (Current Control): The innermost loop regulates the dq-frame converter currents through PI controllers with cross-coupling compensation. This ensures accurate current tracking, reduces steady-state error, and improves dynamic response.
- Middle Layer (Voltage/Power Control): The intermediate loop supervises either the terminal voltage or the exchanged power, depending on the selected mode of operation. Low-pass filters are applied to measured signals in this layer, suppressing high-frequency disturbances so that the controllers act on filtered quantities.
- Outer Layer (Power-Frequency Droop): The outermost loop introduces active power-frequency droop control. This mechanism adjusts the converter frequency according to active power deviations, thereby contributing to system frequency stability.

In parallel, passive harmonic filters are placed at the PCC to attenuate switching harmonics, ensuring compliance with power quality standards, as shown in Figure 2.7.

This layered control structure enables the GFM converter to manage its local voltage profile while simultaneously supporting system-wide frequency stability. Furthermore, by coordinating the inner, middle, and outer loops, the converter can deliver rapid corrective

actions during transients, strengthen grid stability, and enhance resilience under diverse operating conditions.

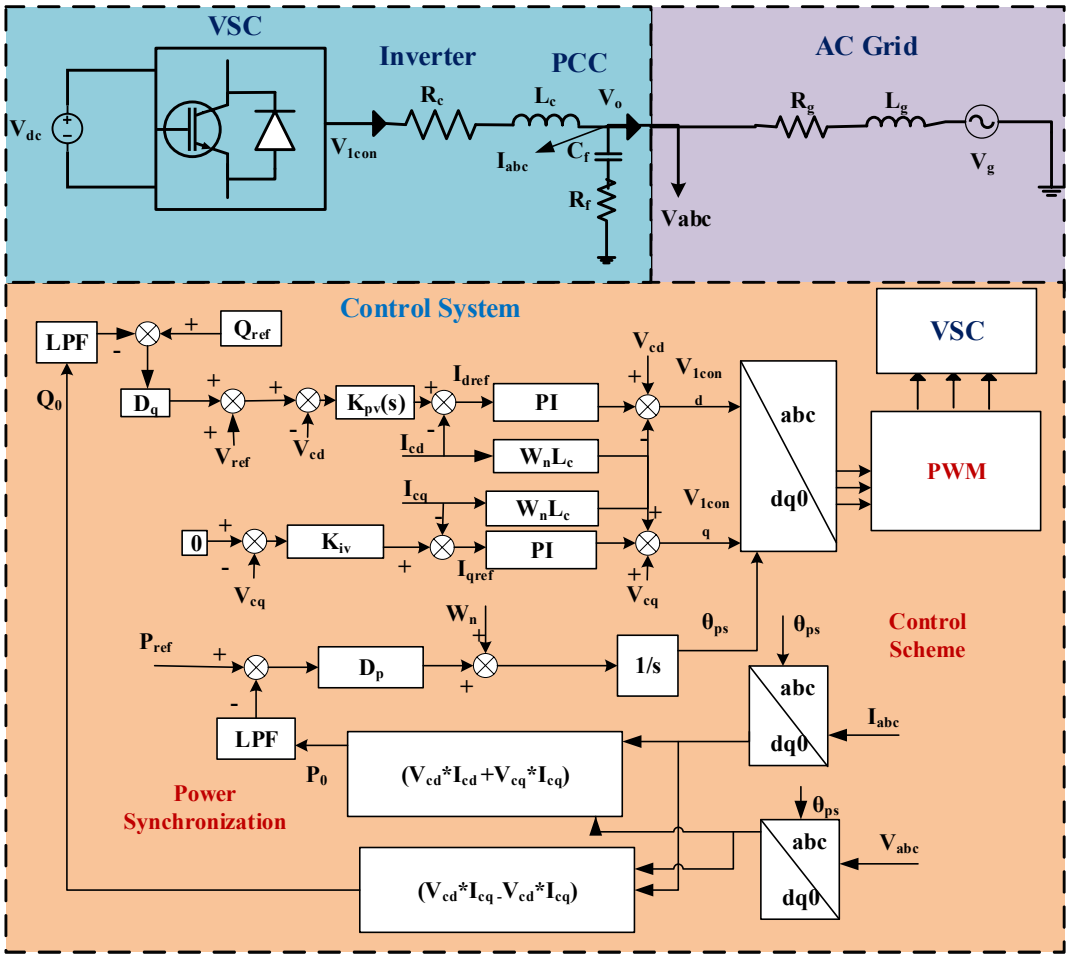

Figure 2.7: Control System Architecture of a Grid-Connected GFM Converter

2.5.2 Power Synchronization

Power synchronization is the defining characteristic of GFM converters. Unlike GFL designs, which depend on PLL for phase tracking, GFM converters establish their own terminal voltage magnitude and frequency reference, which is crucial for islanded systems and networks with limited inertia [123][54].

A widely implemented method to achieve synchronization is frequency-based droop control, in which the converter frequency varies proportionally with deviations in active power. The proportionality factor is determined by the droop gain D_p, which governs the frequency sensitivity to active power imbalance.

As illustrated in Figure 2.8, the reference power P_{ref} is compared with the measured power P_m, obtained by passing the actual power P_0 through a LPF. This filtering stage eliminates high-frequency components and ensures that only the fundamental dynamics are used for frequency regulation, thereby preventing unstable oscillations and promoting smooth adjustment. The filtered power is then processed by the droop block, generating a frequency correction term that modifies the nominal frequency w_n. The resulting frequency deviation $(w_n - w^*)$ is integrated to determine the phase angle θ, which establishes the converter's voltage reference. Control law can be written as:

$$D_p(\text{LPF}) = \frac{\Delta w}{\Delta p} = D_P\left(\frac{w}{s+w_c}\right) \tag{2.35}$$

Where w_c is the LPF cut-off frequency. This representation captures the combined effect of droop gain and filtering on frequency adjustment.

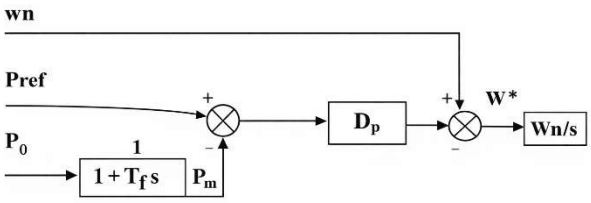

Figure 2.8: Frequency-droop controller for GFM

From the block structure, the active power dynamics can be expressed as:

$$P_0 = (1 + T_f \,.\, s)\left[\frac{1}{D_p}(w_n - w^*) + P_{ref}\right] \tag{2.36}$$

which expands to:

$$P_0 = \frac{T_f(s\,.w_n - s\,.w^*)}{D_p} + \frac{w_n - w*}{D_p} + T_f \,.\, s\,.\, P_{ref} + P_{ref} \tag{2.37}$$

Rearranging (2.37) yields:

$$T_f \frac{1}{D_p} s \cdot w^* = P_{ref} - P_0 - \frac{1}{D_p}(w^* - w_n) \tag{2.38}$$

In this representation, the term $T_f \frac{1}{D_p} s \cdot w^*$ behaves as an equivalent inertia component, while $\frac{1}{D_p}(w^* - w_n)$ provides damping acts. with $T_a = 2H$, the equivalent inertia constant and damping coefficient are given by:

$$H = \frac{1}{2D_p w_c} \ , \ K_d = \frac{1}{D_p} \tag{2.39}$$

Thus, frequency-based droop control naturally provides both inertia and damping, improving the converter's ability to stabilise frequency without relying on PLL-based synchronisation. The tuning of D_p is crucial, as smaller values increase damping but reduce responsiveness, while larger values improve speed of adjustment but risk oscillatory behaviour. In practice, typical settings of $D_p = 0.01$ for active power and $D_q = 0.05$ for reactive power achieve a reasonable balance between stability and performance [123].

Phase Angle-Based Droop Control: The phase angle-based droop method is derived from the classical active power-frequency (P-ω) and reactive power-voltage (Q-V) droop principles that emulate synchronous generator behaviour. In a synchronous machine, an increase in active power output is associated with a shift in rotor angle, while reactive power exchange is governed by terminal voltage. By replicating this characteristic, a converter can achieve autonomous power sharing without requiring communication links [124].

In this framework, the converter terminal phase angle (θ) and voltage magnitude (V) are regulated as functions of active and reactive power deviations from their setpoints. The control laws are expressed as:

$$\theta = \theta_{ref} - D_p(P - P_{ref}), \quad V = V_{ref} - D_q(Q - Q_{ref}) \tag{2.40}$$

Here, θ_{ref} and V_{ref} are nominal references, while P_{ref} and Q_{ref} represent the respective power setpoints. This structure allows converters to share power without communication links, as the steady-state frequency deviation is proportional to the active power error.

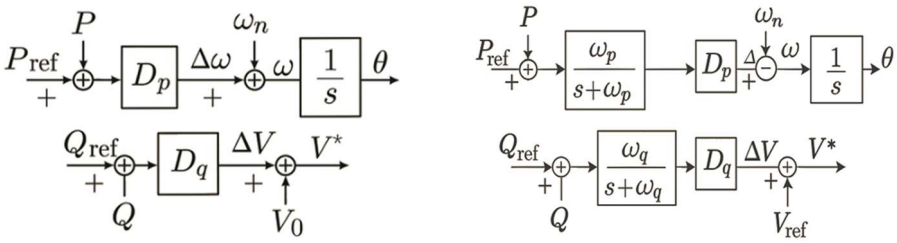

(a) Droop control (b) LPF droop control

Figure 2.9: Different control structure of the PSL-based GFM Control

By setting $\frac{\mathrm{d_w}}{\mathrm{d_t}} = 0$ in equation (2.38) and replacing $\mathrm{T_f}\frac{1}{\mathrm{D_p}}\mathrm{s}\,.\,\mathrm{w}^* = 0$, the steady-state relationship becomes:

$$(\mathrm{w}^* - \mathrm{w_n}) = \frac{1}{\mathrm{D_p}}(\mathrm{P_{ref}} - \mathrm{P_0}), \text{ resulting } \Delta\mathrm{w} = \mathrm{K_p} = \Delta\mathrm{P} \tag{2.41}$$

This indicates that frequency displacement is directly proportional to active power error, ensuring proportional power sharing across multiple converters, consistent with the analogy to synchronous generators [123], [124].

Figure 2.9(a) illustrates this fundamental droop structure, where power deviations are directly mapped to angle and voltage corrections. Although effective, this configuration is sensitive to noise and fast fluctuations in the measured signals. To address this limitation, Figure 2.9(b) introduces low-pass filters in the power measurement channels. These filters suppress high-frequency disturbances, smooth rapid changes, and impart a damping effect similar to virtual inertia. Consequently, the filtered droop control exhibits a more stable and robust transient response while maintaining accurate power sharing.

2.5.3 Linearization and Small-Signal Modelling for GFM Impedance Derivation

The derivation of the small-signal impedance model for GFM converters closely follows the procedure already developed for the GFL case in Section 2.4. Therefore, only the key differences are highlighted here, while the detailed linearization steps are directly referred to the GFL modelling to avoid repetition.

The converter-side filter dynamics remain identical to the GFL case and can be expressed in the dq frame as:

$$\begin{bmatrix}\Delta V_{1cond}\\ \Delta V_{1conq}\end{bmatrix} - \begin{bmatrix}\Delta V_d\\ \Delta V_q\end{bmatrix} = \begin{bmatrix}L_c s + R_c & -w_n L_c\\ w_n L_c & L_c s + R_c\end{bmatrix}\begin{bmatrix}\Delta i_d\\ \Delta i_q\end{bmatrix} \quad (2.42)$$

Where L_c and R_c denote the filter parameters and ω_n is the nominal grid angular frequency.

Power Synchronization Mechanism: In GFL converters, the phase-locked loop determines the angle dynamics by directly tracking the grid voltage. In contrast, GFM converters establish synchronization through their internal power regulation, a process referred to as power synchronization. This mechanism is realized by passing the measured active power through a low-pass filter before it influences the angle dynamics. The filter is described by:

$$P_{LPF} = \left(\frac{W_{LPF}}{s+W_{LPF}}\right) P_0 = G_{LPF} P_0 \quad (2.43)$$

where W_{LPF} denotes the cutoff frequency of the filter and P_0 represents the steady-state active power. The parameter W_{LPF} governs the bandwidth of the filtering process: a higher value yields a faster response but allows more high-frequency components, while a lower value suppresses rapid oscillations at the expense of slower dynamics.

The filtered signal regulates the small-signal angular deviation of the converter, expressed as:

$$\Delta\theta_{ps} = \left(\frac{D_p}{s}\right)(P_{LPF} - P_0) \quad (2.44)$$

This expression is analogous to the PLL transfer in the GFL derivation, and its influence enters the linearization in the same way.

Reference Frame Transformation: The transformation from the grid frame (V_d, V_q) to the converter control frame (V_{cd}, V_{cq}) follows the same trigonometric expansion as in the GFL case. Substituting the angle perturbation $\Delta\theta_{ps}$, the first-order approximation of the voltage perturbation becomes:

$$\Delta V_{cd} \approx \Delta V_d + \Delta\theta_{ps} V_q,\ \Delta V_{cq} \approx \Delta V_q - \Delta\theta_{ps} V_d \quad (2.45)$$

The equivalent expressions for current perturbations and controller-induced voltage perturbations are directly analogous to equations (2.17) and (2.18) of the GFL derivation, but with $\Delta\theta_{ps}$ replacing the PLL dynamics.

Compact Matrix Representation: For compactness, the same notations as in Section 2.4 are used:

$$\Delta V_c = \begin{bmatrix} \Delta V_{cd} \\ \Delta V_{cq} \end{bmatrix},\ \Delta i_c = \begin{bmatrix} \Delta i_{cd} \\ \Delta i_{cq} \end{bmatrix}, \Delta V = \begin{bmatrix} \Delta V_d \\ \Delta V_q \end{bmatrix}$$

with corresponding matrices, A, B, E and Z_{con} defined in the same way as equations (2.19) -(2.23), but with the PLL terms substituted by $\Delta\theta_{ps}$.

The matrices A, B, E, and Z_{con} are built from the system parameters and current state variables. The term Z_{con} represents the filter dynamics, while A, B, and Ecapture the effects of the reference-frame transformations and control actions. The small-signal equations are written in compact form as

$$\Delta V_{1con} - \Delta V_c = Z_{con}\, \Delta i_c \tag{2.46}$$

$$\Delta V_c = A\Delta V \tag{2.47}$$

$$\Delta i_d = B\Delta V \ + \Delta i \tag{2.48}$$

$$\Delta V_{1c} = E\Delta V - \Delta V_{1con} \tag{2.49}$$

Controller and Delay Modelling: The current controller, decoupling terms, and digital delay are represented by matrices C, D, T_{del} identical in structure to the GFL model (equations (2.24) - (2.26)) and are therefore not repeated.

Small-Signal Admittance Derivation: By combining the above equations, the complete small-signal admittance for the GFM converter is obtained as:

$$Y_{vscon} = -\frac{\Delta i}{\Delta V} = \frac{E - T_{del}\, CB + T_{del}\, DB + T_{del}\, A - I}{T_{del}\, D - Z_{con} - T_{del} C} \tag{2.50}$$

with the matrix form:

$$Y_{vscon}(s) = \begin{bmatrix} Y_{vscondd}(s) & Y_{vscondq}(s) \\ Y_{vsconqd}(s) & Y_{vsconqq}(s) \end{bmatrix} \tag{2.51}$$

Outer Control Loops: Finally, the output current references generated by the outer AC voltage controller follow the same structure as the GFL derivation (equation (2.30)), with

controller gains adjusted to reflect the voltage regulation function in GFM operation. The total admittance expression becomes:

$$Y_{vscon} = -\frac{\Delta i}{\Delta v} = \frac{E - T_{del}CB + T_{del}DB + T_{del}A + T_{del}CUAP_0 - I}{T_{del}D - Z_{con} - T_{del}C} \quad (2.52)$$

This yields the full frequency-dependent admittance model of the GFM converter, directly comparable with the GFL case but governed by the power synchronization mechanism instead of the PLL.

Impedance modelling in dq frame is then transformed into pn frame in the same was as for GFL, as described in 2.4.

2.5.4 Inner current controller

The inner current controller in the GFM scheme follows the same basic principle as the GFL case described in Section 2.3.3. Separate PI regulators govern the d - and q-axis current components, ensuring accurate tracking and fast response. The controller transfer function can be written as

$$G_{PI}(s) = K_p + \frac{K_i}{s} \quad (2.53)$$

where K_p and K_i are the proportional and integral gains, respectively. As in the GFL design, current regulation requires careful tuning of the controller parameters. To address the coupling between the d-and q-axis dynamics, additional compensation terms of the form $(\omega_n L_c)$ are included. These terms mitigate cross-coupling effects, thereby improving control precision and dynamic performance.

The regulated current references in the dq frame are subsequently transformed into voltage commands. These are processed by the PWM block, which generates three-phase switching signals for the converter. Accurate PWM operation is essential to minimize harmonic distortion, maintain power quality, and ensure stable interaction with both weak and strong grids.

2.5.5 Outer Loop Control

The GFM outer loop shares similarities with the GFL scheme but differs in its primary objectives. Instead of directly controlling current, it regulates the converter terminal voltage and provides reactive power support.

The control law compares the reference and measured reactive power values and applies a PI regulator to compute the voltage reference:

$$V_{ref}(s) = K_{pv}(Q_{ref}(s) - Q_{meas}(s)) + K_{iv}\int (Q_{ref}(s) - Q_{meas}(s)dt \quad (2.54)$$

where K_{pv} and K_{iv} are the proportional and integral gains. To strengthen stability and ensure coordinated grid interaction, droop characteristics are included. The Q-V droop relation adjusts terminal voltage in response to reactive power variation, while the P-f droop determines frequency changes based on active power exchange. The combined action of the PI regulator and droop laws enables the converter to maintain PCC voltage, support reactive power requirements, and contribute to frequency regulation without conflicting with other grid-connected units.

2.6 Impedance Measurement in the Time domain Model

To confirm the accuracy of the derived impedance models, frequency-domain validation is carried out through detailed time-domain simulations. In this approach, small sinusoidal voltage perturbations are injected at the PCC over a defined frequency range. The corresponding converter current response is then recorded. By computing the ratio of the current perturbation to the applied voltage disturbance, the frequency-dependent admittance is determined. This admittance is subsequently used to verify the consistency of the modelled impedance with the simulated system behaviour.

2.6.1 Time-Domain Simulation Approach for Measuring VSC Small -Signal Admittance

To assess and validate the small-signal admittance of a grid-connected VSC, a detailed time-domain simulation model is developed using MATLAB in the pn reference frame. To extract the admittance, small-signal perturbation voltages (Δv_{pa} , Δv_{pb}, Δv_{pc}) are injected at the PCC across a range of frequencies, as shown in Figure 2.10. The resulting phase voltages

$(\Delta v_a, \Delta v_b, \Delta v_c)$ and currents $(\Delta i_a, \Delta i_b, \Delta i_c)$ on the converter side are recorded. These measurements allow extraction of the VSC admittance through frequency-domain analysis [53]. To obtain the complete 2x2 admittance matrix $Y_{VSC,pn}$, positive- and negative-sequence perturbations are applied separately.

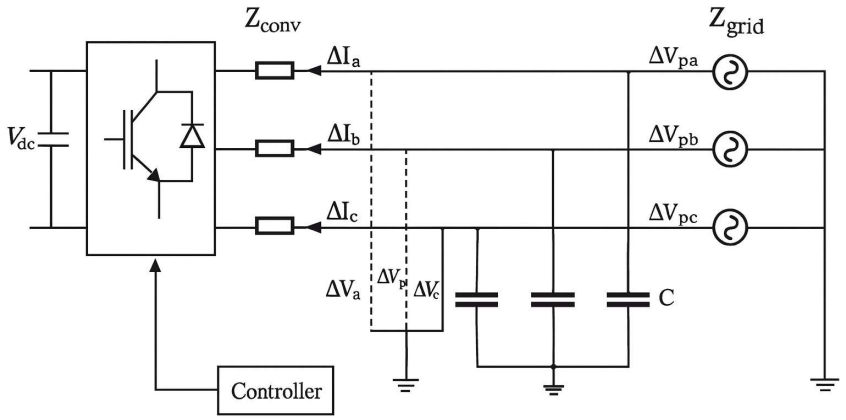

Figure 2.10: Simulation model with perturbation voltages injection analysis

For positive-sequence injection, the perturbation voltages are defined as:

$$\Delta V_{pa} = \Delta V_p \cos(\omega_p t)$$

$$\Delta V_{pb} = \Delta V_p \cos\left(\omega_p t - \frac{2\pi}{3}\right) \tag{2.55}$$

$$\Delta V_{pc} = \Delta V_p \cos\left(\omega_p t + \frac{2\pi}{3}\right)$$

where, ΔV_p is the perturbation voltage amplitude, and $\omega_p = 2\pi f_p$ is the perturbation frequency. The VSC-side response voltage includes a positive-sequence component at ω_p and a negative-sequence component at $(\omega_p - 2\omega_n)$. These are expressed as $\Delta V_{1p} < \Delta\theta_{1vp}$ and $\Delta V_{1n} < \Delta\theta_{v1n}$, respectively, where ΔV_{1p}, $\Delta\theta_{v1p}$, ΔV_{1n}, and, $\Delta\theta_{v1n}$ are derived via FFT analysis of ΔV_a. Similarly. the current responses $i_{1p} < \theta_{i1p}$ and $i_{1n} < \theta_{i1n}$ are obtained from Δi_a.

The relationship between response voltages and currents is given by:

$$\begin{bmatrix} i_{1p} < \theta_{i1p} \\ i_{1n} < \theta_{i1n} \end{bmatrix} = Y_{vscon}pn(\omega_p) = \begin{bmatrix} V_{1p} < \theta_{V1p} \\ V_{1n} < \theta_{V1n} \end{bmatrix} \tag{2.56}$$

Where $Y_{vscon}pn(w_p)$ represents the small-signal admittance matrix at the specified frequency. For the negative-sequence injection, the perturbation voltage is:

$$\Delta V_{pa} = \Delta V_n \cos[(\omega_p - 2\omega_n,)t$$

$$\Delta V_{pb} = \Delta V_n \cos\left[(\omega_p - 2\omega_n)t + \frac{2\pi}{3}\right] \quad (2.57)$$

$$\Delta V_{pc} = \Delta V_n \cos[(\omega_p - 2\omega_n,)t - \frac{2\pi}{3}]$$

This generates negative-sequence responses at $w_p - 2\omega_n$ and positive-sequence response at w_p. The admittance matrix is derived similarly, combining results from both injections:

$$Y_{vscon}pn(\omega_p) = \begin{bmatrix} i_{1p} < \theta_{i1p} & i_{2p} < \theta_{i2p} \\ i_{1n} < \theta_{i1n} & i_{2n} < \theta_{i2n} \end{bmatrix}^{-1} \begin{bmatrix} v_{1p} < \theta_{v1p} & v_{2p} < \theta_{v2p} \\ v_{1n} < \theta_{v1n} & v_{2n} < \theta_{v2n} \end{bmatrix} \quad (2.58)$$

In cases where $\omega_p < 2\omega_n$,the negative frequency $\omega_p - 2\omega_n$ is converted to positive frequency $2\omega_n - \omega_p$ by rewriting the voltage expressions. This transformation also inverts the sequence and phase of the response voltages and currents. Consequently, the admittance matrix is adjusted as:

$$Y_{vscon}pn(\omega_p) = \begin{bmatrix} i_{1p} < \theta_{i1p} & i_{2p} < \theta_{i2p} \\ i_{1n} < (-\theta_{i1n}) & i_{2n} < (-\theta_{i2n}) \end{bmatrix}^{-1} \begin{bmatrix} v_{1p} < \theta_{v1p} & v_{2p} < \theta_{v2p} \\ v_{1n} < (-\theta_{v1n} & v_{2n} < (-\theta_{v2n}) \end{bmatrix}$$

(2.59)

- **Procedure for Admittance Extraction**

This section explains the steps used to compute the VSC admittance from time-domain simulation results. The procedure is applied separately for the cases $\omega_p < 2\omega_n$and $\omega_p > 2\omega_n$. In each case, a small perturbation voltage is injected, the converter response is measured, and the admittance is calculated using frequency-domain information.

a) Admittance Calculation for $\omega_p < 2\omega_n$

Calculate the admittance for $\omega_p < 2\omega_n$, the following steps are carried out:

Step 1. Signal Injection

- A positive-sequence voltage perturbation at frequency- ω_p (Equation 2.56) is applied.
- In addition, a complementary signal at $2\omega_n - \omega_p$ (Equation 2.57) is injected to include frequency-coupling effects.

Step 2. Response Measurement

- The resulting voltage (Δv_a) and current (Δi_a) are recorded for both injected frequencies.

Step 3. Frequency-Domain Conversion

- The time-domain signals are converted into frequency components using FFT.

Step 4. Amplitude and Phase Extraction

- For frequency ω_p,Magnitude ($\Delta v_{1p}, \Delta i_{1p}, \Delta v_{2p}, \Delta_{i2p}$) and phase angles $\Delta\theta_{v1p}, \Delta\theta_{i1p}, \Delta\theta_{v2p}, \Delta\theta_{i2p}$ are extracted.
- For frequency $2\omega_n - \omega_p$,Magnitude ($\Delta v_{1n}, \Delta i_{1n}, \Delta v_{2n}, \Delta i_{2n}$) and phase angle ($\Delta\theta_{v1n}, \Delta\theta_{i1n}, \Delta\theta_{v2n}, \Delta\theta_{i2n}$) are obtained

Step 5. Admittance Computation

The admittance $Y_{VSC}, PN(\omega_p)$ is evaluated using Equation (2.59), based on the extracted magnitude and phase values.

b) Admittance Calculation for $\omega_p > 2\omega_n$

For $\omega_p > 2\omega_n$, the procedure is similar but uses the following excitation structure:

Step 1. Signal Injection

- A positive-sequence Voltage at ω_p (Equation 2.56) is injected.
- A negative-sequence voltage at $2\omega_n - \omega_p$ (Equation 2.57 is superimposed to account for harmonic interactions.

Step 2. Response Measurement

- The resulting voltage (Δv_a) and current (Δi_a) perturbations are measured for both frequencies.

Step 3. Frequency - Domain Conversion

- Time-domain signals are transformed into frequency components using FFT.

Step 4. Amplitude and Phase Extraction

- For w_p: Magnitude ($\Delta v_{1p}, \Delta i_{1p}, \Delta v_{2p}, \Delta_{i2p}$) and phase angles $\Delta\theta_{v1p}, \Delta\theta_{i1p}, \Delta\theta_{v2p}, \Delta\theta_{i2p}$ are extracted.
- For $\omega_p - 2\omega_0$: Magnitude **(**$\Delta v_{1n}, \Delta i_{1n}, \Delta v_{2n}, \Delta i_{2n}$) and phase angle:($\Delta\theta_{v1n}, \Delta\theta_{i1n}, \Delta\theta_{v2n}, \Delta\theta_{i2n}$) are obtained.

Step 5. Admittance Computation

- The admittance $Y_{VSC}, PN(\omega_p)$ is calculated using Equation (2.58), including cross-frequency coupling terms.

This methodology employs a frequency sweep, incrementally increasing the perturbation frequency ω_p across a wide range (typically from 1 Hz to 900 Hz), to obtain the admittance values across a wide frequency range and ensure complete dynamic characterisation of the converter.

2.6.2 Validation

To verify the analytical models, frequency-domain validation was carried out using a frequency-sweep method in time-domain simulations, as described in Section 2.6.1. In this setup, the DC-link voltage was modelled as an ideal voltage source.

2.6.2.1 GFL with Inner Current Controller (ICC)

Figure 2.11 compares the analytical admittance model with the simulation results for a GFL converter operating only with the inner current controller. Two operating points are considered: $I_d = 0.5$ p.u. and $I_d = 0.7$ p.u. The analytical and simulated curves match

closely, confirming the accuracy of the developed ICC model and the results based from the GFL model of Figure 2.2.

The admittance magnitude varies with the d-axis current reference. Increasing the operating current from 0.5p.u. to 0.7p.u. increases the admittance amplitude across the frequency range, showing that the converter becomes more sensitive to grid-voltage disturbances at higher current levels. This behaviour is most clear near resonance frequencies, where the amplification is more noticeable. In contrast, the phase response shows almost no variation between the two operating points, which confirms that the ICC dynamics remain consistent regardless of the current value.

From Figure 2.11(a) and 2.11(d) (positive-positive and negative-negative channels), the magnitude difference between the two current levels is small in the 1-100 Hz region, and negligible above 100 Hz. The phase response in these channels remains unchanged across the entire frequency range. For the cross-coupling channels in Figure 2.11(b) and 2.11(c) (positive-negative and negative-positive), the magnitude variation is more pronounced from 1-118 Hz compared with the direct channels. Beyond approximately 118 Hz, the admittance magnitude behaves similarly to the direct channels, with minimal influence from the operating current. The phase response in the coupling paths also shows negligible change across frequencies.

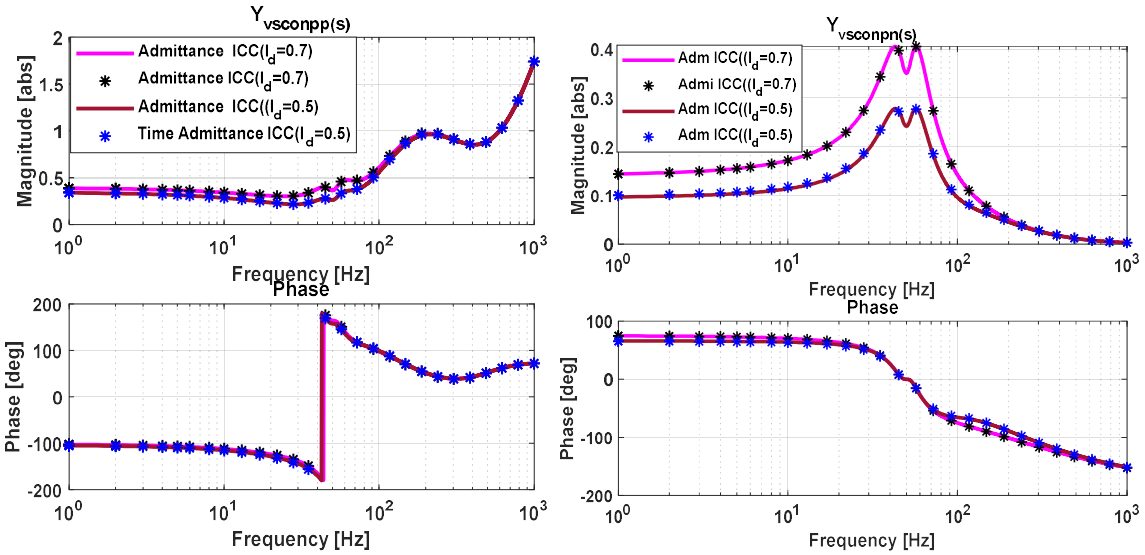

(a) (b)

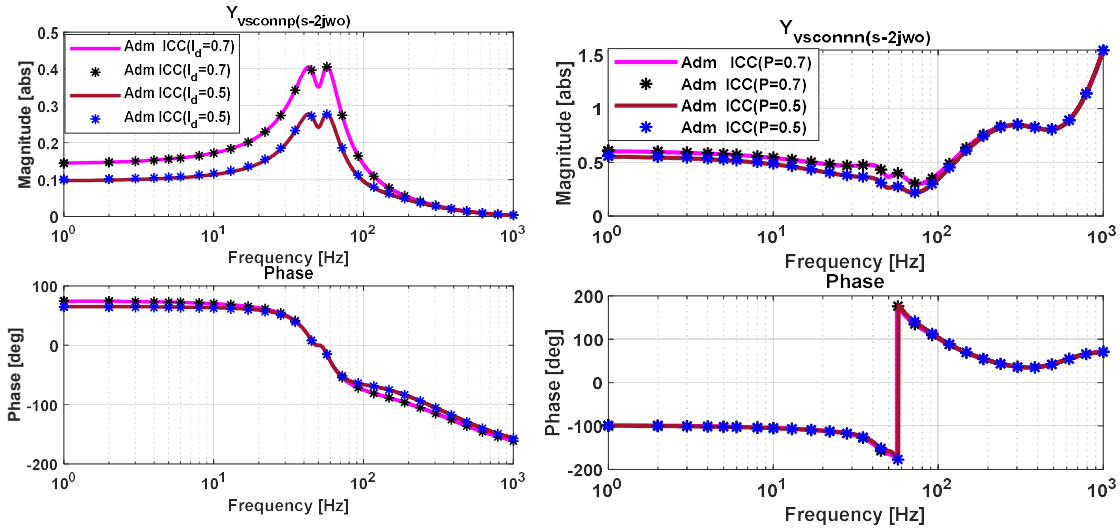

(c) (d)

Figure 2.11: GFL Admittance Validation Considering Only Inner Current Controller

These results apply exclusively to the configuration with the inner current controller, without any outer control loops. In this condition, damping is limited in certain frequency regions, which results in visible resonance peaks. Later sections demonstrate that introducing outer control loops reduces these peaks and enhances overall robustness. Therefore, Figure 2.11 serves as a baseline reference for the admittance behaviour of the ICC-only configuration before adding outer-loop dynamics.

2.6.2.2 GFL with outer controller Loop

In the GFL configuration, the converter uses an outer control loop. For the PV case, this loop regulates active power and AC voltage. For the PQ case, the loop regulates active and reactive power. In both structures, the outer loop works with an inner current controller and a PLL for synchronisation. Figure 2.12 compares the analytical admittance with values obtained from frequency-sweep simulation. The analytical curve and simulation markers show very close agreement across the full frequency range, which verifies the accuracy of the derived model. A clear admittance peak appears near 50 Hz, caused by the fundamental AC voltage response. When PV control is applied, the admittance magnitude becomes higher around this frequency region. In contrast, PQ control produces lower magnitudes between 50-100 Hz. This behaviour shows that PQ control reduces the admittance swing and limits the peak variation in this range. The phase behaviour also differs. Under PV control, the phase varies more strongly as frequency increases. Under PQ control, the phase remains nearer to zero over the same range. For both modes, the phase lies between 90° and 270° at

certain frequencies, which reflects the negative-resistance behaviour typical in converter-dominated systems. Within this range, PQ control still produces a smaller phase shift and therefore a more moderate change in admittance.

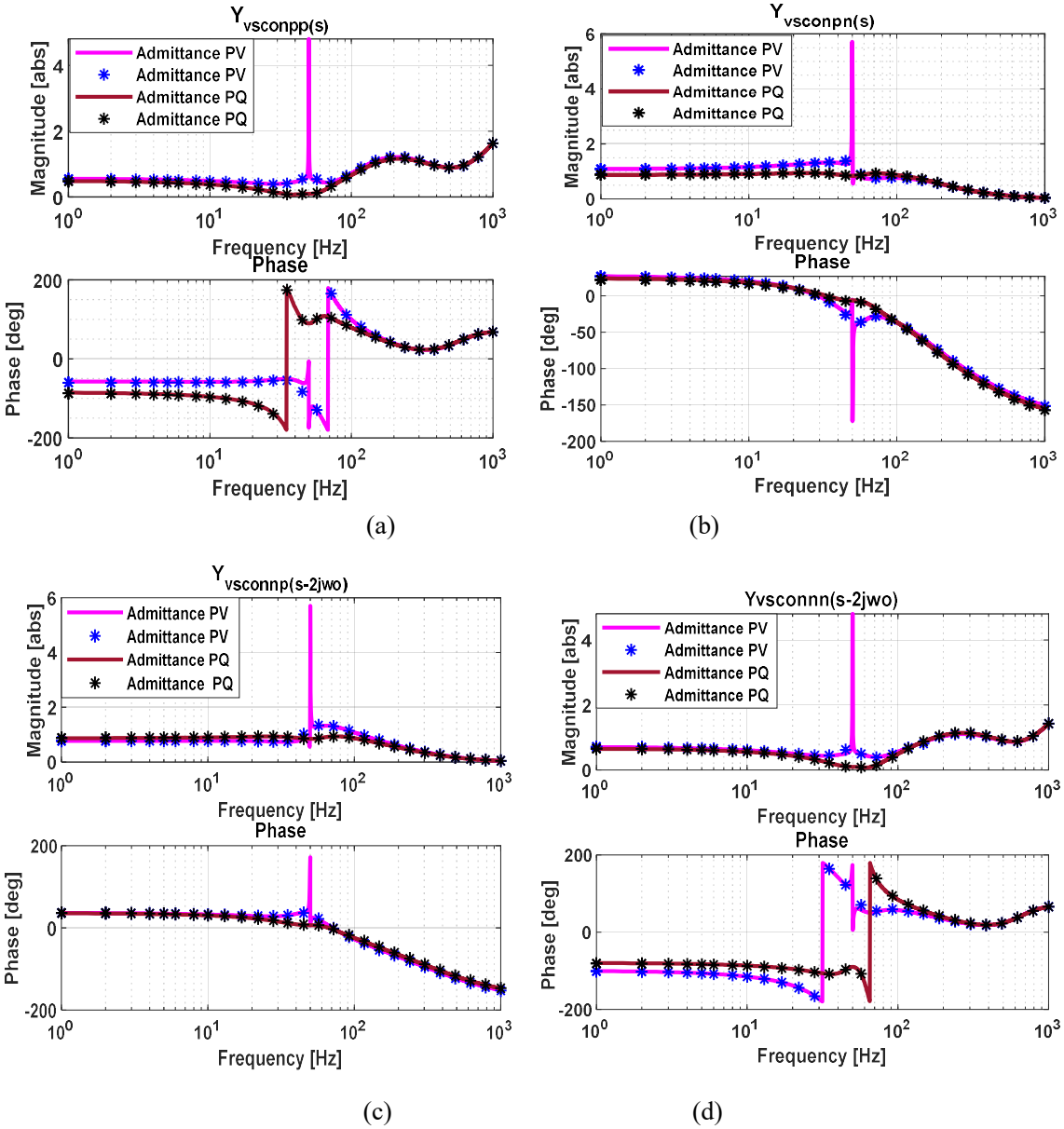

Figure 2.12: Validation of GFL(PV/PQ) Admittance Model Including Outer Control Loop

Overall, the results show that the GFL converter demonstrates different admittance patterns under PV and PQ operation. PV control introduces larger magnitude and phase variation, while PQ control keeps the admittance profile smoother and closer to a resistive characteristic.

2.6.2.3 GFM Validation

Figure 2.13 compares the analytical admittance with the simulated admittance of the GFM converter in the positive-positive (pp) and negative-negative (nn) frames. The two results agree very closely, showing that the analytical model represents the converter behaviour accurately.

In the pp frame, the admittance magnitude stays almost constant at low frequencies. A clear drop then appears near the control bandwidth. After this point, the magnitude increases again as frequency rises. The phase changes smoothly across the frequency range, with a clear shift near the point of strongest interaction, then gradually settles as frequency increases. These changes reflect the expected converter response defined by the control dynamics in this frame. In the (nn) frame, the admittance shows stronger frequency variation. The magnitude reduces more quickly around the control bandwidth and then increases again at higher frequencies. The phase also presents a clear transition near the main dynamic region, aligned with the analytical prediction.

These results show that the analytical admittance expressions accurately follow the simulated response of the GFM converter in both frames. The clear match confirms that the model describes how the admittance magnitude and phase vary with frequency, providing a solid basis for further analysis.

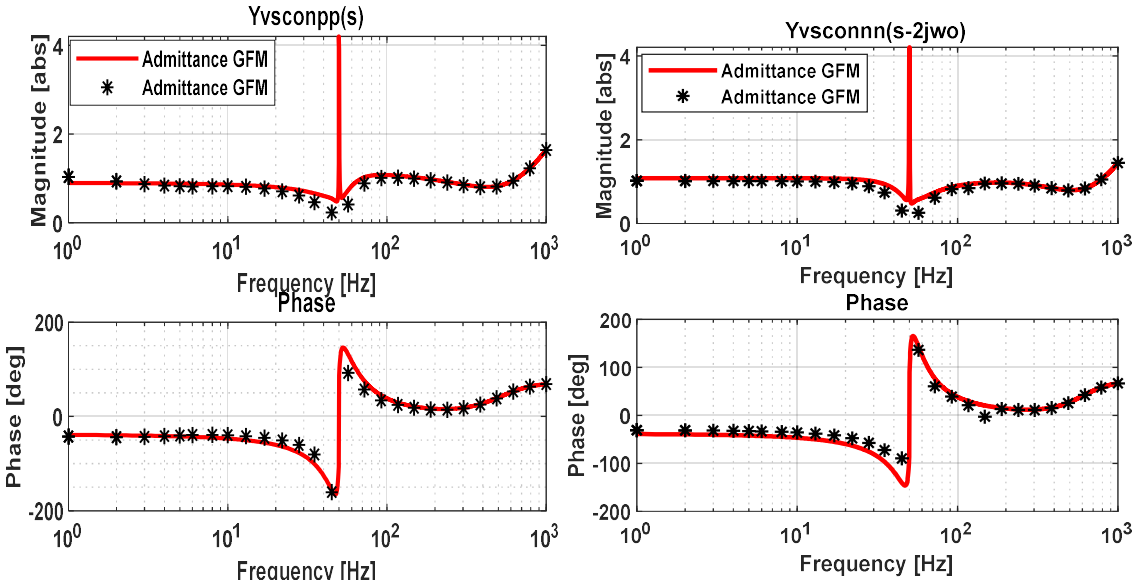

(a) Positive-Positive (pp) Admittance (b) Positive-Negative (nn) Admittance

Figure 2.13: Validation of GFM Converter Admittance Model (a) pp and (b) pn

2.6.2.4 Comparison: GFM vs GFL Admittance Characteristics

Figures 2.14(a) and (b) compare GFM and GFL converters in the positive-positive (pp) and negative-negative (nn) frames. The aim is to show how each unit changes the admittance of the network and how this behaviour varies across frequency. In the pp frame, the GFL converter shows a lower admittance magnitude than the GFM case once the frequency moves above the fundamental. A lower admittance means the GFL unit presents a higher equivalent impedance to the grid. The phase curve also differs, as the GFL angle stays below the GFM angle across most of the range, showing a weaker phase response in this channel.

In the(nn)frame, the trend changes. Here, the GFM converter shows a higher admittance magnitude than the GFL unit, giving the GFL converter a higher equivalent impedance in this sequence. The phase also shifts more strongly for the GFM case, showing a more active angle response. These results show that GFM and GFL converters change the network admittance in different ways in both pp and nn frames. GFM units tend to give higher admittance in the cross-sequence channel and a stronger phase trend, while GFL units show lower magnitude and a softer angle response. This clear difference means that each control method shapes current injection and voltage support in a unique manner. When admittance increases, current flow becomes easier; when admittance decreases, the converter behaves more like an impedance source.

Since impedance is the inverse of admittance, the GFL converter presents a higher impedance in most cases, while the GFM unit provides a lower impedance path. This opposite view confirms the same behaviour: GFM behaves more like a strong current and voltage source, and GFL behaves more like a controlled injection unit with a higher apparent impedance to the grid.

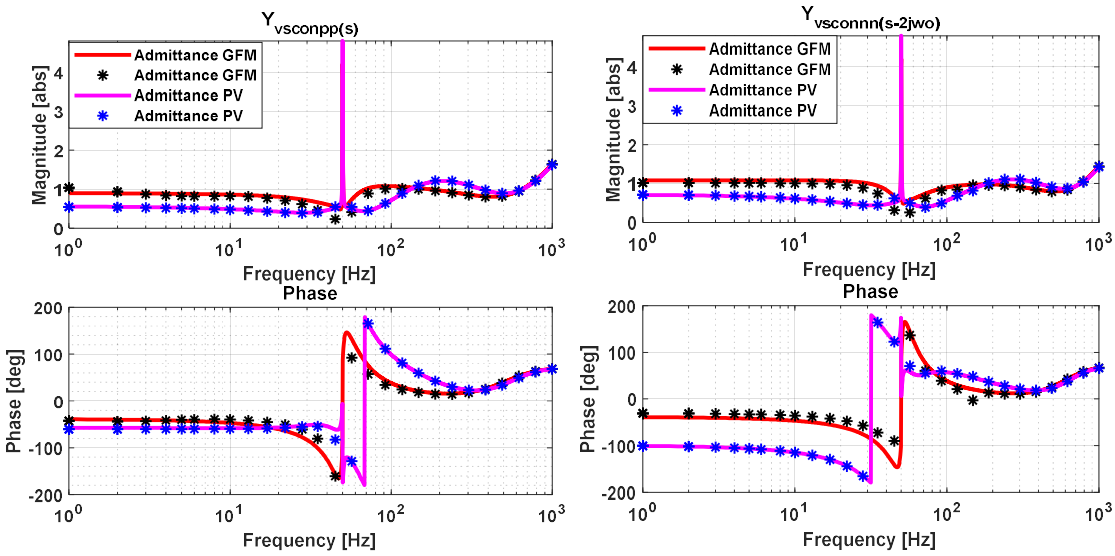

(a) Positive-Positive (pp) Admittance (b) Positive-Negative (nn) Admittance

Figure 2.14: Validation of GFM vs. GFL Admittance Model

2.7 GNC for Impedance-based Stability Analysis

Impedance-based stability assessment has become a critical tool in analysing converter-dominated grids, particularly in modern systems where synchronous inertia is scarce and renewable penetration is high. Two principal frameworks are commonly applied: the SISO approach, suitable for simplified or weakly coupled systems, and the MIMO approach, which is required when cross-coupling between converters and phases cannot be neglected.

When detailed models are accessible, as derived in previous sections, small-signal analysis enables accurate representation of converter-grid interactions. Alternatively, when converters are treated as black boxes, stability can be evaluated through frequency-response identification [125]. This section introduces the SISO stability framework before extending to the more general MIMO formulation using the GNC.

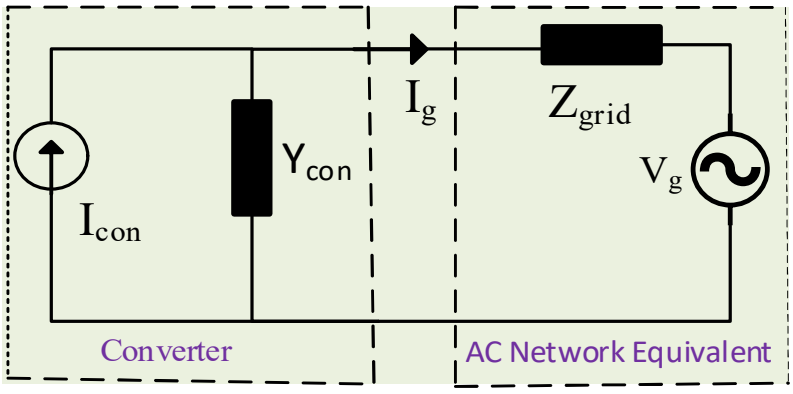

Figure 2.15: Small-signal representation of a converter-connected system

2.7.1 SISO Stability Framework

Figure 2.15 illustrate the small-signal equivalent of grid-connected VSC. In this formulation, the converter is represented as a Norton equivalent, consisting of a controlled current source in parallel with its output admittance $Y_{con}(s)$. The grid is modelled as a Thevenin voltage source in series with its impedance z_{grid} [126].

The Converter Current is expressed:

$$I_{con}(s) = \frac{I_{con}(s)Z_{con}(s)}{Z_{con}(s)+Z_{grid}(s)} - \frac{V_{grid}(s)}{Z_{con}(s)+Z_{grid}(s)} \tag{2.60}$$

Rearranging gives:

$$I_{con}(s) = \left[I_{con}(s) - V_g(s)Y_{con}(s) \right] \frac{1}{1+Y_{con}(s)Z_{grid}(s)} \tag{2.61}$$

The factor $1 + Y_{con}(s)Z_{grid}(s) = 0$, defines the characteristic equation, which indicates that stability is governed by the interaction between the converter admittance and the grid impedance.

(a) Nyquist Analysis

Stability can be evaluated using the Nyquist criterion. The open loop transfer function is expressed as:

$$L(s) = Y_{con(s)}Z_{grid(s)} \tag{2.62}$$

The Nyquist plot of L(s) is examined for encirclements of the critical point (−1,0).

Key Assumption: L(s) does not contain poles in the RHP. This assumption is consistent with conventional practice in power electronic stability studies [125][127]. Under this condition, the system is stable if the Nyquist curve does not encircle (−1,0) for the frequency range $-\infty < w_p < +\infty$. This implies that a sufficient stability margin exists if the magnitude of $Z_{grid}(s)$ remains sufficiently smaller than that of $Z_{con}(s)$ across all frequencies. Resonances and negative damping occur when these impedances interact adversely, leading to unacceptable oscillations or instability.

(b) Stability conditions

The criteria for stability assessment can be explicitly summarized as follow:

- Impedance Ratio Condition: The magnitude ratio between the grid and converter impedances, alongside the phase margin (PM), should satisfy:

$$\frac{|Z_{grid}(f)|}{|Z_{con}(f)|} = 1 \text{ and } PM \leq 0 \tag{2.63}$$

where phase margin is defined as:

$$PM = 180° - [\arg(Z_{grid}(f) - \arg(Z_{ccon}(f))] \tag{2.64}$$

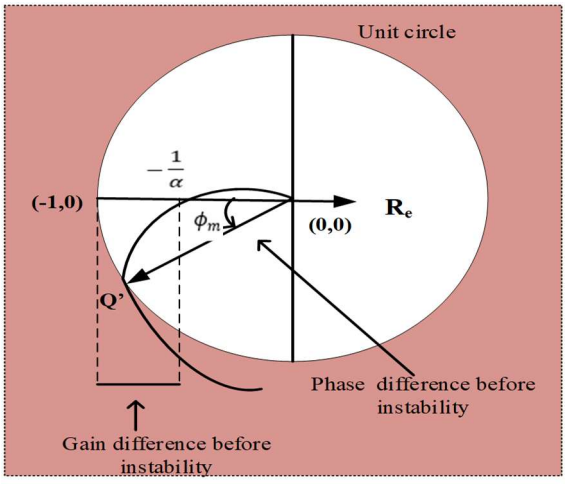

Figure 2.16: Definition of gain margin and phase margin [128]

Equation (2.64) indicates that instability occurs when the loop gains magnitude crosses 0 dB while the phase difference approaches or exceeds 180°, violating the Nyquist stability condition.

Figure 2.16 illustrates this criterion, showing the graphical definition of gain margin (α) and phase margin (ϕ_m). The gain margin represents the inverse distance from the origin to the Nyquist curve intersection with the real axis nearest $(-1,0)$, while the phase margin is the angular displacement between the negative real axis and the curve intersection with the unit circle. and the phase margin is the angle between the negative real axis and the point where the curve meets the unit circle. These margins indicate how close the system is to instability and help identify safe operating regions and possible resonance issues.

Figure 2.15 presents the small-signal equivalent circuit, which demonstrates the interaction between converter admittance and grid impedance. Figure 2.16 then uses the Nyquist plot to show how gain and phase margins relate to stability limits and proximity to unstable behaviour.

2.7.2 Transition to MIMO Stability Analysis

This thesis focuses only on MIMO impedance-based stability analysis because the system contains more than one converter connected to the network. In such multi-converter systems, interactions between control loops and sequence components become dominant, and classical SISO methods are not suitable. Therefore, the Generalised Nyquist Criterion (GNC) is applied, as it provides a strict extension of Nyquist theory to matrix-based transfer functions and supports stability evaluation in interconnected converter systems [127].

The analysis uses the positive-negative (PN) sequence representation. The open loop transfer matrix is:

$$L(s) = Y_{vsc,PN}(s)\, Z_{grid,PN}(s) \tag{2.65}$$

The eigenvalues of $L(s)$ are computed across frequency. Stability is confirmed when no eigenvalue trajectory encircles $(-1,0)$. The number of encirclements equals the number of unstable poles. Frequency-swept impedance data from simulation or measurement is used to form the eigenvalue paths. These plots allow clear observation of stability margins and support accurate controller tuning in weak and multi-terminal systems.

This method gives a reliable and systematic stability assessment for converter-dominated grids and enables clear, visual diagnosis of potential oscillatory behaviour.

2.8 Frequency-Domain Stability Analysis

Figure 2.17 illustrates the closed-loop eigenvalue loci (λ1, λ2) for converter control (PV) with PLL bandwidths of 10, 20, 30, and 40 Hz under a weak grid condition (SCR =1.8, P = 0.9p.u.) from the GFL model of Figure 2.2. The black unit circle denotes the discrete-time stability boundary. For PLL bandwidths between 10 and 30 Hz, both eigenvalues remain well inside the circle, confirming stable operation. At 40 Hz, however, λ1 and λ2 move toward and cross the boundary near the critical point (−1,0), indicating reduced damping and the onset of instability. Thus, stability is maintained for bandwidths up to 30 Hz, whereas higher bandwidths produce unstable dynamics.

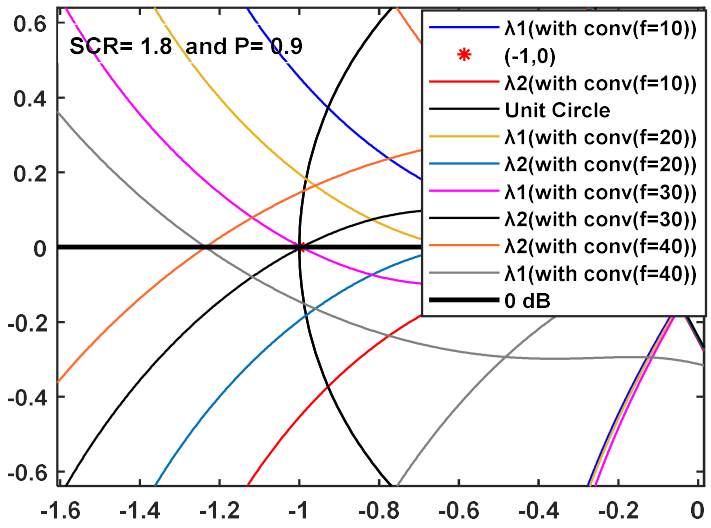

Figure 2.17: Stability Assessment Across Different PLL Frequencies

Figure 2.18. evaluates stability through the impedance-based SISO criterion using Bode diagrams for PLL bandwidths of 10, 20, and 30 Hz. The black trace represents the grid admittance $Y_{grid(pp)}$, while the coloured curves represent the negative converter admittance $-Y_{vsconpp(s)}$. Stability margins are determined from the intersections of these curves: the gain crossover is identified at the magnitude intersection, with the corresponding phase margin obtained from the angular separation at that frequency; conversely, the gain margin is defined at the phase crossover of −180°.

At 10 Hz, he converter admittance remains very low, corresponding to a high impedance. This results in weak coupling between the converter and grid, yielding large stability

margins. At 30 Hz, the converter admittance increases, producing stronger interaction and reduced margins. Resonance conditions appear when the ratio $\frac{Y_{conv(pp)}}{Y_{grid(pp)}}$ approaches −180°, leading to diminished damping in agreement with Nyquist stability.

Figures 2.19 (a)-(b) further analyse the 40 Hz case using eigenvalue-based Nyquist representation. A critical frequency of approximately 128 Hz is identified, where λ1 reaches 0 dB with a −180∘ phase, corresponding marginal stability. Beyond this point, λ1 enters the unstable domain, while λ2 remains separated from the boundary. The Nyquist representation in Figure 2.20 confirms that the trajectory of λ1 is decisive in determining stability. These results highlight that accurate stability prediction requires joint consideration of converter and grid impedance. The frequency-domain eigenvalue shifts directly describe how variations in control bandwidth modify system damping and determine stability boundaries.

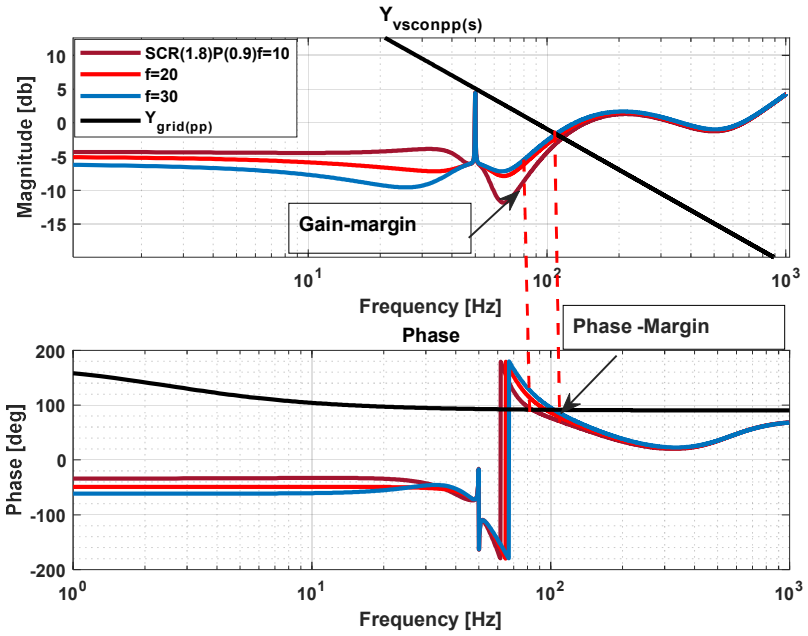

Figure 2.18: Converter Admittance at Various PLL Bandwidths and Its Intersection with Grid Admittance

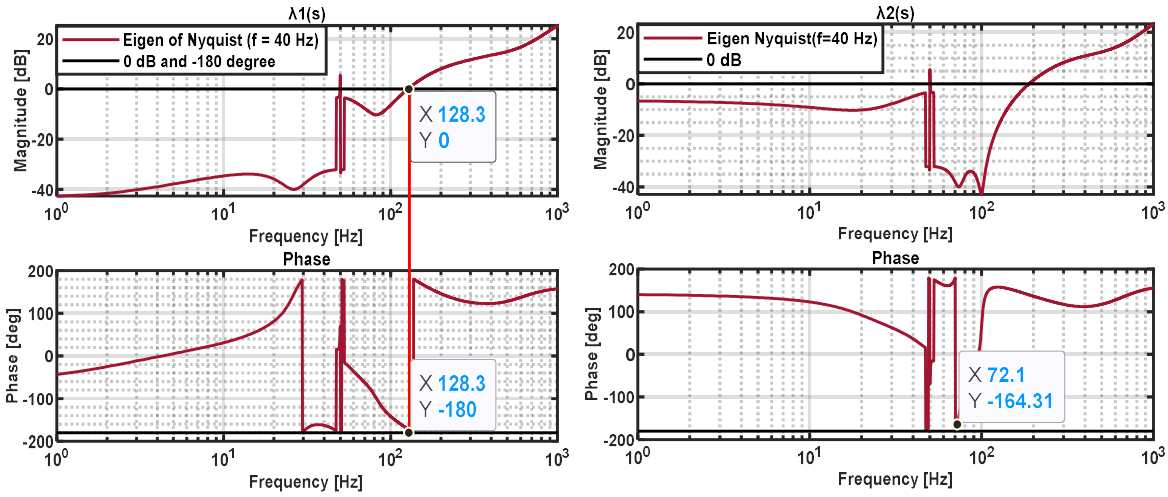

(a) (b)

Figure 2.19: Eigenvalue of Nyquist stability analysis at Frequency of PLL 40 Hz

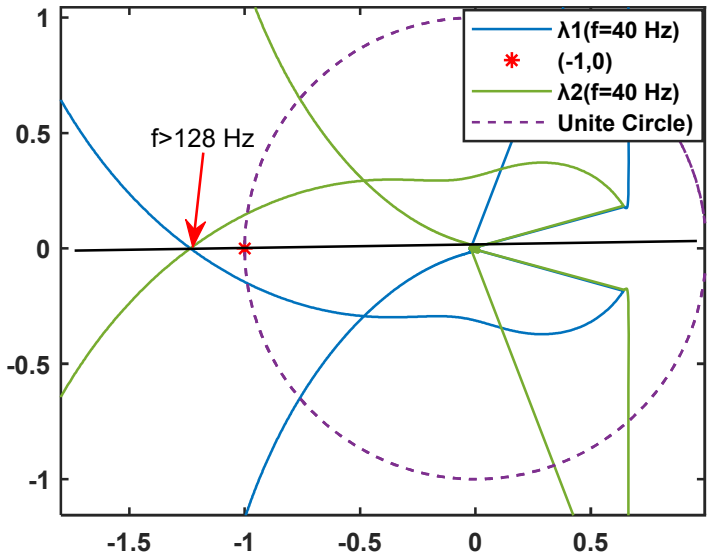

Figure 2.20: Nyquist plot for PLL frequency 40 Hz

2.9 Time -Domain Analysis

Figures 2.21 (a)-(b) present the time-domain simulation results for a weak grid condition (SCR=1.8, P=0.9p.u.) when the PLL bandwidth is increased from 10 Hz to 40 Hz at t = 6 s. Before the bandwidth change, the current components (I_d, I_q) and active power (P) remain stable. Once the bandwidth is raised, oscillations appear immediately and grow rapidly, becoming dominant around t = 6.6 s. The observed resonance occurs at 128 Hz in the abcframe, corresponding to 78 Hz in the dq frame. These results demonstrate that increasing

PLL bandwidth in weak grids leads to instability, thereby validating the conclusions obtained from the frequency-domain analysis.

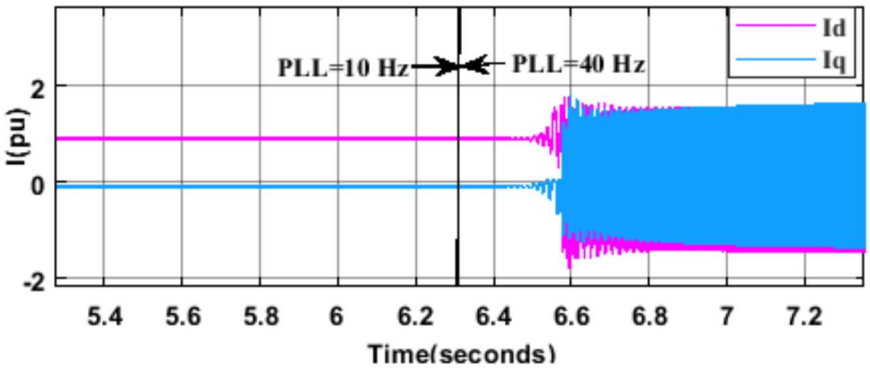

(a)

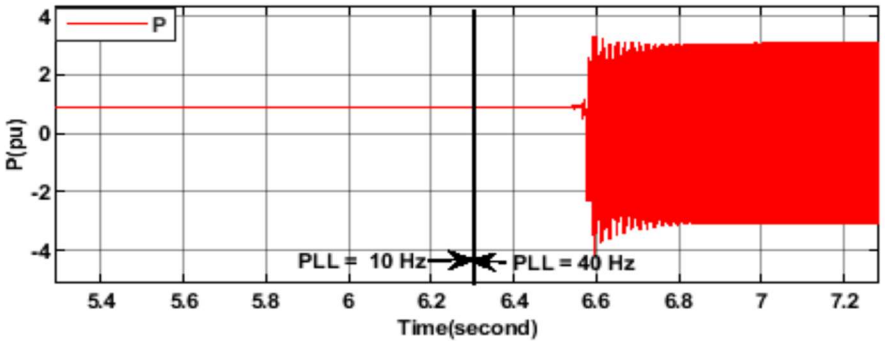

(b)

Figure 2.21: Simulation Waveforms of (I_d, I_q) and active power (P) in $p.u.$

2.10 Summary

This chapter introduced the small-signal models of grid-connected VSCs in GFL and GFM modes. The admittance in the pn frame was derived from the dq frame through a clear transformation step. The chapter then presented how the admittance can be measured in the pn frame through theory and frequency-sweep tests carried out in EMT tools. Both methods produced matching results, showing that the model represents the behaviour of the units and can support later parts of the thesis.

The following key observations are highlight:

- Model development: VSCs were modelled in GFL and GFM modes and expressed in the pn frame.

- Validation: Frequency-sweep tests in EMT tools were used to check the model. The match between the two paths confirmed that the small-signal model is suitable for later analysis.
- Behaviour of both modes: GFL units showed stronger dependence on grid strength due to the PLL and outer loops. GFM units kept stable damping under low short-circuit levels.
- Impedance difference: The two modes produced different admittance shapes, which helps explain their behaviour in weak networks.
- Stability check: An example application of the Generalized Nyquist Criterion was given. The admittance ratio provided a clear way to observe crossings linked to stability.
- Test notes: Frequency-sweep tests must allow enough settling time and must use small injections to stay close to the operating point.

The chapter therefore provides a clear modelling and validation base for later impedance-based stability studies of both converter modes. This foundation supports the case studies and stability assessments presented in the next chapters.

Chapter 3: Analysis of Converter-Network Interaction Dynamics

3.1 Introduction

The rapid growth of VSCs, driven by renewable energy deployment, has changed modern power systems. Unlike conventional synchronous machines, VSCs are governed by fast inner control loops, outer power control, PLLs, and DC-link dynamics. While these features provide accurate regulation of active and reactive power, they also introduce additional dynamic interactions with the surrounding network. As converter penetration increases, the mutual influence between converter control systems and network impedance becomes a dominant factor in system stability. These interactions may lead to oscillatory behaviour, resonance phenomena, or reduced stability margins, affecting both local converters and geographically remote units [129][130].

To analyse these interaction mechanisms rigorously, a small-signal linearised model of the converter–network system is developed. The nonlinear differential equations describing the converter, including current control loops, outer control structure, PLL dynamics, and DC-link behaviour, are formulated in the synchronous reference frame. These equations are linearised around a steady-state operating point using first-order Taylor series expansion. The operating point is determined from power flow conditions and controller reference values.

The resulting linear time-invariant (LTI) state-space representation captures the local dynamic behaviour of the converter under small perturbations and establishes a systematic basis for interaction analysis [12]. From this model, frequency-domain impedance representations are derived by injecting small-signal voltage perturbations at the converter terminals and calculating the corresponding current responses. This procedure ensures that the impedance model is physically consistent with the underlying state-space formulation.

Impedance-based stability analysis is adopted because it enables modular assessment of interconnected subsystems without requiring full disclosure of internal controller parameters. In practical multi-converter systems, especially when converters are owned or operated by different entities, detailed state-space models are often unavailable. Terminal impedance representation allows each subsystem to be characterised independently,

enabling stability evaluation using frequency-domain criteria such as the Generalised Nyquist Criterion [12][70].

Several indices support this analysis. The Generalized Short-Circuit Ratio with Control Influence (GSIM) estimates network strength while including the impact of converter control under steady-state conditions [44][87][100]. The Impedance Margin Ratio (IMR) evaluates the interaction between converters and the grid across frequency and helps detect resonance-related instability [66][69][91][130][131]. GSIM is useful when detailed converter models are unavailable; however, it does not fully capture high-frequency control dynamics. IMR incorporates frequency-dependent behaviour but requires accurate impedance modelling.

This chapter introduces a method to study how a remote converter, connected through a transmission network, changes the impedance seen by a local converter and affects its stability. Earlier work often considers only one converter or focuses only on fundamental frequency behaviour. Here, interaction across a broad frequency range is studied, and the effect of a remote converter is included. The work shows how the control of a remote converter and the strength of the grid can shift resonance and change stability margins.

The work uses small-signal impedance modelling, eigenvalue study, and frequency-domain stability tests. First, the impedance of the remote converter is found for different control settings to show how control design affects interaction. Next, grid strength is varied to observe how combined converter-grid behaviour changes with operating conditions. The analysis covers a wide frequency range so that resonance and impedance peaks are clear. Then, a Nyquist-based test evaluates how the remote converter affects local-side stability when both share the same network.

This approach helps to establish a coherent connection between remote-side behaviour, network characteristics, and local-side stability. The study provides guidance for control design and interaction-aware stability checks in converter-rich grids.

3.2 Interaction Mechanisms in Two-VSC Networks

This section builds directly upon the modelling framework developed in chapter two and concept of Section 3.1 by extending the analysis from a single converter-grid interface to a system comprising two VSCs interconnected through a shared network impedance. The

purpose of this section is to identify and quantify the dynamic coupling mechanisms that arise when multiple converters operate within the same electrical network. This extension is essential because the impedance seen by a converter is no longer determined solely by the passive grid but is actively modified by the control dynamics of the remote converter.

Two-VSC configurations are representative of offshore wind power plants, multi-terminal HVDC systems, and advanced microgrids[132][133].Although structurally simple, this configuration captures the fundamental interaction mechanisms present in larger converter-dominated networks.

Each converter is connected to a common AC bus through a transformer and transmission line. The impedance of these components is frequency-dependent, and their interaction with converter control dynamics shapes the overall system response. When the combined converter and network impedances align within critical frequency ranges, resonance conditions may occur. Under such conditions, small disturbances can be amplified, affecting both converters and the shared bus voltage [6][66][134].

To analyse these mechanisms consistently with Section 3.1, each converter is represented using the previously derived small-signal impedance model. The modelling is performed in the positive–negative sequence (pn) reference frame, which allows accurate representation of asymmetrical and coupled dynamic behaviour in multi-converter systems [135]. The network is then represented using frequency-dependent impedance models for lines, transformers, filters, and equivalent grid sources [136].

The overall interconnected system is then expressed in a unified admittance matrix form [137].This formulation enables systematic stability assessment using eigenvalue analysis and frequency-domain techniques, including impedance ratio evaluation and the Generalised Nyquist Criterion [129][138].These tools allow identification of resonance frequencies, stability margins, and dynamic mode shifts resulting from converter interaction.

Sensitivity studies are conducted by varying grid strength, controller bandwidths, and operating points. Impedance frequency sweeps provide clear identification of critical resonance regions [139]. Through this structured approach, it becomes possible to quantify how a remote converter modifies the effective impedance observed at the terminals of a local converter and how this modification alters stability margins.

The value of this section lies in demonstrating that stability in converter-dominated networks is not solely a function of local controller design or static grid strength. Instead, it is determined by the dynamic interaction between multiple converters mediated by the shared network impedance. By explicitly connecting the impedance formulation of Section 3.1 to a multi-converter configuration, this section establishes a coherent analytical link between component-level modelling and system-level stability assessment.

This integrated framework provides practical guidance for interaction-aware control design and stability evaluation in modern power systems with high converter penetration.

3.2.1 System Configuration

Figure 3.1 illustrates a two-terminal VSC network. The remote converter (VSC-1) and the local converter (VSC-2) are connected to the AC grid through filters, transformers, and transmission paths, forming a representative structure for evaluating interaction effects across spatially separated terminals.

Both VSC-1 (remote terminal) and VSC-2 (local terminal) can operate either as GFM or GFL converters. Therefore, multiple operating combinations are possible:

- GFM-GFM, GFM-GFL, GFL-GFM and GFL-GFL

These combinations allow comprehensive investigation of how different control philosophies influence system-level stability and dynamic performance.

For clarity in Figure 3.1, different control modes are visually distinguished. The red colour is used to represent GFM converters, while black indicates GFL converters. This visual distinction does not imply any structural difference in hardware; it serves only to enhance readability and to help the examiner easily identify the control configuration under study.

Such a particular arrangement serves as a compact but meaningful scheme that reveals primary exchange processes among widely spaced units coupled interconnected through AC networks. It enables a structured investigation of impedance coupling, control interactions, and grid-strength variations, while maintaining analytical tractability for generalized stability assessment and practical extension to multi-terminal systems.

- Remote converter (VSC-1): Connected to the AC system through impedances Z_{c1}, Z_{cg1}, and Z_{g1}, representing its filter, transformer, and transmission line. This path introduces attenuation, phase shift, and time delay associated with long-distance electrical transfer.
- Local converter (VSC-2): Connected through Z_{c2}, Z_{cg2}, and Z_{g2}. Due to its electrical proximity to the reference bus, this unit is more sensitive to disturbances transmitted through the system and therefore serves as the primary terminal for stability assessment.
- Interconnecting impedance: The line impedance Z_L links the two converters and plays a central role in shaping resonance modes, oscillatory power exchanges, and coupled control behaviour.

Both converters operate under hierarchical control, as shown in Figure 3.2. Two outer-loop strategies are considered:

1. PV control, regulating active power and voltage (Figure 3.2a), and
2. PQ control, regulating active and reactive power (Figure 3.2b).
3. GFM control, provides voltage and frequency support (see Figure 2.9(b) in Chapter 2).

These outer loops provide reference values to the inner current controllers described in Chapter 2. Depending on system requirements, either GFL (PV, PQ) or GFM control is applied. This configuration offers a consistent platform for examining stability boundaries, resonance formation, and the influence of remote converter dynamics on the local terminal.

Three network configurations cases are considered in this chapter. One case has strong coupling. The other two cases have weak coupling represented with coupling two and three. The value for each case is shown in Table 2.1,3.1 and 3.2.

Table 3.1: The system parameter for weak and strong Coupling

Parameter	Coupling One	Coupling Two
Rc, Rc2	0.01pu,0.01pu	0.01pu,0.01pu
Lc, Lc2	0.1pu, 0.1pu	0.1pu, 0.1pu
L_1	0.1pu	0.3pu
R_g	0.0167pu	0.0167
R_{g1}	0.0167pu	0.0167
L_g	0.1pu	0.36pu
L_{g1}	0.22pu	0.38pu
L_{cg1}	0.16pu	0.25pu
L_{cg2}	0.18pu	0.26pu
R_{cg1}	0.016pu	0.0167pu
R_{cg2}	0.0167pu	0.0167pu
SCR	3.25pu	1.92

Table 3.2: The system parameter for weak Coupling

Parameter	Coupling - Three
Rc, Rc2	0.01pu,0.01pu
Lc, Lc2	0.1pu, 0.1pu
L_1	0.3pu
R_g	0.0167pu
R_{g1}	0.0167pu
L_g	0.25pu
L_{g1}	0.26pu
L_{cg1}	0.25pu
L_{cg2}	0.38pu
R_{cg1}	0.0167pu
R_{cg2}	0.0167pu
SCR	1.8pu

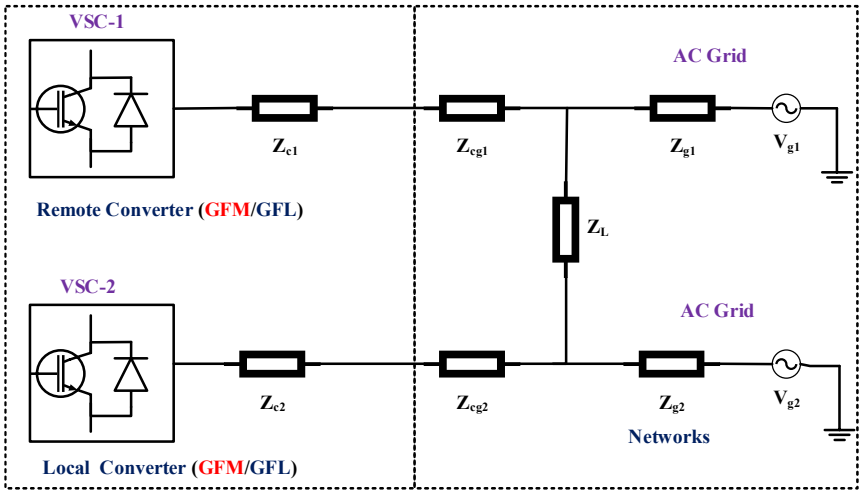

Figure 3.1: Schematic Representation of a Two-Terminal VSC System Connected to AC Grid with Remote and Local Converters

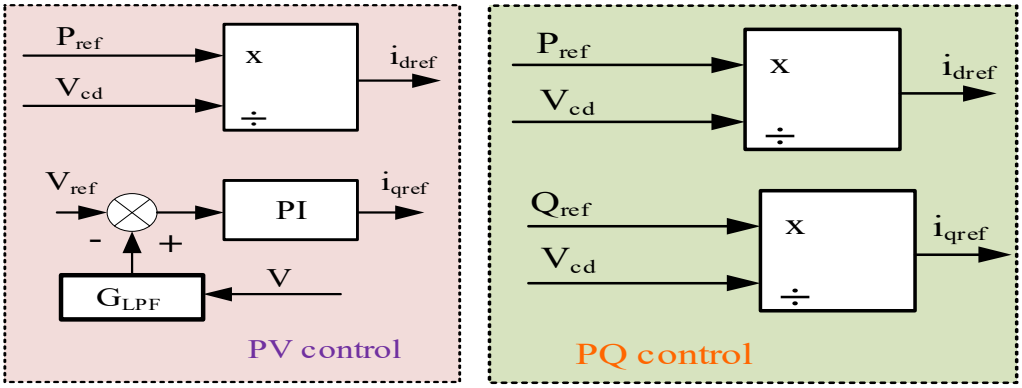

(a) (b)

Figure 3.2: Schematic Diagram for Outer-Loop Control Strategies For GFL (a) PV Control and (b) PQ Control

3.2.2 Impedance Formulation

In Figure 3.3, each VSC is modelled as a controllable AC voltage source connected to the network through distinct impedance components. These include the converter-side filter impedance, the coupling impedance at the PCC, and the grid-side impedance. The two converters are further linked through the interconnecting impedance Z_L Which represents the electrical path between them. Each converter is also connected to its respective AC grid source, V_{g1} and V_{g2}, through impedance Z_{g1} and Z_{g2}.

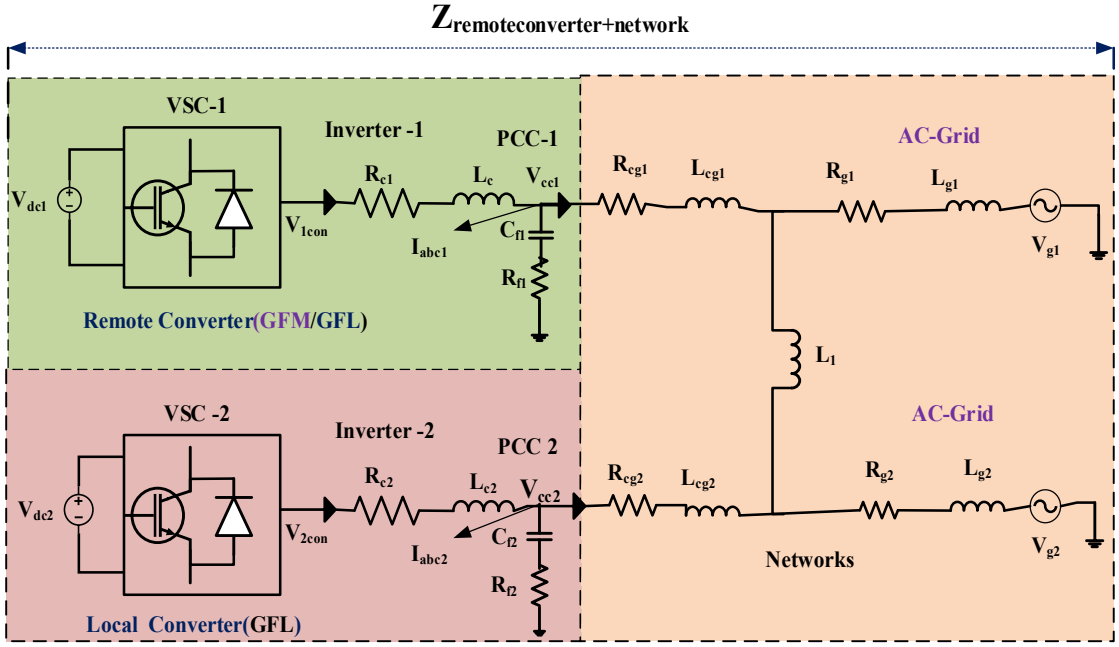

Figure 3.3: VSC Converters Under Different Control Modes Connected to AC Network

For passive elements, impedance expressions are obtained directly from circuit equations. However, in the case of converters, a small-signal model is required to capture the effect of

control dynamics. This is achieved by linearising the converter equations around a steady-state operating point using perturbation methods. The linearised model incorporates the influence of current controllers, PLLs, and other inner loops, thereby providing a frequency-dependent representation of converter behaviour. The derivation steps for a single converter connected to a grid were presented in Chapter 2 and are extended here to the interconnected system.

At the PCC, the small-signal impedance of the converter is defined as the transfer function from a perturbation in PCC voltage (ΔV_{pcc}) to the resulting perturbation in converter current (ΔI_c):

$$Z_{vscon,pn} = \frac{\Delta V_{pcc}}{\Delta I_c} \tag{3.1}$$

In the synchronous reference frame, voltage and current disturbances are expressed as:

$$\Delta V(s) = \begin{bmatrix} \Delta v_p(s) \\ \Delta V_n(s - 2jw_n) \end{bmatrix} \tag{3.2}$$

$$\Delta I(s) = \begin{bmatrix} \Delta i_P(s) \\ \Delta i_n(s - 2jw_n) \end{bmatrix} \tag{3.3}$$

The resulting impedance matrix is

$$Z_{vscon,pn}(s) = \frac{\Delta V(s)}{\Delta I(s)} = \begin{bmatrix} Z_{vscon,pp}(s) & Z_{vscon,pn}(s) \\ Z_{vscon,np}(s - 2jw_n) & Z_{vscon,nn}(s - 2jw_n) \end{bmatrix} \tag{3.4}$$

This matrix represents the coupling between positive- and negative-sequence components, as well as interaction between the d- and q-axes. It provides a complete frequency-domain model of the converter impedance, as introduced in Chapter 2. The region enclosed by the dashed boundary in Figure 3.3 includes only the converter model, excluding the external grid. This separation ensures that the derived impedance characterises the internal converter behaviour independently, supporting analysis of interactions with the network and other converters.

By applying the appropriate transformation matrices, the converter admittances obtained in the dq-frame are expressed in the positive-negative sequence (pn) frame. This frame is preferred for stability studies because it removes coupling effects caused by synchronous

rotation, which simplifies impedance evaluation. In contrast, the synchronous rotating reference frame offers a compact and effective form for representing converter-grid dynamics. Together, these frames enable rigorous frequency-domain stability studies, including the GNC and multi-converter interaction analysis.

3.3 AC Network and Impedance Interaction Characteristics

Figure 3.3 shows two VSC units linked through an AC network, expanding on the layout in Figure 3.1. Each converter connects to its point of common coupling through a filter made of resistance, inductance, capacitance, and damping elements. These electrical parameters, labelled as $(R_{c1}, L_{c1}, C_{f1}, R_{f1})$ for VSC-1 and $(R_2, L_{c2}, C_{f2}, R_{f2})$ for VSC-2, condition the output before it reaches the grid.

At the grid side, each converter connects to the AC network through line resistance and inductance $(R_{g1}, L_{g1})$and (R_{g2}, L_{g2}). An inductor L_1links the two converters, forming the coupling path. This element shapes power exchange affects resonance behaviour, and influences oscillation transfer between the two locations, which makes it important for stability.

This network arrangement clearly shows how power flows between converters through their PCCs and the shared line. Including all filter and grid elements forms a solid basis for small-signal impedance analysis and allows the study of how disturbances from one converter travel through the shared network and affect the other converter.

The purpose of this section is to examine how a remote converter changes the impedance seen at a local terminal. The process follows three steps. First, the remote converter and its link to the grid are characterised. Next, impedance is evaluated at the local terminal while the local converter remains inactive, acting only as a measurement point. Finally, impedance variation caused by the network and the remote converter at the local terminal is assessed using the indices below. This reveals how the network alters the electrical conditions at the converter interface.

1. Impedance Ratio (IR): The IR separates the effect of the remote converter from the grid background. It is defined as the ratio between the combined impedance of the grid and the remote converter and the grid impedance alone. This ratio shows how the presence of the

remote converter changes the impedance at the local terminal. It captures behaviour across the 1 Hz-1 kHz range, where most oscillatory issues appear. The IR is expressed in the positive-negative sequence frame as a 2×2 matrix, enabling study of both magnitude and phase. It gives early insight into weak-grid oscillations and resonance effects.

2. Eigenvalue-based Impedance Ratio (EIR): Direct examination of the IR matrix can be difficult. To ease interpretation, eigenvalue of the IR matrix is studied. These eigenvalues show how the interaction strength and phase change with frequency in a reduced form. Their behaviour reflects the effect of current control, PLL dynamics, and outer control loops. GFL converters often show greater sensitivity to network strength due to PLL action, while GFM units tend to support stronger impedance behaviour. These features appear most clearly between 1 Hz and 1 kHz.

The IR is expressed in the positive-negative sequence frame, and the EIR gives two eigenvalue paths (λ_1, λ_2). Comparing IR and EIR makes it easier to see how magnitude and phase change with frequency and how the remote converter affects the impedance measured at the local terminal and local stability.

In short, IR shows how network impedance varies across frequency, and EIR expresses this variation as two eigenvalue paths that highlight the influence of converter control and network coupling. These tools allow direct assessment of impedance interaction between converters.

Verification is performed through frequency-domain impedance evaluation, eigenvalue checks, and EMT simulations to confirm that the observed impedance behaviour reflects true converter-network interaction.

3.4 Time domain model development

In this work, the time-domain model refers to a detailed dynamic representation of the converter-network system described by differential equations and implemented in a simulation environment. Unlike the frequency-domain impedance model, which is derived from linearised small-signal equations in the Laplace domain, the time-domain model describes the instantaneous behaviour of currents, voltages, control loops, and network elements as functions of time. It therefore captures the physical switching-averaged dynamics and control interactions of the converters under small disturbances, without directly relying on impedance expressions.

To validate the theoretical impedance calculation, an equivalent time-domain model is developed, following the same structure described in Chapter 2. The configuration, shown in Figure 3.4, consists of two converters interconnected through the impedance chain Z_{cg1}, Z_{g1}, Z_{L1}, Z_{cg2}, Z_{g2} . A small disturbance current (ΔI_s) is injected at the terminal of the local converter, and the resulting response (ΔI_R) is observed at the remote converter. By analysing the ratio between the injected disturbance and the measured response, the dynamic interaction between the converters through the AC network can be evaluated.

The disturbance signal is swept across a predefined frequency range using a sinusoidal injection method. For each frequency point, the steady-state amplitude and phase of the response are extracted from the time-domain simulation. This procedure enables the reconstruction of the frequency-dependent impedance behaviour from purely time-domain simulations. The obtained impedance characteristics are then directly compared with the analytically derived small-signal impedance models.

Therefore, in this thesis, the term time-domain model specifically denotes a dynamic simulation model based on differential equations and control system implementation, used to reproduce the small-signal response of the converter-network system in the time domain. It does not represent a separate theoretical formulation; rather, it serves as an independent validation platform for the frequency-domain impedance derivation.

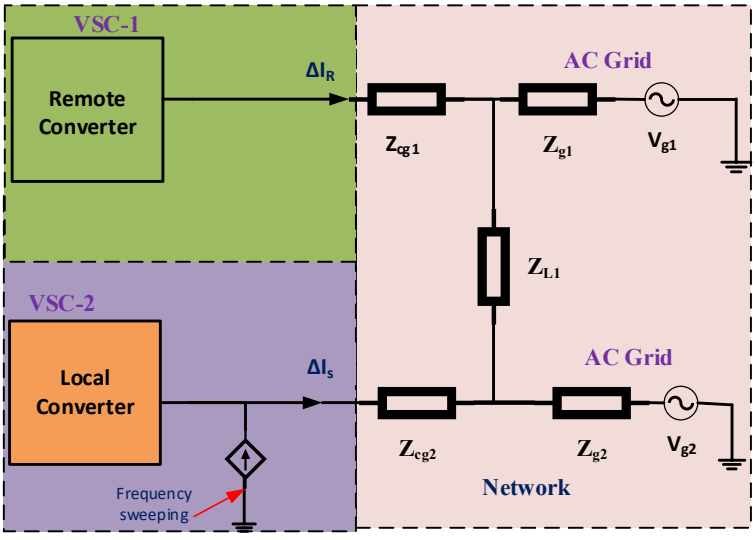

Figure 3.4: Small-Signal Stability Analysis via Disturbance Injection at Local Converter

This approach establishes a direct and logically consistent link between the analytical impedance expressions and the simulated converter-network dynamics. By demonstrating

agreement between the two, the validity of the derived small-signal impedance models for both GFL and GFM converters in interaction with the AC grid is methodically confirmed, without introducing additional modelling assumptions.

3.5 Impedance Calculation for a Two-Converters AC Network

The behaviour of AC networks strongly affects the stability of systems that rely on power converters. To study this behaviour, this section develops an impedance-based method for a system with two converters, as shown in Figure 3.5. The analysis uses two impedance indicators: the IR and the EIR. These tools help to study how each converter interacts with the network.

In the shown network, the remote converter (VSC-1) connects to its AC grid through impedance Z_{g1}. The local converter (VSC-2) connects to its grid through Z_{g2} and is linked to the remote side through the coupling impedance Z_L. Because of this link, VSC-2 may behave closer to its local grid terminal S2 or the remote grid terminal S1, based on the relation between Z_L and Z_{g2}. The IR and EIR help show how each converter affects the grid at each point.

Figure 3.5 shows the impedance seen from the network side of VSC-2, which is the reference point for the calculation. Here, $Z_{vsc1}$is the impedance of the remote converter. The network path includes the converter-to-grid impedances $Z_{cg1}$and Z_{cg2}, the grid impedances $Z_{g1}$and Z_{g2}, and the link impedance Z_L. The red arrow marks the exact reference point used for measurement.

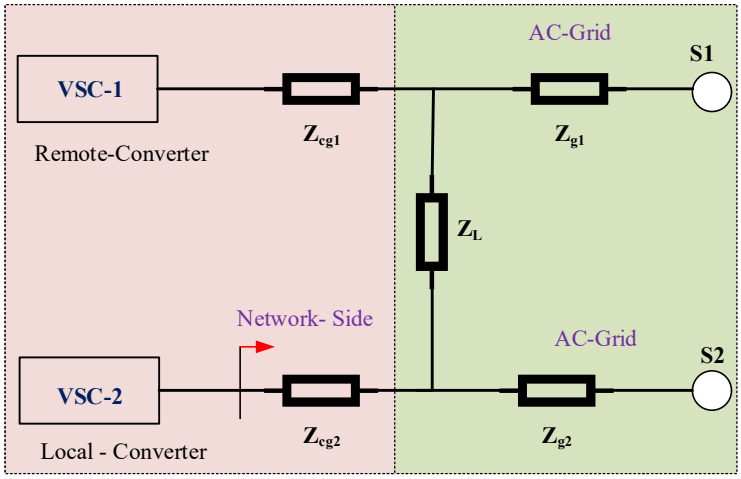

Figure 3.5: Equivalent Impedance Model of Converter-Grid Interaction

The total impedance seen at VSC-2, including the converter and the AC network, is

$$Z_{converter+netwo} = ((Z_{cg1} + Z_{vsc1}) \parallel Z_{g1} + Z_L) \parallel Z_{g2} + Z_{cg2} \quad (3.5)$$

To find the effect of the network alone (without VSC-1), the equivalent network impedance is

$$Z_{network} = (Z_{cg1} \parallel Z_{g1} + Z_L) \parallel Z_{g2} + Z_{cg2} \quad (3.6)$$

The IR that shows the influence of the remote converter on the local point is

$$IR = \left(\frac{Z_{conv+network}}{Z_{network}}\right) \quad (3.7)$$

The eigenvalues of the IR give the EIR, which shows the frequency-domain interaction:

$$EIR = \text{Eigenvalue}(IR) \quad (3.8)$$

This method sets a clear starting point for studying how the remote converter affects the local converter through the AC network. At this point, the purpose is to define the calculation steps and reference point without drawing stability results. Those results will appear in later sections.

3.5.1 Interaction Indicator: IR and EIR

This subsection explains how the indicators describe the interaction between the two units and the AC network.

The IR expresses how strongly the remote unit affects the impedance at the local point. A higher value shows greater influence from the remote side, while a lower value indicates that the local grid has more control.

The EIR separates the interaction into independent modes. Each eigenvalue represents one mode, allowing the analysis to trace how frequency, control loops, grid conditions, and coupling paths shape the system. The purpose here is to interpret these indicators and explain what they reveal about converter-network behaviour

3.5.2 Converter- Network Interaction: Impedance Results

This subsection examines the impedance behaviour of two VSC units linked to an AC network under strong and weak grid conditions. The analysis considers the impedance of the

converter alone and the combined impedance of the converter and the network, $Z_{conv+network}$. The study uses GFL units operating in PQ and PV modes.

The analytical model is compared with time-domain simulations to confirm that both show consistent behaviour. The goal is to describe how the impedance varies with frequency and how grid strength shapes this variation. The IR and EIR show how this interaction patterns develop across the frequency range.

Two coupling conditions, listed in Table 3.1 as Coupling One and Coupling Two, are included to show how the behaviour changes when the link between the converters becomes stronger or weaker. This subsection presents only the impedance trends. Stability findings will be given later, after the interaction mechanisms are fully examined.

3.5.2.1 Strong-Grid (Coupling-One) Case

Figures 3.6(a)-(d) show the impedance of the converter only. The analytical values match the time-domain values from 1-1000 Hz very closely. This match confirms that the model is able to copy the same frequency pattern observed in the time study. Under PV mode, the impedance magnitude increases between 28-100 Hz and reaches a clear rise at around 50 Hz. This comes from the action of the voltage loop, which reacts within that band. Under PQ mode, the magnitude stays very small in that same band because the focus of this mode is to hold active and reactive power, not to regulate voltage.

The phase plots also show a clear change between control types. PQ mode gives higher phase angles from 0-148 Hz, meaning the converter looks more inductive in this range. PV mode gives lower phase angles in this range and therefore shows weaker inductive nature. Above 148 Hz, the two modes follow almost the same phase shape. Only small peaks near 50 Hz can be seen. Both modes become nearly the same at high frequency, showing that the outer loop has very low effect once the frequency becomes large. This pattern appears the same for all four sequence directions (pp, pn, np, nn).

Figures 3.6(e)-(h) give the total impedance when the converter and AC grid are seen together. Again, the analytical results follow the time-domain curves across 1-1000 Hz. The total impedance reveals resonance-type points that depend on the control mode. With PQ mode, a sharper resonance appears near 130 Hz. With PV mode, the resonance is softer and does not peak as much. This shows that both modes look the same at high frequency, but when the frequency is near the resonance area, their effect is different.

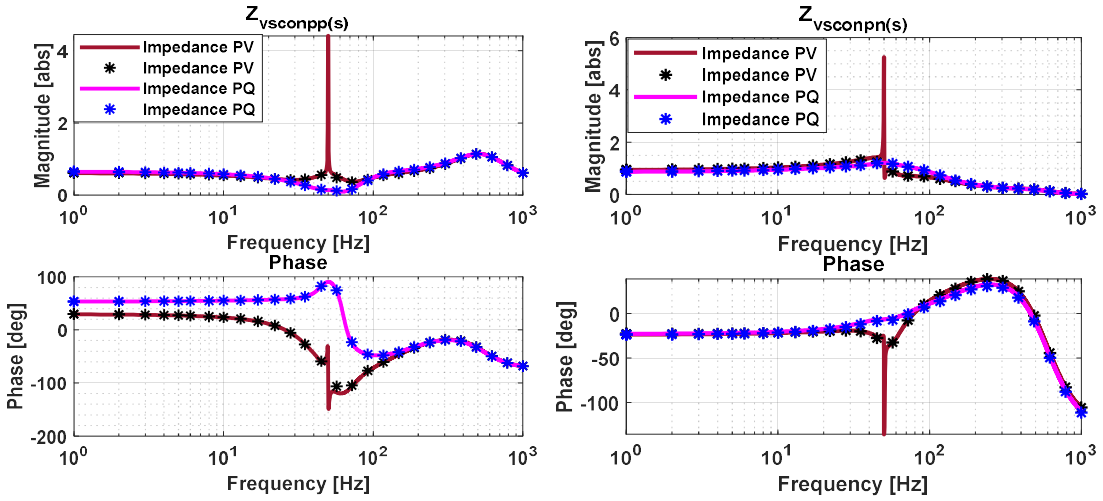
Z vsconpp(s)
Impedance PV
Impedance PV
Impedance PQ
Impedance PQ
Magnitude [abs]
Frequency [Hz]
Phase
Phase [deg]
Frequency [Hz]

(a)

Z vsconpn(s)
Impedance PV
Impedance PV
Impedance PQ
Impedance PQ
Magnitude [abs]
Frequency [Hz]
Phase
Phase [deg]
Frequency [Hz]

(b)

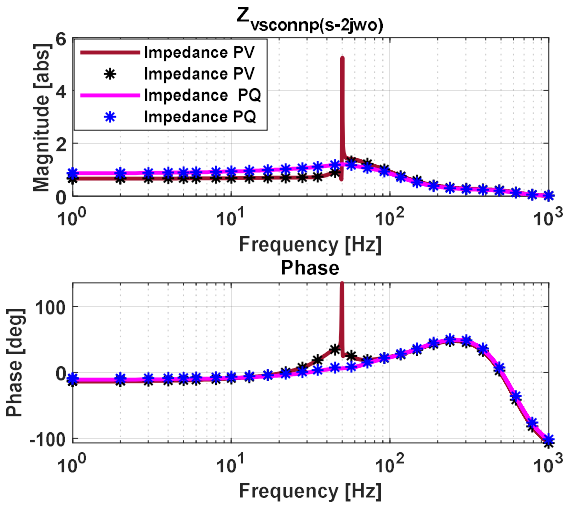
Z vsconnp(s-2jwo)
Impedance PV
Impedance PV
Impedance PQ
Impedance PQ
Magnitude [abs]
Frequency [Hz]
Phase
Phase [deg]
Frequency [Hz]

(c)

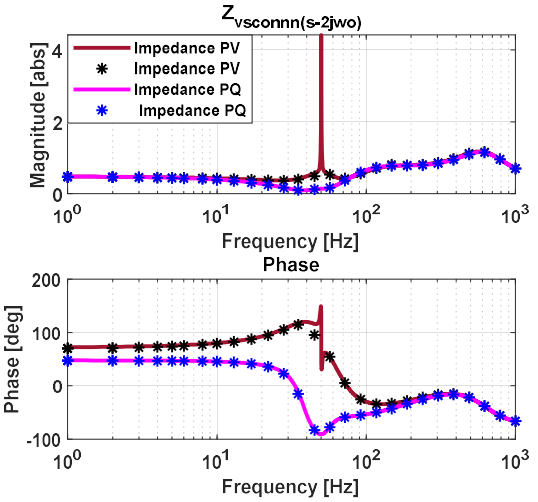
Z vsconnn(s-2jwo)
Impedance PV
Impedance PV
Impedance PQ
Impedance PQ
Magnitude [abs]
Frequency [Hz]
Phase
Phase [deg]
Frequency [Hz]

(d)

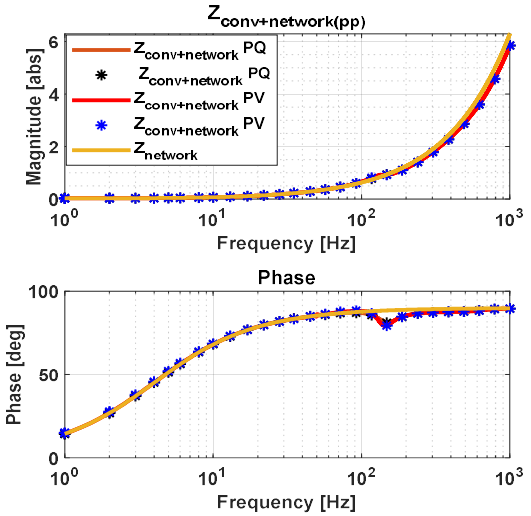
Z conv+network(pp)
Z conv+network PQ
Z conv+network PQ
Z conv+network PV
Z conv+network PV
Z network
Magnitude [abs]
Frequency [Hz]
Phase
Phase [deg]
Frequency [Hz]

(e)

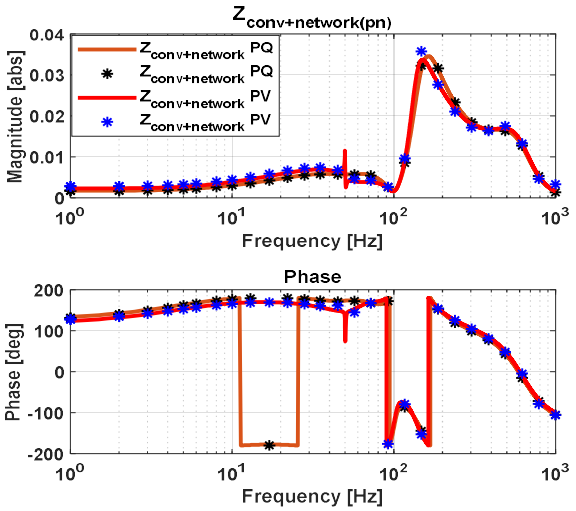
Z conv+network(pn)
Z conv+network PQ
Z conv+network PQ
Z conv+network PV
Z conv+network PV
Magnitude [abs]
Frequency [Hz]
Phase
Phase [deg]
Frequency [Hz]

(f)

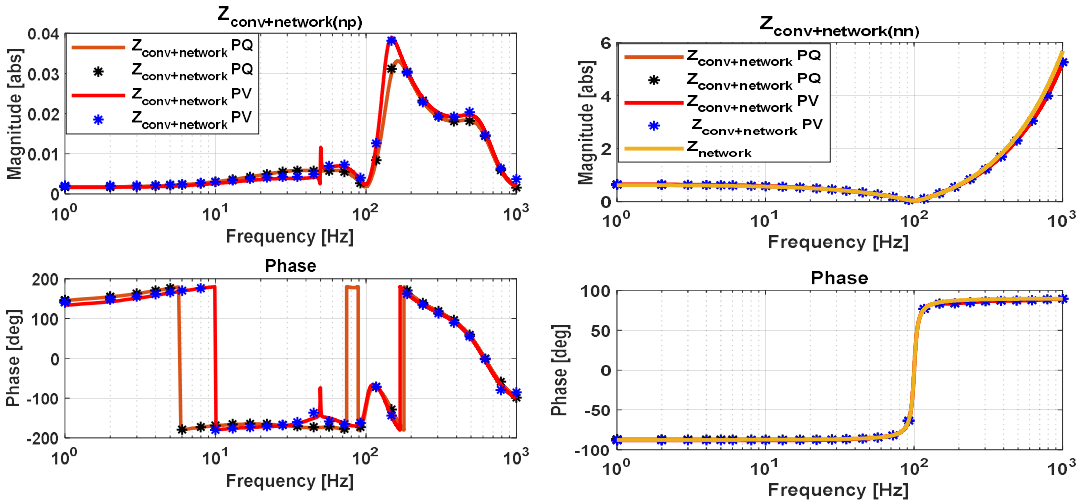

(g) (h)

Figure 3.6: Impedance Validation of Converter under (PV) Control and $Z_{network+network}$ Under PQ and PV Control System Under Coupling One Parameter

The IR plot in Figure 3.7 makes this clearer. The EIR plot in Figures 3.8(a)-(b) also shows that PQ mode gives a stronger impedance change close to 130 Hz, while PV mode gives a smoother shape and offers more damping across that band. This means PQ mode allows higher impedance movement around the resonance, and PV mode holds the impedance movement lower.

IR values stay close to one across the whole range when the grid is strong. Around 128 Hz, the IR is about 1.1 for PV mode and about 1.0 for PQ mode. The phase values are also small in this band, near −9° for PV and −6° for PQ. These numbers show that the link between the converter and network is small in this strong-grid case, and only very small differences appear between the control types.

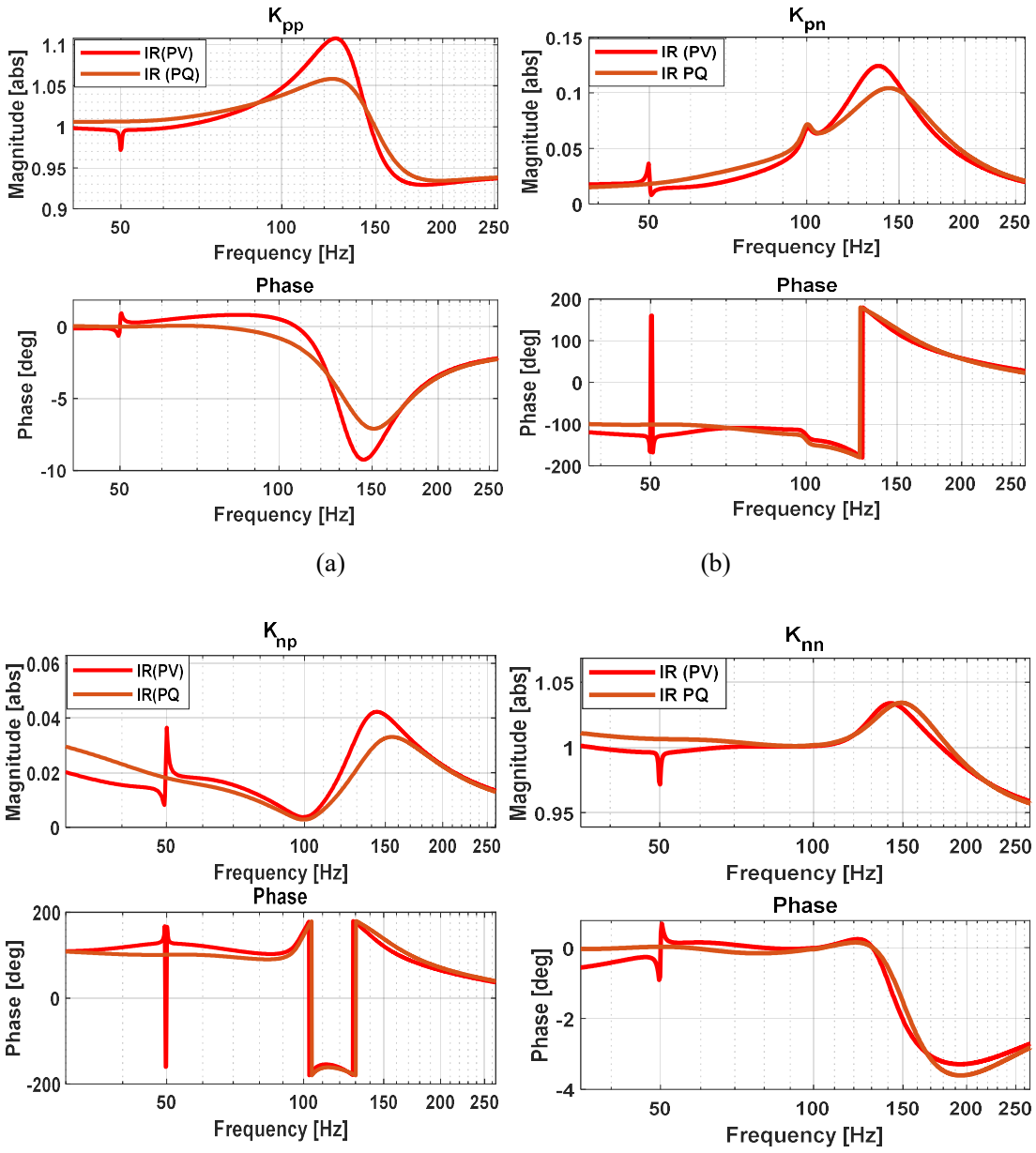

Figure 3.7: IR change Under PQ and PV Control System Under Coupling One Parameters

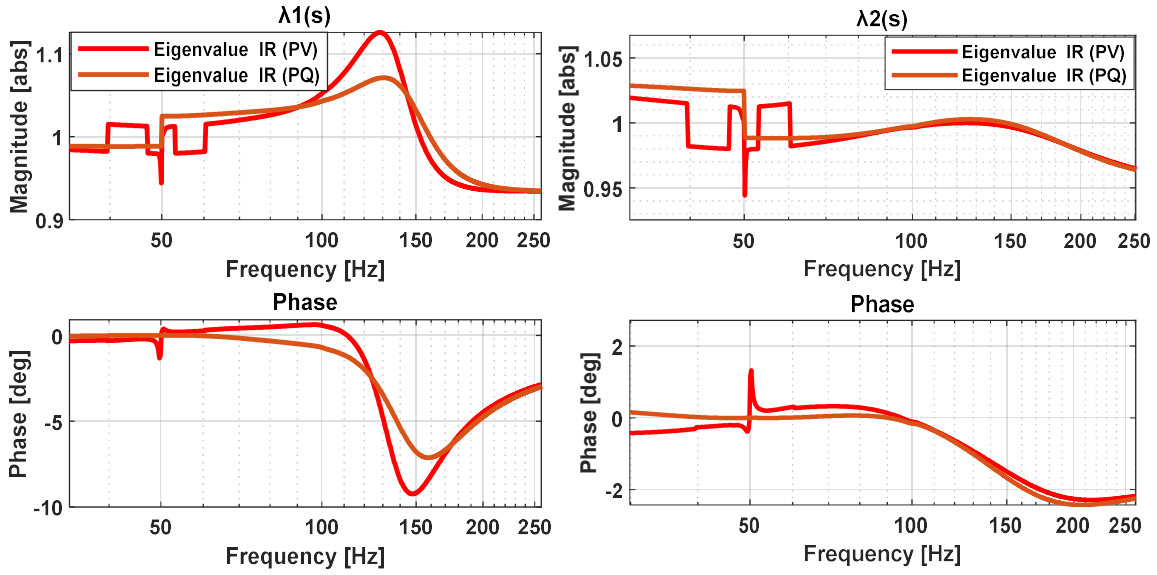

(a) (b)

Figure 3.8: Eigenvalue of IR changes Under PQ and PV Control Under Coupling One Parameters

In short, the impedance model matches the time behaviour very well. In a strong-grid case, the outer loop changes the impedance mainly at low and medium frequency. At high frequency, both modes act almost the same. Near the resonance point, PV mode shows higher impedance rise than PQ, while PQ gives a smoother variation in that area.

3.5.2.2 Weak-Grid (Coupling-Two) Simulation Results

This section explains the case where the grid has low strength. In this state, the grid has high impedance, and the converter experiences strong coupling with the network across the whole frequency range. The main aim here is to show how the impedance shape changes when the grid is weak, and how IR and EIR values move across frequency. The goal is not to comment on strong or weak dynamic safety, but to show clear changes in impedance patterns and how each control mode responds to high external impedance.

Figure 3.9(a) presents the positive-sequence impedance under weak grid. Under PV control, a clear rise appears near 114 Hz, reaching about 3.5p.u. This rise shows that the voltage loop reacts strongly to the high network impedance in that band. From 100-150 Hz, the PV phase moves above 90°, showing a strong loop reaction. In the same band, PQ and GFM stay below 90° and give smoother shapes. Outside this band, the three modes show similar behaviour, though PV remains highest, PQ stays lower than PV, and GFM gives the lowest curve in the positive-sequence view.

The negative-sequence impedance in Figure 3.9(b) remains smooth for all modes. No large rises appear, and all curves stay low. This shows that unbalanced conditions do not create large changes in the negative-sequence direction.

Figure 3.10(a) shows the IR under weak grid. Under PV, the IR reaches about 3.0 near 114 Hz, with phase near −60°. A high IR here means the converter and grid impedances align in a way that produces strong interaction. PQ has a lower peak, a little above 1.1, with phase near −18°, showing weaker interaction than PV. GFM stays close to unity and shows only small phase change, meaning it does not create strong interaction in this state.

Figure 3.10(b) shows the negative-sequence IR. All values remain low. PV has a small peak near 1.3 with phase between −6° and +9°. PQ stays slightly above 1.0, and GFM remains close to 1.0 across the full band. This confirms that negative-sequence influence is small compared with positive-sequence influence in a weak grid.

Figures 3.11(a)-(b) show the EIR. Under PV, the main eigen response λ_1 reaches about 3.02 with phase near −65° at 114 Hz, matching the point seen in the impedance shape. PQ shows lower eigen values, and GFM stays close to unity with minimal phase change. A second eigen pattern appears between 50-80 Hz, but the value stays low and does not show a strong rise.

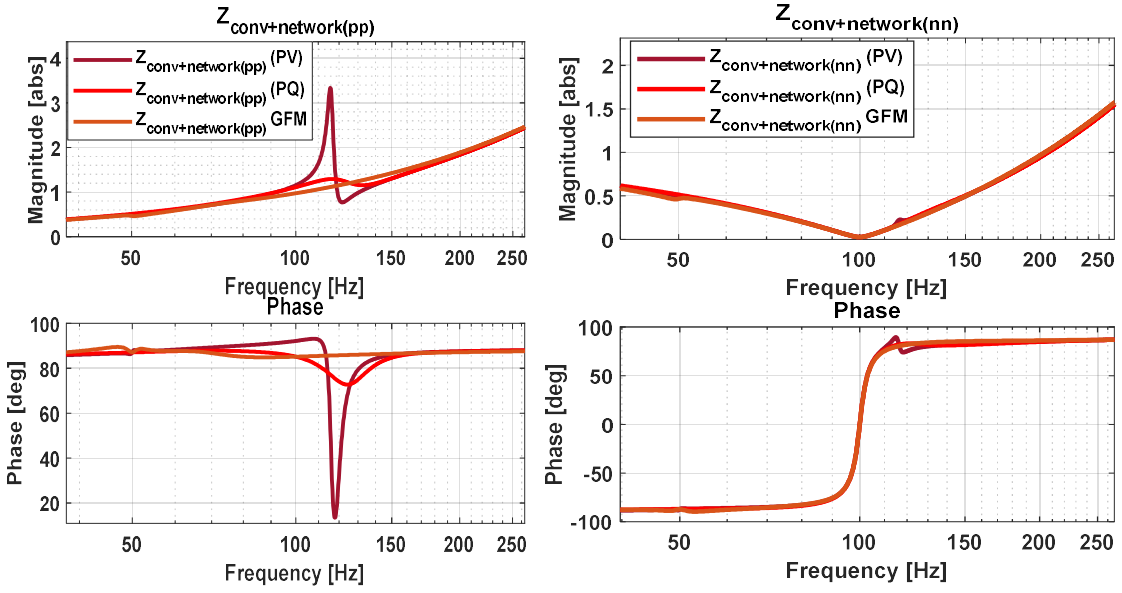

(a) (b)

Figure 3.9: Impedance $Z_{network+networ}$ Under PQ and PV Control System Under Coupling Two Parameters

The IR and EIR curves show that the most important frequency in a weak grid is around 114 Hz. At this point, the PV mode exhibits the largest response and the strongest interaction. The PQ mode remains lower, and the GFM mode stays smooth across the whole range. The high grid impedance in this case increases coupling with the converter and causes the largest impedance to change near this frequency band. These observations are consistent with time-domain simulations between 1 and 1000 Hz, showing that impedance-based methods can locate the main frequency where impedance movement grows and help guide gain tuning when required.

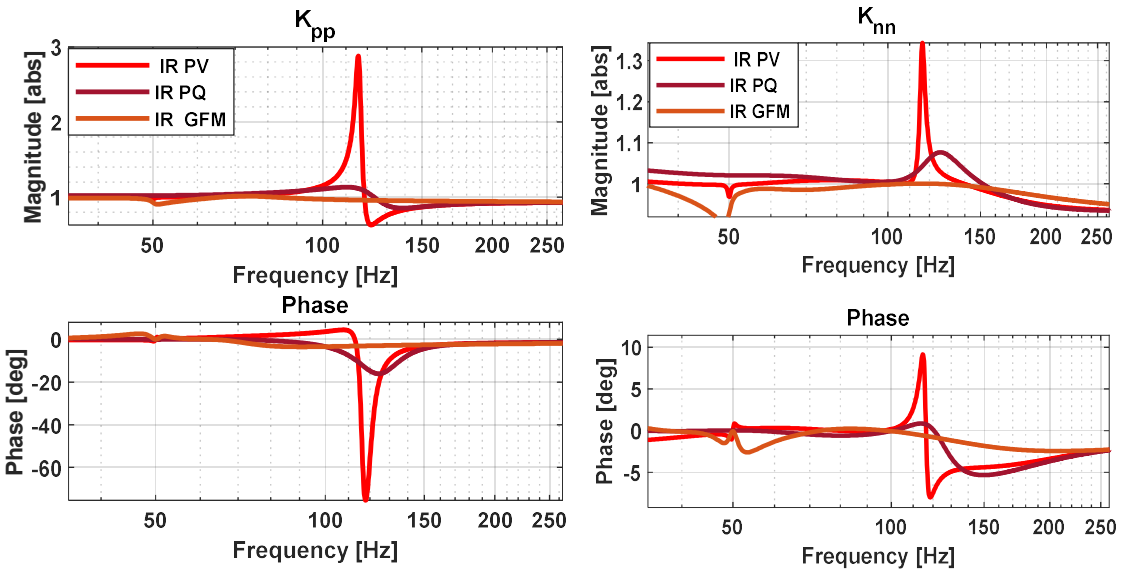

(a) (b)

Figure 3.10: IR change Under PQ and PV Control System Under Coupling Two Parameters

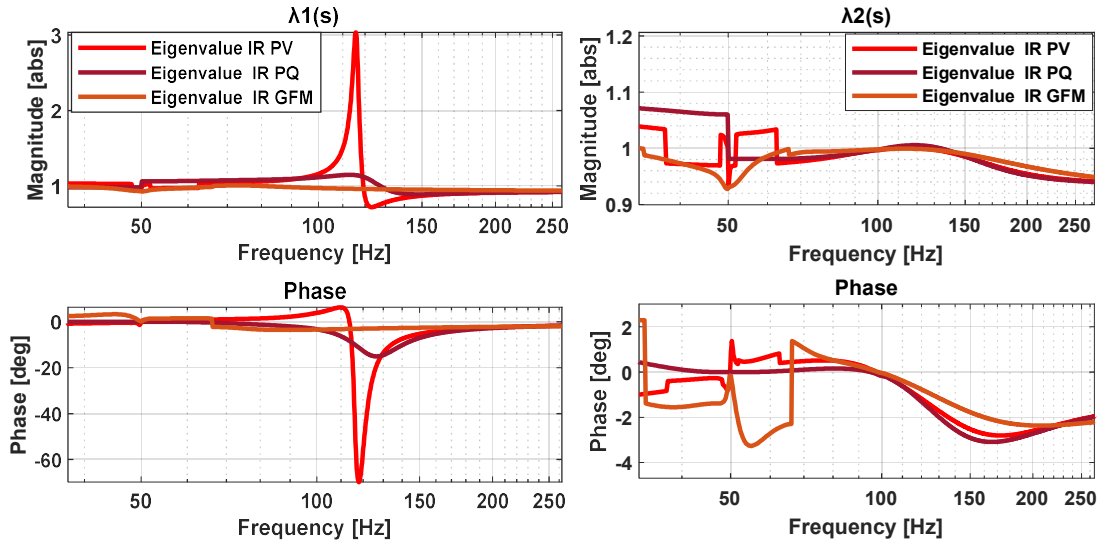

(a) (b)

Figure 3.11: Eigenvalue of IR changes Under PQ and PV Control Under Coupling Two Parameters

3.6 Stability Assessment of Two-Converter Networks

The small-signal stability of converter-dominated systems can be evaluated by analysing the impedance observed from the terminal of the local converter. This formulation captures the interaction between the local converter impedance, $Z_{con\text{-}2}(s) = \frac{1}{Y_{vsc\text{-}2}(s)}$, and the remote converter impedance, $Z_{con\text{-}1}(s)$. The combination of these elements defines the total network impedance that dictates the dynamic response of the interconnected system.

For simplification, the two voltage sources, S_1 and S_2, are represented by a single equivalent source, as illustrated in Figure 3.5. The associated impedances $Z_{g1}(s)$, $Z_{g2}(s)$, and $Z_L(s)$ are then combined to obtain the equivalent network impedance of the two-converter system, expressed in equation (3.15). The operating parameters used for both strong- and weak-grid conditions are provided in Tables 3.1 and 3.2.

From these elements, the equivalent impedance at the terminal of the local converter is derived. Denoted as $Z_{yg1}(s) = Z_{network+conv}(s)$, this represents the interaction between the converter and surrounding network. Multiplying $Z_{yg1}(s)$ by the local converter admittance, $Y_{vsc\text{-}2}(s)$ yields the frequency-dependent eigenvalue loci of the combined system. These loci are plotted using the Nyquist criterion to determine the stability of the two-converter configuration shown in Figure 3.5.

Stability is examined for strong- and weak-grid settings to show how the control mode of the remote converter-PQ, PV, or GFM-changes the impedance seen at the local converter and affects the stability margin.

3.6.1 Stability Under Coupling-One Condition

Figure 3.12 shows Nyquist plots and eigenvalue paths for strong-grid operation with coupling-one values. The local converter runs in PV mode, while the remote converter is tested with PQ, PV, and GFM control modes. The stability trends align with the impedance variation study in Section 3.5.2.1.

From the eigenvalue paths, PQ and PV modes move closer to the point (−1, 0) than GFM. The GFM path stays further away, showing higher damping and lower resonance. The Nyquist plots show that none of the cases cross or loop around (−1, 0), so all cases remain stable.

The distance from the critical point differs across modes. GFM gives the largest stability margin, PQ gives a moderate level, and PV stays closest to the limit, which increases the chance of oscillations. Thus, under strong-grid conditions, GFM gives the best damping behaviour, PQ remains acceptable, and PV needs careful tuning to avoid loss of stability.

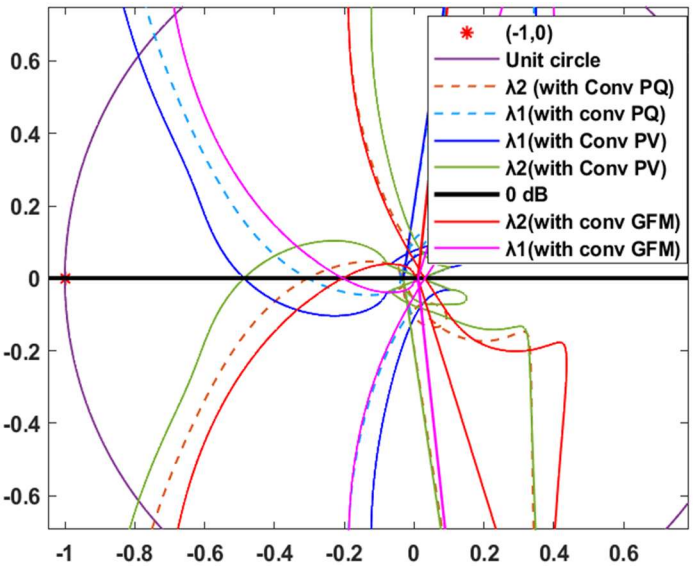

Figure 3.12: Nyquist Plots for Remote Converter (PV and PQ) and GFM Control Mode, with Local Converter in PV Mode under a Specific Coupling one Parameter

3.6.2 Coupling -Two Conditions

Under weak-grid conditions with two coupling parameters, the behaviour of the system changes. Figure 3.13(a) shows Nyquist plots when the remote terminal uses PV, PQ, and GFM control. With PV control, the path circles the point (−1, 0), which signals loss of stability. When the grid becomes weak under the two-parameter setting, this behaviour remains. Figure 3.14(a) presents Nyquist plots for the same modes when the local terminal operates in PV mode. Again, the PV path circles the point (−1, 0), showing loss of stability. PQ and GFM stay clear of this point, so they keep stable operation.

The frequency curves in Figure 3.13(b) supports these observations. With PV control, a strong peak appears near 114 Hz. At that point, the magnitude reaches 0 dB, and the phase moves near 180°, which gives negative damping. PQ and GFM keep smooth magnitude and phase trends, so they stay damped. These effects arise from the combined converter and network impedance, which shapes the interaction. A clear oscillation band appears between 75 and 116 Hz in Figure 3.13(b) of $Z_{conv+network}$, with the main resonance at 114 Hz under PV control. The other modes do not show this effect.

Figure 3.14 presents the eigenvalue results used together with the frequency checks. With PV control, the main eigenvalue reaches a high value and a large phase angle at 114 Hz, matching the unstable path in the Nyquist plot. PQ gives lower values and smaller phase change, while GFM keeps values near one and phase close to zero. These results confirm that PQ and GFM remain stable.

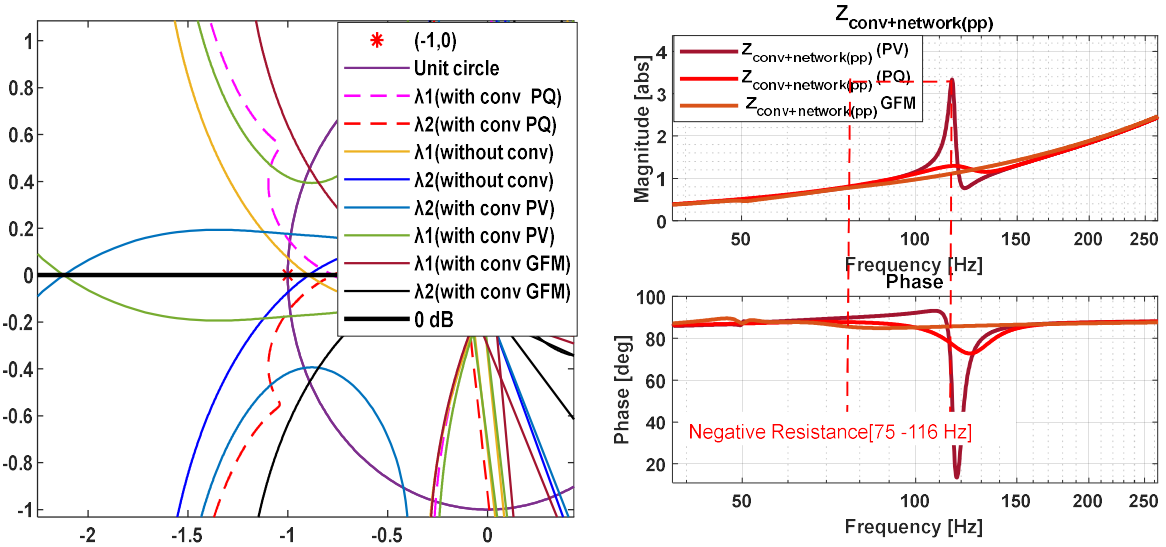

(a) (b)

Figure 3.13: (a) Nyquist Plots Without and with Remote Converter in PV and PQ modes, and with Local Converter operating in PV mode under two coupling parameter conditions; (b) Impedance comparison between $Z_{network+conv}$ and $Z_{network}$

In this converter-connected networks, the relative stability of different control modes is strongly influenced by grid strength and the location of voltage regulation. The results indicate that variations in short-circuit strength and remote-control configuration significantly affect the dynamic response observed at the local connection point. Under strong grid conditions, all operating modes remain stable, albeit with differing stability margins. Grid-forming control maintains the largest distance from the critical stability boundary due to its inherent voltage support and damping capability. PQ control also preserves stable operation, although with comparatively reduced damping, whereas PV control operates closest to the stability limit.

The distinction becomes more pronounced in weak grid scenarios, where the increased grid impedance amplifies control interactions. In this context, PQ control demonstrates superior stability compared to PV control because it regulates active and reactive power without directly enforcing local voltage magnitude. Consequently, PQ operation exhibits weaker

coupling with grid voltage dynamics and reduced sensitivity to PLL interactions, thereby mitigating the risk of resonance amplification. In contrast, PV control actively regulates voltage, which introduces tighter feedback with the grid impedance and PLL dynamics. This stronger coupling can excite oscillatory modes, particularly in weak networks where voltage variations are more pronounced, leading to reduced damping or even instability.

The frequency-domain analysis reveals that PV operation develops a pronounced resonance peak around 114 Hz, indicating the onset of an unstable oscillatory mode, while PQ control maintains stability with modest damping. GFM control continues to exhibit robust behaviour by providing voltage stiffness and additional damping support to the network.

These observations are corroborated by time-domain simulations. As illustrated in Figure 3.18 (Section 3.7.1), when PV control is implemented at the remote terminal in a weak grid with a 30 Hz PLL bandwidth, sustained oscillations emerge due to resonance effects. By comparison, PQ control converges to steady state with acceptable damping, and GFM control remains well-damped throughout the disturbance. The strong agreement between time-domain responses and frequency-domain predictions reinforces the validity of the analytical approach and confirms that PQ control offers improved stability robustness over PV control in weak grid environments primarily due to its reduced voltage-control interaction with the grid.

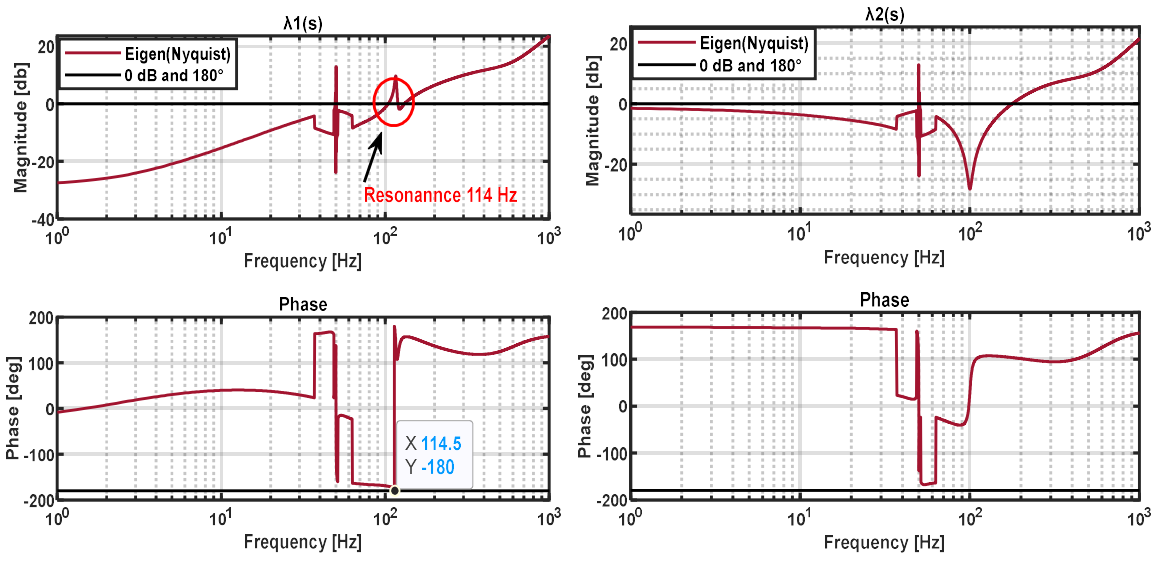

(a) (b)

Figure 3.14: Stability Analysis via Eigen of Nyquist Criterion for PV Control Under Resonance (a) $\lambda 1$ (b) $\lambda 2$

The stability study uses impedance checks, the Nyquist test, eigenvalue paths, and time-domain results. This set of tools allows clear tracking of resonance points, controller effects, and safe operating limits in linked converter grids. A key point is the correct impedance model between the converter and the grid. The Nyquist test uses an impedance ratio. In the multi-input multi-output case, this ratio becomes a matrix, and stability depends on its eigenvalues. Risk increases when an eigenvalue has a phase near ±90° and a magnitude close to one. This situation occurs when controller bandwidth aligns with a grid resonance, causing the controller to introduce oscillations instead of reducing them. A related diagram in Appendix A (Figure A1:2) shows how converter behaviour changes under different control settings.

3.7 System Stability and Varied Converter Characteristics

As have been observed, in power systems with multiple converters, system stability is strongly influenced by the interaction between converter control strategies, network impedance, and converter dynamic characteristics. This section examines, in detail, the effects of control architecture and PLL bandwidth on the stability of interconnected converters, using both frequency-domain and time-domain approaches.

3.7.1 Stability under Changing PLL Bandwidths and Control Modes

Chapter 2 showed that a single converter becomes more sensitive as the PLL bandwidth increases. At 10 Hz it remains stable, at 20 Hz it moves closer to the stability limit, and at 30 Hz it develops a resonance that leads to instability.

This section extends the analysis to two linked converters. Figure 3.15 presents the Nyquist curves of a local converter in PQ mode with a PLL bandwidth of 30 Hz. Two cases are examined. In the first, the remote terminal also operates in PQ mode. In the second, the remote terminal is off. When the remote terminal is off, the curve shifts toward the point (−1, 0). When the remote terminal operates in PQ mode, the curve shifts away from that point, giving the local terminal a larger stability margin.

A similar pattern appears when the local terminal operates in PV mode. As long as the remote terminal stays in PQ mode, the local terminal remains stable, as shown in Figure 3.14(a). This confirms that the control mode of each converter affects the overall behaviour, especially when a fast PLL interacts with the network.

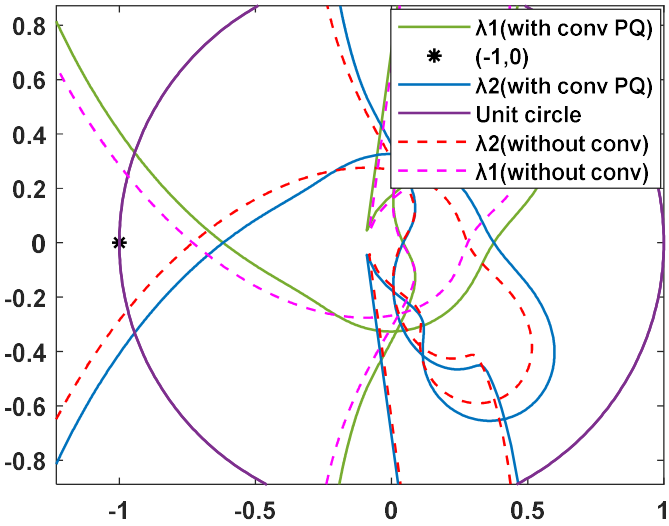

Figure 3.15:Nyquist Analysis with and without Remote Converter Under PQ Control

Time-domain results in Figure 3.16 (a-b) support this point. With a remote PQ unit, the system accepts power up to 1.2p.u. before oscillations appear near 8.9 s at around 1.4p.u. (≈ 8.6). When the remote unit is off, instability begins earlier near 8.3 s at the same power level. This shows that a remote PQ setting increases the safe operating range of the local unit.

Figure 3.17 gives the frequency response of the positive-sequence impedance ratio when the remote side uses PV mode. With a PLL at 25 Hz, a peak of about 1.6 forms at 122 Hz with a phase near 40°, which shows weak damping. Lowering the gains to $K_p = 1.2$ and $K_i = 1.8$ reduces the peak to about 1.4 and shifts the phase to nearly −25°, which improves damping and increases stability space.

Raising the PLL to 30 Hz even with the same gains produces a sharp rise near 2.8 and a phase close to −90°. This means much weaker damping and a smaller stability margin. Faster PLL action increases the coupling between converter control and grid impedance, so resonance grows, and the unit moves close to instability.

When the converter uses PQ mode, resonance stays below 1.2 for both 25 Hz and 30 Hz. Phase movement stays small, showing safe damping and no strong resonance. This confirms that PQ mode tolerates higher PLL speed and avoids sharp peaks.

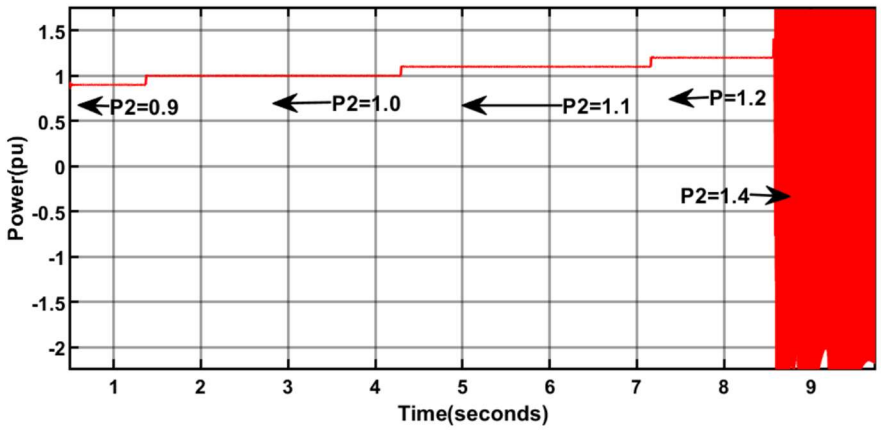

(a)

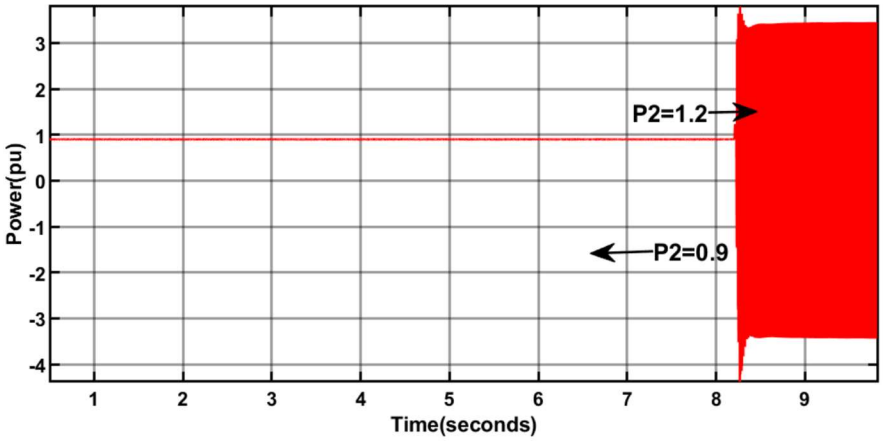

(b)

Figure 3.16: Time domain simulations under varying power levels, (a): with remote converter under PQ control; and (b): without remote converter

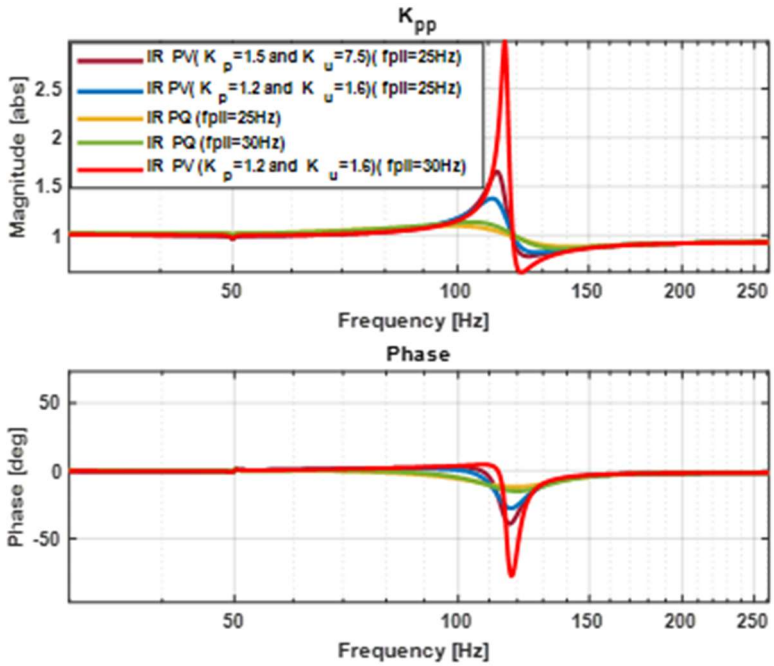

Figure 3.17: IR change at different PLL and PI value

Figure 3.18 shows the time-domain response for a converter operating in PV mode under PLL changes from 10 Hz to 30 Hz. Power, d-axis current, and d-axis voltage remain smooth when the PLL bandwidth is 10 Hz. When the PLL increases to 30 Hz, oscillations appear around 5.5 s and grow until 9s. This behaviour indicates that a faster PLL weakens damping and makes the PV controller sensitive in a weak grid. The PLL tuning applied at the remote PV unit drives this response.

As seen, both GFM and PQ settings stay stable in earlier tests, but this behaviour only affects PV operation. Appendix A supports this result. The passivity plot in Figure (A1:1) shows a loss of passivity when the PLL operates at higher speeds, tested at 25 Hz and 30 Hz. At around 30 Hz, the impedance moves past −180°, indicating negative damping and weaker stability. This confirms that PV operation becomes more sensitive as PLL speed increases in weak grid conditions.

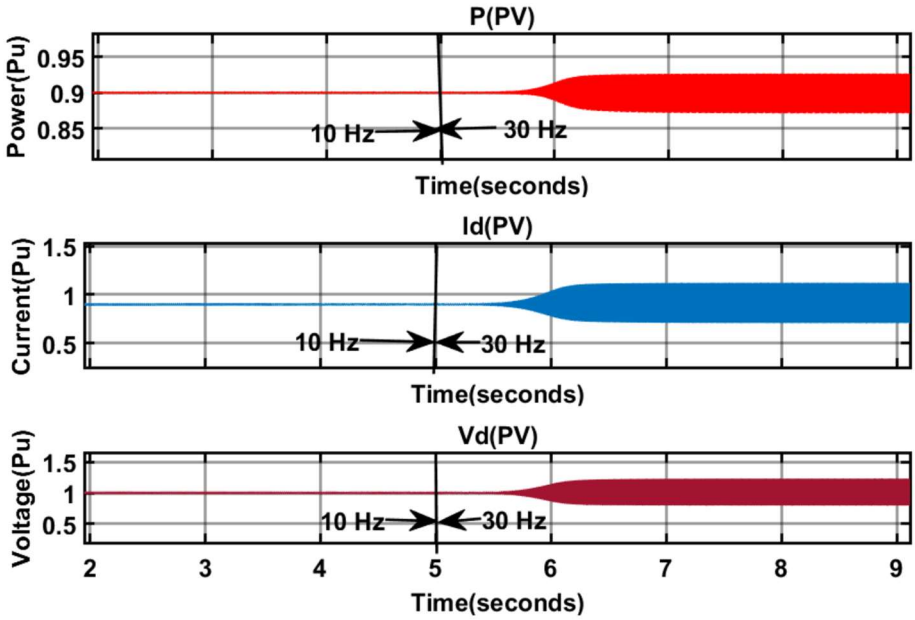

Figure 3.18: Time domain simulation of local converter d-axis voltage and current and active power (P) Under Coupling Two PV with modified PLL parameters in PV mode

Figures 3.16-3.18 show that stability depends on both the control mode and PLL tuning. The impedance seen by the local terminal depends on the remote unit. PV mode causes the largest resonance, PQ mode keeps small peaks, and GFM remains stable because it does not use a PLL.

Nyquist plots reflect this trend. The stability margin is largest when both sides run PQ mode, smaller when the local uses PV and the remote use PQ, smaller again when the local uses PQ and the remote use PV, and lowest when both use PV mode. Remote PV operation gives the weakest damping compared to PQ and GFM settings.

3.7.2 Stability Impact of Active Power Setpoint in PV Control

Figure 3.19 shows how changing the active power setpoint of the remote converter influences stability when using PV outer-loop control. Three power levels are examined: 0.5p.u., 0.9p.u., and 1.0p.u.

When the power setpoint is 0.5p.u., the operation remains stable. The impedance ratio stays close to one with small phase movement, and no strong oscillatory behaviour appears. The converter and network interact weakly, and damping is maintained. This condition is used as a stable reference.

At 0.9p.u., oscillations begin to form. Figures 3.19(a-b) show a sharp rise in the impedance ratio near 115 Hz and a clear phase drop. The eigenvalue plots in Figure 3.20(c) move closer to the imaginary axis, showing reduced damping and higher risk of oscillation.

At 1.0p.u., the interaction becomes stronger. Although the impedance ratio decreases slightly compared with 0.9p.u., the phase path moves nearer to the critical region. Figures 3.19(b-c) show that the eigenvalues shift toward marginal behaviour, meaning the system becomes sensitive to small disturbances. Resonance does not disappear at high power; instead, it changes form and may still threaten stability.

The Nyquist plots in Figure 3.19(d) supports these points. At 0.5p.u., the curve remains far from the point (−1, 0). At 0.9p.u., the curve approaches the boundary, and at 1.0p.u. the separation stays small. The safety margin therefore decreases as the power transfer increases.

These results show that raising the active power setpoint increases the interaction between the converter and the grid. Operation at 0.5p.u. preserves stable behaviour, while higher values such as 0.9-1.0p.u. introduce stronger resonance and reduce stability headroom. Coordinating the power reference with network strength is therefore important, especially in weak-grid conditions. The heat map in Appendix A (Figure A1:3) further illustrates the sensitivity trends that support this observation

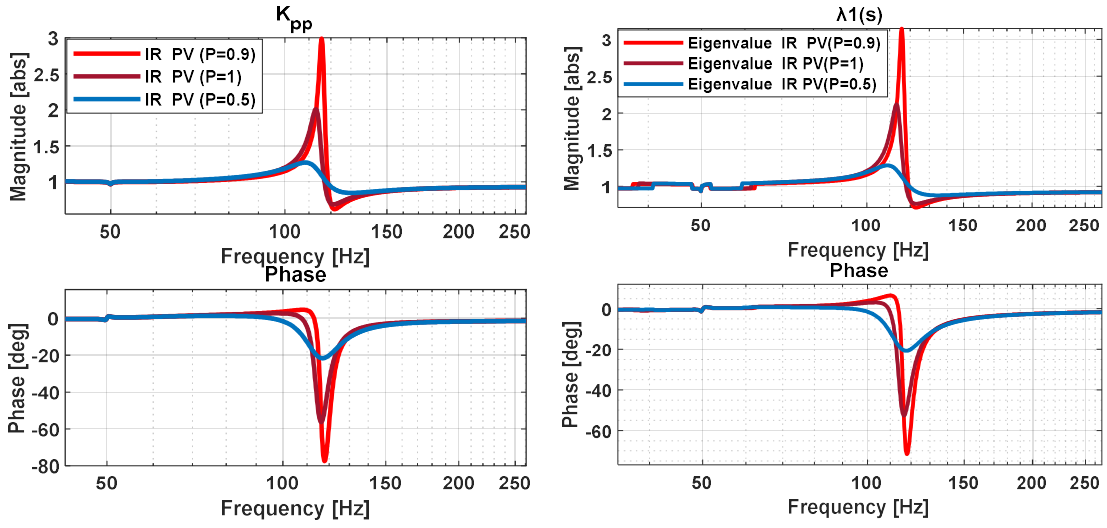

(a) (b)

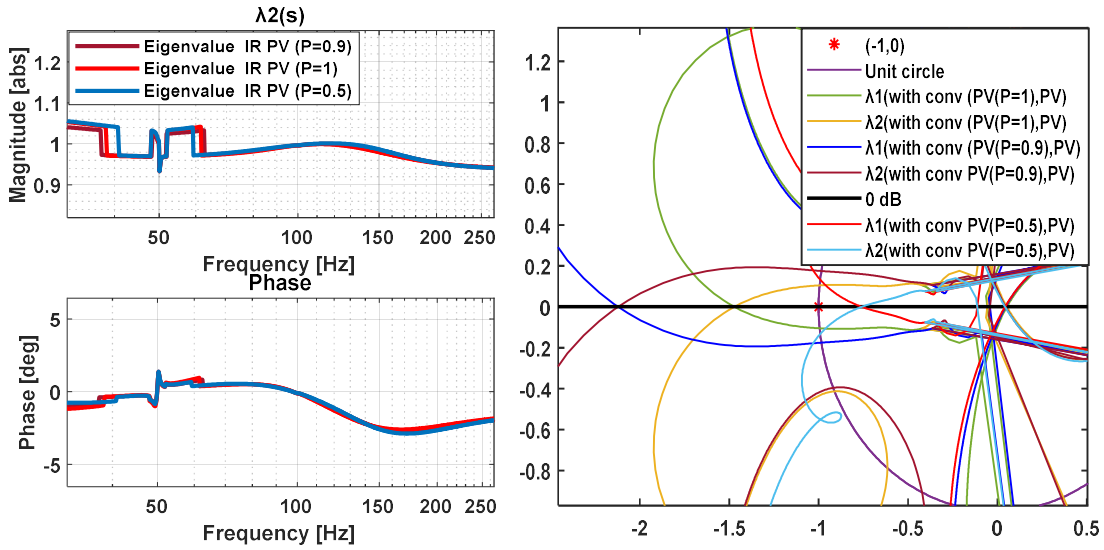

(c) (d)

Figure 3.19: Effect of varying the (P) value in the outer-loop controller on (a) IR, (b-c) EIR, and (d) the Nyquist stability analysis

3.7.3 Operating Modes: VSC 1 Rectifier/Inverter and VSC 2 Inverter

Figures 3.20 and 3.21 show how the converters interact with the AC grid when the remote unit (VSC-1) uses PQ control as either a rectifier or an inverter, while the local unit (VSC-2) regulates AC voltage in PV mode.

When VSC-1 works as a rectifier, it sends 0.9p.u active power from the AC side to the DC link. As seen in Figure 3.20(a) IR response rises sharply around 150-200 Hz, with a phase shift close to +6.6°. This phase behaviour lowers damping and strengthens coupling with the grid, which promotes oscillations. The eigenvalue-based impedance plots in Figures 3.20(b-c) support this trend, showing phase values approaching +9°, which signal reduced damping. The Nyquist plot in Figure 3.20(d) also confirms loss of stability, as clear encirclements of (−1,0) appear.

When VSC-1 operates as an inverter, it receives 0.9pu active power from the DC and provides 0.1pu reactive power to the AC network. Under this condition, the impedance stays damped. The magnitude shows a moderate peak between 66-120 Hz, limited to 1.14pu, and the phase drops to about −15° within 80-172 Hz. This phase path avoids values linked to weak damping. Both impedance and eigenvalue results confirm stable performance, as no positive phase trend appears. The Nyquist diagram supports this conclusion by showing no encirclement of (−1,0) and clear distance from the critical region.

This comparison shows that phase behaviour gives the clearest indication of stability. Magnitude changes alone can appear large, but phase direction fully determines whether the converter operates in a stable or unstable zone.

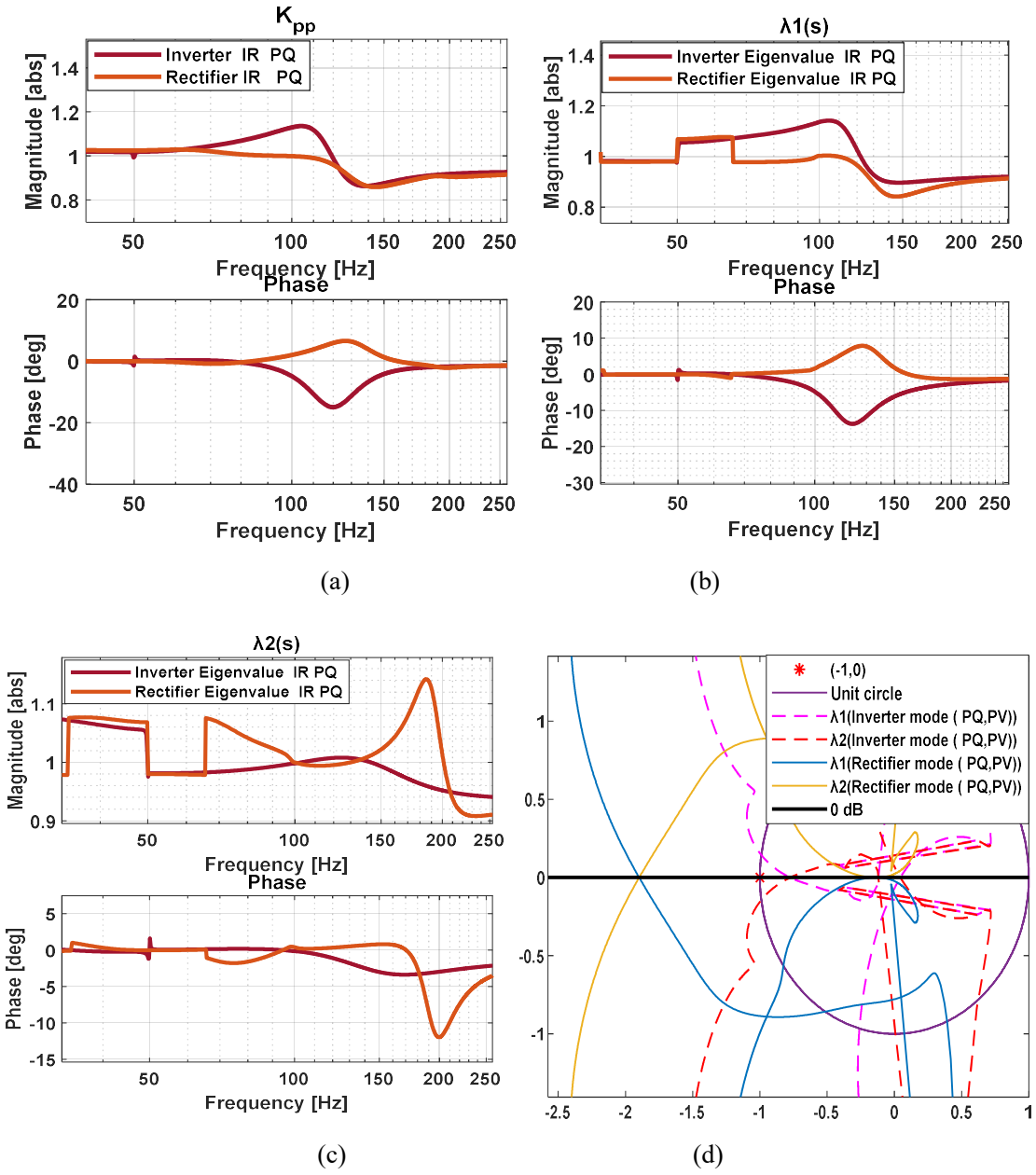

Figure 3.20: Impedance-based analysis with remote converter in PQ mode and local converter in PV mode: (a) IR, (b-c) EIR, (d) Nyquist stability analysis

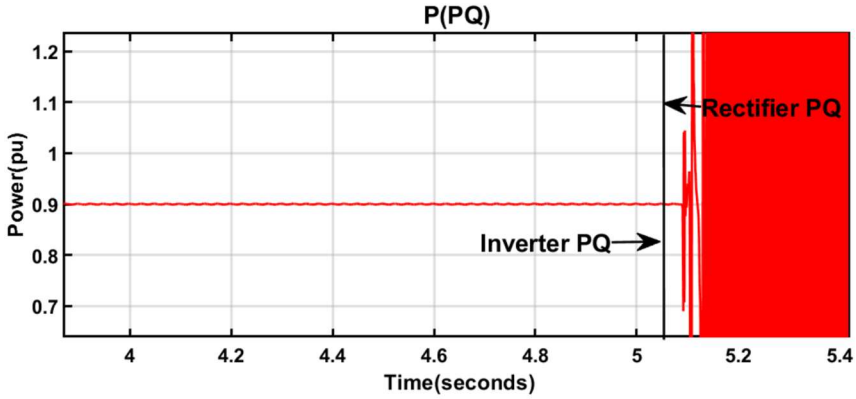

Figure 3.21: Time-domain response with remote PQ mode (inverter/rectifier) and local PV mode

Time-domain results in Figure 3.21 match the frequency-domain observations. During inverter operation, the impedance remains damped, and the system keeps steady behaviour. At t ≈ 5.1 s, VSC-1 switches to rectifier mode while keeping the same active power level. This shift changes the impedance shape, introduces negative damping, and produces a strong resonance peak. Oscillations increase quickly, showing a drop in stability margin. In contrast, inverter mode holds lower resonance, better damping, and stable response. These findings show that impedance-based analysis explains the different responses of inverter and rectifier operation, and that weak grids benefit when converters stay in inverter mode.

3.8 Designing Proposed Impedance Reshaping Method

When the remote unit operates in PV mode, its impedance shows strong interaction with the grid. This behaviour can create resonance and weak damping, especially in networks with many converters. Such effects raise stability concern in the frequency domain. To solve this, a reshaping method for GFL converters in PV mode is introduced. This method adjusts the frequency response to reduce resonance and improve damping. As a result, the converter interacts with the grid in a smoother manner and avoids harmful oscillations in multi-converter conditions.

3.8.1 GFL under PV Control with LPF-Based Outer Loop

In weak converter-dominated grids, PV-controlled GFL units can achieve better stability by applying low-pass filters in the outer loop. Figure 3.22 shows the modified structure. Here, the active and reactive current references pass through LPF blocks before reaching the current controller. These filters limit fast variations in the reference signals. This prevents sudden changes from entering the inner loop and reduces power swings. As a result,

oscillations caused by weak-grid interaction are reduced, and the converter maintains smoother response during disturbances.

Without filtering, the reference channel allows high-frequency components to enter the control loop. This produces sharp resonance peaks in the range affected by the PLL and grid impedance. With LPFs, the open-loop impedance shape changes. The filters reduce high-frequency content while keeping the low-frequency dynamics intact. This lowers the resonance peak and increases the damping margin in the range where the converter and grid exchange power. The reshaped behaviour confirms that filtering directly limits the cause of oscillations and strengthens stability during PV operation.

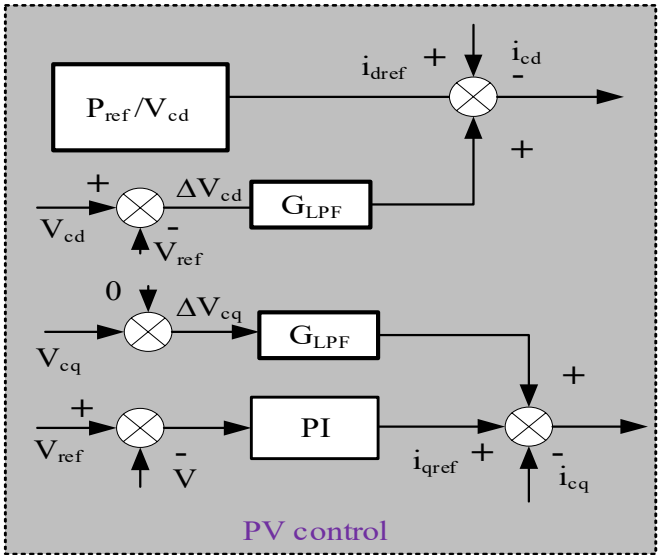

Figure 3.22: To Reshaping GFL Impedance Under PV Control System

The final relation for the reshaped impedance in PV-controlled GFL mode is expressed in (3.13). It gives the current reference variation as a function of voltage changes at the converter terminals:

$$\begin{bmatrix}\Delta i_{dref}\\ \Delta i_{qref}\end{bmatrix} = \begin{bmatrix}-\frac{P_{ref}}{V_d^2} + G_{LPF} & 0\\ V_d\left(K_{pu} + \frac{K_{iu}}{s}\right) & G_{LPF}\end{bmatrix}\begin{bmatrix}\Delta V_{cd}\\ \Delta V_{cq}\end{bmatrix} \tag{3.13}$$

The term G_{LPF} represents the transfer function of the low-pass filter used in the outer loop. It limits the frequency content of the reference signal, so that only slow components pass through, while fast variations are removed. This action reshapes the converter impedance and supports stable operation in weak grids.

3.8.2 Simulation Results for Reshaped GFL

This part explains how the low-pass-filter-based reshaping changes the impedance ratio. Figure 3.24 illustrates the effect on the impedance response. In Figure 3.23(a), the peak magnitude drops from roughly 3.0 to about 1.5, and the phase at the main oscillation point shifts from −70° to −45°. This shows higher damping and lower sensitivity to resonance. The parameters used in this work follow Table 3.1.

Figures 3.23(b) and 3.23(c) indicate that the reshaped unit keeps smaller eigenvalue impedance ratio values at higher frequencies. The steep phase drop seen in the original case does not appear after reshaping. This means the remote unit gives a smaller influence on the measured impedance at the local side, which lowers the chance of instability. Extra evaluation of the remote converter impedance also shows reduced resonance points, supporting the rise in stability limits.

The Nyquist plot in Figure 3.23(d) supports this conclusion. Without reshaping, the curve encircled the critical point (−1, 0), while the reshaped case stays clear of it and keeps a safe margin. With a PLL bandwidth of 30 Hz, the reshaped system maintains stable power transfer after disturbances, while the original PV case shows increasing oscillations. The PLL remains the same, so the improvement results from adjusting the outer loop. The low-pass-filter-based method increases damping, reduces oscillations, and supports stable operation under weak-grid conditions.

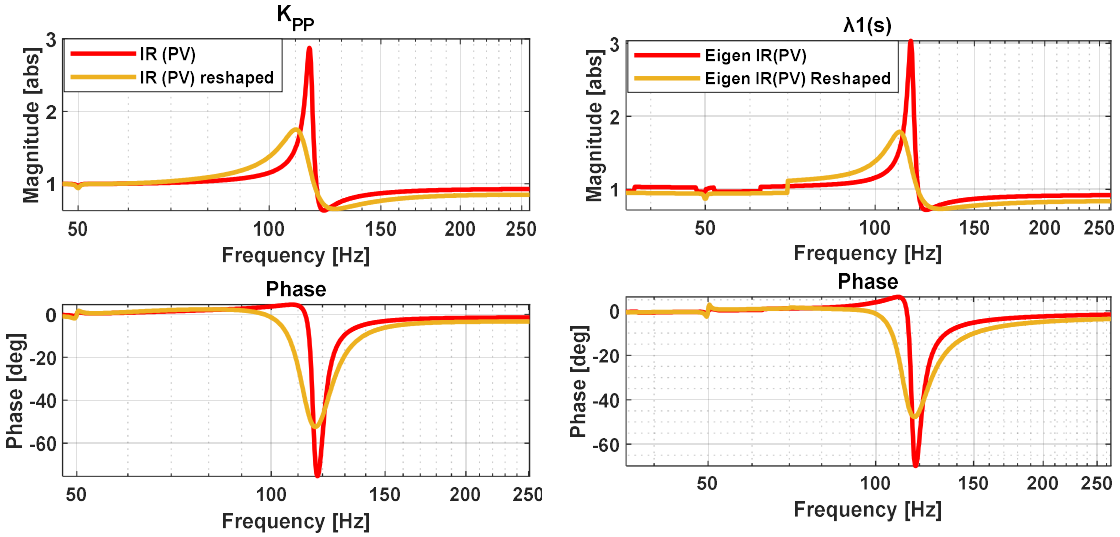

(a) (b)

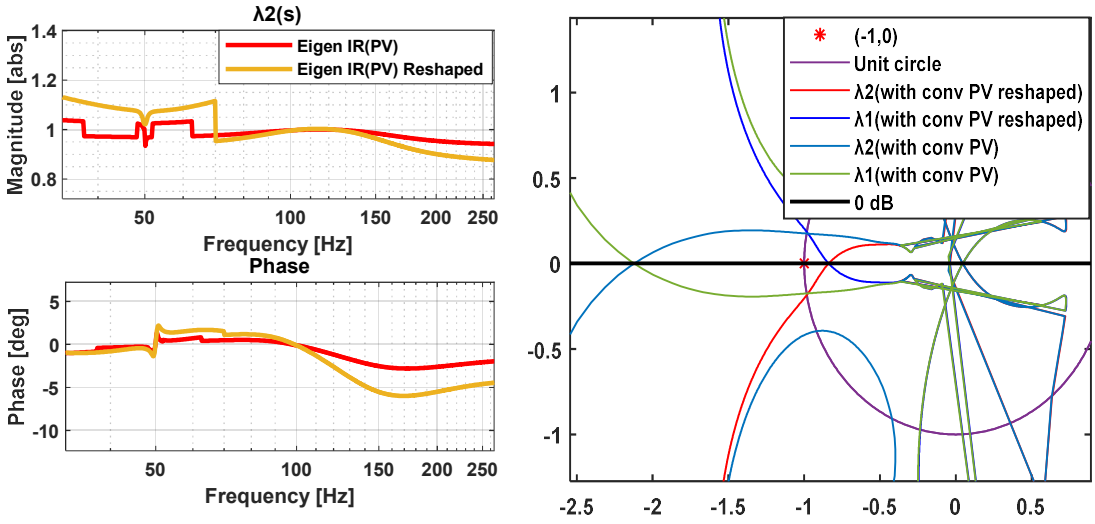

(c) (d)

Figure 3.23: Reshaping of the converter impedance for GFL operation under PV control, showing (a) IR, (b-c) EIR, and (d) Nyquist stability analysis

3.9 SCR, IR, and EIR Relationship in Multi-Converter Networks

The studies in Sections 3.5.2.1 and 3.5.2.2, using the conditions in Table 3.1, show that network strength influences oscillations. When the short-circuit level falls from 3.25 to values below 2.0, resonance appears, as seen in Figures 3.24(a-b). At an SCR of 1.9, the impedance ratio reaches 2.9. A further drop to 1.8 increases the magnitude to 4.5, and a resonance occurs near 115 Hz. Weak supply conditions therefore increase oscillation and reduce damping. SCR alone cannot explain this pattern, so impedance-based evaluation is needed. These findings are derived from the weak grid analyses in Table 2.1,3.1 (Coupling-Two) and Table 3.2 (Coupling-Three).

The EIR plots support this finding. At SCR = 1.8, the EIR peak reaches 4.8 with a phase near −89°, indicating high risk of instability. When SCR increases to 1.9, the peak falls to 3.1 with a phase near −71°, which reflects faster damping recovery.

Figure 3.24(d) confirms this using the Generalised Nyquist Criterion. At SCR = 1.8, the curve forms a loop around (−1, 0). At SCR = 1.9, a similar loop appears with a larger margin, meaning a small change in network strength shifts the system toward or away from unstable operation. However, SCR does not show the cause of the resonance. IR and EIR show the frequency of interaction, the strength of coupling, and the level of oscillatory risk. These measures therefore give clearer direction for improving damping in converter-based grids.

In summary, SCR does not provide a dependable measure of strength or interaction in networks with many converters. It does not capture resonance-driven behaviour that governs oscillatory response. Correct judgement requires IR and EIR, which include converter behaviour and network impedance across frequency. The weakness of SCR becomes more apparent as converter count rises, as discussed in Chapter 4.

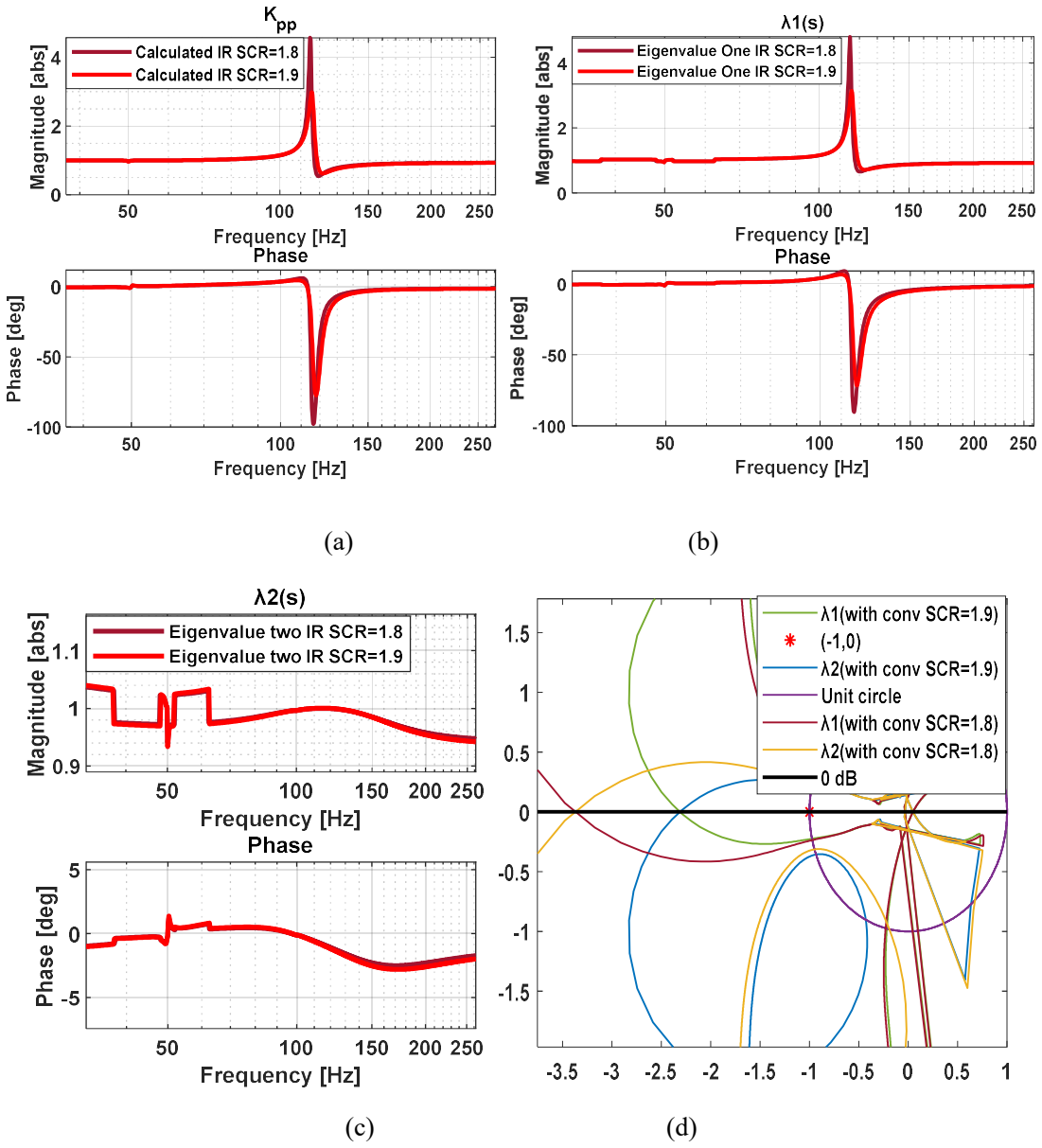

Figure 3.24: SCR Correlation with IR and EIR in Interaction factor for Coupling Two PV

3.10 Summary

This chapter introduced a method to study how a distant converter affects the network and how this changes the stability of an AC system with two VSC units. The goal was to explain

how the behaviour of one converter alters the impedance seen by the other and how this link shapes stability. Two measures were used: the IR and the EIR. These tools showed how control settings and grid strength change the terminal response of the local converter. The analysis focused on the terminal of the local converter, without including its own dynamics in the interaction path.

The study first confirmed the impedance results and checked that frequency-domain and time-domain responses matched. Then, different cases were tested to examine the effects of converter control and grid strength. The results showed how stability changed as the interaction between the converter and the network became stronger.

When the remote converter used GFL control with PV mode, its impact on the network grew, especially in weak grids. In this case, IR and EIR increased and changed the impedance seen at the local converter terminal. The PLL made this effect stronger. Faster PLL action further reduced stability by reducing phase margin. Lower active-power transfer also reduced stability when the remote converter worked as an inverter. These cases led to impedance shifts and higher risk of oscillations around 80-150 Hz. Weak grids showed the highest risk because high IR and EIR made the system more sensitive. Strong grids had lower IR and EIR and better stability. As IR and EIR rose, magnitude moved away from one and phase moved away from zero. EIR also separated positive- and negative-sequence effects, where larger $\lambda 1$ and $\lambda 2$ reflected stronger influence in each sequence.

When the remote converter used GFM control, stability improved. The GFM unit held voltage, fixed its terminal impedance, and limited disturbance spread to the network. As a result, IR and EIR dropped and oscillations reduced. The benefit was greatest in weak grids, where the GFM unit kept impedance nearly constant. Strong grids also improved, though the benefit was smaller because grid support was already high. In general, PV mode gave the highest IR and EIR, followed by PQ, and GFM gave the lowest.

Overall, the results showed that converter-network interaction and stability depend on grid strength, converter control method, and frequency range. Frequencies above the fundamental were the most important. For GFL systems in weak grids, slower PLL action and careful control tuning reduced IR and EIR, lowered interaction, and improved stability.

Chapter 4: Multiple Converter-Network Interactions and the Impact of Control Systems

4.1 Introduction and System Configuration

Chapter 4 examines the dynamic behaviour of several converters connected to a common AC network and evaluates how their control schemes jointly affect stability, while providing deeper analytical insight into the underlying interaction mechanisms and their broader implications for converter-dominated grids. Building on the earlier analysis involving two converters, a three-converter arrangement is introduced to better reflect the complexity present in converter-dominated power systems and to capture additional layers of coupling that arise when multiple control loops operate simultaneously. The topology illustrated in Figure 4.1 is chosen to offer a clear representation while retaining sufficient detail to capture multi-point interactions without introducing unnecessary modelling burden, thereby enabling precise interpretation of dynamic responses. This structure supports careful examination of interaction phenomena across different operating conditions and facilitates rigorous evaluation of stability characteristics under varying control objectives. The inclusion of converters operating under different approaches-GFM and GFL with PV and PQ objectives-effects realistic operating conditions and enables evaluation of how diverse control philosophies operate within a shared network environment. Furthermore, through impedance-based analysis, including the IR and EIR approaches, the framework allows assessment of stability margins and identification of dominant interaction paths, providing a deeper understanding of the behaviour of future converter-dominated networks and strengthening the theoretical foundation for subsequent investigations.

- **System Configuration**

In this structure, local, intermediate, and remote converters are linked through transmission paths with different electrical properties, allowing examination of the effects of separation distance, network strength, and coupling on system dynamics under representative operating scenarios. This configuration is selected because it reproduces important characteristics observed in practical grids, including interaction routes formed by network impedances, variations in electrical proximity, and oscillatory behaviour driven by control dynamics.

Unequal line impedances also allow investigation of resonance phenomena and power exchange patterns that are not visible in simplified or perfectly balanced systems, while supporting the study of coordinated control strategies by showing how disturbances travel across interconnected nodes and influence overall performance.

Figure 4.1 illustrates the network topology of multiple interconnected converters. The green region, representing remote and middle converters, is integrated with the network section through shared electrical interfaces, highlighting their coordinated interaction. This coupling influences system dynamics and propagates control effects toward the local converter, depicted in a distinct colour, thereby emphasizing its operational independence and localized response characteristics.

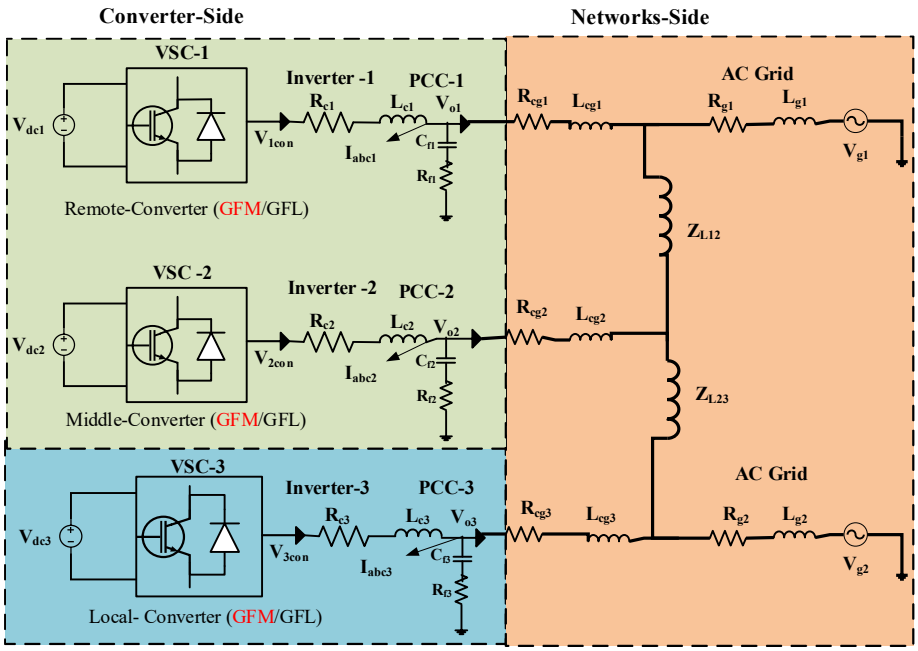

Figure 4.1: Network Topology of Multiple Connected Converters

As shown in Figure 4.1, the converters are placed at PCC-1 (remote), PCC-2 (middle), and PCC-3 (local):

- Local Converter (VSC-3): Its stability is assessed by considering its own characteristic and the rest of the system it is connected.
- Middle Converter (VSC-2): Its electrical location is relatively close to the Local Converter whose stability is under assessment. It is expected that the Middle Converter will have significantly influence on the stability of the Local Converter.
- Remote Converter (VSC-1): Located furthest from the Local Converter and is expected to have relatively minor influence on the stability of the Local Converter.

As in Chapter 3, both GFM and GFL control modes are studied for every converter. This allows direct comparison of the control methods in a network that contains several converters. The focus is on how interaction among the converters shapes the overall behaviour of the system and how each control approach affects stability.

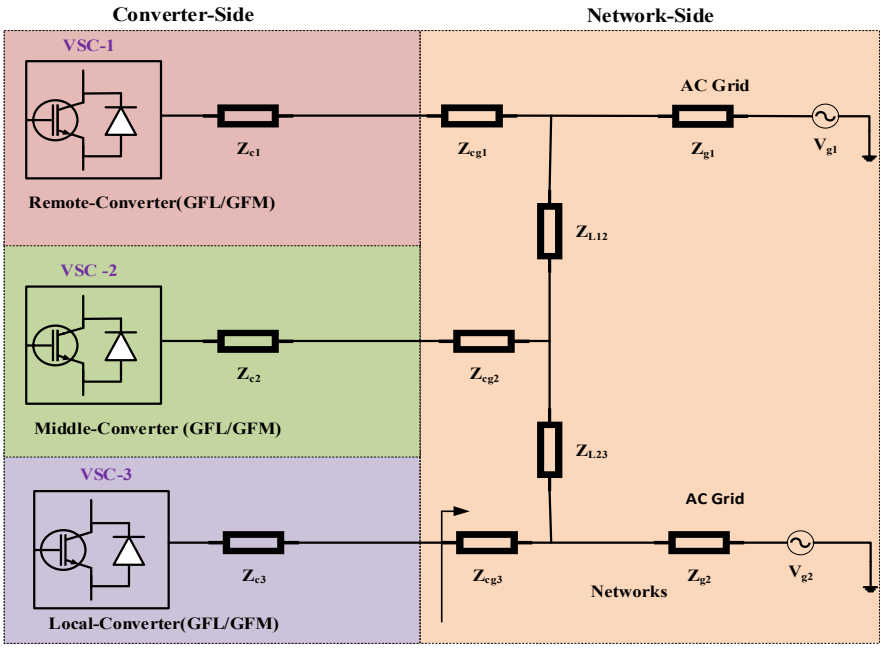

(a)

A simplified equivalent AC network is adopted, as shown in Figure 4.2(a). The three converters are connected through transmission impedances Z_{12} and Z_{23}, while the grid is represented by impedances Z_{g1} and Z_{g2}. Each connection captures the combined effects of line resistance, line inductance, and transformer inductance. This representation enables clear analysis of how converter location and network impedance influence interaction strength and system stability.

Figure 4.2(b) extends the model to an arbitrary number Nof converters. Each converter is represented by its Thevenin equivalent and internal impedance, connected in sequence through network impedances $Z_{(i,i+1)}$ and terminated by the grid impedance Z_g. This general form offers several advantages. It supports analysis with any number of converters without changing the modelling structure. It allows independent examination of converter-network interactions. It clearly defines the total impedance observed by each converter as the sum of its own impedance and neighbouring network elements. In addition, both grid-forming and grid-following operation can be represented through appropriate parameter selection.

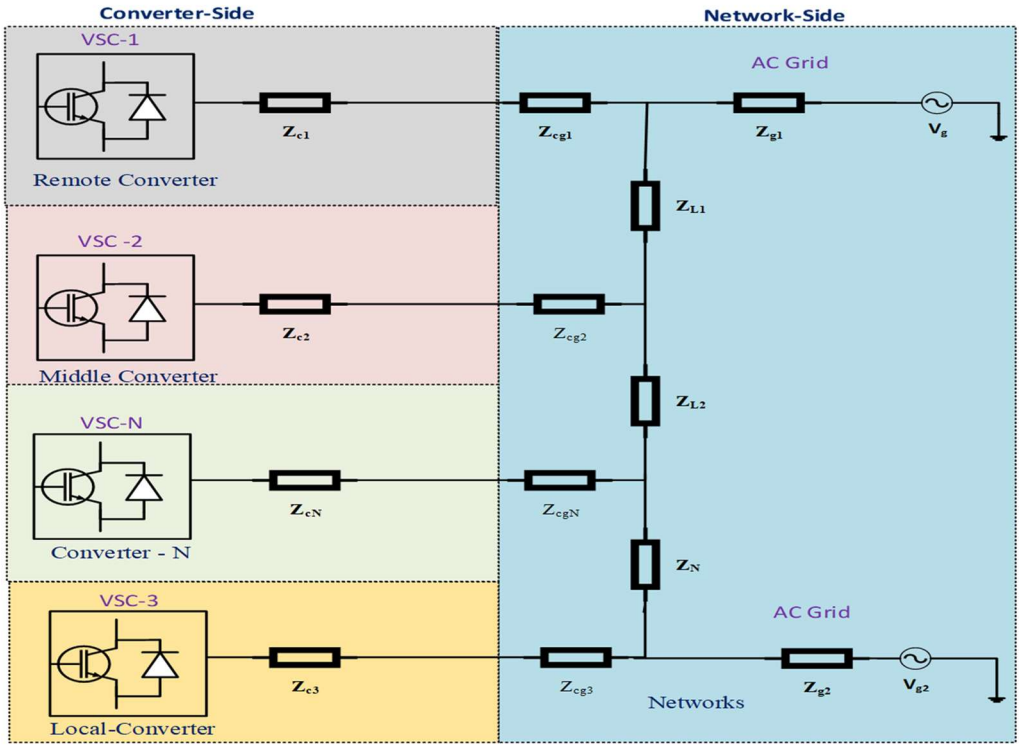

(b)

Figure 4.2: Topological Representation of Multi-VSCs (Three-N) Integrated into an AC Network

By presenting both a three-converter case and a general formulation, the model provides a consistent framework for stability analysis in converter-dominated systems while preserving analytical clarity

4.2 Interaction of Multiple Converters and Network Analysis

The addition of multiple converters within the connected network (seen by the Local Converter VSC-3) significantly modifies the network impedance profile, creating complex resonances and introducing potential instability modes [41]. The IR and EIR metrics, introduced in Chapter 3, are used as primary tools to analyse converter interaction. IR quantifies the contribution of a converter's impedance relative to the total terminal impedance, reflecting its influence on local stability. In the multi-converter configuration, IR is evaluated for VSC-1 and VSC-2 to determine their impact on the stability of VSC-3. EIR extends this approach by identifying network-wide resonant modes through the eigenvalues ($\lambda 1$ for positive sequence and $\lambda 2$ for negative sequence) of the MIMO impedance matrix, enabling precise identification of critical frequencies.

4.3 Impedance Analysis of AC Networks with Multi-VSCs

Based on the structure shown in Figure 4.2, the impedance observed at the terminal of VSC-3 is represented by the equivalent network in Figure 4.3. This model is used to analyse the effect of the surrounding system on the local converter.

The total system impedance see at the VSC-3 connection point is defined as:

$$Z_{conv+network} = [(Z_{cg1} + Z_{vscon1}) \parallel Z_{g1} + Z_{L12}] \parallel (Z_{vscon2} + Z_{Lcg2}) + Z_{L23} \parallel Z_{g2} + Z_{cg3} \tag{4.1}$$

where Z_{vscon1} and Z_{vscon2} represent the impedances of VSC-1 and VSC-2, and symbol $\parallel$ indicates a parallel connection. This impedance includes both line and converter effect and therefore reflects the complete dynamic behaviour seen by VSC-3.

Separately, the network impedance excluding converter dynamics (i.e., when VSC-1 and VSC-2 are disconnected or treated as passive) is expressed as:

$$Z_{network} = [(Z_{g1} + Z_{L12}) \parallel Z_{cg2} + Z_{L23}] \parallel Z_{g2} + Z_{Lcg3} \tag{4.2}$$

This value captures only the passive grid and line properties, without any control interaction. The effect of converters dynamics on the network impedance is quantified using the IR, as previously defined, i.e.:

$$IR_n = \left(\frac{Z_{conv+network}}{Z_{network}}\right) \tag{4.3}$$

The index n indicates the number of converters included in the study. This ratio helps measure how converters modify the apparent impedance seen at the local terminal and extends the impedance-based concept to multi-converter systems.

To study effects across different frequencies, the EIR is used:

$$EIR = \text{Eigenvalue}(IR_n) \tag{4.4}$$

The two main eigenvalues, λ_1 and λ_2, represent the dominant positive-sequence and negative-sequence behaviour. Their change with frequency highlights resonance points and stability concerns. Tracking these values gives clear information about the strength of interaction and the risk of oscillation in the network.

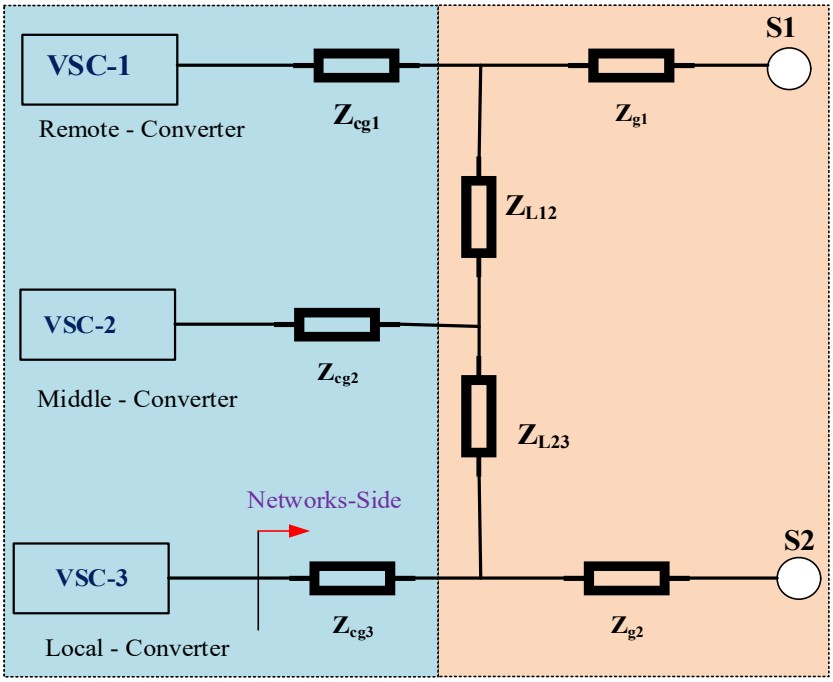

Figure 4.3: Equivalent-Impedance Model of Middle and Remote Converters in AC Network

4.3.1 Multiple Converters -Network Interaction: Impedance Results

This section examines the impedance behaviour of multiple converters under PV and PQ outer-loop strategies in both GFM and GFL operating modes. Two grid-connection conditions are considered: a strong grid (Coupling-One) and a weak grid (Coupling-Two). The parameters for these cases are listed in Table 2.1 and 4.1.

The study uses impedance-based measures, namely the IR and the EIR, across the frequency range of 1-1000 Hz. Particular attention is given to the 50-250 Hz band, where oscillatory behaviour is most likely to emerge. In contrast to the single-converter analysis in Chapter 3, this section considers converter-to-converter Interaction, which becomes critical when multiple converters operate in close electrical proximity. With three converters and three outer-loop control modes (PV, PQ, and GFM), a total of nine configurations is assessed. For each case, resonance frequencies and impedance characteristics are determined. These results allow direct comparison of how control choice and grid strength shape the impedance behaviour of the multi-converter system.

Table 4.1: The system parameter for weak and strong Coupling

Parameter	Coupling One	Coupling Two
Rc, Rc2	0.01pu,0.01pu	0.01pu,0.01pu
Lc, Lc2	0.1pu, 0.1pu	0.1pu, 0.1pu
L_1	0.1pu	0.3pu
R_g	0.0167pu	0.0167
R_{g1}	0.0167pu	0.0167
L_g	0.2pu	0.36pu
L_{g1}	0.22pu	0.38pu
L_{cg1}	0.16pu	0.25pu
L_{cg2}	0.18pu	0.26pu
Lcg3	0.16pu	0.25pu
R_{cg1}	0.016pu	0.0167pu
R_{cg2}	0.0167pu	0.0167pu
Rcg3	0.0167pu	0.0167pu
R_v	0.01pu	0.0167pu
L_v	0.1pu	0.2pu
SCR	3.25pu	1.92pu

4.3.1.1 Coupling-One Simulation Results

Figures 4.4(a)-(c) show the impedance behaviour under different control modes applied to VSC-1 and VSC-2. The plots display how the IR and its EIR change with frequency when each unit operates in either PV or PQ mode.

In Figure 4.4(a), the PV-PV case gives a noticeable rise in the IR around 135-150 Hz, where the magnitude goes above 1.4 and the phase drops below −30°. This increase reflects a higher level of converter-to-grid interaction for this control pairing. The PQ-PQ and PV-PQ cases show smaller variation, although all cases present a clear change close to 115 Hz. The results show that the control choice directly shapes the impedance curve. Due to the strong grid, the interaction does not develop into a resonant effect.

Figures 4.4(b) and 4.4(c) give the eigenvalue view of the IR. The first EIR, $\lambda_1(s)$, shows the largest change in the PV-PV case, where its magnitude and phase vary more over the studied range than in the PQ-PQ and PV-PQ cases. This behaviour points to a more visible EIR shift under PV-PV control. The second eigenvalue, $\lambda_2(s)$, shows smaller changes and remains less affected by frequency. Its role in the overall EIR variation is therefore limited compared with $\lambda_1(s)$. These plots make clear that the choice of control mode affects how impedance spreads across the two EIR, with the PV-PV case showing the most notable change and the other combinations producing weaker deviations.

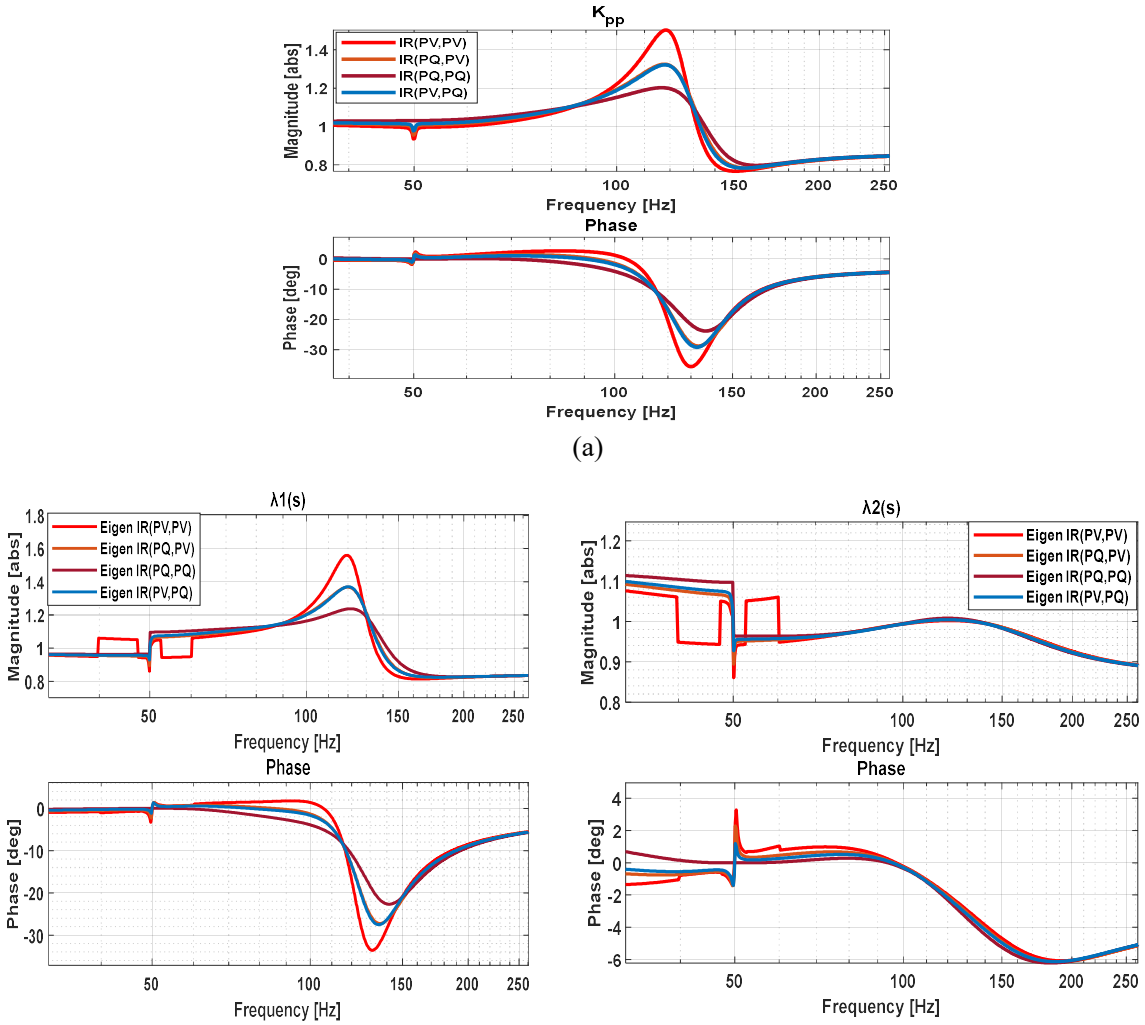

(a)

(b) (c)

Figure 4.4: (a) IR and (b, c) Eigenvalue of IR variations Under PQ and PV Control of Coupling One Parameter

4.3.1.2 Weak-Grid (Coupling Two) Simulation Results

Under the coupling two-network condition, the terminal impedance measured at the VSC-3 connection point is illustrated in Figure 4.5, while the corresponding IR and eigenvalue-based IR responses are presented in Figure 4.6 for different control configurations.

In Figure 4.5, the PV-PV case of $Z_{network+conv}$ exhibits a distinct resonance near 110 Hz. At this frequency, the impedance magnitude exceeds 2p.u., and the phase approaches 180°. This behaviour resembles a negative-resistance effect, caused by the strong interaction between the converter current loops and the reactive behaviour introduced by PV control, along with further interaction with the surrounding network path.

For the other configurations (PQ, PV), (PV, PQ), and (PQ, PQ) the resonance decreases in magnitude in the order listed, which is consistent with the IR and eigenvalue results in Figure 4.6. The interaction value of IR and EIR directly affects the resonance peaks, as determined by the specific control type. The IR plots in Figures 4.6(a) and (b) confirms this behaviour. In the PV-PV case, the IR magnitude rises above 2.1, while the phase extends beyond +90°. As highlighted in Chapter 3, any positive-phase excursion, regardless of IR magnitude, signals high sensitivity to impedance changes and indicates vulnerability to oscillatory interactions. This explains the strong resonance in the PV-PV case.

For mixed configurations (PQ-PV or PV-PQ), the resonance peak is reduced compared with PV-PV but remains significant. In particular, the PQ-PV case demonstrates a strong response because the PV-controlled converter nearest to VSC-3 increases sensitivity to impedance variations, producing higher resonance peaks. In these conditions, IR magnitudes approach 3, with phase values near –100°, suggesting a high risk of oscillatory behaviour. By contrast, the PQ-PQ configuration introduces the least disturbance, since IR values remain close to unity across the frequency range.

The eigenvalue IR in Figures 4.6(c) and (d) provides additional clarification. The dominant eigenvalue is associated with the positive-sequence channel and coincides with the 110 Hz resonance frequency, consistent with the PV-PV impedance variation observed in Figure 4.5. This confirms that positive-sequence dynamics dominate the resonance mechanism. Conversely, the negative-sequence eigenvalue shows only small deviations, with minor oscillations near 50 Hz that remain insignificant compared with the positive-sequence response.

When comparing network strength, it is evident that under strong-grid conditions, the effect of VSC-1 and VSC-2 on the impedance at VSC-3 is minimal. However, under weak-grid conditions, the combined network-converter impedance grows and develops pronounced resonant peaks. This reduction in damping indicates the potential for instability, which will be examined further in the following subsections.

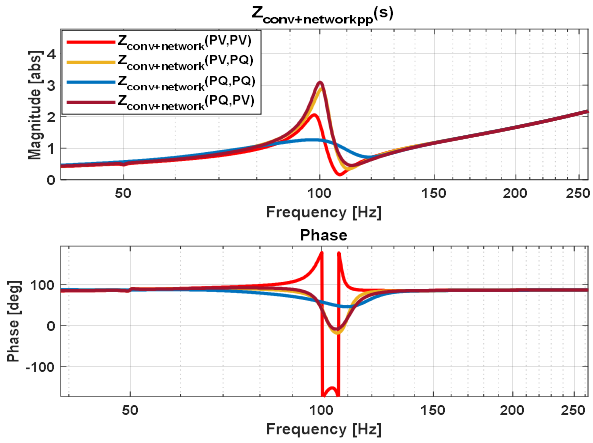

Figure 4.5: $Z_{conv+network}$ variations in GFL Control Under Coupling Two Parameters

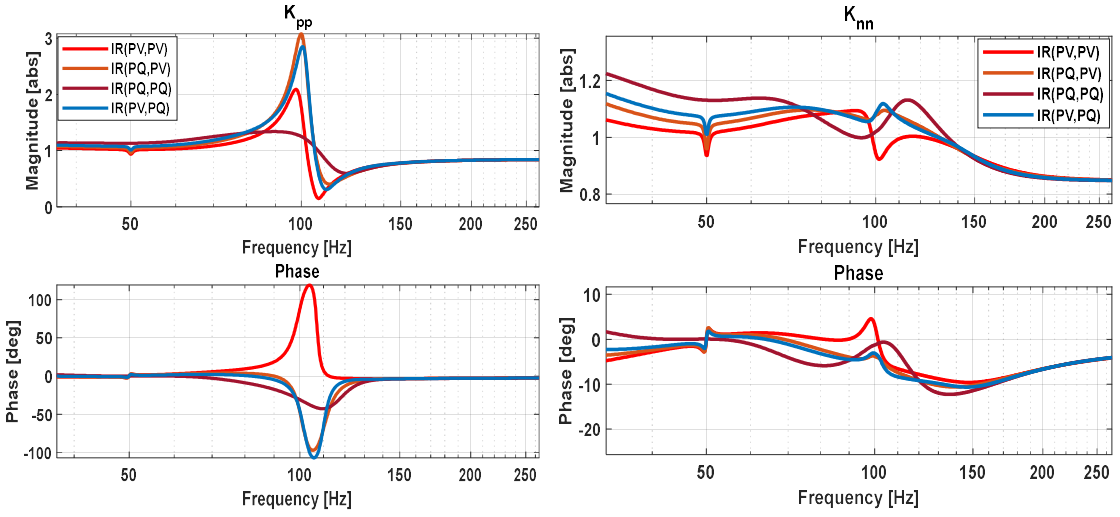

(a) (b)

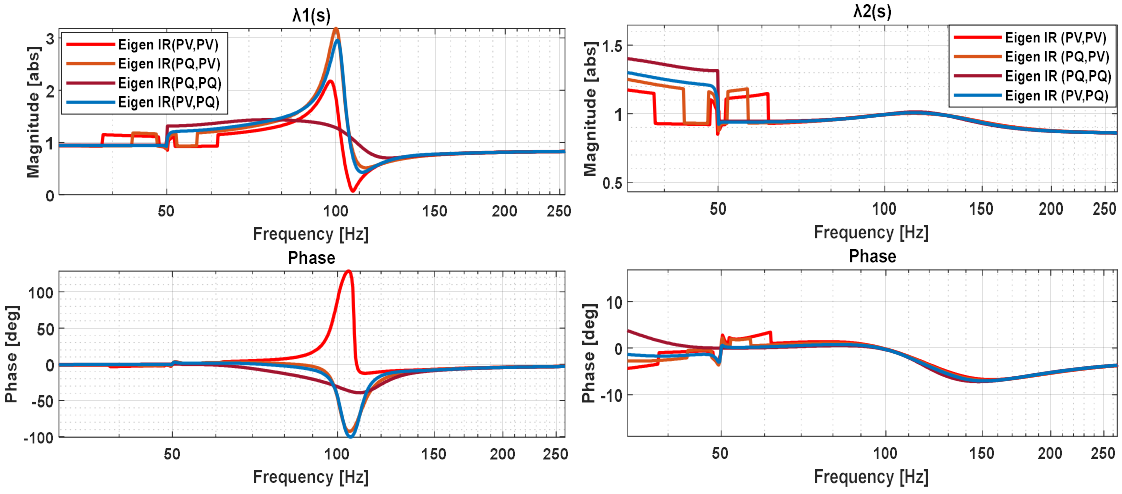

(c) (d)

Figure 4. 6: (a, b) IR and (c, d) EIR variations in GFL Control Under Coupling Two Parameter

4.3.1.3 GFM System Performance Under Coupling-Two

Figure 4.7 shows that the GFM-PV configuration produces the strongest impedance interaction under weak-grid conditions in comparison Figure 4.6(without GFM). The IR exhibits a pronounced peak around 110 Hz, with the phase decreasing below −50°. This behaviour arises because the GFM converter, while providing a voltage and frequency reference similar to a synchronous machine, interacts unfavourably with the PV-controlled converter. In this arrangement, both converters attempt to regulate voltage within overlapping frequency ranges, which intensifies the exchange of power and amplifies oscillatory dynamics, leading to the sharp variation observed in the IR. In addition, the remote GFM converter contributes limited damping support compared with a configuration where the middle converter operates in GFM mode. As a result, its positive influence on the overall impedance response is weaker, further worsening the interaction in this configuration.

The EIR results in Figures 4.8 (a) and (b) further clarifies this effect. The dominant eigenvalue follows the impedance IR behaviour for the GFM-PV case, showing that the interaction peak is linked to the main positive-sequence mode. The second eigenvalue remains nearly unchanged across the range, indicating that negative-sequence effects are small and that the positive-sequence path governs the observed behaviour.

The effect of converter location and control assignment becomes clear when comparing different operating cases. A GFM converter positioned at a central node improves energy exchange between network sections and strengthens voltage regulation under weak conditions. When PQ converters are located at intermediate nodes, they reduce oscillatory active power transfer and limit converter-network interaction, thereby complementing the central GFM unit. In contrast, assigning PV control to the central node while placing the GFM converter at the network boundary increases interaction magnitudes and enhances oscillatory behaviour due to regulation conflicts.

Comparing Figures 4.7 and 4.8 with Figure 4.6 shows that a suitably placed GFM converter significantly reduces interaction value of IR and EIR over the studied range. The improvement is most visible when the GFM converter is located at the central point in the network.

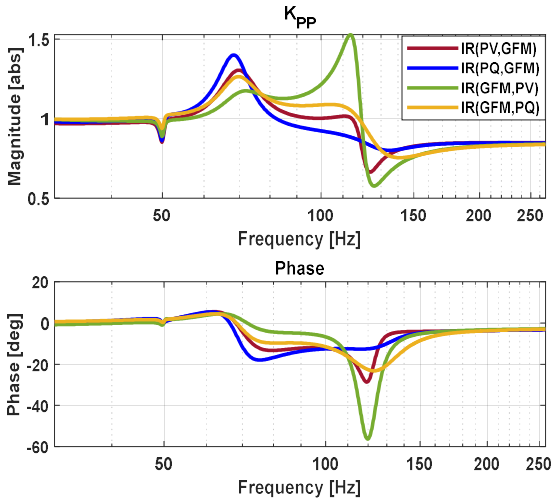

Figure 4.7: IR in GFM and GFL Control Under Coupling Two Parameters

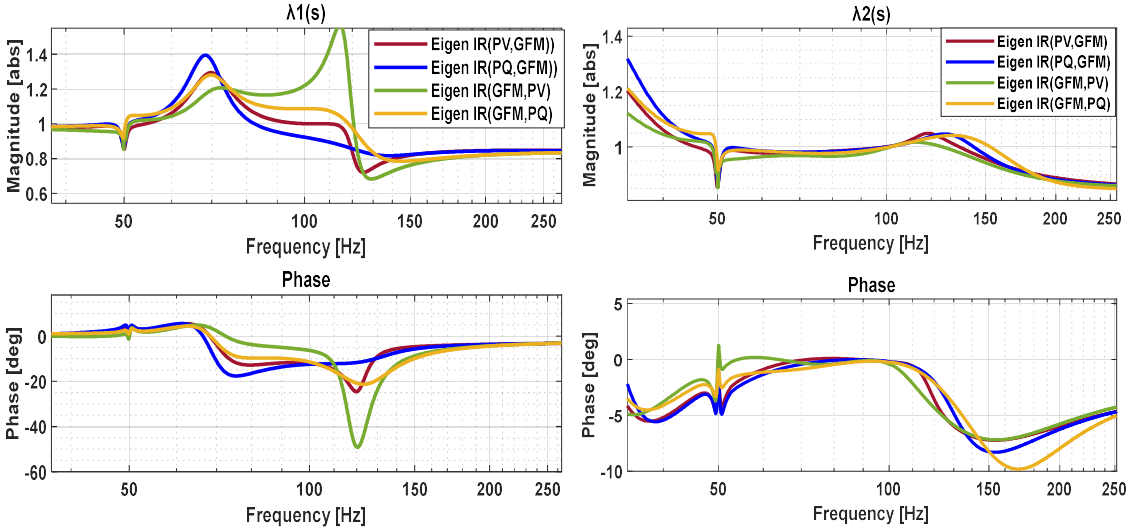

(a) (b)

Figure 4.8: (a) and (b) EIR changes in GFM and GFL Control Under Coupling Two Parameters

4.4 Stability Analysis for Multi-VSCs

The small-signal stability of the three-terminal converter system is evaluated under different network conditions using the GNC. This method highlights the frequency ranges where potential instability may appear and identifies the interaction modes that govern the converters' dynamic behaviour under varying control parameters and impacts on the local converter (VSC-3).

4.4.1 Stability Assessment Under Coupling-One

Under strong-grid conditions, both the Input IR and the EIR remain small, which indicates very limited interaction between the converters and the network. This means the converters interact weakly with the grid, and control settings have little influence on stability.

Figure 4.4 shows the Nyquist paths for four control settings: (PV, PV, PV), (PQ, PV, PV), (PQ, PQ, PV), and (PV, PQ, PV). All paths stay on the stable side and do not circle the critical point (−1, 0). The GNC requirement is satisfied, and oscillations do not appear.

Figure 4.4(a) shows that the IR has only small changes in magnitude and phase, which keeps oscillatory effects low. Figure 4.4(b) shows that the dominant eigenvalue $\lambda_1(s)$ changes slightly as EIR varies. Figure 4.4(c) shows that $\lambda_2(s)$ adds a small effect only.

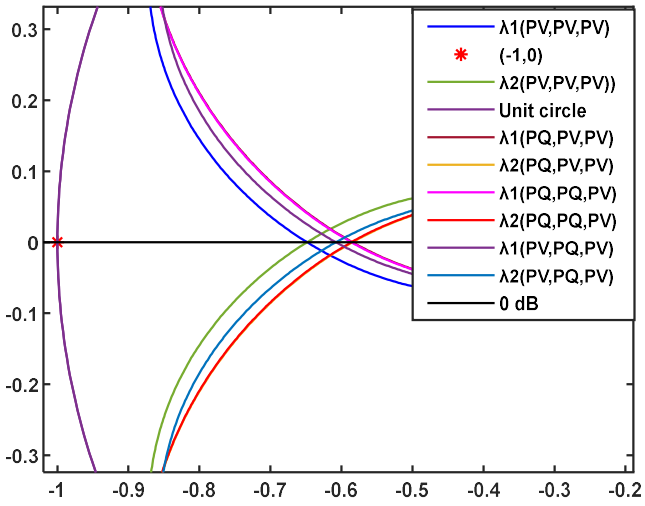

Figure 4.9: Nyquist Stability Analysis of GFL Control Mode in a Three-Converter System

Overall, the analysis demonstrates that, under strong-grid conditions, converter-grid interaction does not introduce resonance. All control choices maintain stable behaviour, as confirmed by both IR and EIR characteristics and the Nyquist plots.

4.4.2 Stability Assessment Under Weak-Grid Coupling

Weak-grid conditions significantly affect the stability characteristics of converter-dominated systems. The increased grid impedance enhances the coupling between converters, reduces effective damping, and raises the susceptibility to resonance, leading to a higher risk of

instability. Figure 4.10 illustrates the Nyquist eigenvalue trajectories for different control configurations under weak-grid operation.

For configurations such as (PV, PV, PV) and (PV, PQ, PV), the dominant eigenvalue moves close to or circles the critical point (−1, 0). This behaviour indicates possible oscillation under the GNC. In these cases, IR grows, and the phase shifts into a negative-resistance area. This outcome is linked to PV control action under low grid stiffness: strong voltage regulation can reinforce oscillation instead of damping it, as seen in Figure 4.6(a) for different K_{pp} values of IR.

The instability risk becomes particularly severe when PV control is applied to converters located close to each other, for instance when both VSC-2 and VSC-3 operate with PV control. In such placements, the control actions strongly interact with the grid dynamics, introducing additional phase lag and diminishing damping, as also illustrated in Figure 4.6(a). These results demonstrate that, under weak-grid conditions, the stability of PV-controlled converters is highly sensitive to parameter settings and the electrical position of the converters. Effective stability therefore requires not only careful tuning of control parameters but also consideration of the surrounding network impedance and careful placement of PV control.

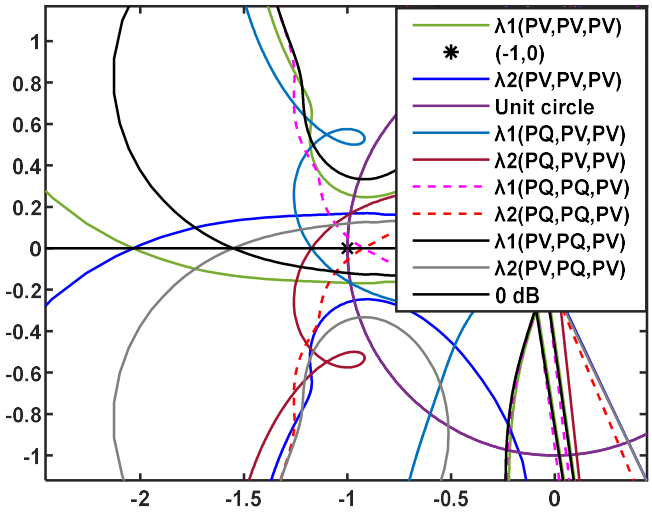

Figure 4.10: Nyquist Stability Analysis of GFL Control Mode in a Three-Converter System

4.4.3 Stability Implications of GFM Integration in M-VSCs

Adding GFM control to a network with several converters can improve stability, but it may also introduce new interactions. Figure 4.11 compares different positions of GFM and GFL units under weak-grid conditions for Coupling-Two. The results show that the stabilising benefit of GFM depends on its location and the control mode of nearby units.

When the GFM unit is placed at a remote terminal, as in the (GFM, PV, PV) case, the eigenvalue paths in Figure 4.11 move close to the stability boundary. This behaviour aligns with the impedance in Figure 4.8(a), which shows a pronounced peak around 80-120 Hz. Here, the GFM's voltage control interacts with the fast voltage loops of the adjacent PV converter, increasing resonance rather than reducing it. As a result, the eigenvalue paths form loops, indicating reduced damping. The effect is more pronounced in weak grids with low IR and EIR value, where the emulated inertia of the GFM interacts unfavourably with the rapid inner-loop dynamics of the PV converters[87].

A similar trend appears in the (PV, PV, GFM) case. Two closely coupled PV units drive strong impedance variation and produce oscillations around 80-120 Hz, independent of whether the third unit operates as GFM or GFL. This shows that PV-PV coupling can dominate the response in weak grids and must be considered when assigning control modes.

Placing the GFM unit at the centre, shown in the (PQ, GFM, PQ) arrangement, produces better damping. The eigenvalues remain clearly separated from the critical boundary, and the impedance in Figure 4.8 (a) has no sharp peak in the 80-120 Hz range. Central placement spreads the stabilising effect through the network and avoids local resonance build-up.

Intermediate layouts, such as (PQ, PQ, PV) or (GFM, PQ, PV), show adequate stability but still display noticeable sensitivity to grid strength. Their impedance plots indicate that tuning of control loops is required to keep sufficient damping.

In summary, both the Nyquist and impedance results show that stability in weak multi-converter grids depends on control mode placement as well as control type. Figures 4.8 and 4.11 highlight that converter-converter and converter-grid interactions shape resonance behaviour, with the most critical effects near 80-120 Hz, mainly affecting VSC-3. Proper GFM positioning, especially at a central point in the network, offers stronger performance under weak-grid conditions.

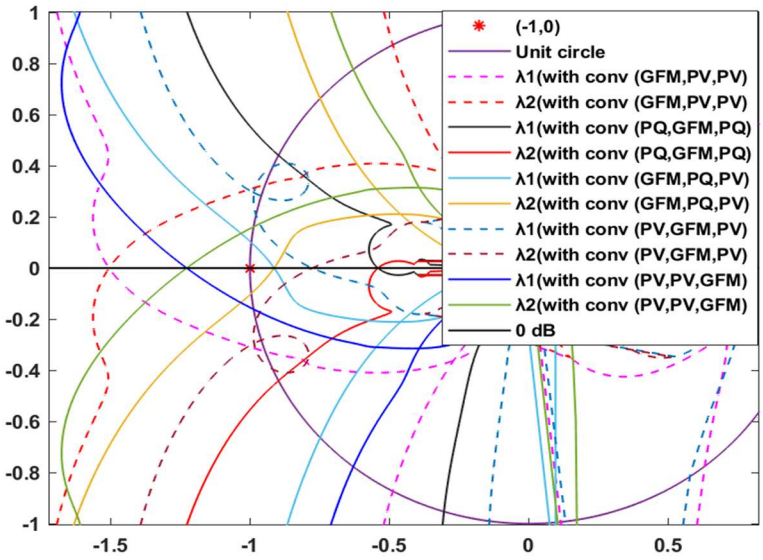

Figure 4.11: Nyquist Stability Analysis of GFM Control Mode in a Three-Converter System

4.4.4 Impact of Power flow Direction on System Stability

The previous analysis considered the case where all converters operated in inverter mode, exporting power from DC-side to AC-side. This subsection examines the alternative configuration where the remote converter functions as a rectifier and the central converter as an inverter, both under GFL control in a weak network condition

Figure 4.12(a) shows that in inverter operation a pronounced resonance occurs between 105 Hz and 115 Hz, with the IR magnitude approaching 3.0 and the phase dropping below −90°.This behaviour indicates strong interaction and limited damping. In rectifier mode the resonance is far smaller, the magnitude stays low, and the phase remains smooth. The response is therefore less reactive and the interaction between converter and grid is weaker in this case.

Figures 4.12(b) and 4.12(c) show the EIR results. In inverter mode one dominant mode reacts strongly in the same frequency range, and another mode follows with a smaller effect. In rectifier mode both modes stay well separated and remain damped across the full range. This confirms that rectifier operation limits modal interaction and keeps the dynamic behaviour in a stable region.

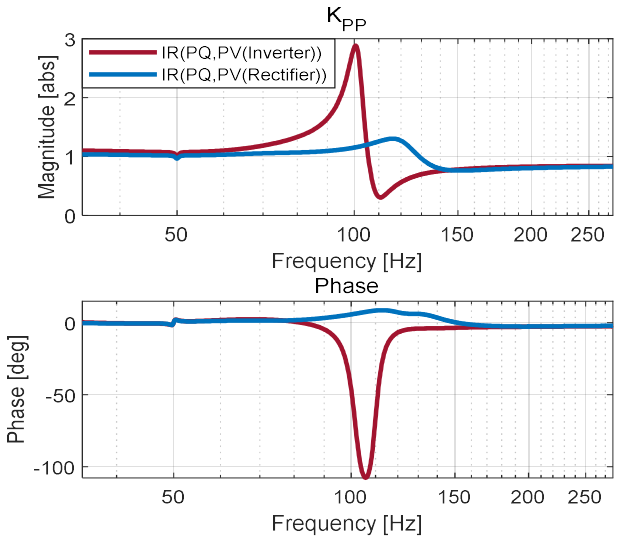

(a)

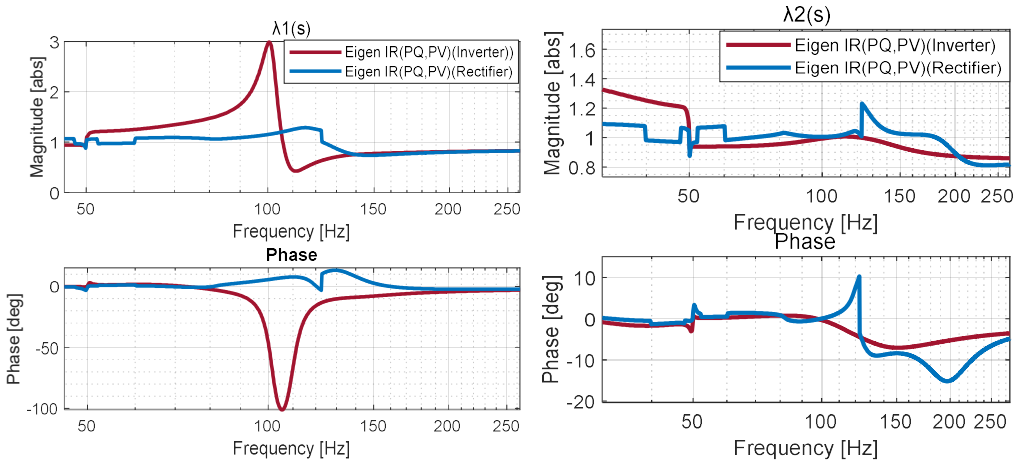

(b) (c)

Figure 4.12: IR (a) and EIR (b, c) changes Under GFL Control in Rectifier and Inverter Modes Under Coupling Two

Figure 4.13 presents the stability view. In inverter mode the eigen-paths encircled the critical point at (−1, 0), indicating unstable behaviour. In rectifier mode the paths remain well separated from the instability boundary, demonstrating stable performance under identical network and control settings.

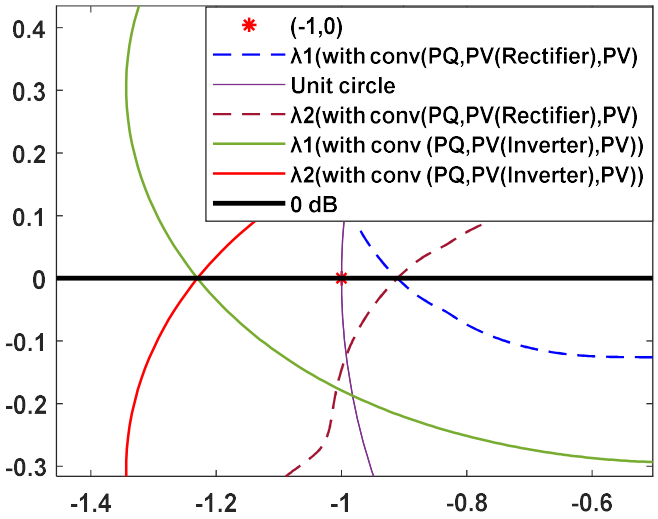

Figure 4.13: Nyquist Plots for Rectifier and Inverter Modes of a Three-Converter System Under Coupling Two Parameters

In short, these results demonstrate that the power-flow direction has a direct effect on converter-grid interaction. Inverter operation in a weak grid leads to strong oscillations and poor damping. Rectifier operation reduces resonance, improves damping, and keeps the dynamic response stable. This difference is linked to how each mode shapes the IR and EIR, and how the modes interact with the weak network.

4.4.5 Stability Outcomes of Muti-VSCs Control Configurations

Table 4.2 summarises the stability performance of the investigated control allocations under weak-grid conditions, drawing on the IR and EIR analyses presented in the preceding sections. The configurations are organised according to the control modes assigned to the remote, middle, and local converters, allowing a systematic assessment of how control selection and placement influence dynamic behaviour.

The results show that stability is governed not only by the chosen control strategy but also by its electrical location within the network. Configurations dominated by PV-controlled grid-following operation exhibit reduced damping due to strong voltage-regulation interactions. In particular, the PV-PV-PV case demonstrates pronounced oscillatory tendencies, as tightly regulated voltage loops amplify resonance through adverse phase characteristics.

The PV-PQ-PV configuration is marked as “instability observed,” which requires clarification. In this arrangement, the PQ-controlled converter alters the effective network

impedance seen by the two PV units, leading to mismatched dynamic responses. The outer PV controllers attempt to maintain voltage magnitude while the intermediate PQ unit injects fixed power, creating an interaction that shifts resonance frequencies and reduces phase margin. This mechanism explains the observed instability and justifies the classification reported in Table 4.2.

Improved behaviour is evident when power control dominates, as in PQ-PQ-PV, where reduced voltage stiffness mitigates interaction strength and enhances damping. Introducing a GFM converter further improves stability; however, the impact depends strongly on placement. When the GFM operates at the middle terminal, it establishes a robust voltage and frequency reference that electrically decouples the remote and local converters, suppressing resonance pathways and increasing stability margins. Conversely, locating the GFM at an outer terminal leaves the internal network section weak, limiting its stabilising influence.

Regarding the examiner's comment on GFM specification, this chapter employs an LPF-based droop-controlled GFM, as illustrated in Figure 2.9(b). This structure is selected because it provides a realistic representation of practical grid-forming behaviour while enabling clear interpretation of impedance characteristics. The low-pass filter shapes the frequency response, avoiding excessive control bandwidth that could otherwise introduce high-frequency interactions, thereby offering a balanced trade-off between dynamic support and robustness.

Overall, the findings confirm that the combination of control mode and electrical position determines stability outcomes, with a centrally located droop-controlled GFM delivering the most favourable performance under weak-grid conditions.

Table 4.2: Summary of Converter Control Interaction and Stability Impact for M-VSCs

Converter Interaction Type (Remote and Middle)	Local Converter Type	Impact on stability
PV-PV	PV	No significant improvement and highly unstable
PV-PQ	PV	Instability observed
PQ-PV	PV	No significant improvement
PQ-PQ	PV	Significant improvement
PQ-GFM	PV	Significant improvement
PV-GFM	PV	Stability is enhanced
GFM-PV	PV	Instability observed
GFM-PQ	PV	Stability is enhanced
PV-PV	GFM	Instability observed

4.5 IR/EIR Analysis with Varying Electrical Separation

This section examines how electrical separation affects converter interaction strength using the IR and EIR methods. These indicators measure how converters influence each other through the network. As their values increase, the coupling between converters becomes stronger, showing higher mutual influence.

The study considers three converters: remote (VSC-1), middle (VSC-2), and local (VSC-3), connected as defined Section 4.3. Four network configurations are defined as follows:

- Z_1: baseline network impedance excluded VSC-1 and VSC-2.
- Z_2: network included only VSC-1.
- Z_3: network included both VSC-1 and VSC-2.
- Z_4: network with only VSC-2 included.

The following IR are expressed:

$$IR_{21} = \frac{Z_2}{Z_1}, IR_{31} = \frac{Z_3}{Z_1}, IR_{32} = \frac{Z_3}{Z_2}, IR_{34} = \frac{Z_3}{Z_4} \quad (4.10\text{-}4.13)$$

Each ratio represents how one converter influences the impedance seen by another:

- IR_{21} shows the influence of VSC-1 on the impedance seen by VSC-3.

- IR_{31} was presented previously, indicating the impact of VSC1 and VSC2 on the impedance change seen by VSC3.
- IR_{32} shows the effect of VSC-2 on VSC-3 when VSC-1 is present.
- IR_{34} indicates the impact of VSC-1 on VSC-3 when VSC-2 is present.

Simulation results for different coupling impedances Z_{L23} and Z_{L21} are presented in Tables 4.3-4.6.

When both coupling impedances are 0.15pu (Table 4.3), IR magnitudes range between 1.04 and 1.76, and phase angles between $-4.3°$ and $-35°$. The corresponding EIR values indicate weak interaction, and both Nyquist and eigenvalue analyses confirm stability. For a PLL bandwidth of 30 Hz, the system remains stable within 80-130 Hz.

When $Z_{L23} = 0.1\,\text{pu}$ and $Z_{L21} = 0.2\,\text{pu}$ (Table 4.4), the interaction strength increases slightly, with $IR_{21} = 1.06$at $-5.7°$. This shows that small changes in electrical separation slightly modify the interaction path. Although the IR and EIR values rise, the system remains stable. Under coupled conditions ($Z_{L23} = 0.15$, $Z_{L21} = 0.15$) as in Table 4.5, the IR magnitude increases to about 2.7 with a phase of 136°. The higher IR and EIR values indicate strong converter-network coupling, leading to oscillation and instability. Nyquist trajectories confirm the loss of stability caused by resonance.

In the asymmetric case ($Z_{L23} = 0.1, Z_{L21} = 0.2$) shown in Table 4.6, IR_{21}reaches 2.9 at $-73°$. This higher interaction value results in instability through a different coupling path, while other impedance ratios remain within stable limits. This indicates that not all separation paths equally affect system stability.

Table 4.3: Simulation Results under Coupling-One Parameters in Frequency range 80-130 Hz with $Z_{L2} = 0.15$ *and* $Z_{L21} = 0.15$, PLL frequency: 30 Hz

Converter number	**IR**		**EIR λ_1**		**EIR λ_2**		**Nyquist (Stability Test Condition)**
	Magnitude	**Phase**	**Magnitude**	**Phase**	**Magnitude**	**Phase**	
Two - Converter (IR_{21})	1.04	$-4.3°$	1.04	$-4.2°$	1	$-1.3°$	stable
Three - Converter (IR_{31})	1.76	$-35°$	1.8	$-33°$	1.18	$-6°$	stable
Three - Converter (IR_{32})	1.32	$-28°$	1.36	$-27°$	1.1	$-3°$	stable
Three - Converter (IR_{34})	1.26	$-24°$	1.3	$-24°$	1	$-1.87°$	stable

Table 4.4 : Simulation Results under Coupling-One Parameters in Frequency range $Z_{L23} = 0.1$ *and* $Z_{L21} = 0.2$, PLL frequency: 30 Hz

Converter number	IR		EIR λ_1		EIR λ_2		Nyquist (Stability Test Condition)
	Magnitude	Phase	Magnitude	Phase	Magnitude	Phase	
Two - Converter (IR_{21})	1.06	-5.7^{o}	1.08	-5.9^{o}	1.008	-1.3^{o}	Stable
Three - Converter (IR_{31})	1.5	-28^{o}	1.56	-27^{o}	1.17	-3.35	stable
Three - Converter (IR_{32})	1.3	-26^{o}	1.34	-25^{o}	1	-1.8^{o}	stable
Three - Converter (IR_{34})	1.2	-21^{o}	1.2	-21^{o}	1	-0.7^{o}	stable

Table 4. 5: Simulation Results under Coupling-Two Parameters in Frequency range $Z_{L23} = 0.15$ *and* $Z_{L21} = 0.15$, PLL frequency: 30 Hz

Converter number	IR		EIR λ_1		EIR λ_2		Nyquist (Stability Test Condition)
	Magnitude	Phase	Magnitude	Phase	Magnitude	Phase	
Two - Converter (IR_{21})	1.26	-12.62^{o}	1.28	-20.7^{o}	1	-2.5^{o}	stable
Three - Converter (IR_{31})	2.6	122^{o}	2.7	136^{o}	1.2	-5^{o}	Unstable
Three - Converter (IR_{32})	1.59	121^{o}	1.63	137^{o}	1	-1.67^{o}	Unstable
Three - Converter (IR_{34})	1.9	120^{o}	2	132^{o}	1.1	-3.6^{o}	Unstable

Table 4.6: Simulation Results under Coupling-Two Parameters in Frequency range $Z_{L23} = 0.1$ *and* $Z_{L21} = 0.2$, PLL frequency: 30 Hz

Converter number	IR		EIR λ_1		EIR λ_2		Nyquist (Stability Test Condition)
	Magnitude	Phase	Magnitude	Phase	Magnitude	Phase	
Two - Converter (IR_{21})	2.7	-73^{o}	2.9	-68^{o}	1.03	-2.8^{o}	Unstable
Three - Converter (IR_{31})	2.1	-102^{o}	2.2	-107^{o}	1.15	-5.6^{o}	stable
Three - Converter (IR_{32})	1.6	-97^{o}	1.67	-104^{o}	1	-3^{o}	stable
Three - Converter (IR_{34})	1.4	-98^{o}	1.5	-106	1	-1.5^{o}	stable

Figures 4.14 and 4.15 summarise the IR magnitudes and phase angles for different electrical separations. Stable conditions occur when IR magnitudes are between 1.04 and 1.76 with phase angles between $-4.3°$ and $-28°$. Even when interaction values increase slightly, stability can still be maintained within this range. When IR magnitudes exceed 2.6 and phase

angles shift to large positive values (around 120°-122°), resonance amplification occurs, leading to reduced damping and instability.

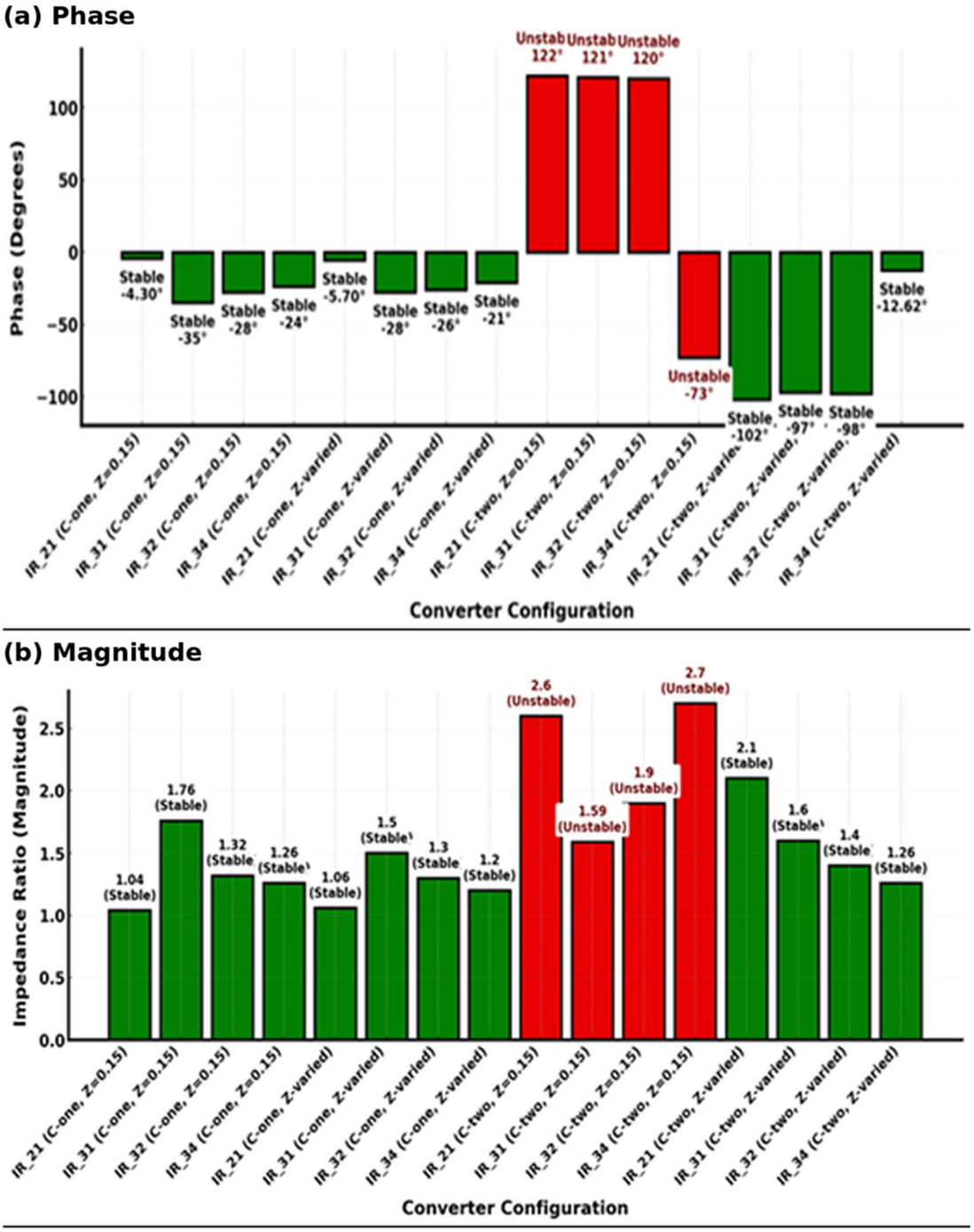

Figure 4.14: IR (a) Phase and (b) Magnitude and Stability Across Various Converter Configurations Illustrated Using Bar Graph Representation

In summary, red areas in the figures indicate strong interactions and instability, while green areas represent weak interactions and stable operation. Positive phase angles are consistently associated with instability, regardless of IR magnitude. As IR values increase, both magnitude and phase must be carefully observed.

The IR method provides a clear and direct way to assess converter-network interaction in multi-converter systems. High IR values with large positive phase shifts indicate strong coupling, resonance, and instability. The results confirm that converter-network interaction strength and overall stability depend on both electrical separation and control allocation. Maintaining stable operation in converter-based AC grids requires careful selection of converter placement, operation, and control modes to minimise interaction and preserve stability margins.

4.6 Converter Impedance Reshaping

In multi-converter AC networks, especially under weak-grid conditions, adverse impedance interactions between converters and the surrounding network can cause resonance and instability. These interactions often appear within specific frequency ranges, such as 90 Hz and 130 Hz. A possible method to mitigate such behaviour is impedance reshaping through carefully designed outer-loop control. By modifying the frequency-dependent behaviour of the converter's output impedance, the resonant peaks are reduced, the IR and EIR are improved, and the system damping increases, leading to enhanced dynamic performance and small-signal stability is strengthened across the operating range.

4.6.1 Impedance Reshaping in GFL Converters

The modified outer-loop control structures for GFL converters under PV and PQ modes are shown in Figure 4.15. In both modes, the dq -axis current references are extended with additional components from the reshaping mechanism.

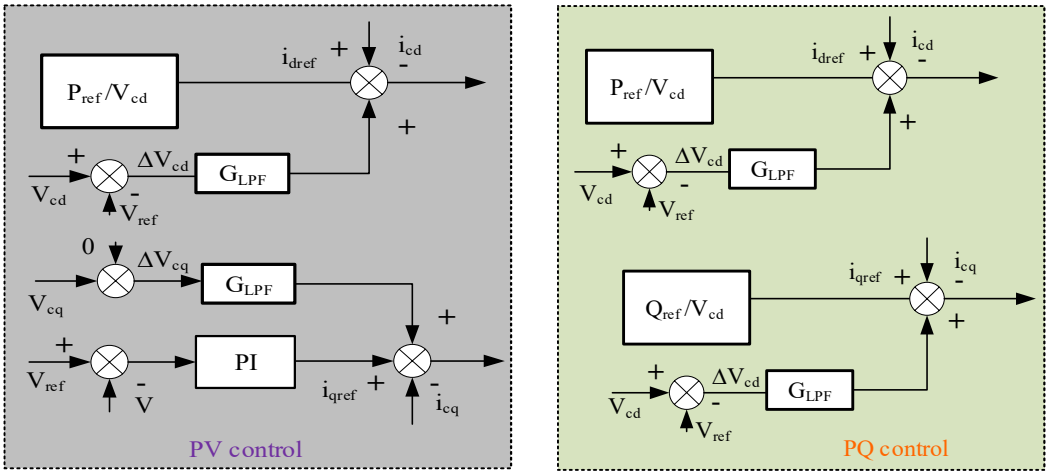

Figure 4.15: Outer Control-Induced Impedance Reshaping in GFL (PQ/PV) Operated MVSCs

The mathematical formulation of these impedance reshaping is expressed in Equations (4.14) and (4.15) for PV and PQ modes, respectively:

$$\begin{bmatrix}\Delta i_{dref}\\ \Delta i_{qref}\end{bmatrix} = \begin{bmatrix} -\frac{P_{ref}}{V_{cd}^2} + G_{LPF} & 0 \\ V_{cd}\left(K_{pu} + \frac{K_{iu}}{s}\right) & G_{LPF}\end{bmatrix}\begin{bmatrix}\Delta V_{cd}\\ \Delta V_{cq}\end{bmatrix} \quad (4.14)$$

$$\begin{bmatrix}\Delta i_{dref}\\ \Delta i_{qref}\end{bmatrix} = \begin{bmatrix} -\frac{P_{ref}}{V_{cd}^2} + G_{LPF} & 0 \\ G_{LPF} & \frac{Q_{ref}}{V_{cd}^2}\end{bmatrix}\begin{bmatrix}\Delta V_{cd}\\ \Delta V_{cq}\end{bmatrix} \quad (4.15)$$

Here, G_{LPF} is the low-pass filter used in the reshaping path. Its cut-off frequency and time constant, with parameter values of Coupling-One = 0.0033 s and Coupling-Two = 0.033 s, are selected to reduce high-frequency effects while preserving the low-frequency dynamics essential for damping.

Figures 4.16(a-c) illustrate how the converter impedance changes after reshaping. Without modification (PV-PV case), the IR magnitude exceeds 2.8pu, and its phase deviates beyond ±90°, indicating strong converter coupling and a high risk of resonance. After reshaping, the IR magnitude decreases, and its phase shifts toward the stable region. This change demonstrates reduced interaction strength and improved damping.

Eigenvalue analysis supports this observation: the dominant mode $\lambda_1(s)$moves to a lower interaction region and further into the stable area, while the secondary mode $\lambda_2(s)$remains

nearly constant due to its negative-sequence characteristics and low EIR value. A similar improvement is observed in the PV-PQ configuration.

The Nyquist contour in Figure 4.16(d) also demonstrates the effect. Without reshaping, the curve encircles the critical point (−1, 0), representing potential instability. After reshaping, the trajectory stays outside the critical region, confirming stability by the Nyquist criterion.

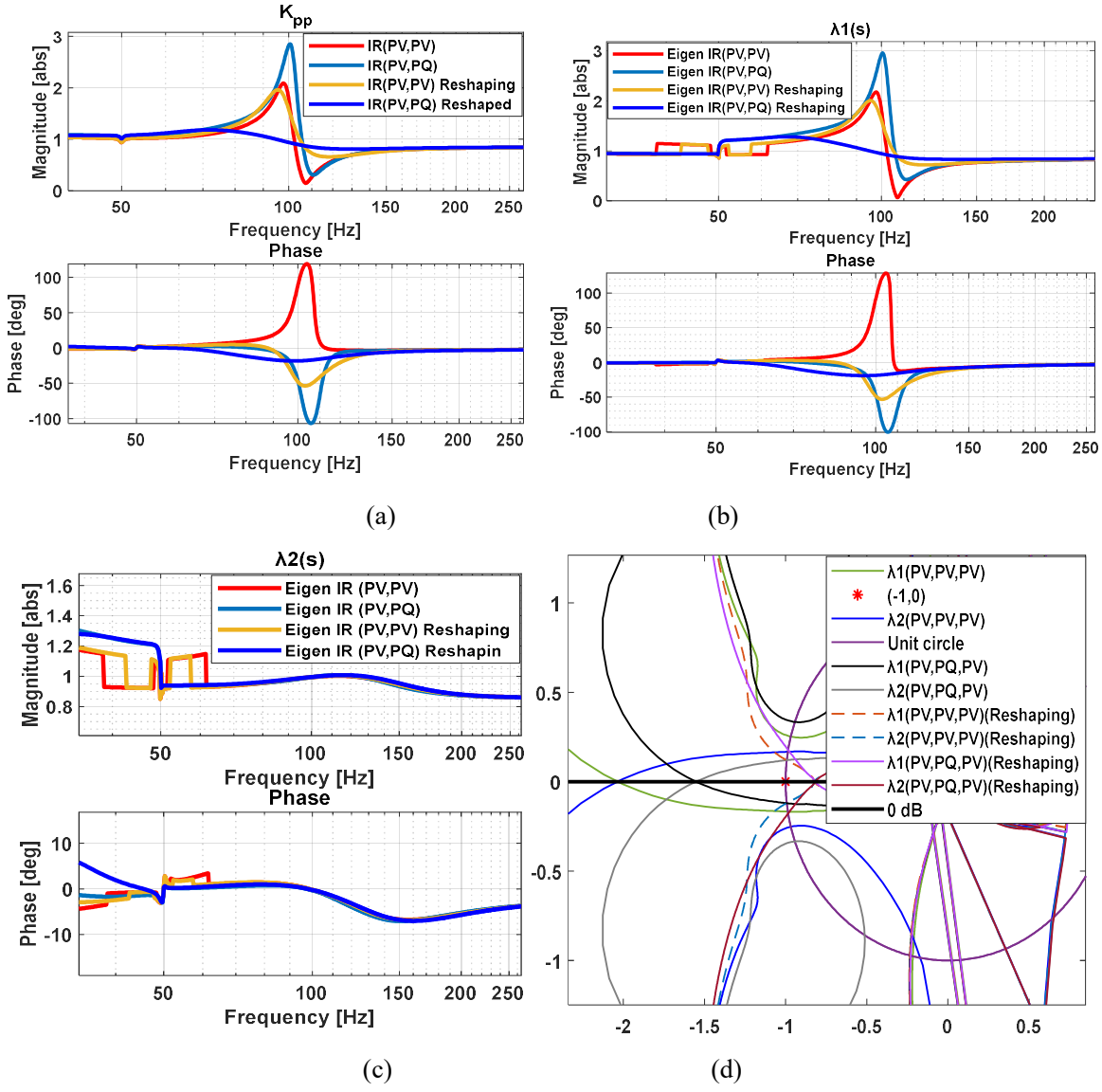

Figure 4.16: IR (a) and EIR (b, c) Changes and Nyquist Plots(d), Due to Reshaping of GFL

The time-domain results shown in Figure 4.17 confirm the effect of impedance reshaping on the dynamic behaviour of the (PV-PV-PV) control system. During the reshaping period, up to 5.0 seconds, the system remains stable and well-damped, with power, voltage, and current showing smooth responses. At 5.0 seconds, the control mode changes from reshaping to

normal operation. Immediately after this transition, a small disturbance produces sustained oscillations in all three quantities. These oscillations persist throughout the simulation, while under the reshaping condition, the same disturbance was fully damped. This clearly demonstrates that impedance reshaping improves system stability by effectively suppressing oscillations and enhancing the overall dynamic performance.

This combined frequency-domain and time-domain analysis shows that adjusting the outer-loop control of GFL converters to reshape their impedance is a practical and effective way to improve stability. By changing the impedance profile, the method reduces resonances, increases damping, and maintains stability under various operating conditions. It also provides a clear approach for tuning the outer-loop controller so that converters meet power delivery requirements while supporting the stability of weak multi-converter networks.

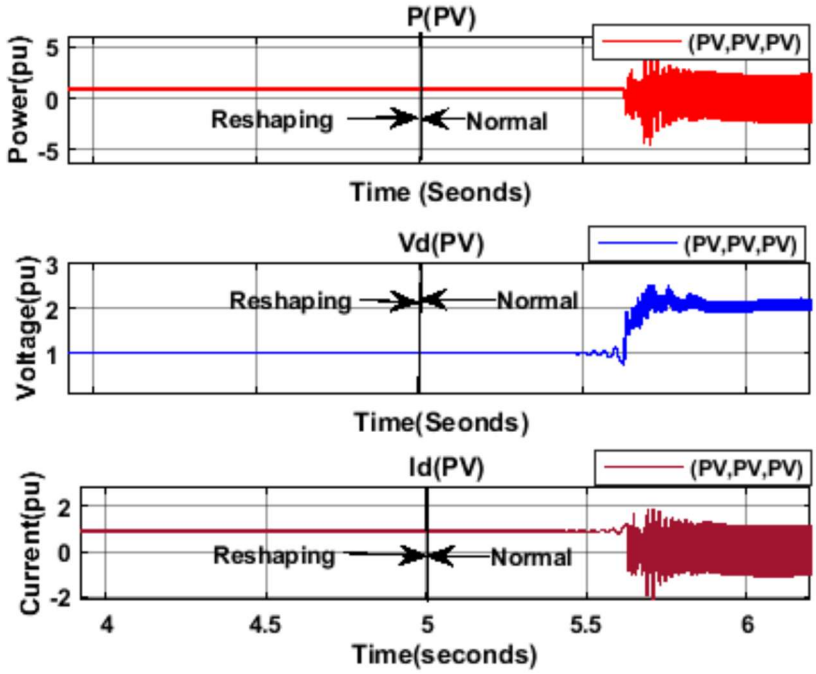

Figure 4.17: Time Domain Simulation -Impedance Reshaping of GFL in (PV, PV, PV) Control System

4.6.2 Impedance Reshaping of GFM Converters

For GFL converters, impedance reshaping can be implemented in the outer-loop controller. However, GFM converters need an additional method to reproduce the damping and coupling effects found in synchronous machines. This is achieved through a virtual impedance approach, as shown in Figure 4.18. The technique adds artificial resistive (R_v)

and inductive (L_v) elements on both the d-axis and q-axis before the voltage regulation stage, with values provided in Table 4.1.

These elements replicate the damping and cross-axis coupling features of synchronous machines. As a result, the impedance reshaping reduces both the IR and the EIR, lowering the overall interaction strength between converters and the grid.

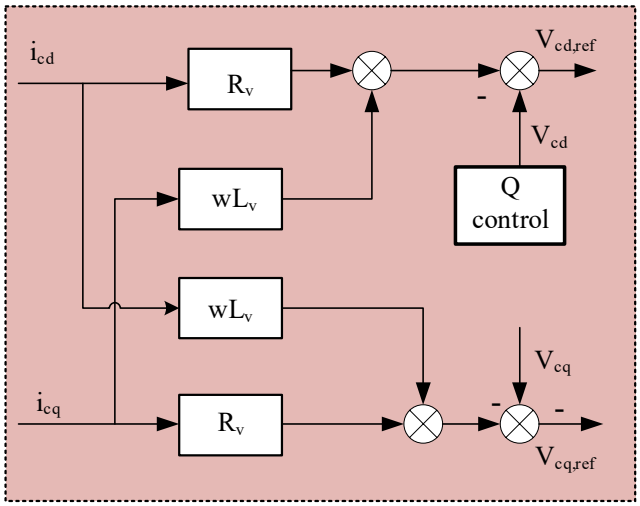

Figure 4.18: Impedance Reshaping through Virtual Resistance in GFM Control

The virtual impedance can be expressed as:

$$Z_{virtual} = \begin{bmatrix} R_v & 0 \\ 0 & R_v \end{bmatrix} + \begin{bmatrix} 0 & \omega L_v \\ -\omega L_v & 0 \end{bmatrix} \tag{4.16}$$

The diagonal terms introduce resistive damping that limits oscillatory components, while the off-diagonal terms provide frequency-dependent inductive coupling between axes. This coupling ensures that d-axis and q-axis responses remain coordinated during transient changes.

The bandwidth of the virtual impedance loop must remain lower than that of the main voltage control loop so that voltage regulation remains accurate and responsive.

Figures 4.19 (a)-(c) show the impact of this method using one GFM and one GFL converter operating in PV mode. Without reshaping, a resonance peak appears near 110 Hz, and the IR and EIR values are high. After applying virtual impedance, both IR and EIR values decrease, and the frequency response becomes smoother. The EIR plots in Figures 4.19 (b)-(c) indicate

a reduction in dominant mode interaction, while the secondary mode shows minimal change, confirming that the reshaped impedance primarily affects the main converter-grid coupling path.

As illustrated in the Nyquist plots for the (GFM, PV, PV) scenario in Figure 4.19(d), the system's stability behaviour is evident. Without virtual impedance, the Nyquist plots encircled the critical point (−1, 0), indicating high sensitivity to small disturbances. When virtual impedance is applied, the contour moves away from this boundary, showing improved stability. Increasing the resistive component R_v further enhances this effect, providing a practical way to strengthen system robustness.

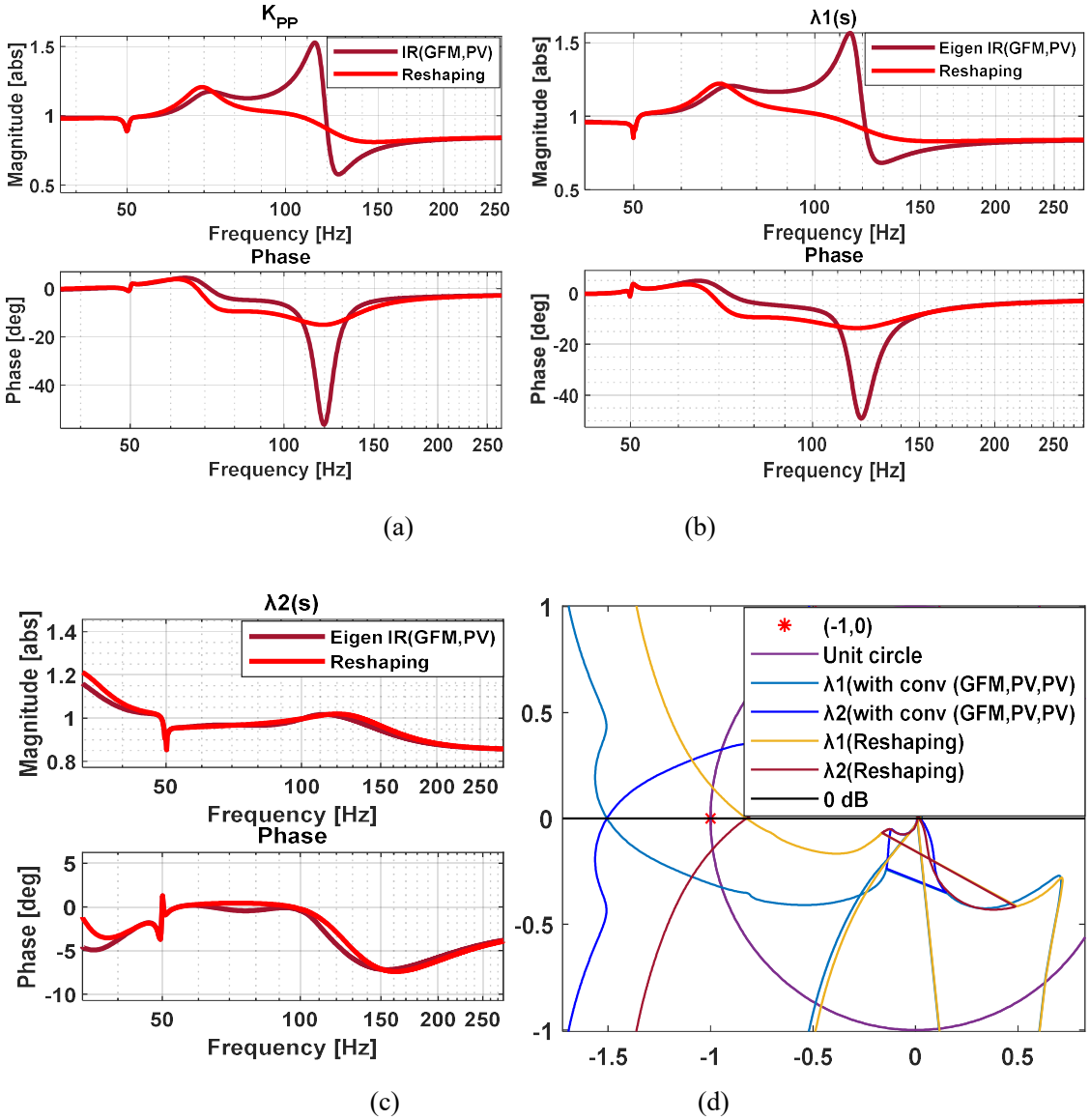

Figure 4.19: IR (a) and EIR (b, c) Changes and Nyquist Plots(d) Due to Reshaping of GFM

The time-domain response in Figure 4.20 shows the effect of impedance reshaping on the stability of the (GFM, PV, PV) system. When the virtual impedance is disabled, noticeable oscillations in both voltage and current begin at around 3.4 seconds after a disturbance, showing limited damping capability during normal operation. When impedance reshaping is applied to the GFM converter, these oscillations disappear, and the system remains stable under the same conditions.

This result confirms that the use of virtual impedance strengthens damping and removes unstable resonances in converter-based networks. The IR and EIR are used to study these effects in the frequency and state-space domains, linking impedance characteristics to system eigenvalues and overall stability. The reshaped impedance modifies the interaction network between converters, improving phase margins and damping performance.

As discussed in this section, combining virtual impedance in GFM units with outer-loop reshaping in GFL converters enhances small-signal stability margins in multi-converter systems [140] . This coordinated approach reduces resonance buildup, increases damping, and ensures stable operation even under weak grid conditions.

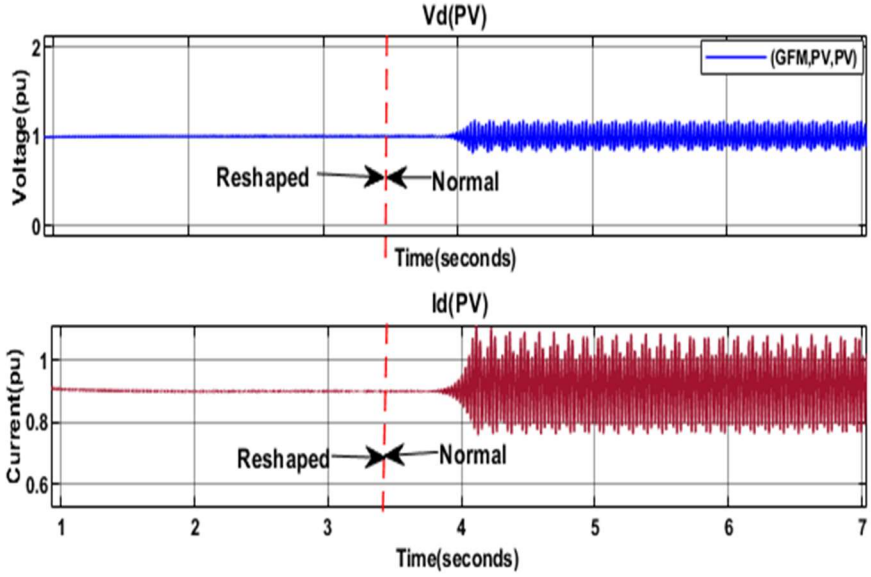

Figure 4.20: Time-Domain Simulation of (GFM, PV, PV) Configuration with Impedance Reshaping Applied to GFM-Controlled Converter

4.7 Effect of Cable Connection on MVSC System Stability

The results in this section show that realistic cable modelling changes the impedance characteristics and interaction behaviour within multi-converter AC systems. These effects

are observed under different control modes and across various frequencies, showing that cable dynamics must be included for an accurate evaluation of converter behaviour [141][142].

Figure 4.21 shows a multi-converter AC network where VSC-1 is connected to the external grid V_{g1}through cable-based transmission lines. The cables are represented using distributed π-sections that include resistance, inductance, and capacitance along a total length of 60 km. This modelling captures the frequency-dependent impedance that affects converter interaction with the grid. The coupling between converters through line parameters and shunt capacitances changes the effective admittance at each PCC, shaping the overall network response.

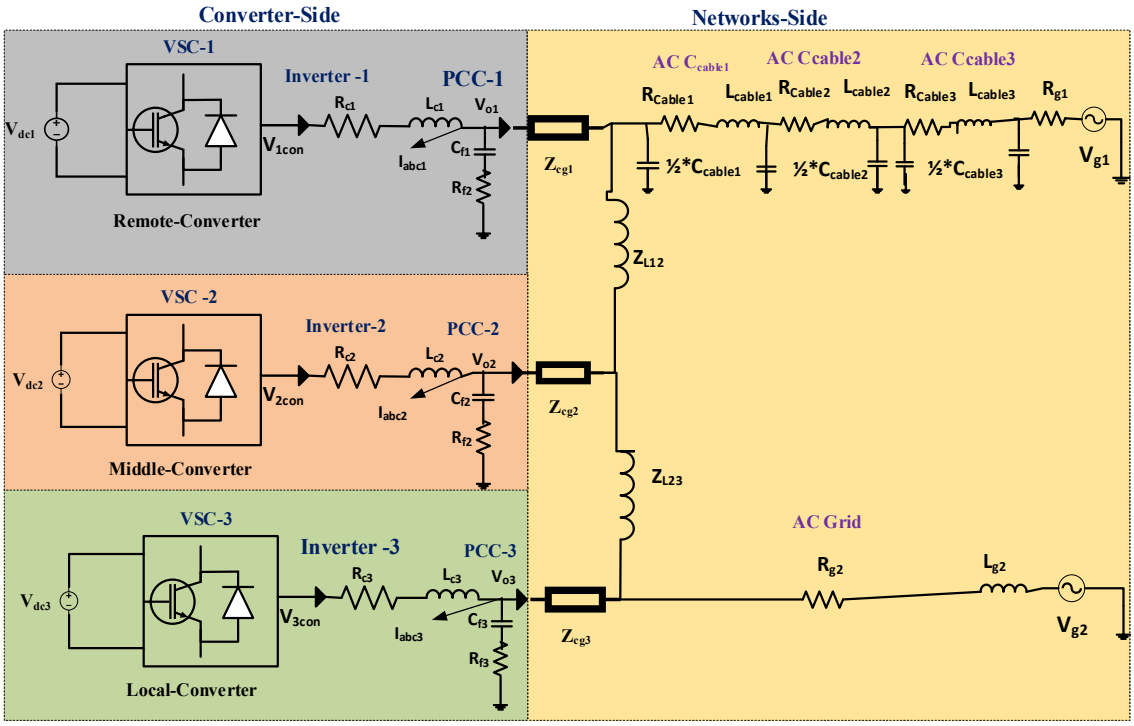

Figure 4.21: Multiple Converters in a Network with Cable Connections

- **AC Grid Impedance with Different π- Sections Approximations**

In the initial model, each cable is represented by three distributed π-sections, with each section covering a 20 km segment. The parameters used are $R_{cable} = 0.01645pu$, $L_{cable} = 0.36052pu$, and $C_{cable} = 0.1pu$, selected to represent measured data from actual cables of similar length. Table 4.6 lists these values. The equivalent impedance observed at PCC-1, through the interconnected cable network from VSC-1, is expressed as

$$Z_{g01} = (Y_{cable1}^{-1} \,||\, Z_{cable1} \,||\, Y_{cable1}^{-1}) + (Y_{cable2}^{-1} \,||\, Z_{cable2} \,||\, Y_{cable2}^{-1}) + (Y_{cable3}^{-1} \,||\, Z_{cable3} \,||\, Y_{cable3}^{-1}) + Z_{Lg1} \quad (4.17)$$

When a different number of π-sections is used, the resistance, inductance, and capacitance values for each segment are scaled accordingly. The same calculation method as in (4.17) is applied to determine the equivalent impedance.

Figures 4.22(a-c) present how the number of π-sections affects the IR in a (PV, PV) converter configuration. With only two sections, the IR magnitude exceeds 2.8 in the 100–110 Hz range, and the phase angle moves beyond ±90°, showing strong resonance and weak damping. When three sections are used, the resonance shifts to a slightly lower frequency, the IR peak decreases, and damping improves. These changes lead to converter interactions that more closely represent the actual network behaviour.

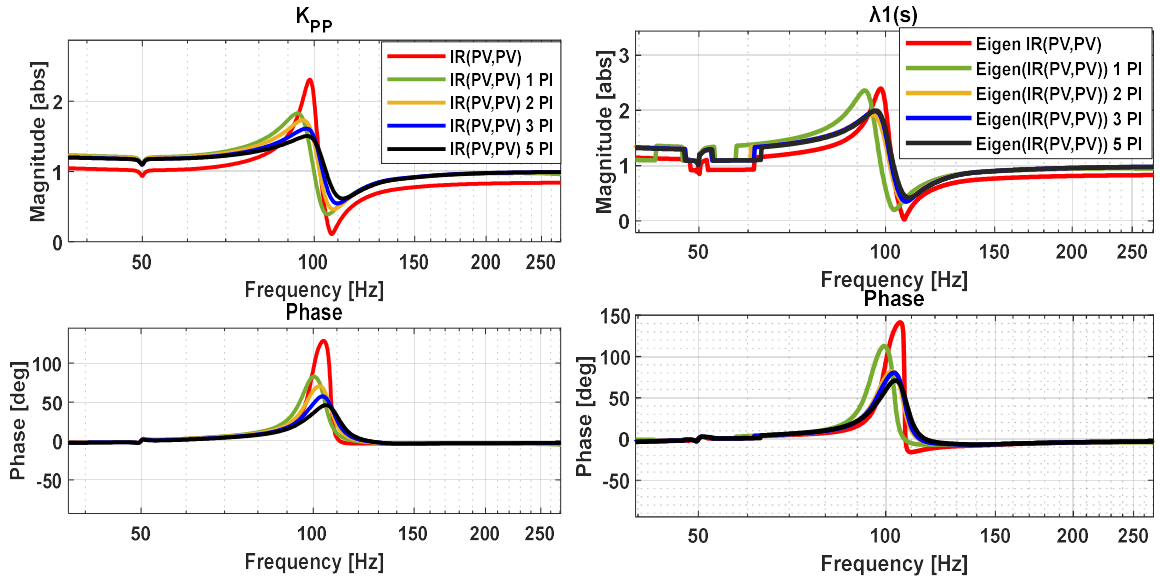

(a) (b)

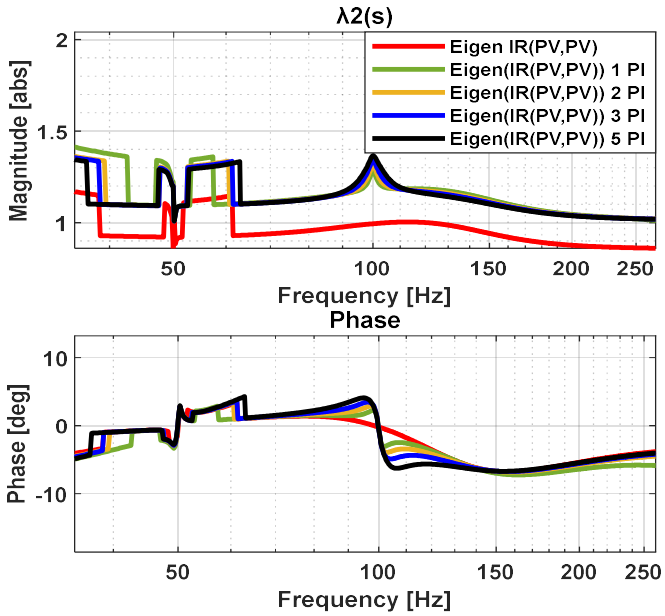

(c)

Figure 4.22: The Impact of shaping the Network system with Cable design.

The EIR results in Figures 4.22(b-c) confirms these findings. The dominant eigenvalue $\lambda_1(s)$shows reduced magnitude and improved damping with three or more sections, while the secondary eigenvalue $\lambda_2(s)$remains almost unchanged. This means that the dominant mode primarily determines the resonance behaviour. Beyond three sections, the improvement is minimal, showing that three π-sections (for a 20 km cable) provide sufficient accuracy without adding unnecessary computational effort.

As shown in Figure 4.23, the inclusion of the cable significantly alters the Nyquist trajectories. Without the cable model, the Nyquist Criteria encircled the critical point (−1, 0), resulting in narrow stability margins and a higher risk of oscillations. When the cable is included, the trajectory shifts away from this critical boundary, increasing both gain and phase margins. This demonstrates that the cable modifies the impedance interaction by reshaping the frequency response and enhancing damping in resonance-prone frequency ranges. Consequently, the system exhibits improved stability, highlighting the importance of accurate cable representation when assessing converter interactions through the IR and EIR framework.

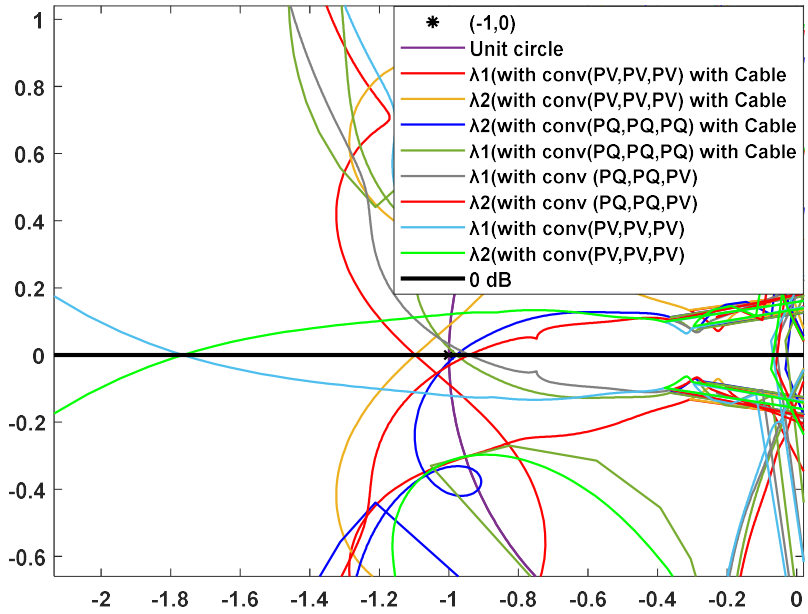

Figure 4.23: Nyquist stability with the Impacts of Cable design

These results highlight that accurate cable representation is essential in converter interaction studies. The IR and EIR methods clearly show how the number of π-sections and cable parameters influence interaction strength and frequency behaviour. Proper modelling ensures that converter dynamics and network coupling are correctly captured for realistic analysis of multi-converter AC systems.

4.8 Summary

This chapter has investigated converter-network interactions in multi-converter AC systems composed of 3 converters, i.e., a remote converter, a middle converter, and a local converter, under different control modes. IR and EIR were used to quantify the impact of the remote and middle converters on the stability of the local converter. These indices provided a clear understanding of the interaction strength and the stability margins, revealing the mechanisms that govern multi-converter dynamics.

- Extending the two-converter analysis in Chapter 3, the results showed that IR and EIR change significantly when interaction between converters increases. After this, the system stability reflected by IR and EIR was seen to depend strongly on converter placement, control design, tuning settings, and power flow direction. Parameter changes adjust the coupling level, but the control mode remains the main factor. Converters with similar impedance shapes in the frequency range also tend to interact

more, which raises the risk of oscillations and shows that electrical proximity guides the overall dynamic response.

- Different converter configurations produced distinct stability behaviours. Systems composed entirely of GFL converters or with a GFM converter placed only at the remote position exhibited strong resonance due to weak damping at the local side terminal. These cases showed high IR and EIR values with sharp impedance peaks, indicating increased oscillatory risk. In contrast, when a GFM converter was positioned at the middle node, it provided effective damping, reduced the apparent network impedance seen by the local converter, and improved stability margins across a wide frequency range. For the PV-PV-PV control combination, higher IR and EIR values reflected stronger interaction and poorer stability. Replacing the middle converter with a GFM unit reduced the interaction, as the GFM control provides low impedance and better damping when interfacing with a weak network. This configuration lessened the oscillatory impact on the local converter and moved the system toward a more stable operating region.
- As the number of converters increased, the interaction with the network also intensified. The degree of interaction was closely related to the IR and EIR values and the phase characteristics of the impedance ratio. When the IR exceeded 2 and the phase shifted negatively, the system approached an unstable region. A positive phase shift indicated stronger coupling, leading to high oscillations and resonance, typically observed between 70 Hz and 250 Hz**.** This frequency range was identified as the most sensitive region for multi-converter interaction and a primary source of instability.
- High IR and EIR values indicated strong coupling and resonance between the units and the network. Both PV and GFM control modes required impedance reshaping to reduce these effects. Adjusting the impedance curve, together with proper tuning of control gains and PLL settings, reduced resonance and improved damping. This showed that reshaping the impedance helps protect the local unit from instability. The IR-EIR method also supports coordinated tuning of GFM and GFL units under weak-grid operation and high-power transfer.
- When comparing inverter operating modes, M-VSCs in rectifier mode were more likely to create strong interaction levels that triggered oscillations and instability. In these cases, the resonance points often moved to higher frequencies, commonly above 110 Hz.

- When both the remote and middle units operated with GFM control, the IR and EIR values increased. Both units attempted to hold the voltage, which raised the interaction level and encouraged oscillations. This showed that placing multiple GFM units in sequence can increase the overall interaction level.
- The network layout also influenced the IR and EIR values. Cable-based networks produced lower interaction and smaller IR and EIR values than networks with only overhead lines. The improvement depended on the control mode and the interaction pattern under weak-grid operation.

Overall, the methodology based on IR and EIR provided a clear and quantitative approach to assess the stability of converter-dominated systems. The results confirmed that coordinated control operation, network configuration, and transmission characteristics collectively determine stability. This method offers a solid basis for designing stable multi-converter AC systems in future interconnected grids.

Chapter 5: Impedance-Based Model Simplification for Converter Network Interaction Analysis

5.1 Introduction

The stability assessment of converter-dominated AC networks depends on an accurate representation of the interaction between converter control systems and the surrounding grid impedance. This chapter explains the need for a clear time domain representation when studying interaction between converters and the surrounding network. Full EMT models are often used because they capture fast switching effects, control dynamics, and network behaviour in detail. Here, EMT is important as a reference to show the level of detail required to represent converter behaviour accurately; however, this work does not rely on a full EMT implementation for all studies. Instead, the discussion uses EMT concepts to justify a simplified approach that retains the key dynamic features affecting stability while avoiding heavy computation. The proposed method replaces detailed switching with a first-order transfer representation of the pulse-width modulation stage, allowing accurate dynamic behaviour without excessive simulation effort. Accurate stability assessment requires capturing the interaction between control loops and grid impedance while keeping the model practical for repeated studies. Large networks with several voltage source converters can lead to long simulation times and increased modelling effort when detailed switching models are used, especially in environments such as MATLAB/Simulink. These challenges make iterative analysis and parameter tuning difficult. To address this issue, a reduced representation is introduced that preserves dominant dynamics relevant to interaction studies while removing states that have limited influence on system behaviour. This approach supports efficient analysis, clear interpretation, and reliable evaluation of converter interactions under varying operating conditions, enabling examiners to follow assumptions, modelling choices, and justification without ambiguity.

This chapter introduces model simplification methods that replace detailed converter models with reduced representations to lower computational effort while preserving accuracy. Simplification is appropriate when a remote converter has limited influence on interaction levels and does not change overall stability. The study continues the development of the IR and EIR approaches introduced earlier and applies them to reduced converter models derived

from detailed descriptions. The focus is on multi-VSC systems, examining how remote converters affect the stability of a local converter and its interaction with the network in both frequency and time domains. Stability results from simplified and detailed models are compared, including the corresponding IR and EIR values. By recognising the separation between fast inner current control and slower outer control, the remote converter can be reduced without losing key stability features, particularly through representation of the inner current controller and LCL interface. This provides clear support for stability assessment suitable for thesis evaluation.

Validation of the reduced-order models is carried out in several stages. First, frequency-domain comparison with detailed EMT models confirms that the resonance frequencies, damping factors, and impedance magnitude and phase are preserved. Second, impedance variation with converter and network interaction is examined using the IR and EIR approaches under changes in grid strength, control mode, power transfer direction, and time delay. Third, time-domain studies confirm that transient behaviour, damping, and disturbance responses match the detailed model in both strong and weak grids. Last, Nyquist-based stability checks under different delays are compared with reference models.

The results show that reduced-order models significantly decrease computational demand while preserving the essential features needed for accurate stability prediction. However, no single simplification strategy is suitable for all cases. The proposed simplified model improves simulation performance in MVSC systems without compromising accuracy. Impedance analysis provides a reliable measure of converter-grid interaction strength. When the interaction is weak, such as in strong grids with low IR values and limited high-frequency coupling, the remote converter can be represented with more aggressive simplification. In contrast, in weak grids with high IR values and substantial active power transfer, simplification must be conservative. In such cases, resonant modes must be retained to preserve critical dynamic behaviour.

5.2 Model Simplification Approaches for Multi-VSC Systems

A common simplification method for converter systems involves simplifying the inner current control loop of the VSC, which operates on a much faster time scale than outer controllers when switching effects are neglected. Simplifying this loop allows larger simulation steps and reduces computational requirements. However, the simplification may

alter the closed-loop frequency response, often requiring retuning of the outer-loop control parameters to restore desired performance [143][144].

Conventional validation of simplified models often relies on the Root Mean Square Error (RMSE) between simplified and detailed simulations. Although RMSE provides a general accuracy measure, it does not capture combined magnitude and phase errors, which may hide critical stability deviations. Reference [143] demonstrates that in weak-grid-connected VSCs, simplified MIMO transfer functions reduced to SISO forms reveal the presence of RHP zeros. These RHP zeros are strongly influenced by grid impedance and active power transfer, placing fundamental constraints on the achievable PLL bandwidth [78]. Subsequent work has provided control gain tuning guidelines to mitigate these effects, validated through real-time digital simulation (RTDS) [77] [145].

Another approach presented in [77][145] applies admittance-based aggregation to represent multiple converters collectively, greatly improving simulation speed. However, this method loses accuracy as the number of converters increases due to unmodelled coupling and parameter sensitivity. Other strategies focus on GFM converters and target primary stability modes, but they often neglect harmonics, which restricts their application in mixed-control networks.

The framework developed in this thesis overcomes these limitations by applying first-order singular perturbation to simplify the grid-side current dynamics of LCL filters. Traditional aggregation or simplification techniques often lose accuracy when converters operate with grids of different parameters or structures. The proposed reduced models maintain essential impedance characteristics that define stability while reducing computational time. Validation is carried out through frequency-domain comparison, IR and EIR-based analysis, time-domain simulation, and stability-region mapping for both strong and weak grids with central and remote converters.

The IR and EIR based approach remains valid for weak grids; however, it requires more accurate modelling because converter–grid interaction is stronger. The method does not lose applicability but calls for careful representation to avoid incorrect stability conclusions. In strong grids, simpler models are sufficient. This clarification aligns the method with the study's scope and confirms that reliable assessment is maintained across different grid strengths.

5.3 Time-Scale Separation Model Reduction

The detailed inner-loop dynamics of the converter, initially derived from the full-order control model presented in Figure 2.11, can be reduced by exploiting the inherent separation between the fast dynamics of the inner current loop and the slower outer control loops. The reduction process begins with a time-delay approximation that effectively removes high-speed dynamics while maintaining the slower control components required for accurate stability representation. In this approach, feed-forward gains from both voltage and current controllers are excluded, as their influence on the impedance response within the studied frequency range is negligible.

Following established modelling practice [77][146], a cascade time-delay representation is adopted for the inner current control loops of the remote VSC. This is especially effective for systems with LCL filters that have large grid-side inductances, as seen in renewable energy applications where converter-grid coupling is mainly inductive. By replacing detailed fast-current dynamics with equivalent time delays, the models achieve substantial computational savings without loss of accuracy in stability prediction. This balance between reduced complexity and preserved fidelity makes the simplified models suitable for both analytical work and large-scale EMT simulation.

Although small-signal modelling is widely applied in evaluating grid-connected converter stability, traditional time-scale separation methods often fail to capture the full frequency-dependent behaviour of converter-grid interaction [146]. This limitation is critical when resonance effects arise from both the LCL filter and current-control dynamics. To address this, the methodology developed here extends the impedance-based stability framework to represent these interactions more accurately. The proposed formulation captures the combined dynamics of the converter, LCL filter, and external grid without neglecting important coupling effects.

5.3.1 Dynamic Modelling LCL Filters for Robust Current Regulation

In both GFL and GFM controls considered in this study, inner current regulation is carried out by PI controllers incorporating cross-coupling compensation and voltage feed-forward terms.

To reduce computational effort in large-scale studies, a simplified control representation is adopted for the GFL case (Figure 5.1). This reduced-order structure is obtained by linearising the controller along the main control axes, applying equivalent delays to reproduce the reference tracking dynamics, and introducing high-value resistors to capture the converter current behaviour. The model maintains the interaction features needed for impedance-based stability analysis while enabling efficient evaluation in both frequency and time domains.

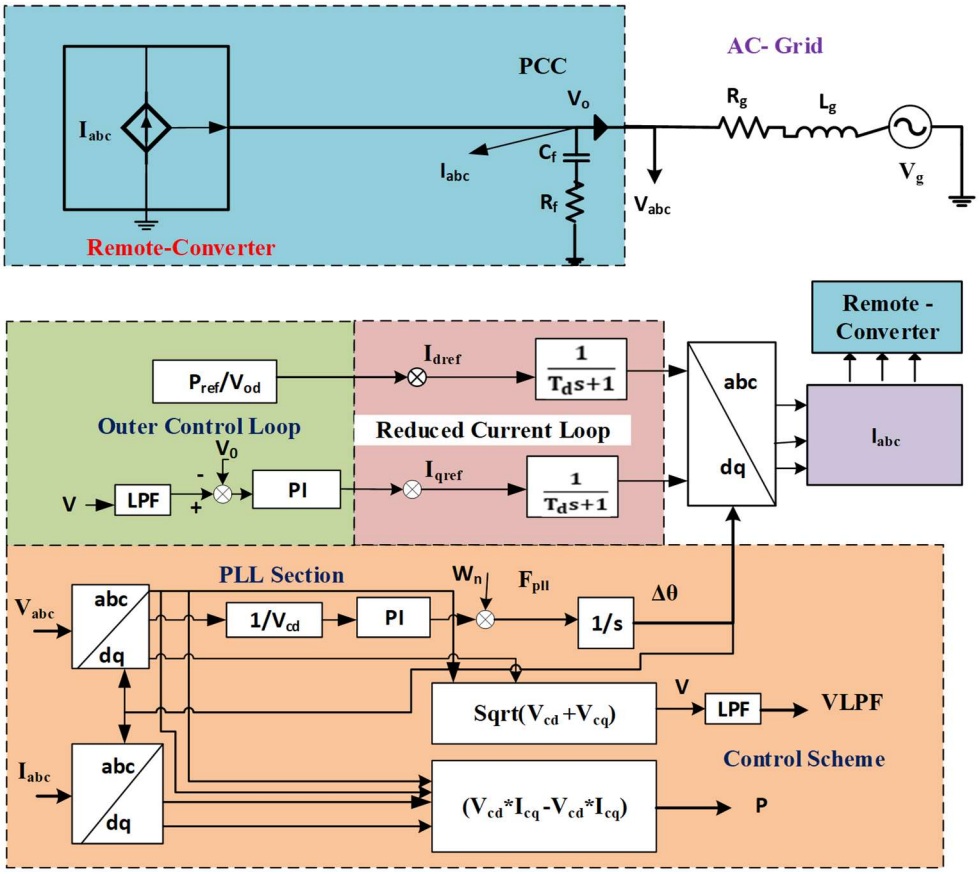

Figure 5.1: Impedance Characteristics of Simplified GFL Converter Model

The derivation begins from the voltage balance across the grid-side inductor,

$$V_0 - V_g = Z_g I_{L_g} = (R_g + sL_g + jwL_g) I_{L_g} \tag{5.1}$$

The voltage across the converter-side inductor is expressed as:

$$V_{1con} - V_0 = (R_c + sL_c + jwL_c) I_{L_c} \tag{5.2}$$

In these equations, V_0 and V_g represents the voltage at the filter capacitor and grid voltages respectively, I_{Lg} denotes converter-side current, and s signifies the Laplace operator.

The current controller dynamics are formulated as:

$$V_{1con} = G_C\left(I^*_{L_c} - I_{L_c}\right) + jwL_cI_{L_c} + h_2V_0 \tag{5.3}$$

where $I^*_{L_c}$ is the reference current, and $G_c = K_{pc} + \frac{K_{ic}}{s}$ denotes the PI regulator. Setting $h_2 = 1$,this becomes:

$$V_{1con} = G_C\left(I^*_{L_c} - I_{L_c}\right) + jwL_cI_{L_c} + V_g \tag{5.4}$$

Subtracting the grid voltage

$$V_{1con} - V_g = G_C\left(I^*_{L_c} - I_{L_c}\right) + jwL_cI_{L_c} \tag{5.5}$$

Substituting (5.1) into (5.3) provides:

$$V_0 - V_g = (R_c + sL_c + jwL_c)I_{L_c} \tag{5.6}$$

Equating (5.4) and (5.5) results in:

$$(R_c + sL_c + jwL_c)I_{L_c} = G_C\left(I^*_{L_c} - I_{L_c}\right) + jwL_cI_{L_c} \tag{5.7}$$

Cancelling the $jwL_cI_{L_c}$ terms and rearranging, we obtain:

$$(R_c + sL_c)I_{L_c} = G_C\left(I^*_{L_c} - I_{L_c}\right)$$

Further simplification leads to:

$$G_cI^*_{L_c} = G_cI_{L_c} + (R_c + sL_c)I_{L_c}$$

Dividing by $G_C$and substituting its expression, the open-loop gain is defined as:

$I^*_{L_c} = I_{L_c} + \frac{(R_c+sL_c)I_{L_c}}{G_c}$, Substituting for G_c:

This leads to the definition of the open -loop gain:

$$G_{OL} = \frac{I^*_{L_c}}{I_{L_c}} = 1 + \frac{(R_c + sL_c)}{K_{pc}+\frac{K_{ic}}{s}} \tag{5.8}$$

Applying pole cancellation techniques ($\frac{K_{ic}}{K_{pc}} = \frac{Rc}{L_c}$) , the closed-loop transfer function is obtained as

$$\frac{I_{Lc}}{I_{L_c}^{*}} = \frac{1}{T_{cl}s+1} \tag{5.9}$$

with the controller gains related to the closed-loop time constant T_{cl} through

$$K_{pc} = \frac{L_c}{T_{cl}} \quad \text{and} \quad K_{ic} = \frac{R_c}{T_{cl}} \tag{5.10}$$

From representative parameters in Table 2.1, practical values of T_{cl} lie in the range of 0.1-1ms, consistent with converter switching frequency, bandwidth, and the dynamic requirements of multi-VSC networks. This parameterisation provides a computationally efficient yet accurate representation of the inner current loop for stability assessment in both frequency and time domains.

5.3.2 Simplified Current and Voltage Control Models

The output -voltage dynamics are described by:

$$V_o = G_m V_{1cond} \tag{5.11}$$

With: $G_m = \frac{K_{ppll}s+K_{ipll}}{c_f s^2 + (R_f+K_{ppll})s+K_{ipll}}$

Here, G_m represents the frequency-dependent behaviour set by the PLL, the filter, and the controller gains.

This work simplifies the current control loop. The voltage loop is taken as reduced because it is slower. In GFM converters, a similar reduction is possible, but the controller design differs. Voltage controllers usually run at a bandwidth three to five times lower than current controllers. The slower response allows stronger reduction, yet the gains must still be tuned with care to keep the dynamic response, limit harmonic distortion, and preserve stability margins.

The proposed framework removes the fast states of the current loop and represents the slower voltage dynamics with a reduced model. The result is compact and efficient, while still capturing the key interactions between the converter and the network. This selective reduction keeps the dominant control-to-network coupling effects and is suitable for stability studies in large multi-VSC grids.

5.4 Small-Signal Modelling of the Simplified Systems

The simplified small-signal model developed in this chapter builds directly on the detailed formulation presented in Chapter 2. It uses reduced-order matrices that preserve the essential dynamic behaviour while lowering computational requirements. This approach is suitable for systems with multiple converters connected to a power network, where the detailed dynamics of each component do not require full investigation. The goal is to improve simulation efficiency without losing important control and interaction features.

The system matrices are expressed as:

$$A = \begin{bmatrix} 1 & V_q F_{pll}(s) \\ 0 & 1 - V_d F_{pll}(s) \end{bmatrix}, B = \begin{bmatrix} 0 & i_q F_{pll}(s) \\ 0 & -i_d F_{pll}(s) \end{bmatrix}, K = \begin{bmatrix} G_m & 0 \\ 0 & G_m \end{bmatrix} \quad (5.12)$$

Two diagonal matrices are introduced to simplify the model:

$$T_{simpf} = \begin{bmatrix} T_{d1} & 0 \\ 0 & T_{d1} \end{bmatrix} \text{ and } T_{del} = \begin{bmatrix} G_d & 0 \\ 0 & G_d \end{bmatrix}$$

Where T_{simpf} represents the inner current control dynamics from Equation (5.9), while T_{del} accounts for digital control and PWM delays.

The outer control loop follows the same structure as in Chapter 2, with specific expressions for PV and PQ control modes:

$$U = \begin{bmatrix} 1 & 0 \\ 0 & K_{pu} + \frac{K_{iu}}{s} \end{bmatrix} \text{ and } P_0 = \begin{bmatrix} -\frac{P_{ref}}{V_d^2} & 0 \\ V_d & V_q \end{bmatrix} \quad (5.13)$$

$$Q_0 = \begin{bmatrix} -\frac{Q_{ref}}{V_d^2} & 0 \\ V_d & V_q \end{bmatrix} \quad (5.14)$$

The resulting small-signal admittance expressions demonstrate the system's dynamic response:

$$Y_{vsconsimpf} = -\frac{\Delta i}{\Delta v} = \frac{T_{del}B + T_{del}UAP_0T_{simpf}}{KI} \quad \text{(PV)} \quad (5.15)$$

$$Y_{vsconsimpf} = -\frac{\Delta i}{\Delta v} = \frac{T_{del}B + T_{del}UAQ_0T_{simpf}}{KI} \quad \text{(PQ)} \quad (5.16)$$

These reduced-order admittance models capture the main interactions between the PLL, the outer-loop controller, and the network impedance while substantially reducing computational effort. Their formulation remains consistent with the $Y_{vscon}pn(s)$ expression defined in Equation (2.34), ensuring full compatibility with the stability assessment procedures established in Chapter 2.

5.5 Impedance Changes in Simplified vs. Detailed Model Simulations

The system's impedance is evaluated with a validation workflow that pairs time-domain simulation and frequency-domain analysis. Each model-the detailed (Det) and the simplified (Simp)-is first assessed on its own, then compared to quantify the error between them. The current-injection method, applied at the local converter terminals (Figure 5.2), is used in both environments. Time-domain (Time) studies are run in MATLAB/Simulink with small perturbations to capture converter-grid interactions. Frequency-domain impedance (Imp) profiles are obtained analytically from the developed models. All studies are executed in MATLAB to ensure consistent setup and a direct basis for comparison.

Abbreviations used throughout text and figures are: Det (Detailed), Simp (Simplified), Imp (Impedance), and Time (Time-domain). Model parameters are listed in Tables 2.1 and 2.2 of chapter 2. Two grid conditions are examined: a strong grid (Coupling One) and a weak grid (Coupling Two), enabling assessment of both models across a broad operating range.

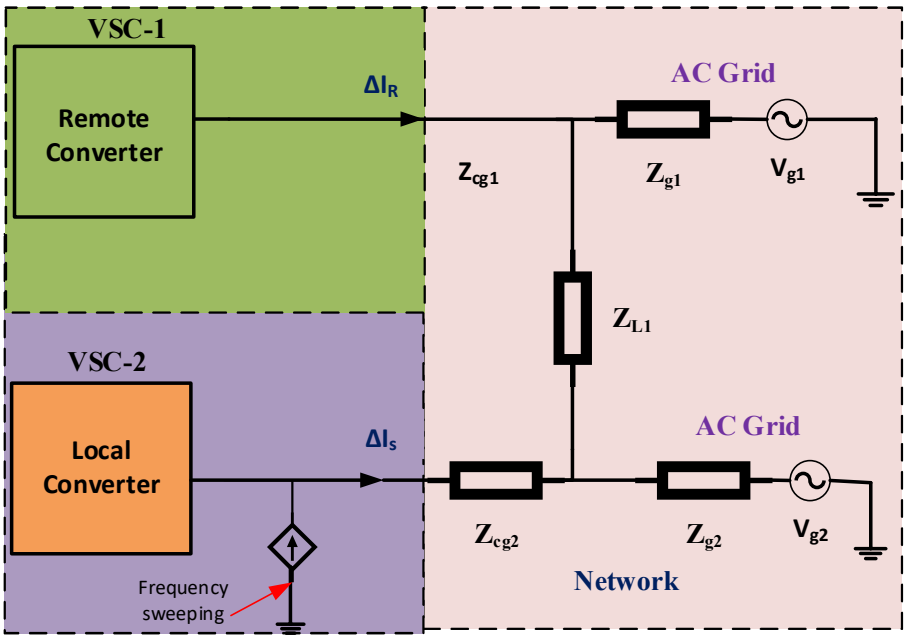

Figure 5.2: Current injection to Analysis Time domain simulation

5.5.1 Impedance Simulation Results Under Coupling-One

This section examines the impedance behaviour of the multi-converter system under Coupling-One using both the detailed and simplified models. The analytical expressions derived in Chapter 2 for the detailed model and in Section 5.4 for the simplified model are compared with frequency-sweep simulation results. Time-domain responses are also analysed to verify the accuracy of the frequency-domain predictions.

For both models, the impedance in PV and PQ control modes is shown in Figure 5.3 as the positive-sequence impedance $Z_{vsconpp}(s)$. The analytical and simulation results agree closely in both magnitude and phase, as seen in Figures 5.3(a) and 5.3(b). The simplified and detailed models remain consistent up to 120 Hz, with small differences at low frequencies and near the 50 Hz resonance peak, mainly due to the influence of the outer control loops.

Model-delay sensitivity was examined by varying the input delay T_{d1}. The best match with the detailed model occurred at $T_{d1} = 0.3ms$ for PV control and $T_{d1} = 0.1ms$ for PQ control, especially within the 50-250 Hz range where converter-grid interactions are most dominant. The time- and frequency-domain validation confirms strong consistency for both models up to 70 Hz when time delay effects are excluded. This verifies the accuracy of the simplified model in representing the remote converter within this frequency range.

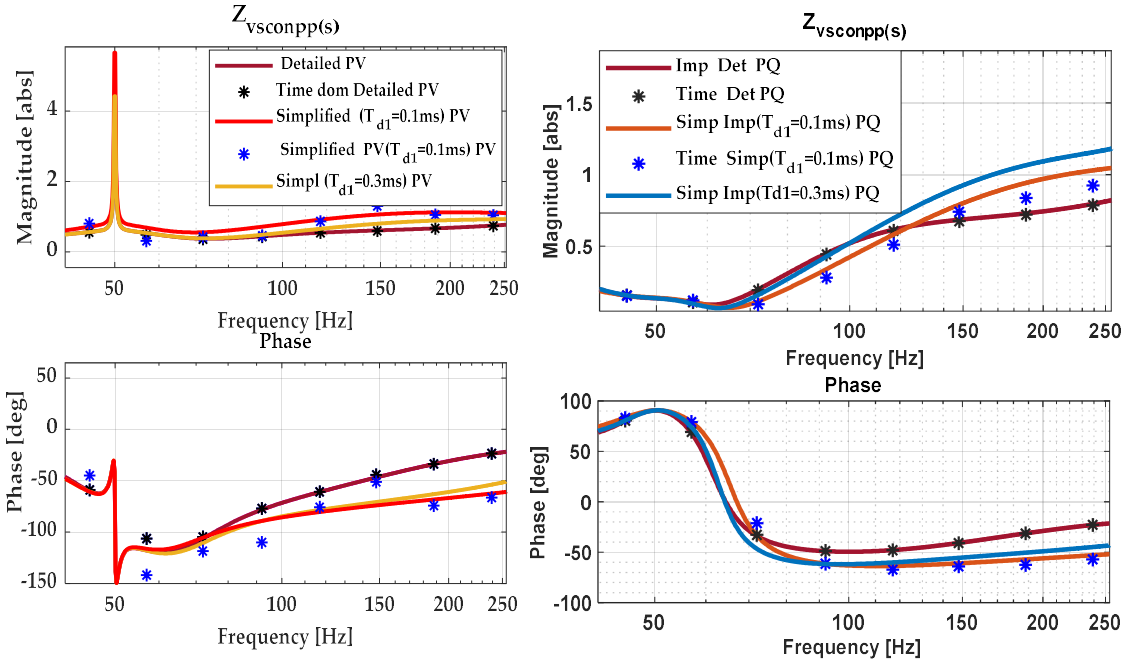

(a) (b)

Figure 5.3: Impedance of remote converter with (a) PV and (b) PQ Control mode

Using the analytical framework from Chapter 3, converter-network interactions were evaluated through IR and EIR analysis. The objective was to determine whether the reduced-order model could reproduce the interaction behaviour of the detailed system, particularly within the dominant frequency range of converter-grid coupling. For simplicity, a single time delay of $T_{d1} = 0.1$ms was used in the simulation.

Figure 5.4(a) compares the combined converter-network impedance $Z_{network+conv}$ with the network impedance $Z_{network}$ for both models. Above 150 Hz, interaction levels decrease, showing damping around 148 Hz where the impedance magnitude reaches approximately 0.9 with phase angles of 77° (PQ) and 79° (PV). The simplified model matches the detailed model well below 150 Hz, though minor deviations appear at higher frequencies. As discussed in Chapter 3, comparing $Z_{network+con}$ with $Z_{network}$ helps assess how the converter affects system impedance and identifies critical frequencies that may lead to resonance.

Figure 5.4(b) presents the IR results. PV and PQ controls show similar trends, except between 100-170 Hz. Under PQ control, IR peaks at 1.1 (121 Hz) with a phase of −8.6°, while PV control reaches 1.16 (130 Hz) with −11° at 150 Hz, indicating slightly stronger interaction in the PV case. The simplified model aligns well with the detailed model below 100 Hz, but small deviations appear beyond 150 Hz.

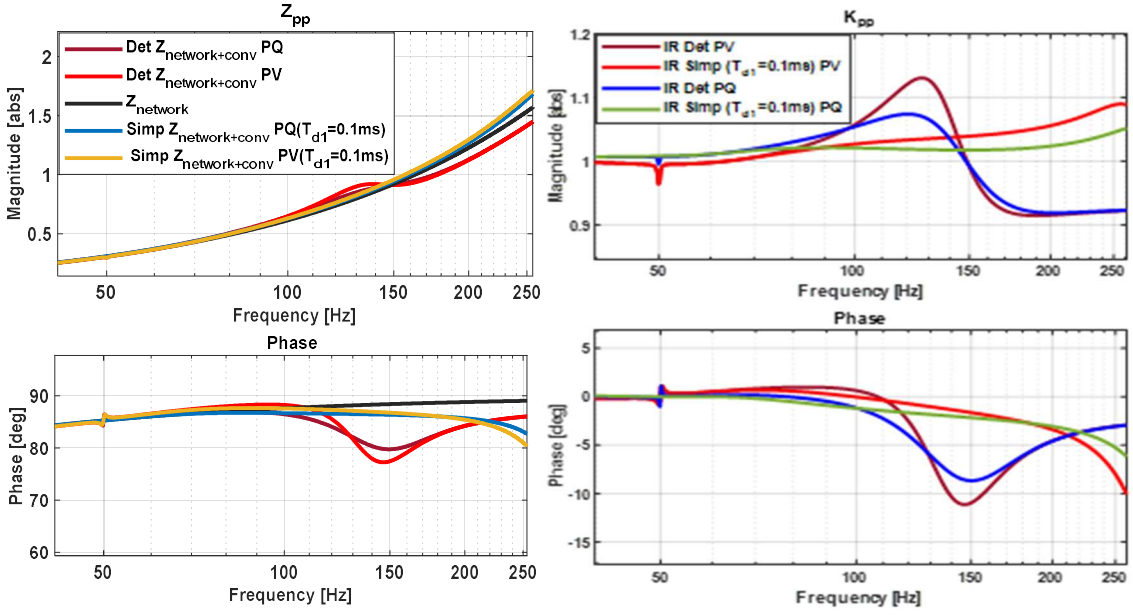

(a) $Z_{network}$ v.s. $Z_{network+con}$ (b) IR

Figure 5.4: (a) Impedance of $Z_{network}$ v.s. $Z_{network+conv}$ and (b) IR change

Eigenvalue analysis in Figure 5.5(a) shows that PV control in the detailed model produces higher magnitudes and more negative phase angles than PQ control, reaching 1.16 at 128 Hz and −11° at 154 Hz, compared with PQ values of 1.08 at 125 Hz and −8.2° at 162 Hz. The simplified model follows the detailed model closely below 100 Hz, with increasing deviations near 150 Hz. At higher frequencies, both models approach ideal behaviour, although PV control shows slightly higher magnitudes around 250 Hz.

Figure 5.5(b) further demonstrates that under PV control, eigenvalue variations are minimal, showing strong consistency. In contrast, PQ control exhibits deviations between 120-220 Hz at $T_{d1} = 0.1$ms, caused by reactive power regulation effects that enhance negative-sequence components and require greater modelling precision.

Comparing Figures 5.4(b) and 5.5(b) shows that IR and eigenvalue results are consistent between 1-50 Hz for both control modes. PV control exhibits stronger interactions between 98-145 Hz, while PQ maintains lower impedance variations overall. The errors remain small, confirming that the simplified model provides an accurate representation of the detailed system across most practical frequency ranges.

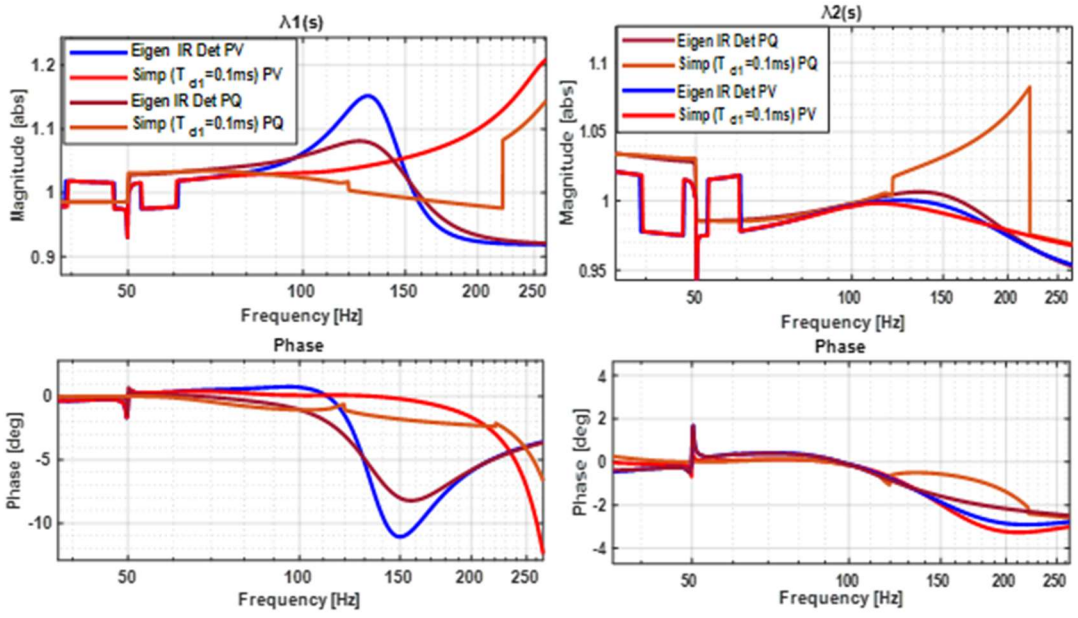

(a) λ1 (b) λ2

Figure 5.5: EIR Analysis for Detailed and Simplified Models Under PV/PQ Control

Overall, Figures 5.4 and 5.5 demonstrate that the impedance variation between the detailed and simplified models remains small, particularly in the strong-grid condition under Coupling-One. The impact of this variation on system stability is further analysed in Section 5.5.3 (Figure 5.8).

5.5.2 Impedance Simulation Results Under Weak-Grid Conditions

The impedance response of the Coupling Two configuration (Tables 2.1 and 2.2) under weak-grid conditions is shown in Figure 5.6(a). The positive-sequence impedance, $Z_{pp}(s)$, demonstrates the influence of converter outer-loop dynamics for both PQ and PV control modes in the detailed and simplified models.

In the detailed model, PQ control reduces the magnitude of the combined network–converter impedance, $Z_{network+conv}$, within the 100-120 Hz range compared to PV control, indicating weaker interaction with the network. PQ control also maintains small peaks with higher damping, showing lower interaction and more stable converter-grid behaviour. The corresponding phase angles remain consistently below 90°.

PV control, in contrast, produces oscillatory behaviour, with phase angles ranging between 70° and 112° in the 75-122 Hz band. It exhibits sharper peaks with lower damping and stronger interaction, which suggests possible resonance caused by high impedance variation. A resonance peak appears near 114 Hz, where negative resistance is observed. Beyond 135 Hz, PV control becomes more sensitive to weak-grid dynamics, indicating stronger network interaction and higher susceptibility to impedance variation.

The simplified model, implemented with a delay of $T_{d1} = 0.1$ms, shows no resonance under either control mode. Under PQ control, the impedance closely follows the network impedance, with only minor phase deviations between 170-230 Hz. PV control, however, shows clear mismatches with the detailed model, especially in the 100-125 Hz range, where both magnitude and phase differ significantly.

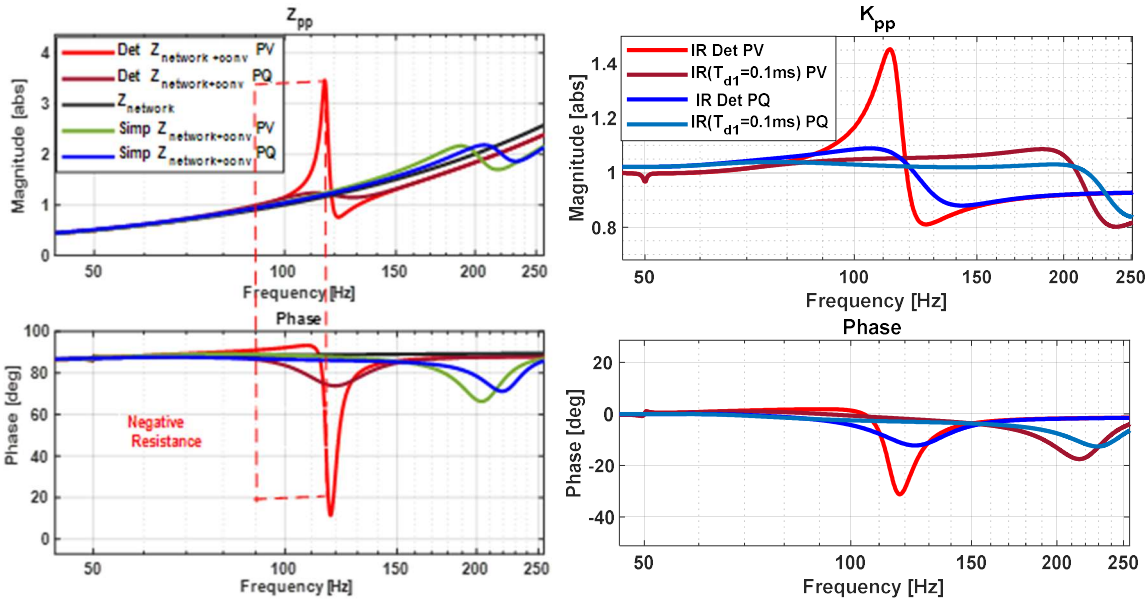

(a) $Z_{network+conv}$ and $Z_{network}$ (b) IR

Figure 5.6: (a) Impedance comparison between $Z_{network+conv}$ and $Z_{network}$; (b) IR

Figure 5.6 (b) presents the IR. Under PQ control, the detailed and simplified models align well up to 120 Hz, with small divergence between 122-205 Hz. Under PV control, the detailed model displays stronger interactions and a reduced IR value, in contrast to the simplified representation. Figures 5.7(a) and 5.7(b) further illustrate this difference. The IR eigenvalues, expressed as 2 × 2 matrices, indicate that PV control increases coupling between converter and network dynamics, while PQ control keeps IR values close to unity, with phase angles between 0° and −15° in the 80-120 Hz range. Under PV control, the IR magnitude increases to about 1.5 with phase shifts approaching 30°, confirming stronger dynamic interaction.

The eigenvalue analysis verifies that the simplified PQ model maintains good accuracy relative to the detailed representation. PV control, however, shows greater discrepancies, particularly near resonance frequencies. For PQ control, impedance variation in Z_{pp} remains small, while differences in Z_{nn} have a more noticeable effect on eigenvalue behaviour. PV control amplifies both magnitude and phase deviations, increasing resonance strength.

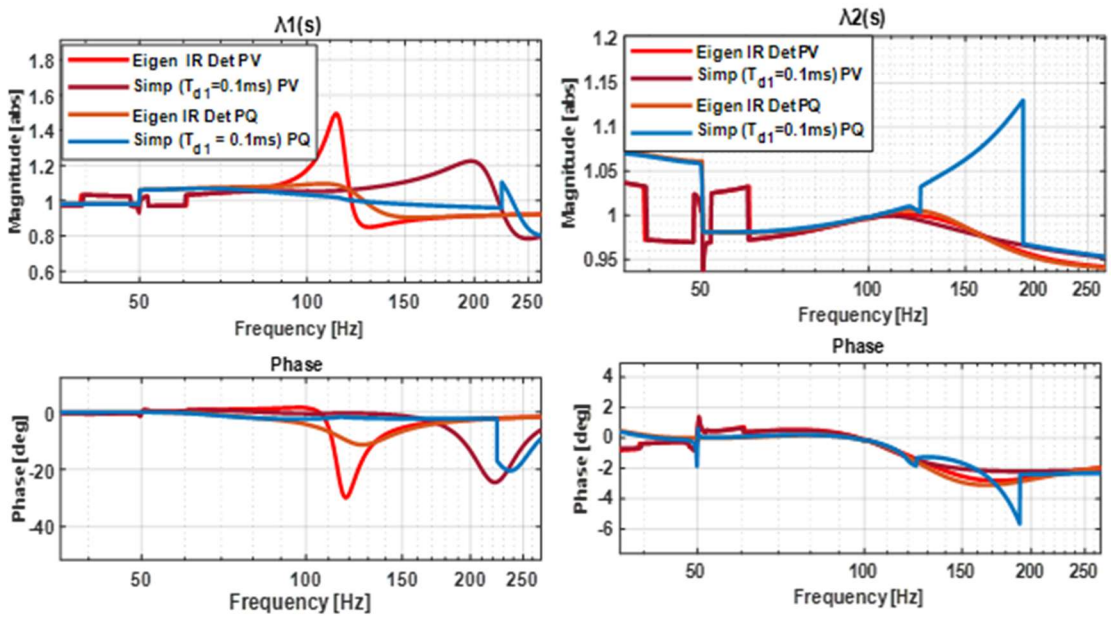

(a) λ1 b) λ2

Figure 5.7: Eigenvalue Movement with Variation in Inertia Ratio (a) λ_1 (b) λ_2

In summary, under weak-grid conditions, PQ control produces smaller impedance variation, reduced resonance amplification, and limited phase deviation, making it less sensitive to network strength. PV control, in contrast, causes larger impedance variation, stronger resonance in the low-frequency range, and higher network interaction, which can lead to adverse dynamic behaviour. Therefore, when simplifying the remote converter model, greater care must be taken for PV-controlled converters. The impact of these impedance variations on overall system stability will be further analysed using both detailed and simplified models.

5.5.3 Nyquist Stability Analysis Under Coupling One and Two

Figures 5.8 and 5.9 show the Nyquist stability analysis of the local PV-controlled converter interacting with a remote converter operating under either PV or PQ control. The analysis uses both detailed and simplified models for Coupling One (strong grid) and Coupling Two (weak grid) configurations.

Under Coupling One, the PQ-controlled system shows excellent agreement between the detailed and simplified models with a delay of $T_{d1} = 0.1$ms. Both models maintain stable margins with respect to the critical $(-1,0)$point, indicating that the simplification introduces negligible error. In the PV-controlled case, however, the simplified trajectory shows slightly

reduced stability margins compared to the detailed model. This difference suggests that the simplified representation becomes less accurate when the system is more sensitive to impedance variation.

The influence of grid strength is more evident under Coupling Two. For PQ control, both models confirm stable operation, consistent with the small impedance variation and interaction values (IR and EIR) discussed in Section 5.5.1. For PV control, the detailed model encircles the $(-1,0)$point, whereas the simplified model does not. This behaviour indicates reduced accuracy of the simplified model in weak-grid conditions. The discrepancy arises because impedance variation in weak networks amplifies the PV controller's sensitivity, leading to deviations between the detailed and simplified responses. Therefore, the simplification method for PV control of the remote converter requires refinement to maintain accuracy under weak-grid conditions.

The local converter is analysed under PV control because this mode is more sensitive to impedance variation and exhibits more to instability tendencies than PQ control, as demonstrated in earlier chapters. Hence, PV control represents the most challenging scenario for assessing the validity of stability system.

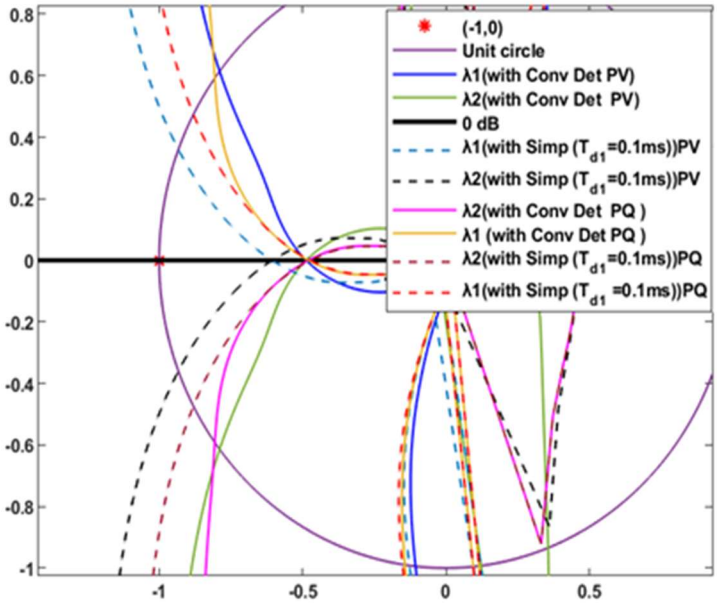

Figure 5.8: Nyquist Stability Comparison between Detailed and Simplified Local PV Converter Models in Coupled System with Remote PV and PQ Converters (Coupling -One parameters)

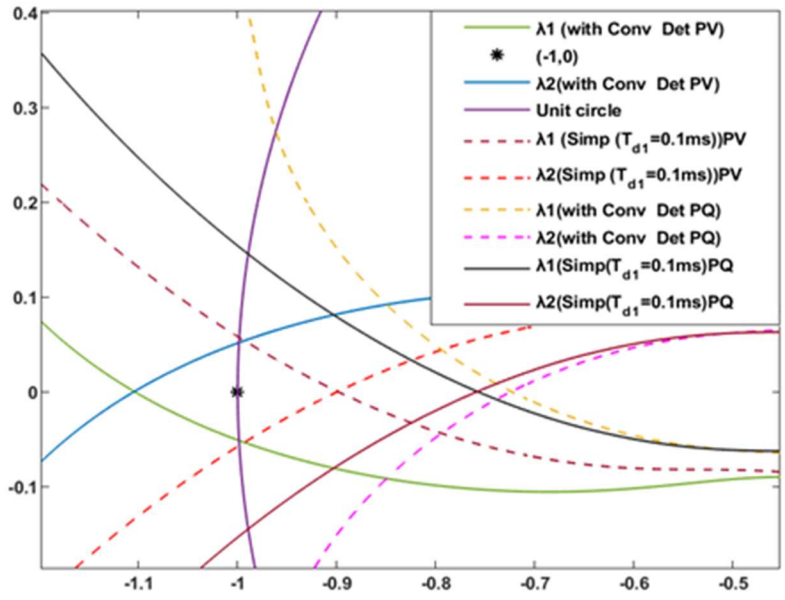

Figure 5.9: Nyquist Stability Comparison between Detailed and Simplified Local PV Converter Models in Coupled System with Remote PV and PQ Converters (Coupling -Two parameters)

To further validate the Nyquist-based findings, Figures 5.10 and 5.11 show the time-domain behaviour of the local converter under Coupling Condition Two for both the detailed and simplified PV models. Before the disturbance, the system remains stable at 10 Hz. At 5 seconds, when the PLL bandwidth increases to 30 Hz, the detailed model begins to show clear oscillations in power, current, and voltage, indicating loss of stability. This behaviour agrees with the Nyquist-based prediction. The simplified model with $T_{d1} = 0.1$ms does not reproduce these oscillations, which shows that it cannot fully capture the dynamic response of the converter under this coupling condition.

In summary, model simplification is used carefully, with full consideration of external network conditions, since the accuracy of stability assessment including IR, EIR, and related indicators depends strongly on both the control mode and the surrounding system strength. For PQ control, strong and weak grids produce consistent behaviour in both the detailed and simplified models because impedance changes and interaction levels remain small. For PV control, simplification is reasonably accurate in strong grids but less reliable in weak grids, where only the detailed model reveals the oscillatory behaviour. This shows that PQ control is robust across different grid strengths, while PV control in weak networks requires more detailed modelling, otherwise simplification may hide instability and underestimate risk.

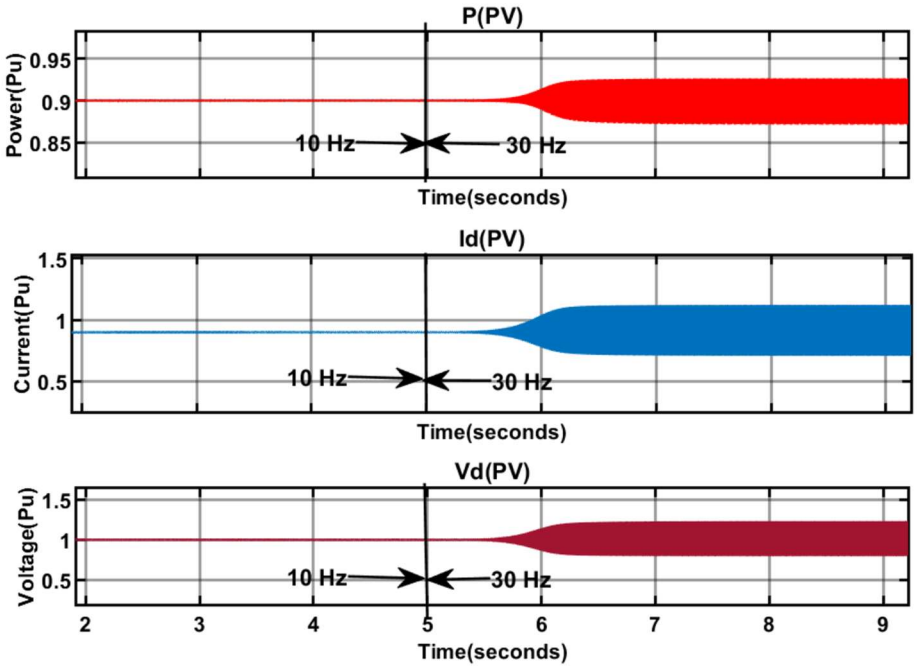

Figure 5.10: Time-Domain Response of Local Converter d-axis Voltage, Current, and Power for Detailed Model Under Coupling Condition Two

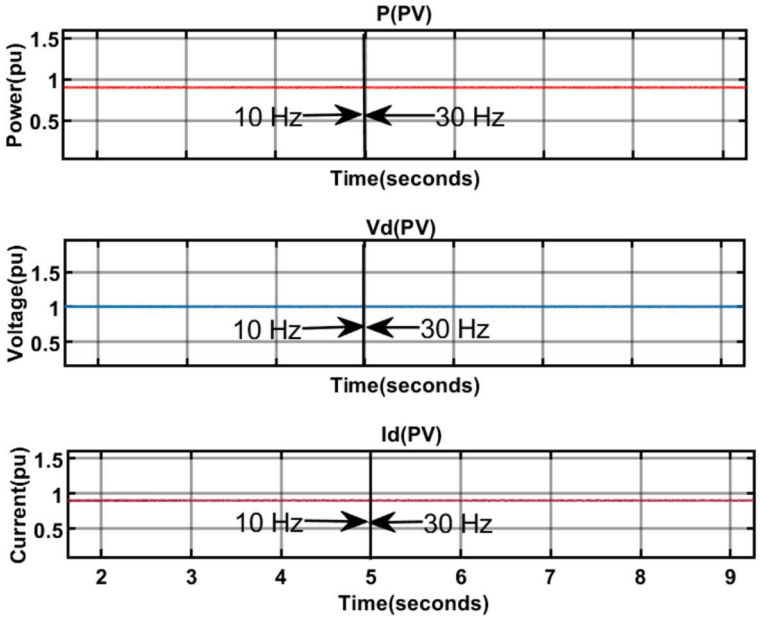

Figure 5.11: Time-Domain Dynamics of Local Converter d-axis Voltage, Current, and Power Using Simplified Model ($T_{d1} = 0.1ms$) Under Coupling Condition Two

5.6 Percentage Error: Detailed vs. Simplified Models

This section evaluates the accuracy of the simplified converter model by comparing it with the detailed representation. The comparison focuses on impedance magnitude, phase, and eigenvalue responses. Numerical integration techniques-specifically the trapezoidal and Simpson's rules-are used to calculate the integrated relative error within the 50-250 Hz frequency range, using a resolution of 2 Hz [147].

For the detailed model, the impedance magnitude and phase are represented as Y_{detm} and Y_{detph}, while Y_{simpm} and Y_{simpph} denote the corresponding quantities for the simplified model. The integrated magnitude and phase errors are defined as:

$$Y_{mdiff} = \int_{50}^{250} \frac{Y_{detm} - Y_{simpm}}{Y_{detm}} df \tag{5.17}$$

$$Y_{phdiff} = \int_{50}^{250} \frac{Y_{detph} - Y_{simpph}}{Y_{detph}} df \tag{5.18}$$

These expressions provide a consistent and reproducible measure of frequency-dependent approximation errors used in Sections 5.6.1 and 5.6.2

5.6.1 Simulation Results for Impedance Error under Coupling-One Configuration

Figures 5.12-5.15 show the comparative error analysis between detailed and simplified multi-VSC models under Coupling-One conditions for PV and PQ control. The study includes three time-delay settings, $T_{d1} = 0.1$, 0.2, and 0.3 ms, and evaluates the remote converter impedance, IR, and EIR.

Figures 5.12 (a) and (b) show that, for remote converter impedance, errors are minimal at $T_{d1} = 0.3\text{ms}$, with PQ control yielding the lowest deviations in both magnitude and phase. Figure 5.13 indicates that IR accuracy peaks at $T_{d1} = 0.3\text{ ms}$, with maximum observed errors of 20% in magnitude and 4° in phase.

Eigenvalue-based IR results in Figures 5.14 and 5.15 reveal that PV control produces slightly higher deviations compared to PQ control. For the second eigenvalue IR, both control modes achieve very close agreement with the detailed model, with peak errors not exceeding 2.5% in magnitude and 0.4° in phase. These results confirm that the proposed model simplification under PQ control yields higher accuracy than that under PV control.

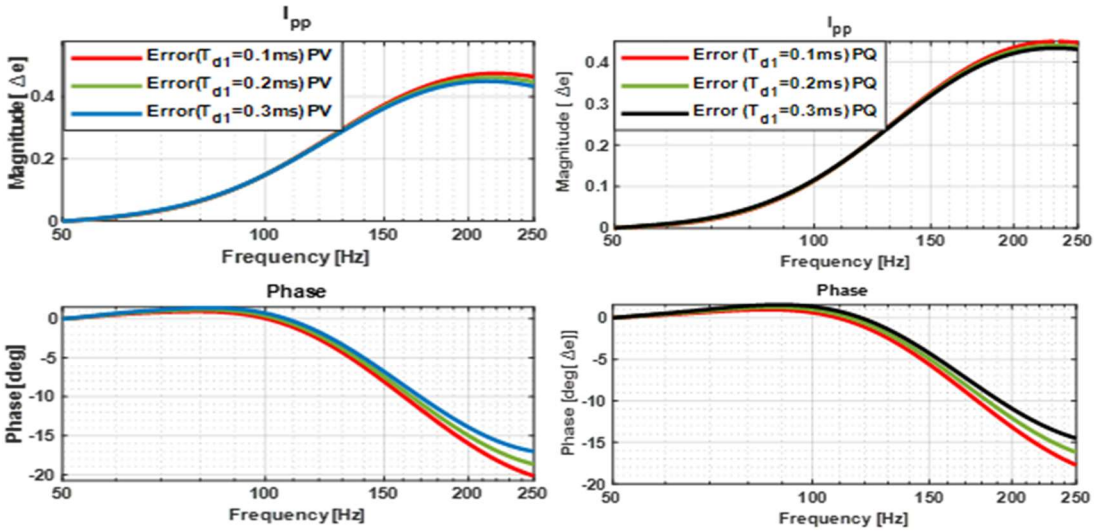

(a) PV (b) PQ

Figure 5.12: Remote converter Impedance error magnitude in (%) and phase (°) for (a) PV and (b) PQ Control modes

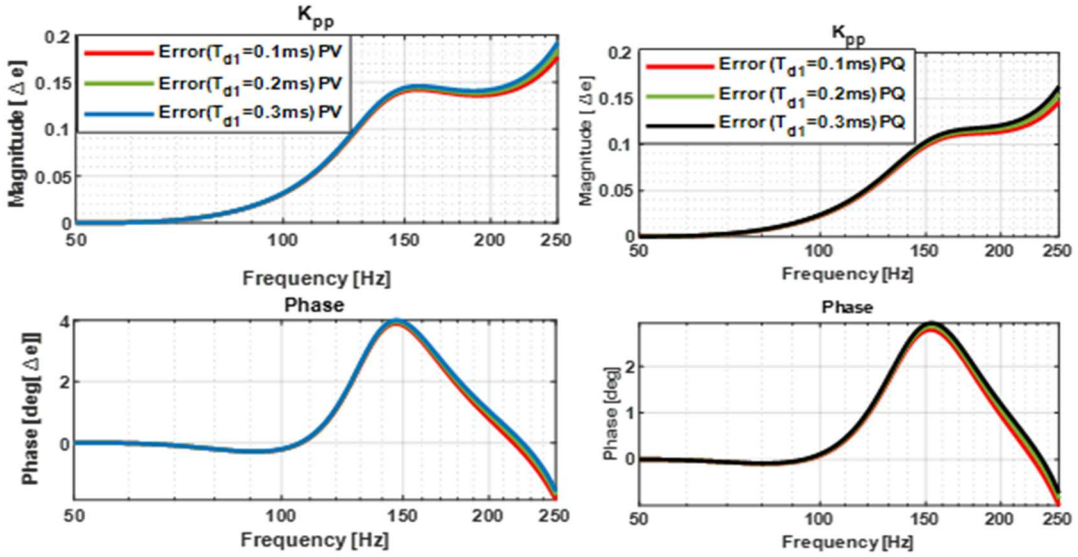

(a) PV (b) PQ

Figure 5.13: IR Mangitude (%) and Phase(°) error for (a) PV (b)PQ Control Modes

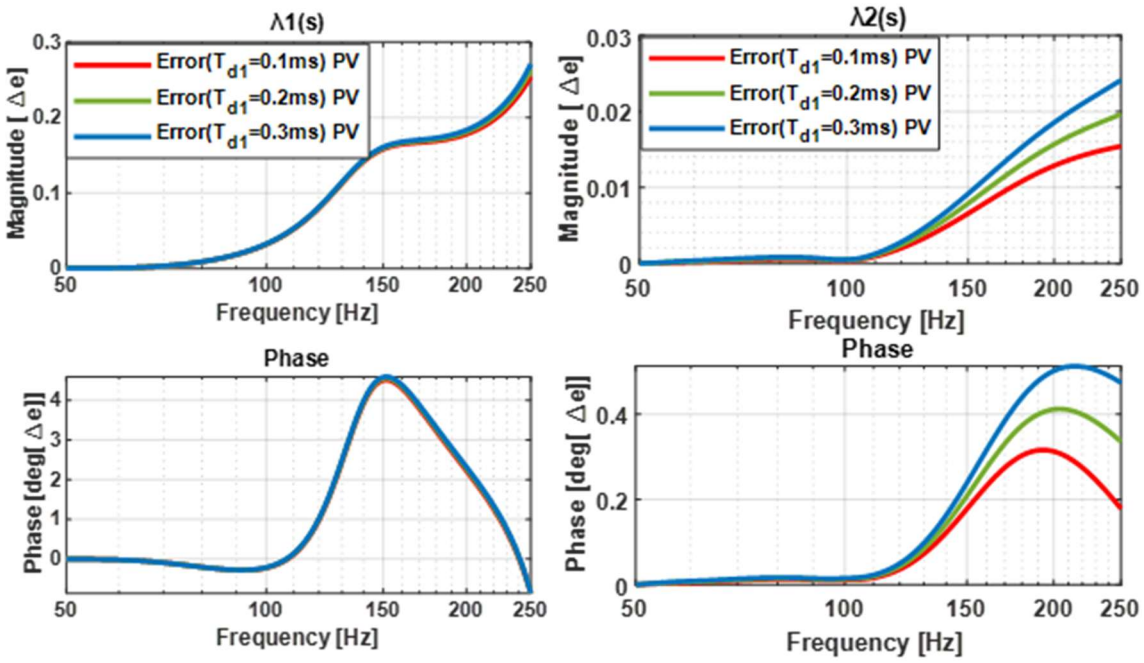

(a) λ1 (b) λ2

Figure 5.14: Eigenvalue of IR change error Magnitude in (%) and phase (°) PV

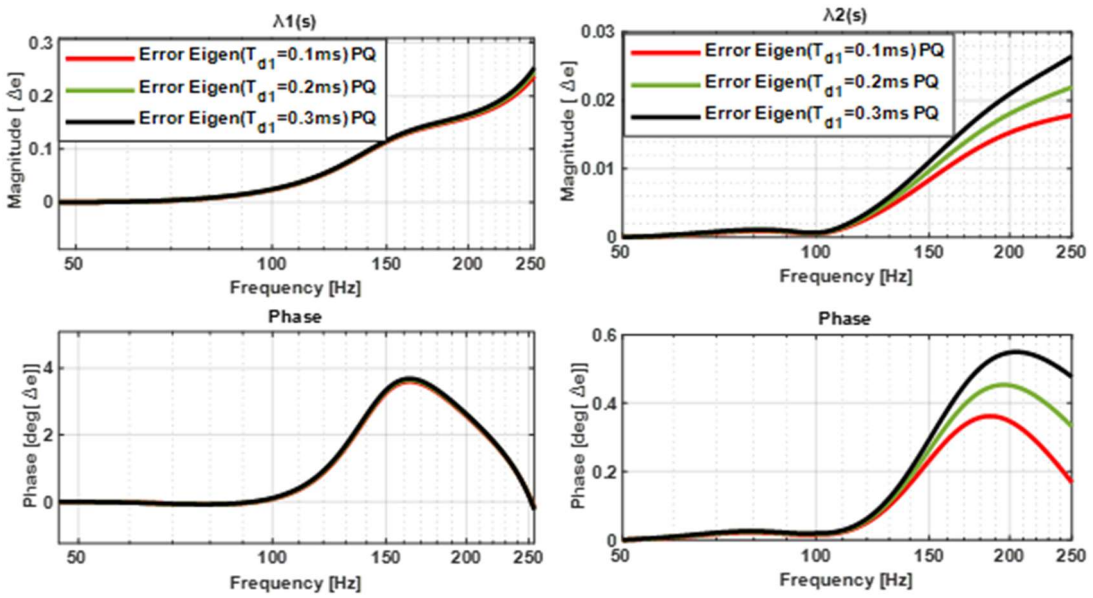

(a) λ1 (b) λ2

Figure 5.15: Eigenvalue of IR change error Magnitude in (%) and phase (°) PQ

Overall, with a suitable time-delay selection, the simplified model maintains good accuracy across the 50-250 Hz frequency range while significantly reducing computational effort. From Figures 5.12-5.15, it can be concluded that the simplified model performs best for PQ control at $T_{d1} = 0.1$ms and for PV control at $T_{d1} = 0.3$ms. However, as discussed in Section 5.5, PV control shows higher impedance variation than PQ control in $Z_{(\text{network+co})}$, IR,

and EIR. The stability implications of these observations will be addressed in the subsequent analysis.

5.6.2 Simulation Results for Impedance Error under Coupling-Two Configuration

Under Coupling-Two (weak grid) conditions, Figures 5.16-5.19 compare the detailed and simplified models for PV and PQ control modes at $T_{d1} = 0.1$, 0.2, and 0.3 ms. The aim is to examine how simplification influences the accuracy of impedance representation.

Figure 5.16 shows that, for the remote converter impedance with I_p reference, PV control produces greater deviations than PQ control, consistent with Section 5.5.1. The maximum errors are about 4.5% in magnitude and 20°in phase. The smallest deviations for both control modes occur at $T_{d1} = 0.3$ms, indicating that accuracy improves with increased delay. The converter impedance itself remains unaffected by coupling unless the operating conditions change.

Figure 5.17 shows that IR errors depend on frequency. PV control presents its highest deviations between 100 Hz and 150 Hz, while PQ control reaches maximum discrepancies between 200 Hz and 250 Hz. The lowest IR errors for both modes occur at $T_{d1} = 0.1$ms.

Figures 5.18 and 5.19 illustrate the eigenvalue errors of the IR under PV and PQ controls. In Figure 5.18(a), representing λ_1, PV control shows larger deviations between detailed and simplified models, confirming its higher sensitivity to simplification and time-delay representation. In contrast, Figure 5.19(a), corresponding to $\lambda_1$under PQ control, exhibits much smaller discrepancies across the same frequency range. For the second eigenvalue (λ_2) in Figures 5.18(b) and 5.19(b), both control modes show close agreement between detailed and simplified models. The maximum observed error is limited to 2% in magnitude and 0.4°in phase, confirming that $T_{d1} = 0.1$ms provides the most accurate representation.

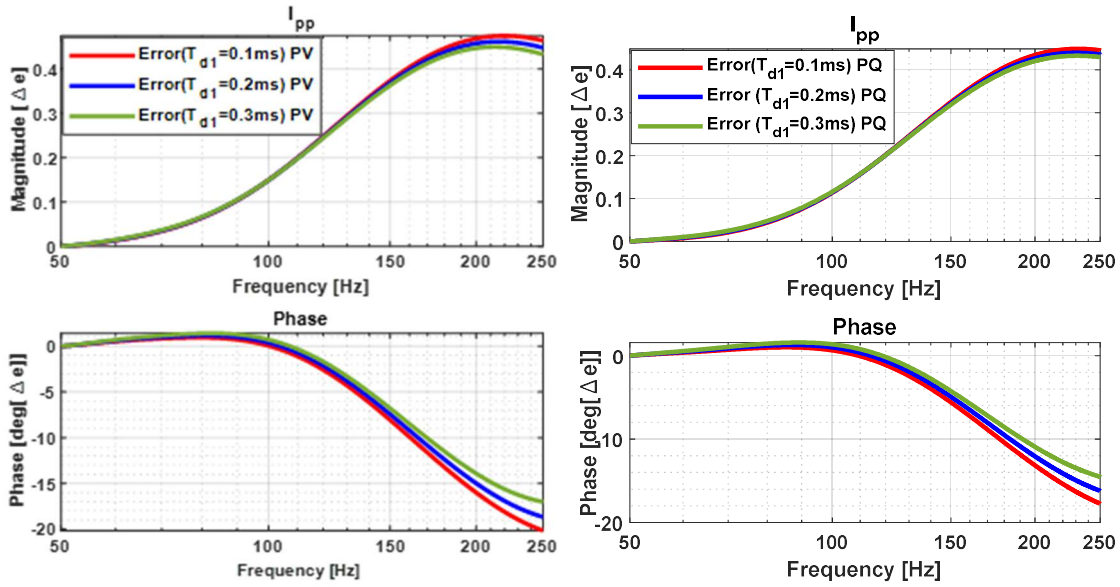

(a) (b)

Figure 5.16: Impedance of remote converter percentage error Magnitude in (%) and phase (°) (a) PV and (b) PQ Control mode

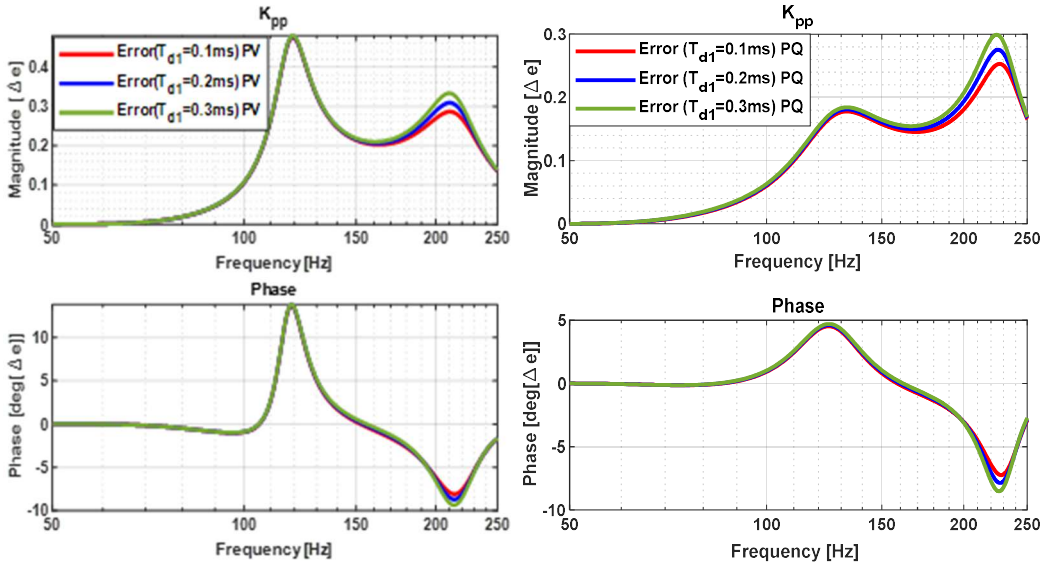

(a) (b)

Figure 5.17: IR percentage error Magnitude in (%) and phase (°) (a) PV (b)PQ

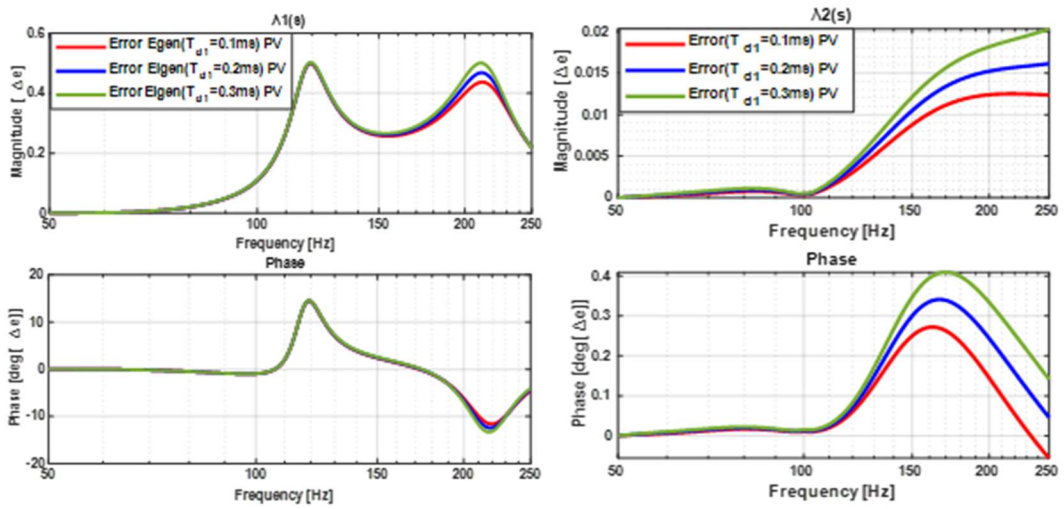

(a) (b)

Figure 5.18: EIR change error PV Magnitude in (%) and phase (°)

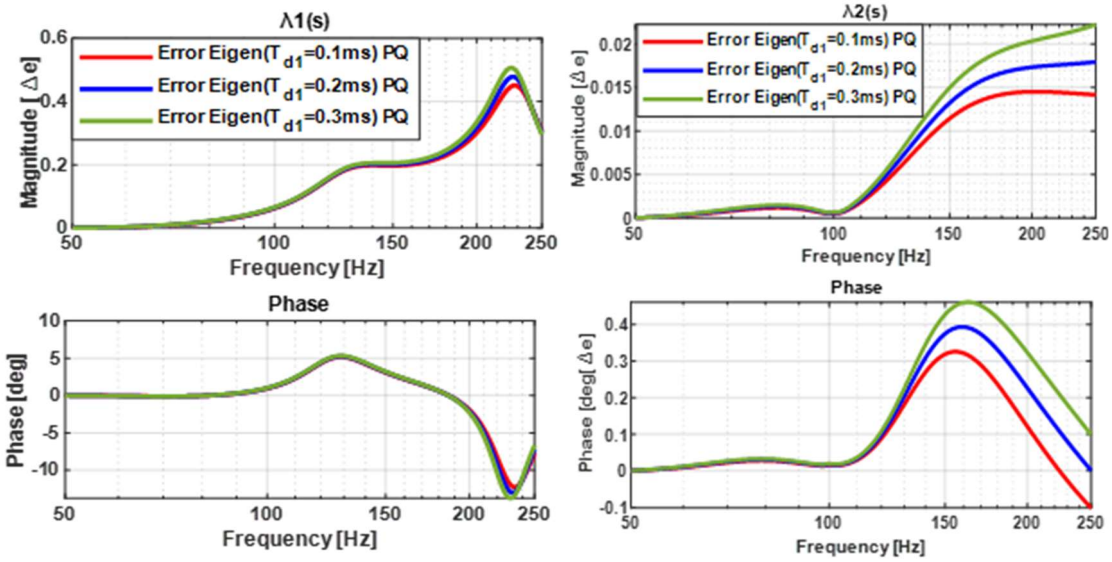

(a) (b)

Figure 5.19: EIR change error Magnitude in (%) and phase (°) PQ

The main purpose of model simplification in this work is to reduce computational effort while retaining sufficient accuracy for stability assessment. Simplification must preserve the influence of each converter on the local converter being analysed. When the remote converter's influence is weak, indicated by low IR and EIR values, a simplified representation with slightly higher error is acceptable. However, under strong interaction or weak network conditions, even small simplification errors can distort stability margins and lead to inaccurate conclusions.

The comparisons confirm this dependency. Results show that the accuracy of reduced-order models depends strongly on network strength and converter control mode. PQ-controlled converters maintain acceptable accuracy across both strong and weak grids, with errors remaining within limits that do not affect stability assessment. PV-controlled converters, however, exhibit larger deviations, especially in weak networks, where simplification errors alter the impedance profile and compromise reliability.

This outcome highlights the importance of adjusting simplification strategies according to converter type and system condition. The error analysis not only measures deviations but also identifies frequency regions where precision is most critical. Aligning the simplification level with interaction strength ensures that stability evaluation remains both accurate and efficient.

5.7 Lead-Lag Compensation for improved Modelling Accuracy

Lead-lag compensation improves stability by shaping the dynamic response and refining steady-state performance, thereby maintaining reliable control operation[148]. In converter-dominated networks, as discussed in Sections 5.5 and 5.6, the degree of model simplification directly affects the accuracy of stability assessment.

When remote converters under PV control are evaluated in weak-grid conditions (Coupling Two) using both the IR and EIR methods, a notable discrepancy arises. The detailed model identifies the actual instability mechanism, while the simplified representation incorrectly suggests stable behaviour. This difference occurs because reduced-order models fail to reproduce the critical phase variation that governs stability margins in systems with low short-circuit strength. The balance between simplification and accuracy therefore becomes essential. Simplification reduces computational demand and improves usability, but it can distort impedance variation and overlook important dynamic interactions. Without careful validation, such approximations may lead to misleading conclusions.

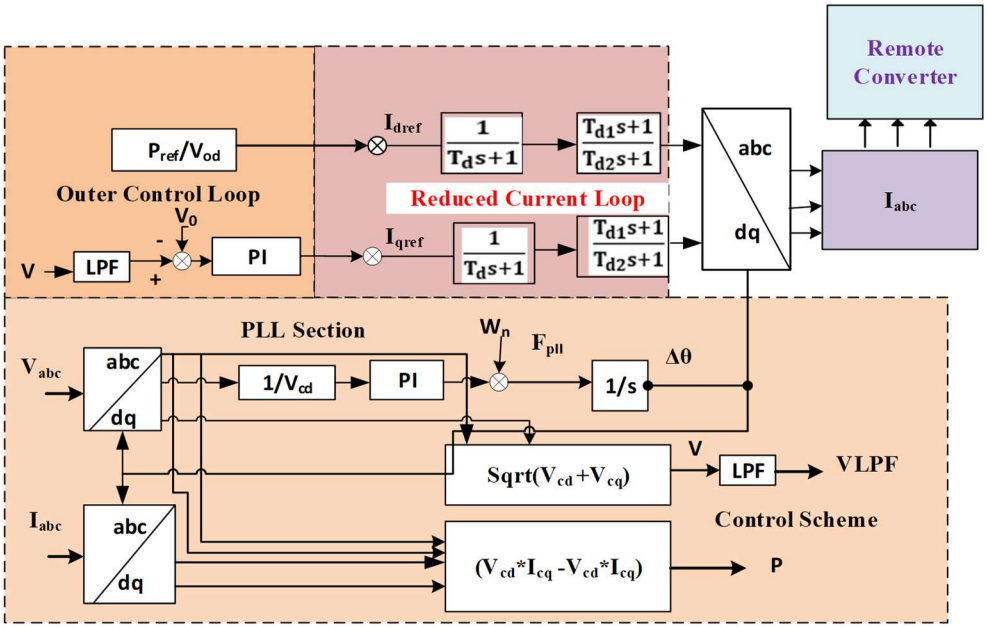

Figure 5.20: Error Reduction analysis of the Remote Converter

To overcome this limitation, lead-lag compensation, illustrated in Figure 5.20, is applied to align simplified model responses with those of the detailed representation. By correcting the phase error introduced through simplification, this method restores the fidelity of impedance behaviour. Consequently, the stability analysis remains accurate, reliable, and practically applicable, even when simplified models are used.

5.7.1 Proposed Lead-lag Compensator

To address this, a lead-lag compensator is integrated into the digital controller, significantly reducing modelling errors across a range of coupling parameters and control modes. The basic structure of the compensator is given by:

$$G(s) = \frac{[1+0.1T_n*s]}{[1+0.2T_n*s]} \tag{5.19}$$

In this expression, the time constant $T_n = \frac{1}{f}$ (with f = 250 Hz) adjusts the dynamic response to align with the target frequency spectrum. The coefficient ratio (0.1:0.2) produces a lead-lag profile optimized to enhance phase margin and closed-loop stability.

For greater precision, Equation (5.19) presents a refined multi-stage compensator design:

$$G_C(s) = K_c.\left(\frac{1+\alpha T_1 s}{1+T_1 s}\right).\left(\frac{1+\beta T_2 s}{1+T_2 s}\right).e^{-T_{do}s} \tag{5.20}$$

In this formulation, K_c denotes the dimensionless compensator gain, α and β are the lead/lag ratios $(\alpha > 1, \beta < 1)$ and $T_1 = \frac{1}{2\pi flead}$, $T_2 = \frac{1}{2\pi flag}$ with $f_{lead} = 250$ Hz and $f_{lag} = 50$Hz define the transition boundaries for lead and lag compensation. The exponential term $e^{-T_{do}s}$,with $T_{d0} = 0.3$ms, accounts for digital control delay. This advanced configuration reduces impedance modelling errors by approximately 1% within the critical frequency range, outperforming Equation (5.19-5.20). Further steps appear in Appendix D.

The accuracy of simplification is quantified by an impedance error metric, defined as:

$$\epsilon = \int_{wmin}^{wmax} | Z_{det}(j\omega) - Z_{simp}(j\omega) |^2 \, d\omega \tag{5.21}$$

This integral evaluates deviations between detailed and simplified impedance models across the 50-250 Hz spectrum, emphasizing larger discrepancies for prioritized correction.

5.7.2 Improving Model Accuracy with Lead-Lag Compensation

The simplified converter model can reproduce the main impedance features of the full-order system, but accuracy decreases when phase deviations appear in the 50-250 Hz range. To address this limitation, a lead-lag compensator is introduced. This adjustment significantly improves the match between simplified and detailed models, ensuring that the simplified representation remains dependable without compromising the interpretation of stability margins.

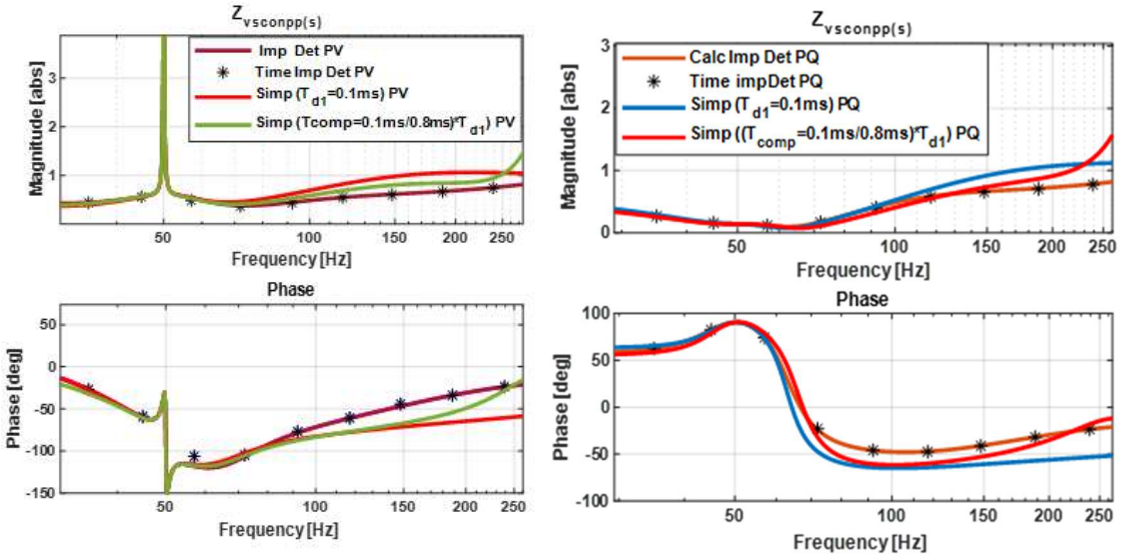

(a) (b)

Figure 5.21: Impedance of remote converter comparison between detailed and simplified with lead-lag (a) PV and (b) PQ Control mode

Figure 5.21(a) shows that, under PV control, the compensated model reproduces both magnitude and phase responses with high precision. A similar improvement is observed for PQ control in Figure 5.21(b). The Nyquist diagrams in Figure 5.22 confirm this agreement, demonstrating that the compensated simplified model preserves stability for the (PV, PV) configuration under Coupling One conditions.

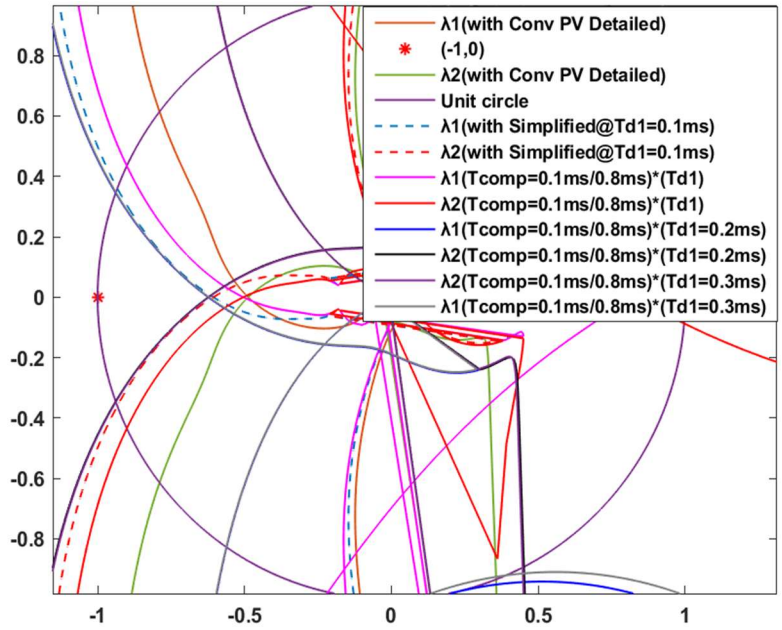

Figure 5.22: Nyquist Plots with Lead-Lag Compensation Under Coupling-One PV Control

The proposed compensation method effectively achieves precise phase alignment between detailed and simplified models by methodically minimizing the error defined in Equation (5.22). This error quantifies the normalized difference between the frequency responses of the detailed (Y_{det}) and simplified (Y_{simp}) models, serving as a critical performance measure:

$$E = \left|\left(\frac{Y_{det}(f) - Y_{simp}(f)}{Y_{det}(f)}\right)\right| \tag{5.22}$$

Minimizing this error requires an adaptive compensation transfer function, defined in Equation (5.23):

$$\Delta Y = G(s).E = \frac{[1+0.1T_n s]}{[1+0.2T_n s]} \left| \left(\frac{Y_{det}(f) - Y_{simp}(f)}{Y_{det}(f)} \right) \right| \quad (5.23)$$

The coefficient ratio of 0.1:0.2 provides effective phase correction, while the time constant T_n allows the model to adapt under varying grid strengths. Figure 5.23 illustrates this adjustment for weak-grid (PV, PV) cases with T_{d1}= 0.3ms. The Nyquist results show that the compensated simplified model nearly overlaps with the detailed impedance, confirming that simplification remains valid even under challenging grid conditions.

This validation is particularly important for PV control, where the system is more prone to instability, and small modelling errors can distort stability assessment. In contrast, PQ operation retains higher accuracy without requiring significant compensation. The proposed lead–lag approach therefore ensures that the simplification process does not reduce accuracy, while also highlighting how targeted compensation can close the gap between detailed and simplified models in practical studies.

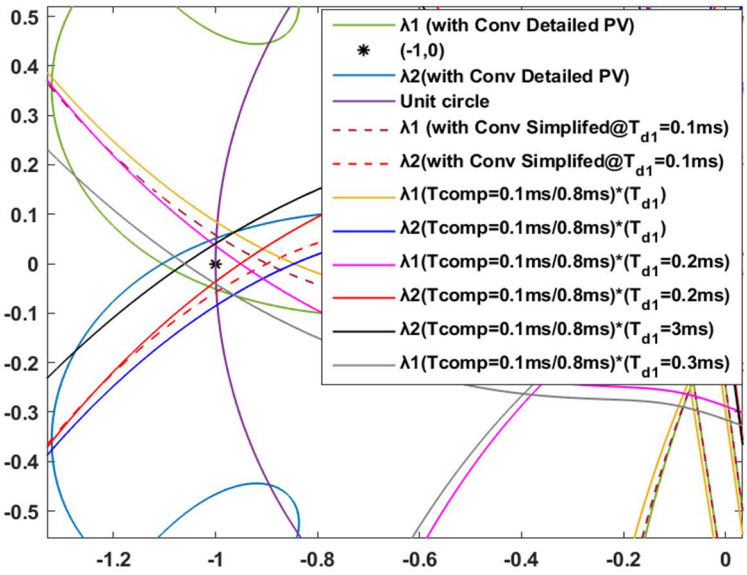

Figure 5.23: Nyquist Plots with Eror Reduction Under Coupling-Two PV Control

5.8 Stability Assessment of PV/PQ-Controlled Converters Using Impedance-Based Indices

To further assess the impact of modelling errors on stability studies, two enhanced impedance-based indices are proposed. These indices measure the deviation between the detailed and simplified representations of converter impedance within a selected frequency

band. The purpose is to quantify the reduction in accuracy that arises when simplified models are used instead of fully detailed ones.

The Enhanced Magnitude Error Index, $\mathcal{E}_{\mathrm{m}}$, is defined as

$$\mathcal{E}_m = \sum_{\mathrm{n}=50}^{250} \frac{1}{\mathrm{n}} \cdot \left| \frac{\mathrm{Z_{detm}(f) - Z_{simpm}(f)}}{\mathrm{Z_{detm}(f)}} \right| \tag{5.24}$$

where $\mathrm{Z_{detm}}$ denotes the impedance magnitude obtained from the detailed model and $\mathrm{Z_{simpm}}$ represents the simplified approximation. The summation is taken over discrete frequency points in the range 50-250 Hz. A weighting factor of $\frac{1}{\mathrm{n}}$ is applied to emphasise the contribution of lower frequencies, where converter control dynamics strongly shape the impedance and where modelling errors are more likely to affect the evaluation of converter–network interactions.

The Enhanced Phase Error Index, $\mathcal{E}_{\phi}$, is given by

$$\mathcal{E}_{\phi} = \sum_{\mathrm{n}=50}^{250} \frac{1}{\mathrm{n}} \cdot \angle \left| \frac{\mathrm{Z_{detph}(f) - Z_{simpph}(f)}}{\mathrm{Z_{detph}(f)}} \right| \tag{5.25}$$

where $\mathrm{Z_{detph}}$ and $\mathrm{Z_{simpph}}$ denote the phase responses of the detailed and simplified impedance models, respectively. This index captures the deviation in phase angle across the same frequency band. The weighting ensures that deviations at low frequencies are more visible, since these have greater impact on phase margin and resonance.

Together, $\mathcal{E}_{\mathrm{m}}$ and $\mathcal{E}_{\phi}$ provide a clear measure of the trade-off between simplification and accuracy in impedance representation. By quantifying both magnitude and phase errors, these indices allow a direct evaluation of how much essential stability information is preserved or lost when simplified models are adopted.

5.8.1 Index-Based Analysis Under Coupling-One

The accuracy of the simplified impedance model is examined using index-based evaluation for both PV and PQ control modes under Coupling-One conditions. Three indices are employed: the Impedance Error Index, the IR Error Index, and the EIR Error Index. These indices, derived from Equations (5.23) -(5.25), quantify the deviation between the simplified and detailed models, and the results are summarized in Tables 5.1 and 5.2.

For PV control (Table 5.1), the simplified model achieves its best accuracy at a T_{d1} of 0.3ms. At this point, the Impedance Error Index registers a magnitude of 0.17 and a phase error of 1.83. The IR Error Index shows a magnitude of 0.0926 with a phase deviation of 1.2619, while the EIR Error Index produces a magnitude of 0.1121 with phase deviations of 1.5616 and 0.2547 for the two eigenvalue components. These values confirm that, under PV control, the simplified model closely reproduces the detailed impedance characteristics when the time delay is set to 0.3ms.

For PQ control (Table 5.2), the highest accuracy is achieved at a shorter T_{d1} of 0.1ms. At this delay, the Impedance Error Index records a magnitude of 0.15 with a phase error of 2.02. The IR Error Index reaches its minimum magnitude of 0.0764 with a phase of 1.0055, while the EIR Error Index yields a magnitude of 0.1011 and phase deviations of 1.5279 and 0.1788. These results demonstrate that the simplified model effectively represents the impedance behaviour of PQ-controlled systems with improved fidelity at a shorter delay compared to PV control.

Overall, the comparison reveals that the simplified model reliably captures stability-relevant impedance behaviour under both control modes. The difference in optimal T_{d1}= 0.3ms for PV control and 0.1ms for PQ control emphasises the need to select delay parameters according to the specific control strategy to maximise modelling accuracy.

Table 5.1: Coupling one Index results under PV control model

Time Delay T_{d1}	**Coupling One PV Control**							
	Impedance Error Index		**IR Error Index**		**EIR Error Index**			
	Magnitude	**Phase**	**Magnitude**	**Phase**	**Magnitude λ_1**	**Phase λ_1**	**Magnitude λ_2**	**Phase λ_2**
0.1 ms	0.16	2.51	0.0950	1.3087	0.1184	1.6411	0.0070	0.1529
0.2 ms	0.16	2.03	0.0940	1.2860	0.1152	1.5998	0.0086	0.2057
0.3 ms	0.17	1.83	0.0926	1.2619	0.1121	1.5616	0.0103	0.2547
1 ms	0.23	2.96	0.1030	1.3706	0.1200	1.6995	0.0186	0.4789

Table 5.2: Coupling one Index results under PQ control model

Time Delay Td1	**Coupling One PQ Control**							
	Impedance Error Index		**IR Error Index**		**EIR Error Index**			
	Magnitude	**Phase**	**Magnitude**	**Phase**	**Magnitude λ_1**	**Phase λ_1**	**Magnitude λ_2**	**Phase λ_2**
0.1 ms	0.15	2.02	0.0764	1.0055	0.1011	1.5279	0.0086	0.1788
0.2 ms	0.16	1.83	0.0786	1.036	0.1030	1.5509	0.0101	0.2325
0.3 ms	0.17	1.80	0.088	1.0625	0.1047	1.5724	0.0117	0.2815
1 ms	0.23	2.34	0.0956	1.2941	0.1147	1.6823	0.0205	0.5201

5.8.2 Index-Based Analysis Under Coupling-Two

Tables 5.3 and 5.4 provide the error evaluation of the simplified impedance model under Coupling-Two conditions for PV and PQ control modes. The analysis considers three indices: the Impedance Error Index, the IR Error Index, and the EIR Error Index.

For PV control (Table 5.3), the best accuracy is observed at a T_{d1} of 0.3ms. At this delay, the Impedance Error Index shows a magnitude of 0.17 with a phase deviation of 1.83. The IR Error Index records its lowest magnitude of 0.1987 with a corresponding phase of 3.288. The EIR Error Index at this point produces a magnitude of 0.2404, while the eigenvalue phases are 4.0684 and 0.20, with a very small eigenvalue magnitude of 0.0105. These results indicate that the simplified model most accurately reflects the detailed system behaviour at 0.3ms under PV operation.

For PQ control (Table 5.4), the highest accuracy is reached at a shorter delay of 0.1ms. At this delay, the Impedance Error Index registers a magnitude of 0.15 with a phase of 2.02. The IR Error Index achieves the smallest magnitude error of 0.1518 with a phase of 2.7259. The EIR Error Index presents a magnitude of 0.2214, with eigenvalue phases of 3.9844 and 0.1166, and a very small eigenvalue magnitude of 0.0085. These values confirm that PQ control yields reliable accuracy at shorter delays compared to PV control.

The comparison shows a clear distinction between the two modes: PV control requires a longer delay (0.3ms) for optimal modelling, while PQ control achieves its best accuracy at a shorter delay (0.1ms). This difference highlights the sensitivity of Coupling-Two to time-delay selection, with PV mode being more prone to error growth when the delay increases.

Table 5.3: Coupling Two Index results under PV control model

Time Delay Td1	**Coupling Two PV Control**							
	Impedance Error Index		**IR Error Index**		**EIR Error Index**			
	Magnitude	**Phase**	**Magnitude**	**Phase**	**Magnitude λ_1**	**Phase λ_1**	**Magnitude λ_2**	**Phase λ_2**
0.1 ms	0.16	2.51	0.2168	3.5517	0.2695	4.5619	0.0071	0.1020
0.2 ms	0.16	2.03	0.2064	3.4097	0.2529	4.2919	0.0088	0.1494
0.3 ms	0.17	1.83	0.1987	3.288	0.2404	4.0684	0.0105	0.2
1 ms	0.23	2.96	0.185	2.8605	0.2123	3.3405	0.0214	0.4673

Table 5.4: Coupling Two Index results under PQ control model

Time Delay Td1	Coupling Two PQ Control							
	Impedance Error Index		IR Error Index		EIR Error Index			
	Magnitude	Phase	Magnitude	Phase	Magnitude λ_1	Phase λ_1	Magnitude λ_2	Phase λ_2
0.1 ms	0.15	2.02	0.1518	2.7259	0.2214	3.9844	0.0085	0.1166
0.2 ms	0.16	1.83	0.1663	2.8782	0.2448	4.2779	0.0103	0.1313
0.3 ms	0.17	1.80	0.1725	2.9462	0.2522	4.3935	0.0101	0.1792
1 ms	0.23	2.34	0.2159	3.4393	0.29	5	0.0207	0.4363

To further illustrate the error distribution, Appendix B (Figure B1:1) presents heat maps of EIR phase λ_1, EIR magnitude λ_1, IR phase, and IR magnitude across a delay range of 0.1-1.0ms. The visualisation shows that, in Coupling-One, both PV and PQ modes maintain low errors throughout the delay range, confirming limited delay impact on accuracy. In contrast, Coupling-Two demonstrates increasing error with delay, particularly under PV control, where deviations rise sharply beyond 0.3ms. PQ control also shows error growth, though less severe compared to PV.

These findings establish clear delay thresholds for accurate simplified modelling. In strong coupling (Coupling-One), the model maintains reliability across a wide delay range. In weak coupling (Coupling-Two), however, precise delay tuning is essential, especially under PV control, to prevent large deviations in stability prediction.

5.8.3 Quantitative Model Validation Using Euclidean Distance

To further assess the model simplification accuracy, the Euclidean distance is applied as:

$$\left|Y_{vsconD} - Y_{vsconsimp}\right| = \sqrt{\sum_{i=1}^{n} \left(Z_{vsconDi} - Z_{vsconsimpi}\right)^2} \quad (5.26)$$

This approach is selected for its ability to amplify error visibility and systematically identify optimal time delays (T_{d1}), overcoming limitations of prior methods in 5.7 could not capture effectively.

The study considers two network configurations Coupling One and Coupling Two and examines both PV and PQ control modes. The evaluation is carried out using the Impedance Error Index, IR Error Index, and EIR Error Index. It is important to note that impedance error values remain unaffected by network strength, which explains the identical impedance error results for both Coupling One and Coupling Two cases under PV and PQ control.

From Tables 5.5-5.6, PV control achieves its lowest error at $T_{d1} = 0.3ms$, where the Euclidean distance across impedance magnitude, phase, and extended impedance indices is minimized. Conversely, PQ control shows better performance at $T_{d1} = 0.1ms$, with consistently smaller error indices across all measures.

These trends remain valid when extending the analysis to Coupling Two scenarios (Tables 5.7-5.8), which include multiple converter interactions. This consistency demonstrates that the chosen methodology is effective even under more complex operating conditions.

The strategic selection of time delays directly enhances computational efficiency without compromising model integrity. By targeting the inner-loop current controllers the fastest dynamics in power electronic systems simplified models enable larger simulation time steps, significantly reducing computational overhead while retaining fidelity for stability studies.

Table 5.5: Coupling one Index results under PV control model

Time Delay Td1	Coupling One PV Control							
	Impedance Error Index		IR Error Index		EIR Error Index			
	Magnitude	Phase	Magnitude	Phase	Magnitude λ_1	Phase λ_1	Magnitude λ_2	Phase λ_2
0.1 ms	0.24	2.65	0.4365	1.5047	0.4673	1.8814	0.2263	0.1526
0.2 ms	0.24	2.25	0.4326	1.4824	0.4618	1.8422	0.2235	0.2063
0.3 ms	0.27	2.10	0.4291	1.4580	0.4565	1.8054	0.2214	0.2561
1 ms	0.56	4.33	0.4268	1.4563	0.4456	1.7578	0.2262	0.5136

Table 5.6:Coupling one Index results under PQ control model

Time Delay Td1	Coupling One PQ Control							
	Impedance Error Index		IR Error Index		EIR Error Index			
	Magnitude	Phase	Magnitude	Phase	Magnitude λ_1	Phase λ_1	Magnitude λ_2	Phase λ_2
0.1 ms	0.32	2.02	0.3591	1.0027	0.3890	1.5292	0.2150	0.1732
0.2 ms	0.37	1.81	0.3645	1.0285	0.3954	1.5521	0.2141	0.2271
0.3 ms	0.42	1.77	0.3700	1.0595	0.4014	1.5736	0.2141	0.2763
1 ms	0.72	2.34	0.4039	1.2912	0.4347	1.6840	0.2172	0.5160

Table 5.7: Coupling Two Index results under PV control model

Time Delay Td1	Coupling Two PV Control							
	Impedance Error Index		IR Error Index		EIR Error Index			
	Magnitude	Phase	Magnitude	Phase	Magnitude λ_1	Phase λ_1	Magnitude λ_2	Phase λ_2
0.1 ms	0.24	2.65	0.5966	3.6902	0.6672	1.5822	0.3480	0.5142
0.2 ms	0.24	2.25	0.6029	3.7266	0.6789	1.5822	0.3396	0.5142
0.3 ms	0.27	2.10	0.6093	3.7672	0.6907	1.5822	0.3340	0.5142
1 ms	0.56	4.33	0.6528	4.1467	0.7379	1.5822	0.3188	0.5142

Table 5.8:Coupling Two Index results under PQ control model

Time Delay Td1	Coupling Two PQ Control							
	Impedance Error Index		IR Error Index		EIR Error Index			
	Magnitude	Phase	Magnitude	Phase	Magnitude λ_1	Phase λ_1	Magnitude λ_2	Phase λ_2
0.1 ms	0.32	2.02	0.4900	2.5448	0.5868	3.7054	0.3184	0.1162
0.2 ms	0.37	1.81	0.4997	2.6218	0.5781	3.8430	0.3201	0.1548
0.3 ms	0.42	1.77	0.5093	2.7011	0.5869	3.9698	0.3209	0.2024
1 ms	0.72	3.33	0.5686	3.2596	0.6560	4.6239	0.2998	0.4631

5.8.4 Error Metrics Index for Different Coupling Configurations

Figure 5.24 illustrates a 3D representation of the magnitude (panel a) and phase (panel b) error metrics for four control configurations, involving couplings between weak and strong grids with PV and PQ control targets. Each configuration is assessed at time delays of $0.1\ \text{ms}, 0.3\ \text{ms},$ and $1.0\ \text{ms}$. The displayed indices are the Impedance Error Index (blue), Impedance Ratio Error Index (green), and Eigenvalue Error Index (red). The Magnitude Error Index $\mathcal{E}_{\text{m}}$ and Phase Error Index $\mathcal{E}_{\phi}$, defined in Equations (5.24) and (5.25), quantify the deviation between detailed and simplified impedance models through frequency-dependent weighting and delay compensation.

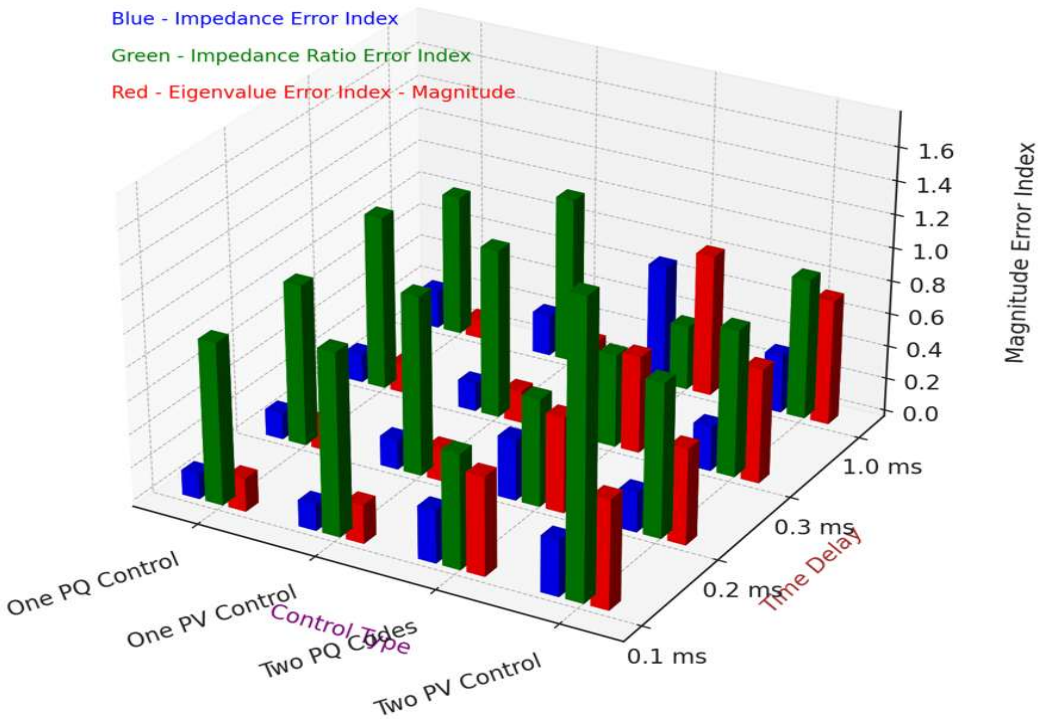

(a) Magnitude

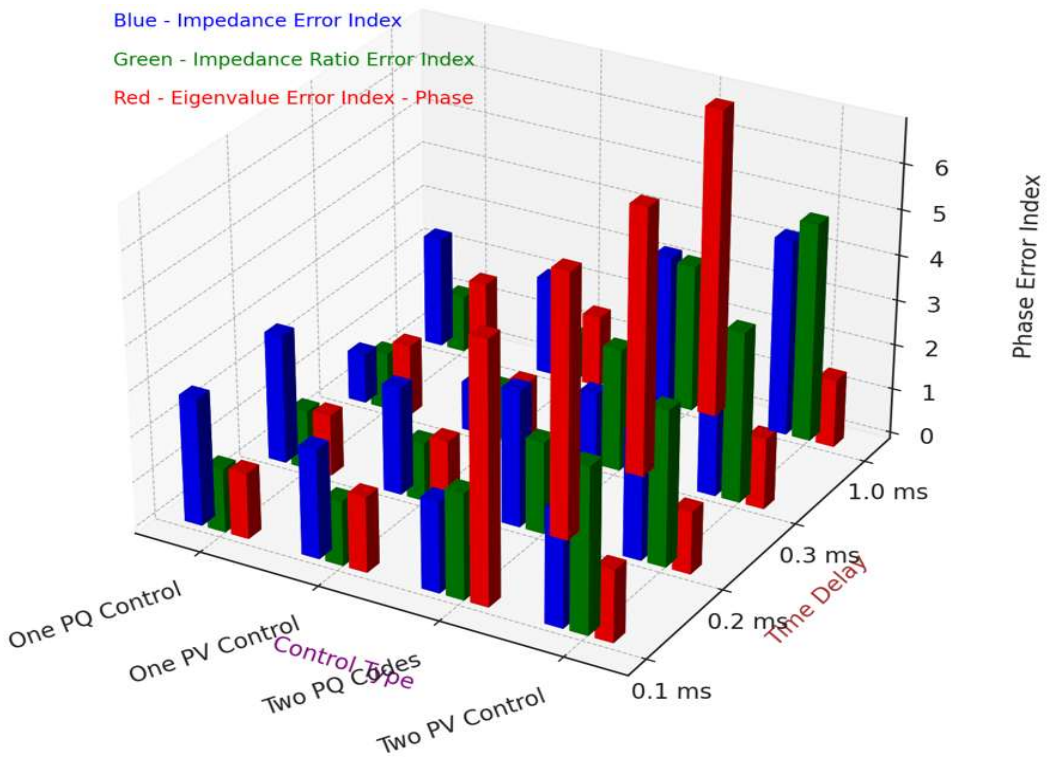

(b) Phase

Figure 5.24: 3D chart of Error Metrices Index for Different Coupling Configuration

The results confirm that careful selection of delay parameters enables the simplified model to reproduce the dynamic response of the detailed model with high accuracy for stability evaluation. The 3D representation further reveals the delay threshold at which accuracy begins to deteriorate, providing a direct basis for determining controller parameters that ensure both computational efficiency and reliable impedance-based stability assessment in converter-dominated power systems.

5.9 Chapter Summary

This chapter studied how simplified impedance models can support the analysis of converter behaviour under different grid strengths. The work examined converters operating with PV and PQ control and compared their responses using the IR and EIR approaches. The objective was to retain the important dynamic characteristics of the converters while removing model components that have limited influence on the main system behaviour.

The results show that when a remote PV converter operates in a weak grid, even small modelling errors caused by simplification can significantly influence the stability of a nearby converter. Therefore, the influence of the converter being simplified must be considered before reducing its model. If the converter has a small impact on the overall system behaviour, the simplified model can tolerate a larger modelling error. However, if the converter strongly affects system stability, even small simplification errors may lead to inaccurate stability conclusions.

At low frequencies, both PV and PQ simplified models follow the behaviour of the detailed model closely. At higher frequencies, the PQ-controlled converter maintains good accuracy across a wider range of grid strengths. In contrast, PV control requires additional lead–lag compensation with properly tuned delay values to keep the simplified model close to the detailed response under weak grid conditions.

The results also indicate that model simplification can reduce computational effort, which is useful when analysing systems with many converters.

Although the proposed methods demonstrate useful performance, the limitations of these approaches have not been discussed in detail in this chapter. Further investigation is therefore required to better understand the possible restrictions of the simplified modelling methods when applied to more complex converter-based power systems.

Chapter 6: Conclusions and Future Work

6.1 General Conclusions

This thesis presented a structured approach for modelling the behaviour of converter-based units and examining their influence on the dynamic response of networks dominated by power-electronic devices. The work followed the structure defined in the thesis index, with each chapter contributing to the central objective: the development of frequency-domain tools that characterise converter dynamics across a wide range of operating conditions. These tools were formulated to explain how multiple converters interact through their control systems, filter arrangements, and operating points in both GFM and GFL modes. The results demonstrated how these interactions shape the surrounding network's response and affect commonly used stability indicators. Each chapter progressed systematically toward this objective, and the complete framework now provides a robust basis for analysing stability in converter-dominated power systems.

The first part developed the frequency-domain models that form the base of the whole study. These models relied on small-signal parts that describe how each block in the control and filter chain shapes the impedance during operation. Every block was added with a clear reason so that the reader could follow the way each part contributes to the full form. Current loops, voltage loops, filters, and outer parts were presented in a direct order, linking their aims to the behaviour seen in the impedance. Only parts with real influence on the response were kept. This approach allowed the models to show clear relations between control aims, physical parts, and the impedance that appears when a converter is placed in a network of any strength.

The second part examined what happens when several units operate in the same region. The focus was on how the impedance of each unit interacts with the impedance of the surrounding area. Certain patterns appear when both sides shape the response in similar ways. These patterns may lead to oscillations when levels of control, loading, or distance between units occur. The study linked these features back to the small-signal parts introduced earlier, which helped clarify why the combined response moves toward an unstable region under some conditions. By keeping each observation tied to the core expressions of the model, the work kept the discussion clear and direct.

To measure the level of interaction between a converter and the network, two indices were developed. The first one, IR, came from the 2×2 impedance ratio in the pn frame. The second one, EIR, came from the eigenvalues of the same ratio. One eigenvalue showed the behaviour of the pp frame, and the other showed the behaviour of the nn frame. These indices gave a clear measure of coupling strength and identified points where resonance may appear. Their values matched the features seen in the time-domain tests, which confirmed that the models captured the true behaviour of the units under study.

After presenting these indices, the work examined how different control aims shape the interaction level. Units that adjust real-power transfer showed strong variation in the index angle at high loading. These units reacted sharply to changes in control settings and created high peaks when several of them shared the same region. Units that regulate real and reactive power separately stayed closer to stable conditions across a wider range of settings. These findings agreed with the expressions from the modelling stage and helped explain why each unit responds in a certain way under load.

A control design was then introduced to reduce the interaction level in units that showed strong coupling with the network. The design added an outer block that supports the current controller with a compensating element. This adjustment improved damping and reduced steep peaks in the impedance profile. Frequency-domain and time-domain tests confirmed the improvement, and the change in index values showed that the behaviour moved toward a more stable region.

The effect of placement in the network was also studied. When a unit with strong damping ability was placed at a central point, the overall stability margin improved. When this same unit was placed in a remote area, the improvement became smaller. The work showed that this behaviour follows from the impedance structure of the network and the way each converter shapes the region around it. The analysis also showed that suitable control choices reduce IR and EIR values and help maintain stable operation.

The study then presented reduced-order models linked to the behaviour shown by IR and EIR. These models kept the key features needed to capture resonance while reducing simulation time. Their accuracy remained strong in the 50-250 Hz range, which is the most important for interaction studies. Units that regulate real and reactive power together were captured well with fewer parts. Units that regulate real-power transfer needed a phase-

compensating part to match the full model. A lead-lag element was enough to achieve close agreement. When a remote PV unit operates in a weak area, even small errors in the reduced model can affect the stability picture of the local converter, so the amount of simplification must match the influence of the unit. When a unit has low impact, larger simplifications can be tolerated; when a unit has strong impact, the reduced model must be more accurate.

In summary, the thesis developed a clear and practical framework for studying regions with several converter-based units. The work showed how control settings, filter structures, operating points, and placement influence the impedance shape and the interaction level. The proposed methods identify resonances, compare control strategies, and guide stability improvement. The framework supports planning of renewable-rich networks and is adaptable to larger systems and advanced converter technologies.

6.2 Prospects for Further Research

The work completed here opens several directions that can help advance impedance-based stability studies and the understanding of interaction in networks with many converters:

1. Large Networks with Different Converter Types: Systems that combine two-level converters, modular units, and line-commutated devices may show strong interaction effects. Extending the IR and EIR ideas to these mixed units can show how their controls affect one another.
2. Use in System Reduction and Limited Data Conditions: Future work can study how the IR and EIR ideas can guide model reduction in large grids, especially when only part of the system data is available. This can help keep accuracy while lowering the effort needed to study stability.
3. Use of Field Data: IR and EIR can be expanded using data measured in real grids. This can include the effect of parameter shifts, noise, and changes in operation that appear during daily use.
4. Hardware-Based Validation: Implement the developed impedance and interaction models using hardware-in-the-loop (HIL) and real-time digital simulation (RTDS) platforms to evaluate performance under realistic operational conditions.

These points can support future studies that aim to improve stability margins, refine control tuning, and help expand networks that contain many converters units.

Bibliography

[1] L. Xie et al., ‘The role of electric grid research in addressing climate change’, Nat. Clim. Chang., vol. 14, no. 9, pp. 909–915, Sep. 2024, doi: 10.1038/s41558-024-02092-1.

[2] B. Brown and S. J. Spiegel, ‘Coal, climate justice, and the cultural politics of energy transition’, Glob. Environ. Polit., vol. 19, no. 2, pp. 149–168, Jan. 2019, doi: 10.1162/glep_a_00501.

[3] Q. Hassan et al., ‘The renewable energy role in the global energy Transformations’, Renewable Energy Focus , vol. 48, Mar. 2024, doi: 10.1016/j.ref.2024.100545.

[4] Desnz, ‘Energy Trends March 2025’, Mar. 2025. Accessed: Oct. 28, 2025. [Online]. Available: https://assets.publishing.service.gov.uk/media/67e4f5d855239fa04d412067/Energy_Trends_March_2025.pdf

[5] G. Brindley, G. Willems, L. Ramirez, P. Cole, V. Klonari, and J. Bickley, ‘Wind energy in Europe TEXT AND ANALYSIS: Giuseppe Costanzo’.

[6] L. Meegahapola, A. Sguarezi, J. S. Bryant, M. Gu, E. R. Conde D., and R. B. A. Cunha, ‘Power system stability with power-electronic converter interfaced renewable power generation: Present issues and future trends’, Jul. 01, 2020, MDPI AG. doi: 10.3390/en13133441.

[7] S. Lumbreras, H. Abdi, and A. Ramos, Transmission Expansion Planning: The Network Challenges of the Energy Transition. Springer International Publishing, 2020. doi: 10.1007/978-3-030-49428-5.

[8] A. Adib, B. Mirafzal, X. Wang, and R. Blaabjerg, ‘On stability of voltage source inverters in weak grids’, IEEE Access, vol. 6, pp. 4427–4439, Dec. 2017, doi: 10.1109/ACCESS.2017.2788818.

[9] D. Al Kez, A. M. Foley, F. Ahmed, and D. J. Morrow, ‘Overview of frequency control techniques in power systems with high inverter-based resources: Challenges and mitigation measures’, Oct. 01, 2023, John Wiley and Sons Inc. doi: 10.1049/stg2.12117.

[10] Y. Chen, L. Xu, A. Egea-Alvarez, B. Marshall, M. H. Rahman, and A. D. Oluwole, 'MMC Impedance Modeling and Interaction of Converters in Close Proximity', IEEE J. Emerg. Sel. Top. Power Electron., vol. 9, no. 6, pp. 7223–7236, Dec. 2021, doi: 10.1109/JESTPE.2020.3031489.

[11] C. Henderson, A. Egea-Alvarez, and L. Xu, 'Analysis of optimal grid-forming converter penetration in AC connected offshore wind farms', International Journal of Electrical Power and Energy Systems, vol. 157, Jun. 2024, doi: 10.1016/j.ijepes.2024.109851.

[12] A. Rygg, 'Impedance-based Methods for Small-signal Analysis of Power Electronics Dominated Systems', PhD thesis, Norwegian University of Science and Technology (NTNU), Trondheim, Norway, 2018. Accessed: Mar. 07, 2025. [Online]. Available: http://hdl.handle.net/11250/2584000

[13] National Grid ESO, 'Navigation', National Grid Electricity System Operator (ESO). Accessed: Aug. 16, 2025. [Online]. Available: https://www.nationalgrideso.com/future-energy/pathway-2030-holistic-network-design

[14] Department for Energy Security and Net Zero, 'Clean Power 2030: Action Plan: A new era of clean electricity', Dec. 2024. Accessed: Jul. 22, 2025. [Online]. Available: https://www.gov.uk/government/publications/clean-power-2030-action-plan/clean-power-2030-action-plan-a-new-era-of-clean-electricity-main-report

[15] National Grid ESO, 'Beyond 2030 A national blueprint for a decarbonised electricity system in Great Britain', Mar. 2024. Accessed: Jul. 24, 2025. [Online]. Available: https://www.nationalgrideso.com/future-energy/beyond2030

[16] P. P. J. V. S. et al. Kundur, 'Definition and classification of power system stability', IEEE, vol. 19, no. 3, pp. 1387–1401, 2004, doi: 10.1109/TPWRS.2004.825981.

[17] N. Hatziargyriou et al., 'Definition and Classification of Power System Stability - Revisited & Extended', IEEE Transactions on Power Systems, vol. 36, no. 4, pp. 3271–3281, Jul. 2021, doi: 10.1109/TPWRS.2020.3041774.

[18] C. Henderson, D. Vozikis, D. Holiday, X. Bian, and A. Egea-Àlvarez, 'Assessment of grid-connected wind turbines with an inertia response by considering internal dynamics', Energies (Basel)., vol. 13, no. 5, 2020, doi: 10.3390/en13051038.

[19] U. Perera, A. M. T. Oo, and R. Zamora, ‘Sub Synchronous Oscillations under High Penetration of Renewables—A Review of Existing Monitoring and Damping Methods, Challenges, and Research Prospects’, Nov. 01, 2022, MDPI. doi: 10.3390/en15228477.

[20] C. Henderson, A. Egea-Alvarez, and L. Xu, ‘Analysis of multi-converter network impedance using MIMO stability criterion for multi-loop systems’, Electric Power Systems Research, vol. 211, Oct. 2022, doi: 10.1016/j.epsr.2022.108542.

[21] S. Subedi, Y. Gui, and Y. Xue, ‘Applications of Data-Driven Dynamic Modeling of Power Converters in Power Systems: An Overview’, IEEE Trans. Ind. Appl., pp. 1–23, 2025, doi: 10.1109/TIA.2025.3529797.

[22] G. R. Mugambi et al., ‘Methodologies for offshore wind power plants stability analysis’, Oct. 2024, [Online]. Available: http://arxiv.org/abs/2410.13521

[23] Ha Thi Nguyen, ‘Frequency Characterization and Control for Future Low Inertia Systems’, PhD thesis, Technical University of Denmark (Danmarks Tekniske Universitet), Lyngby, Denmark, 2018.

[24] P. Makolo, R. Zamora, and T. T. Lie, ‘The role of inertia for grid flexibility under high penetration of variable renewables - A review of challenges and solutions’, Sep. 01, 2021, Elsevier Ltd. doi: 10.1016/j.rser.2021.111223.

[25] K. Strunz, K. Almunem, C. Wulkow, M. Kuschke, M. Valescudero, and X. Guillaud, ‘Enabling 100% Renewable Power Systems Through Power Electronic Grid-Forming Converter and Control: System Integration for Security, Stability, and Application to Europe’, Proceedings of the IEEE, vol. 111, no. 7, pp. 891–915, Jul. 2023, doi: 10.1109/JPROC.2022.3193374.

[26] M. Muftić Dedović, A. Mujezinović, N. Dautbašić, A. Alihodžić, A. Memić, and S. Avdaković, ‘Estimation of Power System Inertia with the Integration of Converter-Interfaced Generation via MEMD during a Large Disturbance’, Applied Sciences (Switzerland), vol. 14, no. 2, Jan. 2024, doi: 10.3390/app14020681.

[27] S. Hu, J. Yang, Y. Wang, Y. Zhao, and C. Chao, ‘Inertia and Primary Frequency Response Requirement Assessment for High-Penetration Renewable Power Systems Based on Planning Perspective’, Sustainability (Switzerland), vol. 15, no. 23, Dec. 2023, doi: 10.3390/su152316191.

[28] S. Shahzad and E. Jasińska, ‘Renewable Revolution: A Review of Strategic Flexibility in Future Power Systems’, Jul. 01, 2024, Multidisciplinary Digital Publishing Institute (MDPI). doi: 10.3390/su16135454.

[29] F. D. Bianchi, J. L. Domínguez-García, and O. Gomis-Bellmunt, ‘Control of multi-terminal HVDC networks towards wind power integration: A review’, Mar. 01, 2016, Elsevier Ltd. doi: 10.1016/j.rser.2015.11.024.

[30] H. Wu, F. Zhao, and X. Wang, ‘A Survey on Impedance-Based Dynamics Analysis Method for Inverter-Based Resources’, IEEE Power Electronics Magazine, vol. 10, no. 3, pp. 43–51, Sep. 2023, doi: 10.1109/MPEL.2023.3303104.

[31] N. Liu, H. Wang, D. Zhou, H. Shi, and Z. Chen, ‘Comprehensive review of power system oscillations in large-scale power electronic-based renewable energy power plants’, Jul. 01, 2023, American Institute of Physics Inc. doi: 10.1063/5.0148188.

[32] A. Taghvaie, T. Warnakulasuriya, D. Kumar, F. Zare, R. Sharma, and D. M. Vilathgamuwa, ‘A Comprehensive Review of Harmonic Issues and Estimation Techniques in Power System Networks Based on Traditional and Artificial Intelligence/Machine Learning’, 2023, Institute of Electrical and Electronics Engineers Inc. doi: 10.1109/ACCESS.2023.3260768.

[33] N. Johansson, L. Ängquist, and H. P. Nee, ‘A comparison of different frequency scanning methods for study of subsynchronous resonance’, IEEE Transactions on Power Systems, vol. 26, no. 1, pp. 356–363, Feb. 2011, doi: 10.1109/TPWRS.2010.2046345.

[34] G. Amico, ‘Wind farm high frequency electrical resonances: impedance-based stability analysis and mitigation techniques’, University of Strathclyde, Glasgow, 2019. doi: https://doi.org/10.48730/9y5y-k667.

[35] M. S. Annakkage, C. Karawita, and U. D. Annakkage, ‘Frequency scan-based screening method for device dependent sub-synchronous oscillations’, IEEE Transactions on Power Systems, vol. 31, no. 3, pp. 1872–1878, May 2016, doi: 10.1109/TPWRS.2015.2442653.

[36] X. Wang, F. Blaabjerg, and W. Wu, ‘Modeling and analysis of harmonic stability in an AC power-electronics- based power system’, IEEE Trans. Power Electron., vol. 29, no. 12, pp. 6421–6432, 2014, doi: 10.1109/TPEL.2014.2306432.

[37] X. Wang and F. Blaabjerg, ‘Harmonic Stability in Power Electronic-Based Power Systems: Concept, Modeling, and Analysis’, IEEE Trans. Smart Grid, vol. 10, no. 3, pp. 2858–2870, May 2019, doi: 10.1109/TSG.2018.2812712.

[38] M. Cespedes and J. Sun, ‘Impedance modeling and analysis of grid-connected voltage-source converters’, IEEE Trans. Power Electron., vol. 29, no. 3, pp. 1254–1261, 2014, doi: 10.1109/TPEL.2013.2262473.

[39] M. R. D., ‘Input filter considerations in design and applications of switching regulators’, Proc. IEEE IAS’76, vol. 11, pp. 91–107, 1976, Accessed: Jul. 26, 2022. [Online]. Available: https://cir.nii.ac.jp/crid/1573387450557085184.bib?lang=en

[40] J. Sun, ‘Impedance-based stability criterion for grid-connected inverters’, IEEE Trans. Power Electron., vol. 26, no. 11, pp. 3075–3078, 2011, doi: 10.1109/TPEL.2011.2136439.

[41] C. M. Wildrick, F. C. Lee, B. H. Cho, and B. Choi, ‘A Method of Defining the Load Impedance Specification for A Stable Distributed Power System’, 1995.

[42] S. D. Sudhoff and S. F. Glover, ‘Admittance space stability analysis of power electronic systems’, IEEE Trans. Aerosp. Electron. Syst., vol. 36, no. 3 PART 1, pp. 965–973, 2000, doi: 10.1109/7.869516.

[43] F. Liu, J. Liu, H. Zhang, and D. Xue, ‘Stability issues of Z+Z type cascade system in hybrid energy storage system (HESS)’, IEEE Trans. Power Electron., vol. 29, no. 11, pp. 5846–5859, 2014, doi: 10.1109/TPEL.2013.2295259.

[44] J. Sun, ‘Impedance-based stability criterion for grid-connected inverters’, IEEE Trans. Power Electron., vol. 26, no. 11, pp. 3075–3078, 2011, doi: 10.1109/TPEL.2011.2136439.

[45] H. Gong, D. Yang, and X. Wang, ‘Impact analysis and mitigation of synchronization dynamics for dq impedance measurement’, IEEE Trans. Power Electron., vol. 34, no. 9, pp. 8797–8807, Sep. 2019, doi: 10.1109/TPEL.2018.2886096.

[46] S. Shah, P. Koralewicz, V. Gevorgian, and R. Wallen, ‘Sequence Impedance Measurement of Utility-Scale Wind Turbines and Inverters - Reference Frame, Frequency Coupling, and MIMO/SISO Forms’, IEEE Transactions on Energy Conversion, vol. 37, no. 1, pp. 75–86, Mar. 2022, doi: 10.1109/TEC.2021.3093516.

[47] Y. Liao and X. Wang, ‘Impedance-Based Stability Analysis for Interconnected Converter Systems with Open-Loop RHP Poles’, IEEE Trans. Power Electron., vol. 35, no. 4, pp. 4388–4397, Apr. 2020, doi: 10.1109/TPEL.2019.2939636.

[48] B. Wen, D. Boroyevich, R. Burgos, P. Mattavelli, and Z. Shen, ‘Small-Signal Stability Analysis of Three-Phase AC Systems in the Presence of Constant Power Loads Based on Measured d-q Frame Impedances’, IEEE Trans. Power Electron., vol. 30, no. 10, pp. 5952–5963, Oct. 2015, doi: 10.1109/TPEL.2014.2378731.

[49] A. Rygg, M. Molinas, C. Zhang, and X. Cai, ‘A Modified Sequence-Domain Impedance Definition and Its Equivalence to the dq-Domain Impedance Definition for the Stability Analysis of AC Power Electronic Systems’, IEEE J. Emerg. Sel. Top. Power Electron., vol. 4, no. 4, pp. 1383–1396, Dec. 2016, doi: 10.1109/JESTPE.2016.2588733.

[50] G. C. Paap, ‘Symmetrical components in the time domain and their application to power network calculations’, IEEE Transactions on Power Systems, vol. 15, no. 2, pp. 522–528, May 2000, doi: 10.1109/59.867135.

[51] G. Amico, A. Egea-Alvarez, P. Brogan, and S. Zhang, ‘Small-Signal Converter Admittance in the Frame: Systematic Derivation and Analysis of the Cross-Coupling Terms’, IEEE Transactions on Energy Conversion, vol. 34, no. 4, pp. 1829–1838, Dec. 2019, doi: 10.1109/TEC.2019.2924922.

[52] S. Shah and L. Parsa, ‘Impedance Modeling of Three-Phase Voltage Source Converters in DQ, Sequence, and Phasor Domains’, IEEE Transactions on Energy Conversion, vol. 32, no. 3, pp. 1139–1150, Sep. 2017, doi: 10.1109/TEC.2017.2698202.

[53] L. Harnefors, M. Bongiorno, and S. Lundberg, ‘Input-admittance calculation and shaping for controlled voltage-source converters’, IEEE Transactions on Industrial Electronics, vol. 54, no. 6, pp. 3323–3334, Dec. 2007, doi: 10.1109/TIE.2007.904022.

[54] R. W. Kenyon, D. Maksimovic, and R. Erickson, ‘The Renewables Driven Intersection of Power Systems and Power Electronics: Dynamics, Simulation, and Novel Frequency Control’, 2013. Accessed: Apr. 29, 2025. [Online]. Available: https://www.proquest.com/dissertations-theses/renewables-driven-intersection-power-systems/docview/2720364800/se-2

[55] L. Xu, L. Yao, and C. Sasse, ‘Grid integration of large DFIG-based wind farms using VSC transmission’, IEEE Transactions on Power Systems, vol. 22, no. 3, pp. 976–984, Aug. 2007, doi: 10.1109/TPWRS.2007.901306.

[56] P. Beaumont et al., ‘Impact of Voltage Source Converter (VSC) Based HVDC Transmission on AC System Protection A technical report to the System Protection Subcommittee of the Power System Relaying and Control Committee’.

[57] M. N. I. Sarkar, L. G. Meegahapola, and M. Datta, ‘Reactive power management in renewable rich power grids: A review of grid-codes, renewable generators, support devices, control strategies and optimization Algorithms’, IEEE Access, vol. 6, pp. 41458–41489, May 2018, doi: 10.1109/ACCESS.2018.2838563.

[58] R. Zeng, ‘Design, Analysis, and Operation of Hybrid Modular Multilevel Converters for HVDC Applications’, Mar. 2015. doi: 10.48730/a24g-w684.

[59] Z. L. W. D. L. Z. Z. W. and J. Z. Huanhai Xin, ‘Generalized-impedance and Stability Criterion for Grid-connected Converters’, Systems and Control, Jun. 2017, doi: https://doi.org/10.48550/arXiv.1706.05625.

[60] D. Dimitropoulos, X. Wang, and F. Blaabjerg, ‘Stability Analysis in Multi-VSC (Voltage Source Converter) Systems of Wind Turbines’, Applied Sciences (Switzerland), vol. 14, no. 8, Apr. 2024, doi: 10.3390/app14083519.

[61] H. Guo, Z. Zhang, and Z. Xu, ‘Impedance modelling and stability analysis of modular multilevel converter with different types of grid-forming control schemes’, IET Generation, Transmission and Distribution, vol. 17, no. 2, pp. 337–353, Jan. 2023, doi: 10.1049/gtd2.12668.

[62] F. Dai, D. Zeng, S. Liu, and G. Wang, ‘A practical impedance modeling method of MMC-HVDC transmission system for medium- and high-frequency resonance analysis’, Electric Power Systems Research, vol. 212, Nov. 2022, doi: 10.1016/j.epsr.2022.108636.

[63] T. Chen, D. Feng, X. Wu, C. Lu, and B. Xu, ‘Modeling and stability analysis of interaction between converters in AC-DC distribution systems’, Front. Energy Res., vol. 10, Feb. 2023, doi: 10.3389/fenrg.2022.1035193.

[64] J. Bialek, ‘What does the GB power outage on 9 August 2019 tell us about the current state of decarbonised power systems?’, Energy Policy, vol. 146, Nov. 2020, doi: 10.1016/j.enpol.2020.111821.

[65] M. Kazem BAKHSHIZADEH, Ł. Kocewiak, J. HJERRILD Ørsted Offshore Fredericia, D. Frede BLAABJERG, and C. Leth BAK, ‘Mohammad Kazem Bakhshizadeh (modow@orsted.dk) Grid Converter Stability Aspects in Offshore Wind Power Plants’.

[66] S. F. Panah and H. Liu, ‘Methods for Stability Analysis in Converter-Dominated Power Systems: A Comparative Approach in Weak and Strong Grid’, in 2025 International Conference on Electronics and Renewable Systems (ICEARS), IEEE, Feb. 2025, pp. 38–45. doi: 10.1109/ICEARS64219.2025.10941113.

[67] T. Xue, J. Lyu, H. Wang, and X. Cai, ‘A Complete Impedance Model of a PMSG-Based Wind Energy Conversion System and Its Effect on the Stability Analysis of MMC-HVDC Connected Offshore Wind Farms’, IEEE Transactions on Energy Conversion, vol. 36, no. 4, pp. 3449–3461, Dec. 2021, doi: 10.1109/TEC.2021.3074798.

[68] M. Val Escudero, G. Lietz, J. Mahseredjian, D. Ramasubramanian, and B. Jayasekara, ‘Principles and Practical Considerations for the Use of Time-Domain Simulation Software Programs in Power System Dynamics Analysis’, 2024, pp. 101–158. doi: 10.1007/978-3-031-47821-5_3.

[69] Y. Zhu, T. C. Green, X. Zhou, Y. Li, D. Kong, and Y. Gu, ‘Impedance Margin Ratio: a New Metric for Small-Signal System Strength’, IEEE Transactions on Power Systems, 2024, doi: 10.1109/TPWRS.2024.3371231.

[70] C. Henderson et al., ‘Exploring an Impedance-Based SCR for Accurate Representation of Grid-Forming Converters’, in IEEE Power and Energy Society General Meeting, IEEE Computer Society, 2022. doi: 10.1109/PESGM48719.2022.9916733.

[71] M. Zhao, X. Yuan, J. Hu, and Y. Yan, ‘Voltage Dynamics of Current Control Time-Scale in a VSC-Connected Weak Grid’, IEEE Transactions on Power Systems, vol. 31, no. 4, pp. 2925–2937, Jul. 2016, doi: 10.1109/TPWRS.2015.2482605.

[72] Y. Li, Q. Liu, B. Wu, Y. Wang, and Q. Huang, ‘Impedance Transfer Functions Fitting Methods of Grid-connected Inverters: Comparison and Application’, in 2022 International Conference on Power Energy Systems and Applications, ICoPESA 2022, Institute of Electrical and Electronics Engineers Inc., 2022, pp. 331–336. doi: 10.1109/ICoPESA54515.2022.9754427.

[73] X. Wang, Y. He, D. Pan, H. Zhang, Y. Ma, and X. Ruan, ‘Passivity Enhancement for LCL-Filtered Inverter With Grid Current Control and Capacitor Current Active Damping’, IEEE Trans. Power Electron., vol. 37, no. 4, pp. 3801–3812, Apr. 2022, doi: 10.1109/TPEL.2021.3111677.

[74] Y. Liao, H. Wu, X. Wang, M. Ndreko, R. Dimitrovski, and W. Winter, ‘Stability and Sensitivity Analysis of Multi-Vendor, Multi-Terminal HVDC Systems’, IEEE Open Journal of Power Electronics, vol. 4, pp. 52–66, 2023, doi: 10.1109/OJPEL.2023.3234803.

[75] K. Jacobs, Y. Seyedi, L. Meng, U. Karaagac, and J. Mahseredjian, ‘A comparative study on frequency scanning techniques for stability assessment in power systems incorporating wind parks’, Electric Power Systems Research, vol. 220, Jul. 2023, doi: 10.1016/j.epsr.2023.109311.

[76] N. Pogaku, M. Prodanović, and T. C. Green, ‘Modeling, analysis and testing of autonomous operation of an inverter-based microgrid’, IEEE Trans. Power Electron., vol. 22, no. 2, pp. 613–625, Mar. 2007, doi: 10.1109/TPEL.2006.890003.

[77] F. Göthner, J. Roldán-Pérez, R. E. Torres-Olguin, and O. M. Midtgård, ‘Reduced-Order Model of Distributed Generators with Internal Loops and Virtual Impedance’, IEEE Trans. Smart Grid, vol. 13, no. 1, pp. 119–128, Jan. 2022, doi: 10.1109/TSG.2021.3120323.

[78] S. Eberlein and K. Rudion, ‘Impact of Inner Control Loops on Small-Signal Stability and Model-Order Reduction of Grid-Forming Converters’, IEEE Trans. Smart Grid, vol. 14, no. 4, pp. 2812–2824, Jul. 2023, doi: 10.1109/TSG.2022.3220723.

[79] M. Kabalan, P. Singh, and D. Niebur, ‘Nonlinear Lyapunov Stability Analysis of Seven Models of a DC/AC Droop Controlled Inverter Connected to an Infinite Bus’, IEEE Trans. Smart Grid, vol. 10, no. 1, pp. 772–781, Jan. 2019, doi: 10.1109/TSG.2017.2752146.

[80] Y. Gu, N. Bottrell, and T. C. Green, ‘Reduced-Order Models for Representing Converters in Power System Studies’, IEEE Trans. Power Electron., vol. 33, no. 4, pp. 3644–3654, Apr. 2018, doi: 10.1109/TPEL.2017.2711267.

[81] N. Shabanikia and S. A. Khajehoddin, ‘Weighted Dynamic Aggregation Modeling of Grid-Following Inverters to Analyze Renewable DG Integrated Microgrids’, IEEE Transactions on Industrial Electronics, vol. 71, no. 1, pp. 583–594, Jan. 2024, doi: 10.1109/TIE.2023.3243269.

[82] H. Huang, Y. Lin, Y. Zhou, Y. Zhao, P. Zhang, and L. Fan, ‘Data-driven modeling of power system dynamics: Challenges, state of the art, and future work’, Sep. 01, 2023, Institute of Electrical and Electronics Engineers Inc. doi: 10.23919/IEN.2023.0023.

[83] M. J. Li, C. K. Tse, and M. Yi, ‘The Impact of Inverter-Based Resources (IBRs) on Cascading Failures in Power Systems’, IEEE Transactions on Power Systems, vol. 39, no. 4, pp. 5946–5955, Jul. 2024, doi: 10.1109/TPWRS.2023.3339684.

[84] G. Grdenic, F. J. C. Garcia, N. D. M. D. Campos, F. Villella, and J. Beerten, ‘Model Order Reduction of Voltage Source Converters Based on the Ac Side Admittance Assessment: From EMT to RMS’, IEEE Transactions on Power Delivery, vol. 38, no. 1, pp. 56–67, Feb. 2023, doi: 10.1109/TPWRD.2022.3179836.

[85] M. A. Torres L., L. A. C. Lopes, L. A. Morán T., and J. R. Espinoza C., ‘Self-tuning virtual synchronous machine: A control strategy for energy storage systems to support dynamic frequency control’, IEEE Transactions on Energy Conversion, vol. 29, no. 4, pp. 833–840, Dec. 2014, doi: 10.1109/TEC.2014.2362577.

[86] M. Khan, W. Wu, and L. Li, ‘Grid-forming control for inverter-based resources in power systems: A review on its operation, system stability, and prospective’, Apr. 27, 2024, John Wiley and Sons Inc. doi: 10.1049/rpg2.12991.

[87] C. Henderson, A. Egea-Alvarez, T. Kneuppel, G. Yang, and L. Xu, ‘Grid Strength Impedance Metric: An Alternative to SCR for Evaluating System Strength in Converter Dominated Systems’, IEEE Transactions on Power Delivery, 2023, doi: 10.1109/TPWRD.2022.3233455.

[88] Y. Han et al., ‘Modeling and stability analysis of LCL-type grid-connected inverters: A comprehensive overview’, IEEE Access, vol. 7, pp. 114975–115001, 2019, doi: 10.1109/ACCESS.2019.2935806.

[89] Y. K. Wu, W. H. Yang, Y. L. Hu, and P. Q. Dzung, ‘Frequency regulation at a wind farm using time-varying inertia and droop controls’, in IEEE Transactions on Industry Applications, Institute of Electrical and Electronics Engineers Inc., Jan. 2019, pp. 213–224. doi: 10.1109/TIA.2018.2868644.

[90] J. Zhu, C. D. Booth, G. P. Adam, A. J. Roscoe, and C. G. Bright, ‘Inertia emulation control strategy for VSC-HVDC transmission systems’, IEEE Transactions on Power Systems, vol. 28, no. 2, pp. 1277–1287, 2013, doi: 10.1109/TPWRS.2012.2213101.

[91] R. Aljarrah, B. B. Fawaz, Q. Salem, M. Karimi, H. Marzooghi, and R. Azizipanah-Abarghooee, ‘Issues and Challenges of Grid-Following Converters Interfacing Renewable Energy Sources in Low Inertia Systems: A Review’, IEEE Access, vol. 12, pp. 5534–5561, 2024, doi: 10.1109/ACCESS.2024.3349630.

[92] X. Lin, J. Yu, R. Yu, J. Zhang, Z. Yan, and H. Wen, ‘Improving Small-Signal Stability of Grid-Connected Inverter under Weak Grid by Decoupling Phase-Lock Loop and Grid Impedance’, IEEE Transactions on Industrial Electronics, vol. 69, no. 7, pp. 7040–7053, Jul. 2022, doi: 10.1109/TIE.2021.3095791.

[93] A. Singhal, T. L. Vu, and W. Du, ‘Consensus Control for Coordinating Grid-Forming and Grid-Following Inverters in Microgrids’, IEEE Trans. Smart Grid, vol. 13, no. 5, pp. 4123–4133, Sep. 2022, doi: 10.1109/TSG.2022.3158254.

[94] Y. Teng, W. Deng, W. Pei, Y. Li, L. Ding, and H. Ye, ‘Review on grid-forming converter control methods in high-proportion renewable energy power systems’, Global Energy Interconnection, vol. 5, no. 3, pp. 328–342, Jun. 2022, doi: 10.1016/j.gloei.2022.06.010.

[95] H. Zhu and S. Q. Alex Huang Vassilis Kekatos Radu Marculescu Surya Santoso, ‘Data-driven Modeling and Graph Learning for Power System Operations Committee’, Aug. 2024. Accessed: Sep. 29, 2025. [Online]. Available: https://hdl.handle.net/2152/129561 https://doi.org/10.26153/tsw/56064

[96] Â. J. J Rezek, C. D. Alberto Coelho, J. E. Manuel Vicente, J. Antonio Cortez, and P. Ricardo Laurentino, ‘The Modulus Optimum (MO) Method Applied to Voltage Regulation Systems: Modeling, Tuning and Implementation’.

[97] Y. Chen and L. Xu, ‘Coupling Admittance Analysis of VSC Connected to Weak Grid System in Sequence-Frame’.

[98] C. Henderson, A. Egea-Alvarez, S. Fekriasl, T. Knueppel, G. Amico, and L. Xu, 'The Effect of Grid-Connected Converter Control Topology on the Diagonal Dominance of Converter Output Impedance', IEEE Open Access Journal of Power and Energy, vol. 10, pp. 617–628, 2023, doi: 10.1109/OAJPE.2023.3316297.

[99] L. Harnefors, 'Modeling of three-phase dynamic systems using complex transfer functions and transfer matrices', IEEE Transactions on Industrial Electronics, vol. 54, no. 4, pp. 2239–2248, Aug. 2007, doi: 10.1109/TIE.2007.894769.

[100] J. Rocabert, A. Luna, F. Blaabjerg, and P. Rodríguez, 'Control of power converters in AC microgrids', IEEE Trans. Power Electron., vol. 27, no. 11, pp. 4734–4749, 2012, doi: 10.1109/TPEL.2012.2199334.

[101] F. Milano, F. Dörfler, G. Hug ETH Zürich, D. J. Hill, and G. Verbič, 'Foundations and Challenges of Low-Inertia Systems', Dublin, Ireland, Aug. 2018. doi: 10.23919/PSCC.2018.8450880.

[102] P. Unruh, M. Nuschke, P. Strauß, and F. Welck, 'Overview on grid-forming inverter control methods', Energies (Basel)., vol. 13, no. 10, May 2020, doi: 10.3390/en13102589.

[103] S. Alshahrani, K. Khan, M. Abido, and M. Khalid, 'Grid-Forming Converter and Stability Aspects of Renewable-Based Low-Inertia Power Networks: Modern Trends and Challenges', May 01, 2024, Springer Nature. doi: 10.1007/s13369-023-08399-z.

[104] M. Tozak, S. Taskin, I. Sengor, and B. P. Hayes, 'Modeling and Control of Grid Forming Converters: A Systematic Review', IEEE Access, vol. 12, pp. 107818–107843, 2024, doi: 10.1109/ACCESS.2024.3437236.

[105] R. Rosso, X. Wang, M. Liserre, X. Lu, and S. Engelken, 'Grid-Forming Converters: Control Approaches, Grid-Synchronization, and Future Trends - A Review', 2021, Institute of Electrical and Electronics Engineers Inc. doi: 10.1109/OJIA.2021.3074028.

[106] S. Rogalla et al., 'Grid-forming converters in interconnected power systems: Requirements, testing aspects, and system impact', IET Renewable Power Generation, Nov. 2024, doi: 10.1049/rpg2.12967.

[107] Y. Gu and T. C. Green, ‘Power System Stability With a High Penetration of Inverter-Based Resources’, Proceedings of the IEEE, vol. 111, no. 7, pp. 832–853, Jul. 2023, doi: 10.1109/JPROC.2022.3179826.

[108] A. Jain, J. N. Sakamuri, and N. A. Cutululis, ‘Grid-forming control strategies for black start by offshore wind power plants’, Wind Energy Science, vol. 5, no. 4, pp. 1297–1313, Oct. 2020, doi: 10.5194/wes-5-1297-2020.

[109] D. B. Rathnayake et al., ‘Grid Forming Inverter Modeling, Control, and Applications’, IEEE Access, vol. 9, pp. 114781–114807, 2021, doi: 10.1109/ACCESS.2021.3104617.

[110] G. Song, B. Cao, and L. Chang, ‘Review of Grid-forming Inverters in Support of Power System Operation’, Chinese Journal of Electrical Engineering, vol. 8, no. 1, pp. 1–15, Mar. 2022, doi: 10.23919/CJEE.2022.000001.

[111] I. Ray, ‘Review of impedance-based analysis methods applied to grid-forming inverters in inverter-dominated grids’, May 01, 2021, MDPI AG. doi: 10.3390/en14092686.

[112] L. Antonio De Souza Ribeiro, F. D. Freijedo, F. De Bosio, M. Soares Lima, J. M. Guerrero, and M. Pastorelli, ‘Full Discrete Modeling, Controller Design, and Sensitivity Analysis for High-Performance Grid-Forming Converters in Islanded Microgrids’, IEEE Trans. Ind. Appl., vol. 54, no. 6, pp. 6267–6278, Nov. 2018, doi: 10.1109/TIA.2018.2847635.

[113] P. Sun, H. Xu, J. Yao, Y. Chi, S. Huang, and J. Cao, ‘Dynamic Interaction Analysis and Damping Control Strategy of Hybrid System With Grid-Forming and Grid-Following Control Modes’, IEEE Transactions on Energy Conversion, vol. 38, no. 3, pp. 1639–1649, Sep. 2023, doi: 10.1109/TEC.2023.3249965.

[114] F. Dörfler and D. Groß, ‘Control of Low-Inertia Power Systems’, Robotics, and Autonomous Systems Annu. Rev. Control Robot. Auton. Syst. 2023, vol. 15, pp. 415–460, 2025, doi: 10.1146/annurev-control-052622.

[115] R. V. Ferreira, S. M. Silva, H. M. A. Antunes, and G. Venkataramanan, ‘Dynamic Analysis of Grid-Connected Droop-Controlled Converters and Synchronverters’, Journal of Control, Automation and Electrical Systems, vol. 30, no. 5, pp. 741–753, Oct. 2019, doi: 10.1007/s40313-019-00482-x.

[116] Y. Shan, J. Hu, M. Liu, J. Zhu, and J. M. Guerrero, ‘Model Predictive Voltage and Power Control of Islanded PV-Battery Microgrids with Washout-Filter-Based Power Sharing Strategy’, IEEE Trans. Power Electron., vol. 35, no. 2, pp. 1227–1238, Feb. 2020, doi: 10.1109/TPEL.2019.2930182.

[117] W. Issa, S. Sharkh, and M. Abusara, ‘A review of recent control techniques of drooped inverter-based AC microgrids’, Apr. 01, 2024, John Wiley and Sons Ltd. doi: 10.1002/ese3.1670.

[118] P. ; A. G. K. ; S. M. et al. Christensen, ‘High Penetration of Power Electronic Interfaced Power Sources and the Potential Contribution of Grid Forming Converters’, Brussels, Belgium, Jun. 2020. Accessed: Feb. 20, 2025. [Online]. Available: https://www.entsoe.eu/events/2020/01/30/workshop-on-high-penetration-of-power-electronic-interfaced-power-sources-and-the-potential-contribution-of-grid-forming-converters

[119] C. Li, Y. Huang, H. Deng, X. Zhang, and H. Zhao, ‘A novel grid-forming technology for transient stability enhancement of power system with high penetration of renewable energy’, International Journal of Electrical Power and Energy Systems, vol. 143, Dec. 2022, doi: 10.1016/j.ijepes.2022.108402.

[120] H. Zhang, W. Xiang, W. Lin, and J. Wen, ‘Grid Forming Converters in Renewable Energy Sources Dominated Power Grid: Control Strategy, Stability, Application, and Challenges’, Journal of Modern Power Systems and Clean Energy, vol. 9, no. 6, pp. 1239–1256, Nov. 2021, doi: 10.35833/MPCE.2021.000257.

[121] J. Matevosyan et al., ‘Grid-forming inverters: Are they the key for high renewable penetration?’, IEEE Power and Energy Magazine, vol. 17, no. 6, pp. 89–98, Nov. 2019, doi: 10.1109/MPE.2019.2933072.

[122] G. Cui, Z. Chu, and F. Teng, ‘Control-Mode as a Grid Service in Software-Defined Power Grids: GFL vs GFM’, IEEE Transactions on Power Systems, vol. 40, no. 1, pp. 314–326, 2025, doi: 10.1109/TPWRS.2024.3404339.

[123] K. Vatta Kkuni, S. Mohan, G. Yang, and W. Xu, ‘Comparative assessment of typical control realizations of grid forming converters based on their voltage source behaviour’, Dec. 01, 2023, Elsevier Ltd. doi: 10.1016/j.egyr.2023.05.073.

[124] Y. Li, Y. Gu, and T. C. Green, ‘Revisiting Grid-Forming and Grid-Following Inverters: A Duality Theory’, IEEE Transactions on Power Systems, vol. 37, no. 6, pp. 4541–4554, Nov. 2022, doi: 10.1109/TPWRS.2022.3151851.

[125] L. Xu, H. Xin, L. Huang, H. Yuan, P. Ju, and D. Wu, ‘Symmetric Admittance Modeling for Stability Analysis of Grid-Connected Converters’, IEEE Transactions on Energy Conversion, vol. 35, no. 1, pp. 434–444, Mar. 2020, doi: 10.1109/TEC.2019.2943255.

[126] J. Samanes et al., ‘Control Design and Stability Analysis of Power Converters: The MIMO Generalized Bode Criterion’, IEEE J. Emerg. Sel. Top. Power Electron., vol. 8, no. 2, pp. 1880–1893, Jun. 2020, doi: 10.1109/JESTPE.2019.2941829.

[127] C. R. Shah, M. Molinas, S. Føyen, S. D’Arco, R. Nilsen, and M. Amin, ‘Single Coordinate Bode Plots for Stability Evaluation of MIMO Power Electronics Systems via a Frequency Coupling Corrective Factor’, Nov. 21, 2024. doi: 10.36227/techrxiv.173220610.07636645/v1.

[128] K. Najdek and R. Nalepa, ‘The Frequency-and the Time-Domain Design of a Dual Active Bridge Converter Output Voltage Regulator Based on the D-Decomposition Technique’, IEEE Access, vol. 9, pp. 71388–71405, 2021, doi: 10.1109/ACCESS.2021.3078410.

[129] M. Amin and M. Molinas, ‘Small-Signal Stability Assessment of Power Electronics Based Power Systems: A Discussion of Impedance-and Eigenvalue-Based Methods’, IEEE Trans. Ind. Appl., vol. 53, no. 5, pp. 5014–5030, Sep. 2017, doi: 10.1109/TIA.2017.2712692.

[130] A. Lunardi, L. F. N. Lourenço, E. Munkhchuluun, L. Meegahapola, and A. J. S. Filho, ‘Grid-Connected Power Converters: An Overview of Control Strategies for Renewable Energy’, Energies (Basel)., vol. 15, no. 11, Jun. 2022, doi: 10.3390/en15114151.

[131] J. Sun, ‘Frequency-Domain Stability Criteria for Converter-Based Power Systems’, IEEE Open Journal of Power Electronics, vol. 3, pp. 222–254, 2022, doi: 10.1109/OJPEL.2022.3155568.

[132] F. Ahmadloo and S. Pirooz Azad, ‘Grid interaction of multi-VSC systems for renewable energy integration’, IET Renewable Power Generation, vol. 17, no. 5, pp. 1212–1223, Apr. 2023, doi: 10.1049/rpg2.12676.

[133] P. Wang, P. Liu, T. Gu, N. Jiang, and X. P. Zhang, ‘Small-Signal Stability of DC Current Flow Controller Integrated Meshed Multi-Terminal HVDC System’, IEEE Transactions on Power Systems, vol. 38, no. 1, pp. 188–203, Jan. 2023, doi: 10.1109/TPWRS.2022.3168023.

[134] L. Xiong, X. Liu, Y. Liu, and F. Zhuo, ‘Modeling and Stability Issues of Voltage-source Converter-dominated Power Systems: A Review’, Nov. 01, 2022, China Electric Power Research Institute. doi: 10.17775/CSEEJPES.2020.03590.

[135] M. Cheah-Mane, A. Egea-Alvarez, E. Prieto-Araujo, H. Mehrjerdi, O. Gomis-Bellmunt, and L. Xu, ‘Modeling and analysis approaches for small-signal stability assessment of power-electronic-dominated systems’, Jan. 01, 2023, John Wiley and Sons Ltd. doi: 10.1002/wene.453.

[136] C. Gao, S. Fei, Y. Ma, J. Xu, K. Wang, and G. Li, ‘Multi-Domain-Mapping-Based Impedance Calculation Method for Oscillatory Stability Analysis of VSC-Based Power System’, IEEE Transactions on Power Systems, 2024, doi: 10.1109/TPWRS.2024.3401590.

[137] N. Cifuentes, M. Sun, R. Gupta, and B. C. Pal, ‘Black-Box Impedance-Based Stability Assessment of Dynamic Interactions between Converters and Grid’, IEEE Transactions on Power Systems, vol. 37, no. 4, pp. 2976–2987, Jul. 2022, doi: 10.1109/TPWRS.2021.3128812.

[138] R. D. Middlebrook, ‘Measurement of loop gain in feedback systems’, International Journal of Electronics, vol. 38, no. 4, pp. 485–512, 1975, doi: 10.1080/00207217508920421.

[139] D. Yang and Y. Sun, ‘Generalized Impedance-Based Stability Analysis for System-Level Small-Signal Stability Assessment of Large-Scale Power Electronics-Dominated Power Systems’, in Proceedings of the Energy Conversion Congress and Exposition - Asia, ECCE Asia 2021, Institute of Electrical and Electronics Engineers Inc., May 2021, pp. 2069–2074. doi: 10.1109/ECCE-Asia49820.2021.9479401.

[140] C. R. Shah, M. Molinas, R. Nilsen, and M. Amin, ‘Impedance Reshaping of GFM Converters with Selective Resistive Behaviour for Small-signal Stability Enhancement’, in Conference Proceedings - IEEE Applied Power Electronics Conference and Exposition - APEC, Institute of Electrical and Electronics Engineers Inc., 2024, pp. 1619–1626. doi: 10.1109/APEC48139.2024.10509416.

[141] B. Liang, J. He, and C. Wang, ‘Resonance propagation analysis for inverter-dominated multi-AC-bus systems’, IET Renewable Power Generation, vol. 15, no. 10, pp. 2149–2159, Jul. 2021, doi: 10.1049/rpg2.12094.

[142] Q. C. and W. G. Zhong, ‘Static Synchronous Generators for Distributed Generation and Renewable Energy’, Mar. 2009, doi: https://doi.org/10.1109/PSCE.2009.4840013.

[143] G. Wu et al., ‘Impact of Non-Minimum-Phase Zeros on the Weak-Grid-Tied VSC’, IEEE Trans. Sustain. Energy, vol. 12, no. 2, pp. 1115–1126, Apr. 2021, doi: 10.1109/TSTE.2020.3034791.

[144] P. Vorobev, P. H. Huang, M. Al Hosani, J. L. Kirtley, and K. Turitsyn, ‘High-fidelity model order reduction for microgrids stability assessment’, IEEE Transactions on Power Systems, vol. 33, no. 1, pp. 874–887, Jan. 2018, doi: 10.1109/TPWRS.2017.2707400.

[145] A. Safavizadeh, T. Vahabzadeh, S. Ebrahimi, and J. Jatskevich, ‘Admittance-Based Aggregated Modeling of ConverterInterfaced Resources with Heterogeneous Parameters for Transient Analysis of Multi-Converter Systems’, IEEE Journal of Emerging and Selected Topics in Industrial Electronics, pp. 1–12, Jun. 2024, doi: 10.1109/jestie.2024.3416241.

[146] I. P. Nikolakakos, H. H. Zeineldin, M. S. El-Moursi, and J. L. Kirtley, ‘Reduced-Order model for Inter-Inverter oscillations in islanded Droop-Controlled microgrids’, IEEE Trans. Smart Grid, vol. 9, no. 5, pp. 4953–4963, Sep. 2018, doi: 10.1109/TSG.2017.2676014.

[147] G. K. Smyth, ‘Numerical Integration’, In Encyclopedia of Biostatistics; John Wiley & Sons: Hoboken, NJ. USA, pp. 3088–3095, 1997.

[148] A. W. Aurela, ‘The charge excess and momentum spectrum of cosmic ray muons in the vertical direction’, Doctoral Dissertation, Durham University, Durham, UK, 1965. Accessed: Aug. 08, 2025. [Online]. Available: http://etheses.dur.ac.uk/10511/

Appendix A: Chapter 3 Figures

1. Passivity Checking:

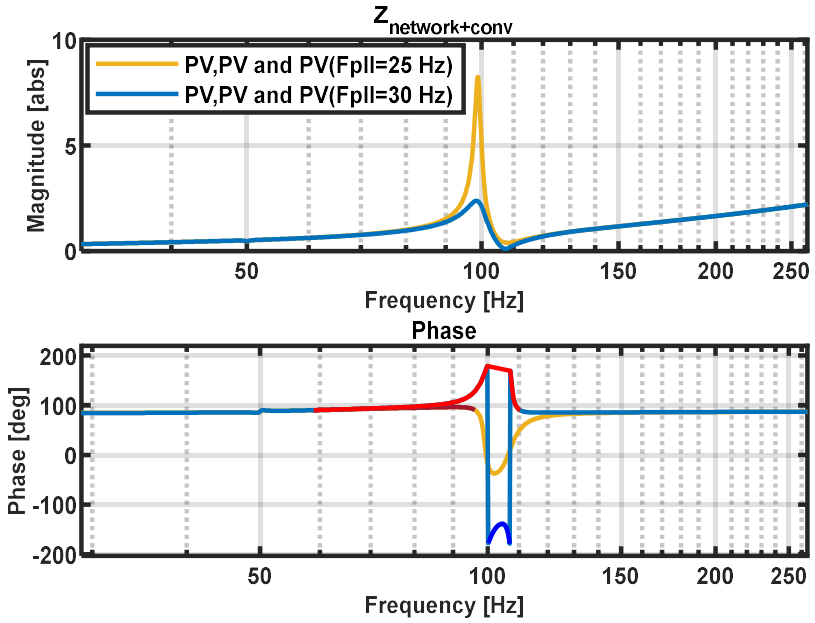

Figure A1:1 Assessment of Different PLLs for the (PV, PV) System

Figure A1.1 presents the converter input impedance when both terminals operate in PV mode. The two curves correspond to different PLL bandwidths:

Gold curve: $f_{PLL} = 25$ Hz and Blue curve: $f_{PLL} = 30$ Hz

- The assessment uses the frequency-domain impedance

$$Z(j\omega) = | Z(j\omega) | \ e^{j\phi(\omega)},$$

where passivity requires:

$$\Re\{Z(j\omega)\} \geq 0 \Leftrightarrow -90^{\circ} \leq \phi(\omega) \leq 90^{\circ}.$$

❖ Magnitude behaviour

- The 25 Hz PLL (gold) shows a sharper and higher resonant peak. A large impedance magnitude at resonance indicates strong energy exchange and a narrow stability margin.

- The 30 Hz PLL (blue) produces a broader and lower peak, indicating less amplification of grid-converter interactions and therefore improved damping.

❖ **Phase behaviour and Quadrant Mapping**

The phase angle directly reveals whether the impedance remains inside the passivity region.

Gold (25 Hz):

- Around the resonant frequency, the phase drops below –90°.
- This forces the Nyquist point into the third quadrant (negative real, negative imaginary).
- This region is non-passive, showing that the converter injects negative damping at that frequency.

Blue (30 Hz):

- The phase remains closer to the passivity boundary and enters the third quadrant only shallowly.
- It exits this region more quickly.
- This behaviour indicates weaker non-passive pockets and higher stability margin.

Table: Passivity in terms of quadrants:

Phase Range	Quadrant	Interpretation
$-90° < \phi < 0°$	4th	Passive region (positive real part).
$0° < \phi < 90°$	1st	Passive region.
$-180° < \phi < -90°$	3rd	Non-passive, negative damping.
$90° < \phi < 180°$	2nd	Non-passive, reactive dominance.

Therefore:

- Gold curve: deeper and wider movement in the third quadrant, confirming loss of passivity around resonance.
- Blue curve: limited third-quadrant excursion with faster recovery to the passive region.

❖ **Summary of Passivity Check**

- A wider passivity violation occurs with the 25 Hz PLL, caused by slower angle tracking and stronger coupling to the resonant mode.
- The 30 Hz PLL restricts the violation to a narrow frequency band, improving damping and ensuring that most of the impedance stays inside the first and fourth quadrants, where the real part remains positive.
- The figure shows that PLL bandwidth has direct control over the depth, width, and severity of the non-passive region, which is key when assessing stability of converter-dominated systems.

2. Converter network Interaction

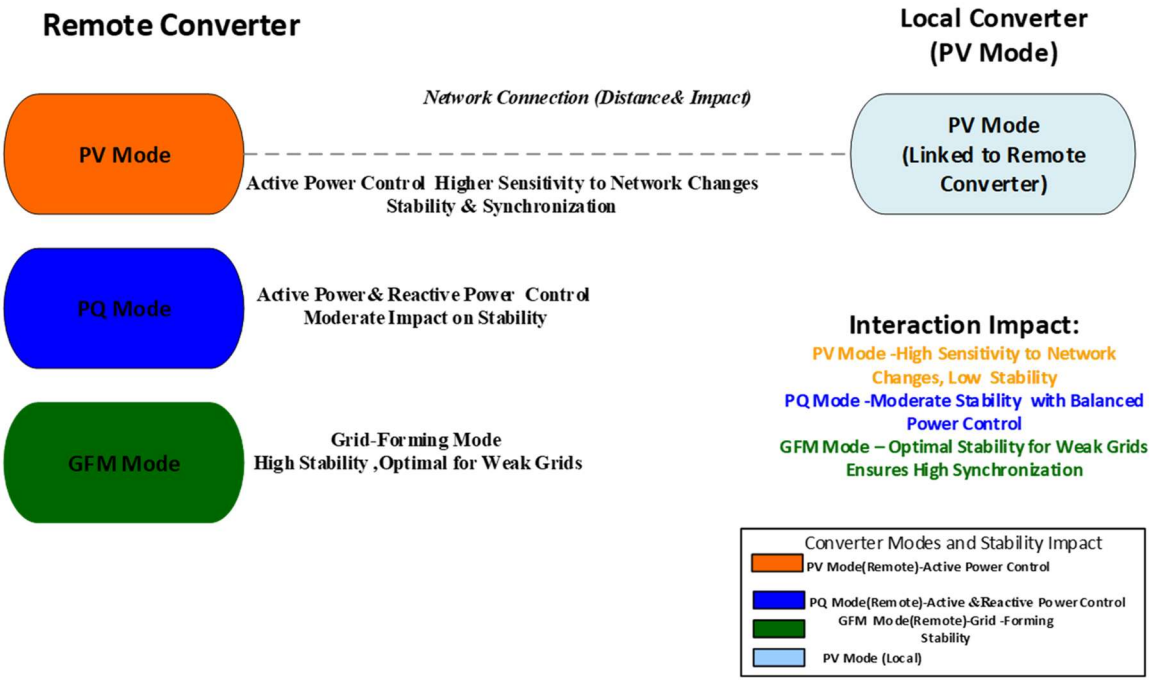

Figure A1:2 Influence of Control Parameter Interactions on Network Dynamics

Figure A1.2 - Influence of Control Parameter Interactions on Network Dynamics

- PV mode: Highly sensitive to weak-grid conditions; strong dependency on grid strength and remote-converter behaviour.
- PQ mode: Moderate sensitivity; delivers more stable and predictable power regulation.

- GFM mode: Most robust; maintains synchronisation and limits influence of network variations.
- Key Highlight: Coordinated tuning between converters is essential, especially when both operate in PV mode, to avoid adverse control interactions.

3. Varying P

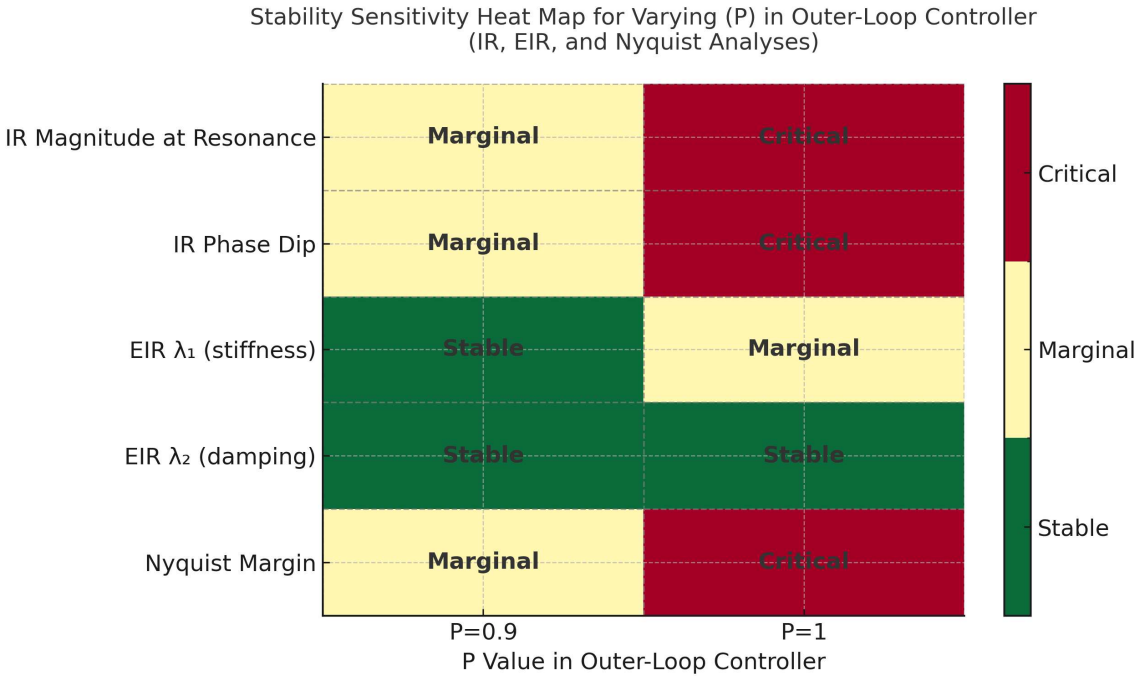

Figure A1: 3 Stability Sensitivity Heat Map for Varying Active Power (P)

Figure A1.3 - Stability Sensitivity Heat Map for Varying Active Power (P) (Summary)

- Low/medium power-loop gains: acceptable impedance metrics (resonance, phase, eigenvalues).
- Near unity gain: increased resonance, reduced phase margin, and eigenvalue movement toward marginal stability.
- Nyquist margin also decreases as gain increases.
- Key Highlight: Higher active-power gains raise instability risk; moderate gain provides the best stability performance trade-off.

Appendix B: Chapter 5 Figures

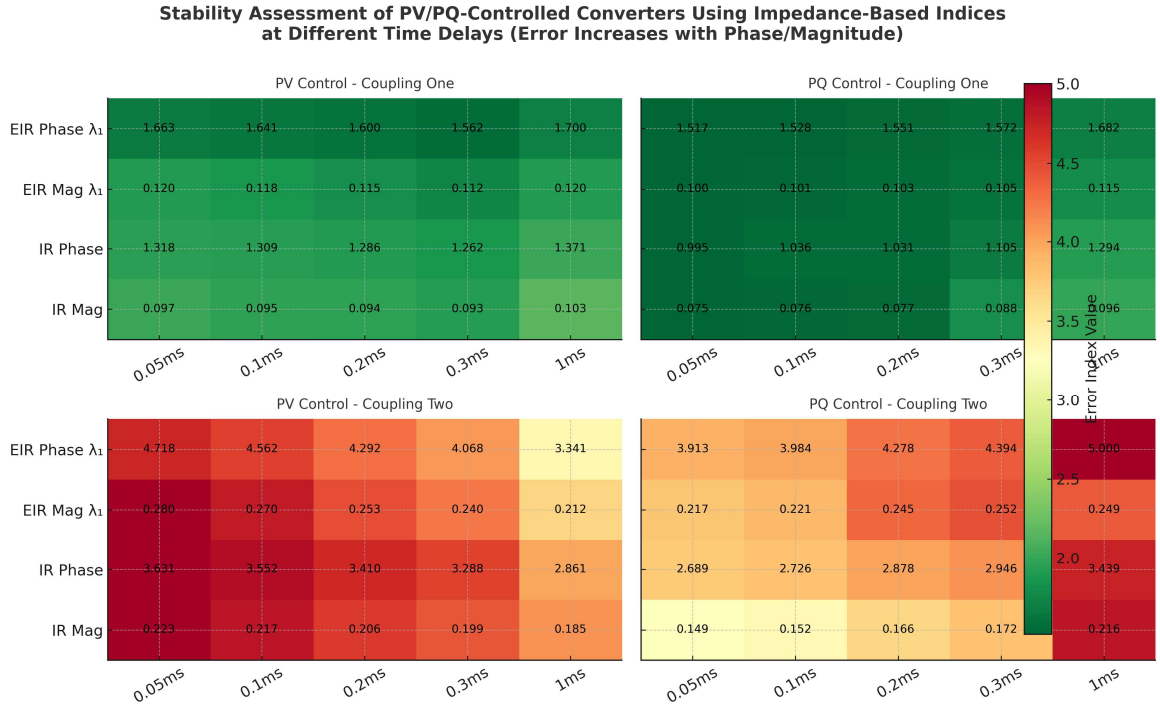

Figure B1:1 Impedance-Based Stability Indices Highlighting Best (Green) and Worst (Red) Delay Performance

This Figure B1:1 compares four impedance-based stability indices under varying control modes (PV/PQ) and coupling conditions. Green regions indicate low sensitivity to time delay and therefore better stability, while red regions mark high sensitivity and degraded stability. PV control under strong coupling (Coupling Two) shows the greatest performance deterioration as delay increases, whereas PQ control and weak-coupling scenarios maintain more favourable stability margins across all indices

Appendix C: Derivation and Calculation Concept

This appendix summarises the derivations and calculation steps used in the thesis. Full mathematical details and foundational proofs follow the sources cited in [54][34]. Where appropriate [54][34] for background and intermediate steps to keep the main document focused and readable.

Scope and mapping:

- Coordinate transformations: $abc \rightarrow \alpha\beta$, $\alpha\beta \rightarrow dq$, and $dq0$.
- Inverter modelling: averaged models and linearised forms used in the control design.
- PLL for GFL converters: derivation of $v_{abc} \rightarrow dq$under a rotating frame aligned to the estimated grid angle.
- Current controller: inner-loop model, transfer functions, and tuning relations.
- Power controller: active/reactive power regulation and outer-loop dynamics.
- GFM controller: voltage-forming structure, virtual impedance terms, and small-signal representation.
- Small-signal models: linearisation about operating points and state-space forms used for stability analysis.

Appendix D: Chapter 5 Derivation of Equations

❖ Conceptual Justification of the 0.1: 0.2 Lead-Lag Ratio

I. Compensator Structure (Series Connection)

The compensator $G_C(s)$is formed by a series connection of four standard elements used in impedance shaping: a gain block, a lead compensator, a lag compensator, and a digital delay. Since the blocks are in series, their transfer functions multiply:

$$G_C(s) = K_c\, G_{lead}(s)\, G_{lag}(s)\, G_{delay}(s)$$

The gain K_c sets the overall magnitude level.

II. Lead Compensator (Phase Boost near f_{lead})

The lead compensator is a first-order network with a zero placed before a pole:

$$G_{lead}(s) = \frac{1 + \alpha T_1 s}{1 + T_1 s}, \alpha > 1$$

This structure provides positive phase around the selected lead frequency.

III. Lag Compensator (Low-Frequency Gain and High-Frequency Attenuation)

The lag compensator is a first-order network with a pole placed before a zero:

$$G_{lag}(s) = \frac{1 + \beta T_2 s}{1 + T_2 s}, \beta < 1$$

The pole is located at $\omega_{p2} = 1/T_2$, and the zero at

$\omega_{z2} = 1/(\beta T_2)$.

Since $\beta < 1$, the pole appears at a lower frequency than the zero. This introduces phase lag and smooths the impedance at higher frequencies.

IV. Digital Control Delay

Sampling, computation, and PWM introduce an effective delay T_{d0}, modelled as

$$G_{delay}(s) = e^{-T_{do}s}, T_{d0} = 0.3 \text{ ms}$$

V. Final Compensator Expression

Combining all components gives:

$$G_C(s) = K_c(\frac{1 + \alpha T_1 s}{1 + T_1 s})(\frac{1 + \beta T_2 s}{1 + T_2 s})e^{-T_{do}s}$$

VI. Conceptual Interpretation

- $K_c$adjusts the overall magnitude.
- The lead term ($\alpha > 1$) increases phase near 250 Hz.
- The lag term ($\beta < 1$) improves low-frequency behaviour and reduces high-frequency effects near 50 Hz.
- The delay term represents digital implementation.

Together, these elements align the simplified and measured impedance models, reducing the modelling error to about 1% in the critical frequency range used for stability assessment.

❖ **Purpose of the Lead-Lag Compensator**

The lead-lag compensator corrects the mismatch between simplified impedance models and detailed EMT responses under weak-grid conditions. Simplified models may indicate stability while EMT simulations show instability. The compensator aligns both models in the frequency domain.

The time constants are centred at 250 Hz to target the dominant interaction mode.

❖ **Rationale for the 0.1: 0.2 Ratio**

The 0.1: 0.2 ratio is obtained from constrained frequency-domain optimisation and not from trial-and-error. It satisfies the following conditions:

- Phase Margin Improvement: Ensures a minimum of 45°, with typical values near 55° at 250 Hz.
- Bandwidth Preservation: Maintains the crossover frequency at 250 Hz without shifting resonant modes.
- Nyquist Stability Compliance: Prevents encirclement of the critical point under all tested conditions.
- High-Frequency Noise Control: Limits excessive gain and ensures digital feasibility.
- Model Matching Accuracy: Minimises magnitude and phase error between EMT and simplified models in the 50-250 Hz range.

❖ **Multi-Stage Compensation**

For higher accuracy, a multi-stage compensator with explicit delay modelling is applied. With lead dynamics at 250 Hz, lag dynamics at 50 Hz, and a delay of 0.3ms, the impedance error is reduced below 1% across the full critical frequency band while maintaining strict stability margins

Author's Publications

The author has also published the following article during the PhD study:

I. Gebremedhin, T., Xu, L., Chen, Y., & Chen, D. (2024). Assessment of Interactions of Multiple Converters and Network Considering Impedance Change. 2024 IEEE PES Innovative Smart Grid Technologies Europe (ISGT EUROPE), 1–5. https://doi.org/10.1109/ISGTEUROPE62998.2024.10863807

Abstract: This paper addresses the stability challenges arising from the integration of multiple converters into an AC network, spotlighting on potential instabilities generated by the interplay between converter control loops and the network's passive components. Employing an impedance-based approach that incorporates impedance ratio (IR) and examining a different control configuration such as active and reactive Power (PQ) and active Power and AC voltage (PV), alongside other parameters like phase-Locked loop (PLL), this work examines methodically the dynamic interactions. Through IR, it evaluates the individual impacts of converter (remote converter) on network equivalents, thereby elucidating how the interaction between converters and the broader network influences overall system stability. Ultimately, the proposed methodology aids in identifying impedance variations and potential instabilities in grid-tied converters, offering a roadmap for the perceptive design of converters and network parameter configurations.

II. Gebremedhin, T., Chen, Y., Xu, L. and Chen, D., 2024, December. Interactions and stability analysis of grid-forming and grid-following converters in close proximity: an impedance-based approach. In IET Conference Proceedings CP902 (Vol. 2024, No. 32, pp. 263-269). Stevenage, UK: The Institution of Engineering and Technology. https://doi.org/10.1049/icp.2024.4588

Abstract: This paper addresses the stability challenges of integrating multiple converters into AC networks, focusing on potential instabilities from interactions between converter control loops and network components. The increasing penetration of renewable energy necessitates a transition from grid-following (GFL) to grid-forming (GFM) control, particularly under weak-grid conditions. Using impedance-based models, this study investigates the impact of remote grid-forming converters on the stability of local converters.

Innovative methods, such as eigenvalue and impedance ratio (IR) analyses, evaluate system stability through frequency-dependent impedance changes. By representing the contributions of grid-forming and grid-following converters through impedance ratio (IR) value calculations, this methodology identifies impedance variations and potential instabilities in grid-tied converters, offering a roadmap for optimizing converter design and network parameters. The study also compares the impedance and stability of remote converters under grid-forming control with power synchronization and grid-following with Phase Locked Loop (PLL) (PV or PQ control modes) under varying frequency disturbances. The proposed methods and behaviours of grid-forming converters in network interactions are validated through time-domain simulations and analytical analysis, providing robust strategies for the stable integration of remote converters into AC networks

III. Gebremedhin, T. B. (2025). Model Reduction for Multi-Converter Network Interaction Assessment Considering Impedance Changes. Electronics, 14(16), 3285. https://doi.org/10.3390/electronics14163285

Abstract: This paper addresses stability issues in modern power grids arising from extensive integration of power electronic converters, which introduce complex multi-time-scale interactions. A symbolic simplification method is proposed to accurately model grid-connected converter dynamics, significantly reducing computational complexity through transfer function approximations and yielding efficient reduced-order models. An impedance-based approach utilizing impedance ratio (IR) is developed for stability assessment under active-reactive (PQ) and active power-AC voltage (PV) control strategies. The impacts of Phase-Locked Loop (PLL) and proportional-integral (PI) controllers on system stability are analysed, with a particular focus on quantifying remote converter interactions and delineating stability boundaries across varying network strengths and configurations. Furthermore, time-scale separation effectively simplifies Multi-Voltage Source Converter (MVSC) systems by minimizing inner-loop dynamics. Validation is conducted through frequency response evaluations, IR characterizations, and eigenvalue analyses, demonstrating enhanced accuracy, particularly with the application of lead–lag compensators within the critical 50-250 Hz frequency band. Time-domain simulations further illustrate the adaptability of the proposed models and reduction methodology, providing an effective and computationally efficient tool for stability assessment in converter-dominated power networks.

IV. **Submission pending**: Gebremedhin, T., Chen, Y., Xu, L. and Chen, D.," Impedance-Based Characterisation of Grid-Forming and Grid-Following Converter Interactions in Multi-VSC Systems"

Abstract: This paper presents an impedance-based analysis of stability in converter-dominated AC networks, focusing on interaction between grid-forming (GFM) and grid-following (GFL) converters. GFL units rely on PLL synchronisation and are sensitive to short-circuit ratio, factors that trigger resonances in weak grids. GFM units behave as controlled voltage sources with power-synchronisation, providing frequency and voltage regulation that strengthens the network. The method characterises frequency-dependent behaviour using impedance ratio and eigenvalue evaluation to identify resonance, damping, and oscillatory modes. Two- and three-converter cases, including hybrid GFL-GFM-GFL layouts, test the roles of control mode, device placement, and separation distance. Results show GFM converters keep impedance-ratio magnitude near unity with phase between 0° and −5°, which limits negative-resistance effects and reduces converter-network interaction. PQ-controlled GFLs are more stable than PV-controlled units, which show larger resonance shifts under weak synchronisation. Placement is critical: centrally sited GFMs deliver higher damping and better transient performance than boundary siting. Increasing separation strengthens interaction and shifts resonance toward lower frequencies. Time-domain EMT simulations confirm the analysis and provide thresholds for secure operation. The study provides clear design rules: position GFM converters at central nodes and pair them with PQ-controlled GFL units to achieve reliable performance in weak, renewable-dominated grids.